Universitat Politècnica de Catalunya
BarcelonaTech

Escola Tècnica Superior d'Enginyers de Camins, Canals i Ports de Barcelona

Doctoral Program in Civil Engineering

Doctoral Thesis

Wave Propagation Problems with Aeroacoustic Applications

Author:
Hector Espinoza

Supervisors:
Prof. Ramon Codina
Prof. Santiago Badia

2015

Acta de Calificación de Tesis Doctoral

Curso Académico: 2014-2015
Nombres y Apellidos: Héctor Gabriel, Espinoza Román
Programa de doctorado: Ingeniería Civil
Unidad estructural responsable del programa: ETSECCPB

Resolución del tribunal

Reunido el Tribunal designado a tal efecto, el doctorando / la doctoranda expone el tema de la su tesis doctoral titulada: *Wave Propagation Problems with Aeroacoustic Applications.*

Acabada la lectura y después de dar respuesta a las cuestiones formuladas por los miembros titulares del tribunal, éste otorga la calificación:

☐ NO APTO ☐ APROBADO ☐ NOTABLE ☐ SOBRESALIENTE

(Nombre, apellidos y firma) Presidente/a		(Nombre, apellidos y firma) Secretario/a
(Nombre, apellidos y firma) Vocal	(Nombre, apellidos y firma) Vocal	(Nombre, apellidos y firma) Vocal

El resultado del escrutinio de los votos emitidos por los miembros titulares del tribunal, efectuado por la Escuela de Doctorado, a instancia de la Comisión de Doctorado de la UPC, otorga la MENCIÓN CUM LAUDE:

☐ SÍ ☐ NO

(Nombre, apellidos y firma) Presidente de la Comisión Permanente de la Escuela de Doctorado	(Nombre, apellidos y firma) Secretario de la Comisión Permanente de la Escuela de Doctorado

_____ a _____ de _____ de _____.

to my family

Acknowledgement

I would like to acknowledge the help and constant support of my advisors Ramon Codina and Santiago Badia. Their guidance, scientific rigor and valuable suggestions made this work possible.

Additionally, I appreciate the opportune help from my workmates Joan Baiges, Matías Ávila and Christian Muñoz in various code implementation aspects. In addition, I would like to mention Ernesto, Fermin, Ester, Arnau and Alexis with whom I shared office during my doctoral period.

Likewise, I would like to mention Oscar Fruitos, Alberto Ferriz, Martí Coma and Luis Fernández from CIMNE-TTS where I worked in many interesting projects.

In addition, I would like to thank the support received from the EUNISON project (EU-FET grant 308874), specially from Oriol Guasch and Marc Arnela regarding the voice simulation cases.

Moreover, I would like to acknowledge Johan Hoffman and Niyazi Cem Degirmenci for their support during my short stay at Kungliga Tekniska Högskolan (Royal Institute of Technology) in Stockholm, Sweden. Additionally, I would like to mention Aurélien, Jeannette, Bärbel and Rodrigo whom I met at KTH.

Not to mention the support of my family that despite the distance is always with me in many ways.

Finally, I would like to acknowledge the Formación de Profesorado Universitario program from the Spanish Ministry of Education for their support through the doctoral grant AP2010-0563.

Abstract

The present work is a compilation of the research produced in the field of wave propagation modeling. It contains in-depth analysis of stability, convergence, dispersion and dissipation of spatial, temporal and spatial-temporal discretization schemes. Space discretization is done using stabilized finite element methods denoted with the acronyms ASGS and OSS. Time discretization is done using finite difference methods including backward Euler (BE), 2nd order backward differentiation formula (BDF2) and Crank-Nicolson (CN).

Firstly, we propose two stabilized finite element methods for different functional frameworks of the wave equation in mixed form. These stabilized finite element methods are stable for any pair of interpolation spaces of the unknowns. The variational forms corresponding to different functional settings are treated in a unified manner through the introduction of length scales related to the unknowns. Stability and convergence analysis is performed together with numerical experiments. It is shown that modifying the length scales allows one to mimic at the discrete level the different functional settings of the continuous problem and influence the stability and accuracy of the resulting methods.

Then, we develop numerical approximations of the wave equation in mixed form supplemented with non-reflecting boundary conditions (NRBCs) of Sommerfeld-type on artificial boundaries for truncated domains. Stability and convergence analyses of these stabilized formulations including the NRBC are presented. Additionally, numerical convergence tests are evaluated for various polynomial interpolations, stabilization methods and variational forms. Finally, several benchmark problems are solved to determine the accuracy of these methods in 2D and 3D.

Afterwards, we analyze time marching schemes for the wave equation in mixed form. The problem is discretized in space using stabilized finite elements. On the one hand, stability and convergence analyses of the fully discrete numerical schemes are presented. On the other hand, we use Fourier techniques (also known as von Neumann analysis) in order to analyze stability, dispersion and dissipation. Additionally, numerical convergence tests are presented for various time integration schemes, polynomial interpolations (for the spatial discretization), stabilization methods and variational forms. Finally, a 1D example is solved to analyze the behavior of the different schemes considered.

Later, we present various application examples and compare the numerical results of the different algorithms i.e. ASGS or OSS stabilization and BE, BDF2 or CN time marching schemes. Additionally, comparison with experiments is performed in some cases.

Finally, conclusions are drawn including the research achievements and future work.

Resumen

El presente trabajo es una compilación de la investigación producida en el campo de modelado de propagación de ondas. Contiene análisis de estabilidad, convergencia, dispersión y disipación de discretizaciones espaciales, temporales y espacio-temporales. La discretización espacial se hace usando elementos finitos estabilizados denotados por los acrónimos ASGS y OSS. La discretización temporal se hace usando métodos de diferencias finitas incluyendo backward Euler (BE), backward differentiation formula de 2do orden (BDF2) y Crank-Nicolson (CN).

En primer lugar, proponemos dos métodos de elementos finitos estabilizados para diferentes marcos funcionales de la ecuación de ondas en forma mixta. Estos métodos de elementos finitos estabilizados son estables para cualquier par de espacios de interpolación de las incógnitas. Las formas variacionales que corresponden a los diferentes marcos funcionales son tratadas de manera unificada a través de la introducción de longitudes de escalado relacionadas con las incógnitas. Estabilidad y convergencia son analizadas junto con experimentos numéricos. Se muestra como modificando las longitudes de escalado se puede reproducir a nivel discreto los diferentes marcos funcionales del problema continuo y como influencian la estabilidad y precisión de los métodos resultantes.

Luego, desarrollamos aproximaciones numéricas de la ecuación de ondas en forma mixta complementadas con condiciones de frontera de no-reflexión (NRBCs) de tipo Sommerfeld sobre fronteras artificiales para dominios truncados. Análisis de estabilidad y convergencia de estas formulaciones estabilizadas incluyendo la NRBC son presentados. Adicionalmente, pruebas de convergencia son llevadas a cabo para varias interpolaciones polinomiales, métodos de estabilización y formas variacionales. Finalmente, varios problemas de referencia son resueltos para determinar la precisión de estos métodos en 2D y 3D.

Después, analizamos esquemas de discretización temporal para la ecuación de ondas en forma mixta. El problema es discretizado en el espacio utilizando elementos finitos estabilizados. Por un lado, análisis de convergencia y estabilidad de los esquemas numéricos totalmente discretos son presentados. Por otro lado, usamos técnicas de Fourier (también conocidas como análisis de von Neumann) con el fin de analizar estabilidad, dispersión y disipación. Adicionalmente, pruebas numéricas de convergencia son presentadas para varios esquemas de integración temporal, interpolaciones polinomiales (para la discretización espacial), métodos de estabilización y formas variacionales. Finalmente, un ejemplo 1D es resuelto para analizar el comportamiento de los diferentes esquemas numéricos considerados.

Más tarde, presentamos varios ejemplos de aplicación y comparamos los resultados numéricos de los diferentes algoritmos. Por ejemplo estabilización ASGS/OSS y esquemas de integración temporal BD/BDF2/CN. Adicionalmente, se compara los resultados

numéricos con resultados experimentales en algunos casos.

Por último, las conclusiones son presentadas incluyendo los logros obtenidos en esta investigación y el trabajo futuro.

Contents

List of Figures

Chapter 1

Introduction

1.1 Motivation

Nowadays, aeroacoustics is a research topic of considerable interest with many practical applications. One application is in transport such as aeronautics and automotive design. In aeronautics there is trailing edge, landing gear and high lift systems sound. In automotive applications there are car/motorcycle body and helmet sound. Another application is voice simulation in which the vocal folds and vocal tract are taken into account in order to model the human voice.

Stringent regulation imposes the reduction of the perceived sound of automobiles and aircraft. For instance, the Advisory Council for Aeronautics Research in Europe includes a 50% cut in CO_2 emission per passenger-kilometer, an 80% cut in NO_x emissions, and a halving of perceived aircraft noise [1]. Additionally, NASA's Environmentally Responsible Aviation Project (ERA) has set goals for noise and emissions reduction and fuel performance improvements. This includes the N+1, N+2 and N+3 goals for the years 2015, 2020 and 2025 which set sound reduction levels of -32 dB, -42 dB and -71 dB with respect to the sound emitted by a Boeing 737-800 [2].

The advent of quieter jet engines has made noticeable the sound generated aerodynamically from landing gear and high lift systems. In new electric or efficient internal combustion engines for automotive applications it will probably happen something similar and other sources of sound will gain importance such as aerodynamic generated sound, contact sound (tyre-road contact) and frame/bodywork vibration sound.

Voice simulation can have medical applications to understand how voice problems arise and how they can be treated. Additionally, understanding the human phonation process can contribute to vocal training and development of new speech compression and synthesis algorithms and prosthetic larynges [3]. A research project directly related to voice simulation is the project Extensive Unified-Domain Simulation of the Human Voice (EUNISON) [4] in which we are currently participating.

Some publications where the reader is referred for voice simulation also known as human phonation simulation are [3, 5–7].

The sound produced in the applications described is broadband. It means it includes many frequencies. In some cases, one frequency or some frequencies can be dominant. Simulation methods include frequency domain and time domain methods. Time domain

methods are intrinsically broadband while frequency domain methods are single-band.

Aeroacoustics can be modeled using direct or indirect/hybrid computation. Hybrid computation involves an acoustic analogy, a flow solver and a wave propagation solver. Direct computation does not introduce any approximation but can be more computationally expensive. Wave propagation is modeled in time domain either with the irreducible wave equation or the mixed wave equation. The mixed wave equation becomes a natural option in problems involving moving domains because the equation can be set in an arbitrary Lagrangian-Eulerian frame of reference [5]. The present research focuses on the wave propagation part of hybrid aeroacoustic computation using the wave equation in mixed form. Spatial and temporal discretization is analyzed extensively and several application examples are shown.

1.2 Overview

Several methods have been used for the study of aeroacoustics and wave propagation. These methods vary from purely analytical to numerical methods. Among numerical methods, finite element methods (FEM), finite volume methods (FV), finite difference methods (FD) and boundary element methods (BEM) have been used for the study of wave propagation.

With respect to finite element methods, inf-sup stable elements and stabilized finite elements have been used in aeroacoustics and wave propagation.

The mathematical models used in aeroacoustics and wave propagation are diverse, among them we have: the classical scalar wave equation, the scalar Helmholtz equation, the linearized Euler equations, the wave equation in mixed form, the incompressible Navier-Stokes equations and the full Navier-Stokes equations.

In wave propagation non-reflecting boundaries (NRB) are needed. Several non-reflecting boundary conditions (NRBC) and non-reflecting boundary layers (NRBL) have been devised. Among NRBC, the Sommerfeld radiation condition is a classical example. Among NRBL, the Perfectly Matched Layer (PML) is very popular.

1.3 Wave Equations

1.3.1 Introduction

A wave equation is a PDE (Partial Differential Equation) that describes waves. Waves are commonly found in many physical phenomena such as: acoustics, fluid dynamics, elastodynamics and electromagnetics. We will focus on waves propagating in fluids.

A wave propagating in air is historically known as sound because, for a certain frequency range, human beings are able to hear it when the wave reaches our auditory system. Some authors refer to noise propagation but we prefer to call it sound propagation for generality.

Waves can be described in time domain or frequency domain. Time is denoted as $t \in (0, T)$ and angular frequency is denoted as ω. Both time and frequency domain analysis involve a spatial domain $\Omega \subset \mathbb{R}^d$, where d is the dimension of the spatial domain ($d = 1, 2, 3$). Let $\boldsymbol{x} \in \Omega$ be any point of the spatial domain Ω and let Γ be the boundary of the spatial domain Ω. From hereafter, we will refer to vectors in $\mathbb{R}^d$ simply as vectors.

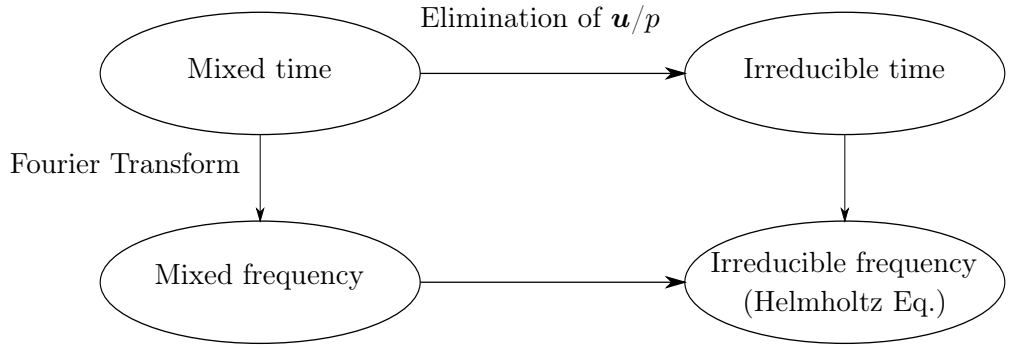

Figure 1.1: Wave equations in time/frequency domain

Given that complex numbers will appear at some point, we will refer to complex numbers or real numbers explicitly, but whenever we omit the complex or real specification real values have to be assumed.

Named after Leonhard Euler, Euler's Formula establishes a relationship between trigonometric functions and the complex exponential function. For any $x \in \mathbb{R}$ it holds:

$$\mathrm{e}^{\mathrm{i}x} = \cos x + \mathrm{i} \sin x, \tag{1.1}$$

where e is the base of the natural logarithm, i is the imaginary unit, $\cos(\cdot)$ and $\sin(\cdot)$ are the trigonometric functions cosine and sine respectively and x is given in radians. The formula is still valid if x is a complex number but across this document we will restrict x to real numbers.

1.3.2 Wave Equations in time domain and frequency domain

Fig. 1.1 shows a sketch of the relationship of the wave equations in time and frequency domain.

Time domain analysis uses the scalar wave equation in its irreducible form (1.2):

$$\frac{1}{c^2}\partial_{tt} p' - \Delta p' = f', \tag{1.2}$$

where $p'(\boldsymbol{x}, t)$ is the unknown (real valued scalar function), f' is a forcing term and c is the wave speed.

Additionally, time domain analysis can involve the vector wave equation in irreducible form (1.3):

$$\frac{1}{c^2}\partial_{tt} \boldsymbol{u}' - \Delta \boldsymbol{u}' = \boldsymbol{f}', \tag{1.3}$$

where $\boldsymbol{u}'(\boldsymbol{x}, t)$ is the unknown (real valued vector function) and $\boldsymbol{f}'$ is a forcing term.

Notice that the vector wave equation in irreducible form (1.3) has no practical interest since the regularity requirement for the vector unknown $\boldsymbol{u}'$ is the same as the regularity requirement for the scalar unknown p' in the scalar wave equation in irreducible form (1.2) but the number of unknowns is d times bigger in the vector wave equation with respect to the scalar wave equation.

Furthermore, time domain analysis can involve the wave equation in mixed form (1.4)-(1.5):

$$\mu_p \partial_t p' + \nabla \cdot \boldsymbol{u}' = f_p, \tag{1.4}$$
$$\mu_u \partial_t \boldsymbol{u}' + \nabla p' = \boldsymbol{f}_u, \tag{1.5}$$

where $p'(\boldsymbol{x}, t)$ and $\boldsymbol{u}'(\boldsymbol{x}, t)$ are the unknowns, with p' real valued scalar function and $\boldsymbol{u}'$ real valued vector function, $\mu_p > 0$ and $\mu_u > 0$ are the parameters of the equation and $[f_p, \boldsymbol{f}_u]$ are forcing terms.

Notice that the number of unknowns in the wave equation in mixed form is $d+1$ times the number of unknowns in the scalar wave equation in irreducible form, but the regularity requirements in space and time are less stringent for both p' and $\boldsymbol{u}'$.

On the contrary, frequency domain analysis involves using the Scalar Helmholtz Equation (1.6):

$$\Delta \hat{p} + k^2 \hat{p} = \hat{f}_k, \tag{1.6}$$

where $\hat{p}(\boldsymbol{x})$ is the unknown (complex valued scalar function), k is the wavenumber corresponding to a certain angular frequency ω and $\hat{f}_k$ is a forcing term.

Additionally, frequency domain analysis can involve the Vector Helmholtz Equation (1.7):

$$\Delta \hat{\boldsymbol{u}} + k^2 \hat{\boldsymbol{u}} = \hat{\boldsymbol{f}}_k, \tag{1.7}$$

where $\hat{\boldsymbol{u}}(\boldsymbol{x})$ is the unknown (complex valued vector function), k is the wavenumber corresponding to a certain angular frequency ω and $\hat{\boldsymbol{f}}_k$ is a forcing term.

Notice that the Vector Helmholtz equation (1.7) has no practical interest since the regularity required for the vector unknown $\hat{\boldsymbol{u}}$ is the same as the regularity required for the scalar unknown $\hat{p}$ in the Scalar Helmholtz equation (1.6) but the number of unknowns is d times bigger.

Additionally, frequency domain analysis can involve the Helmholtz Equation in mixed form (1.8) - (1.9):

$$-\mathrm{i}\mu_p \omega \hat{p} + \nabla \cdot \hat{\boldsymbol{u}} = \hat{f}_p, \tag{1.8}$$
$$-\mathrm{i}\mu_u \omega \hat{\boldsymbol{u}} + \nabla \hat{p} = \hat{\boldsymbol{f}}_u, \tag{1.9}$$

where $\hat{p}(\boldsymbol{x})$ and $\hat{\boldsymbol{u}}(\boldsymbol{x})$ are the unknowns, ω is the angular frequency, $\mu_p > 0$ and $\mu_u > 0$ are parameters of the equation and $\hat{f}_p$ and $\hat{\boldsymbol{f}}_u$ are forcing terms.

Notice that the number of unknowns in the Mixed Helmholtz equation is $d+1$ times the number of unknowns in the Scalar Helmholtz Equation, but the regularity requirements (in space) are less stringent for both $\hat{p}$ and $\hat{\boldsymbol{u}}$.

Until now, we have expressed wave equations in terms of either p' or $\boldsymbol{u}'$ or both. Additionally we have used their complex counterparts $\hat{p}$ or $\hat{\boldsymbol{u}}$. There is one more approach which uses the Velocity Potential ψ. The velocity potential wave equation is written as:

$$\frac{1}{c^2} \partial_{tt} \psi - \Delta \psi = f_\psi, \tag{1.10}$$

from which we can extract p' or $\boldsymbol{u}'$ as follows:

$$p' = -\mu_u \partial_t \psi + f_{\psi,p}, \tag{1.11}$$
$$\boldsymbol{u}' = \nabla \psi, \tag{1.12}$$

where $\nabla f_{\psi,p} = \boldsymbol{f}_u$.

Notice that the wave equation in mixed form is in agreement with the velocity potential wave equation taking $f_\psi = \mu_p \partial_t f_{\psi,p} - f_p$.

Now let us consider the complex counterpart $\hat{\psi}$ and let us write the Helmholtz Equation in terms of the complex velocity potential:

$$\Delta\hat{\psi} + k^2\hat{\psi} = \hat{f}_\psi, \tag{1.13}$$

from which we can extract $\hat{p}$ or $\hat{\boldsymbol{u}}$ as follows:

$$\hat{p} = \mathrm{i}\mu_u \omega \hat{\psi} + \hat{f}_{\psi,p}, \tag{1.14}$$
$$\hat{\boldsymbol{u}} = \nabla\hat{\psi}, \tag{1.15}$$

where $\nabla \hat{f}_{\psi,p} = \hat{\boldsymbol{f}}_u$.

Wave equations in time domain or frequency domain are related to each other. Unknowns, coefficients and forcing terms of the equations are related. In the next paragraphs we show these relationships for the unknowns and coefficients only. The relationship between forcing terms is trivial.

The coefficients μ_p and μ_u that characterize the mixed wave equation (1.4) - (1.5) are related to the wave speed c appearing in irreducible form of the scalar wave equation (1.2) or vector wave equation (1.3) as follows:

$$c^2 = (\mu_p \mu_u)^{-1}. \tag{1.16}$$

The wavenumber k characterizes the Scalar Helmholtz equation (1.6) and the Vector Helmholtz Equation (1.7) and is related to the wave speed c appearing in irreducible form of the wave equation (1.2) as follows:

$$\omega = kc = 2\pi f, \tag{1.17}$$

where ω is the angular frequency and f is the frequency.

Assuming harmonic behavior of p' with angular frequency ω and phase angle ϕ, we can write:

$$p'(\boldsymbol{x}, t) = \Re\left(\hat{p}(\boldsymbol{x})\,\mathrm{e}^{-\mathrm{i}\omega t}\right) = \Re(\hat{p})\cos(\omega t) + \Im(\hat{p})\sin(\omega t) = |\hat{p}|\cos(\omega t - \phi), \tag{1.18}$$

where $\Re()$ and $\Im()$ stand for real part and imaginary part respectively, $|\hat{p}|$ is the magnitude of $\hat{p}$ defined as $|\hat{p}| := \sqrt{(\Re(\hat{p}))^2 + (\Im(\hat{p}))^2}$ and $\phi := \arctan\left(\frac{\Im(\hat{p})}{\Re(\hat{p})}\right)$ is the argument of $\hat{p}$. Similarly, we can write:

$$\boldsymbol{u}'(\boldsymbol{x}, t) = \Re\left(\hat{\boldsymbol{u}}(\boldsymbol{x})\,\mathrm{e}^{-\mathrm{i}\omega t}\right) = \Re(\hat{\boldsymbol{u}})\cos(\omega t) + \Im(\hat{\boldsymbol{u}})\sin(\omega t). \tag{1.19}$$

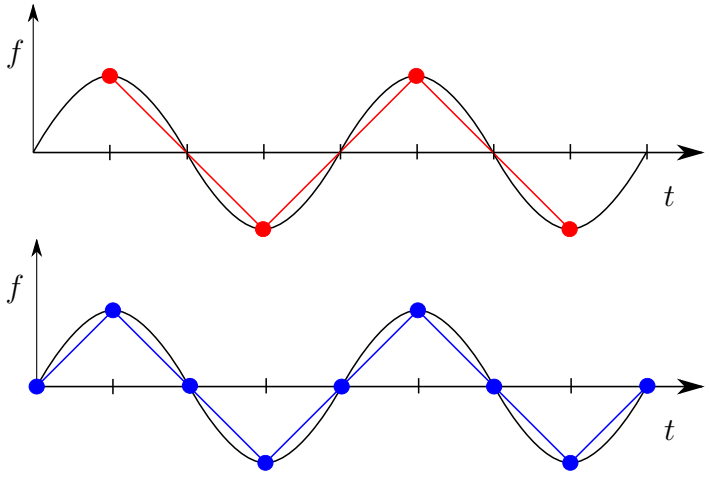

Figure 1.2: Nyquist frequency

The wave equation (scalar irreducible (1.2) , vector irreducible (1.3) or in mixed form (1.4) - (1.5)) is solved in a spatial domain Ω and in a time interval $(0, T)$ with appropriate initial and boundary conditions.

The Helmholtz Equation in scalar, vector or mixed form ((1.6), (1.7) or (1.8) - (1.9)) is solved in a domain Ω and for a given wavenumber k with appropriate boundary conditions.

Notice that frequency domain analysis solves the wave problem for one angular frequency ω whereas time domain analysis solves the wave problem for the full range of frequencies involved. The only limit for the frequencies captured in the time domain analysis (at time-discrete level) is the time step used for time discretization.

1.3.3 Nyquist Frequency

Named after Harry Nyquist, the Nyquist frequency is one half of the sampling rate of a discrete signal processing system. The Nyquist frequency is used in time domain and spatial domain. The time domain sampling of a function is measured in samples per unit time. The spatial domain sampling of a function will be samples per unit distance.

The Nyquist frequency represents the maximum frequency that can be accurately reproduced by a discrete signal processing system. We can say the same but the other way around: given a signal with a certain frequency, we will need a sampling rate twice as big to accurately capture the signal.

In Fig. 1.2 we have a function f with frequency f sampled with with $2f$ samples per unit time. The second figure is the same function f sampled with $4f$ samples per unit time.

The Nyquist frequency can be translated to numerical methods to find the time step size Δt and the mesh size h. Let us assume acoustic waves in air of frequency $f = 20000$ Hz (extreme case). The wave speed is $c = 340$ m/s. For the given frequency and wave speed, the wavelength is $\lambda = \frac{c}{f} = 0.017$ m The time step required will be $\Delta t = \frac{1}{40000}$ s or smaller and the mesh size required will be $h = 0.0085$ m or smaller.

1.3.4 Acoustic Waves in Fluids

Wave propagation in fluids is known as Acoustics. The wave speed is a property of the fluid media. It can be computed as:

$$c^2 = \left.\frac{\partial p}{\partial \rho}\right|_s, \tag{1.20}$$

where p is the thermodynamical pressure (absolute pressure) and ρ is the mass density. The s indicates a process with constant entropy.

An ideal gas has a simple equation of state defined as:

$$p = \rho R_\mathrm{s} T, \tag{1.21}$$

where R_s is the specific ideal gas constant and T is the absolute temperature. The specific ideal gas constant is related to the universal ideal gas constant R_u through:

$$R_\mathrm{s} = \frac{R_\mathrm{u}}{M}, \tag{1.22}$$

where M is the molar mass of the gas and $R_\mathrm{u} = 8.3144\,\mathrm{m^3\,Pa\,K^{-1}\,mol^{-1}}$.

Then, for an ideal gas the equation defining the speed of sound is:

$$c^2 = \gamma \frac{p}{\rho} = \gamma R_\mathrm{s} T, \tag{1.23}$$

where γ is the specific heat ratio (1.4 for air).

In air, the sound speed can be considered constant for any wave frequency. That brings us to the concept of dispersive and non-dispersive media. In dispersive media the wave speed is dependent of the frequency of the wave. On the other hand, in non-dispersive media the wave speed is independent of the frequency.

In a fluid the parameters of the wave equation in mixed form are taken as:

$$\mu_p = \frac{1}{\rho_0 c^2}, \quad \mu_u = \rho_0, \tag{1.24}$$

where ρ_0 is the mass density and c is the speed of sound, with both ρ_0 and c in the reference state.

1.3.5 Wave Energy

The wave equation in mixed form has an internal structure of energy conservation.

Let us define e as the energy density (energy per unit volume) in a point of a domain as:

$$e = \frac{1}{2}\left(\mu_p p'^2 + \mu_u |\boldsymbol{u}'|^2\right), \tag{1.25}$$

where $e_p = \frac{1}{2}\mu_p p'^2$ is the potential energy density and $e_k = \frac{1}{2}\mu_u |\boldsymbol{u}'|^2$ is the kinetic energy density. For a plane wave the kinetic and potential energy are the same.

Let E be the total energy of the domain in consideration:

$$E = \int_\Omega e \, \mathrm{d}\Omega, \tag{1.26}$$

let $\boldsymbol{i}$ be the wave intensity in a given point of the domain:

$$\boldsymbol{i} = p'\boldsymbol{u}', \tag{1.27}$$

let I_b be the total power going from the domain to the outside through the boundary Γ:

$$I_b = \int_\Gamma \boldsymbol{n} \cdot \boldsymbol{i} \, \mathrm{d}\Gamma, \tag{1.28}$$

let i_f be the energy per unit time per unit volume added by the forcing terms:

$$i_f = p' f_p + \boldsymbol{u}' \cdot \boldsymbol{f}_u, \tag{1.29}$$

and, finally, let I_f be the total power added to the domain by the forcing terms:

$$I_f = \int_\Omega i_f \, \mathrm{d}\Omega. \tag{1.30}$$

Then, the energy conservation statement can be written as:

$$\frac{\mathrm{d}E}{\mathrm{d}t} + I_b = I_f. \tag{1.31}$$

Additionally, it holds:

$$\partial_t e + \nabla \cdot \boldsymbol{i} = i_f. \tag{1.32}$$

1.4 Non-Reflecting Boundaries (NRB)

1.4.1 Introduction

Partial Differential Equations (PDE) involve a domain where the unknowns have to be determined. The domain can be space ($\Omega_f \subseteq \mathbb{R}^d$), time $(0, T)$ or space-time ($\Omega_f \times (0, T)$).

Let us concentrate in the spatial part of the domain and let us consider a numerical approximation method to solve the PDE. We are interested in Finite Elements, but the numerical method can be Finite Differences or Finite Volumes. Recall that we have used $\subseteq$ to define Ω_f, this means that some PDEs might need infinite or semi-infinite spatial domains in order to be solved. That brings a problem since we cannot discretize all $\mathbb{R}^d$ with a finite number of elements of finite size h. So, instead of solving the PDE in Ω_f, we solve it in $\Omega \subset \Omega_f$ such that meas(Ω) is finite. Obviously, the boundary Γ of Ω is designed smooth enough and with a convenient shape. Then, another question arises: we know the boundary condition to impose on the boundary Γ_f of Ω_f but we do not know what to impose on Γ.

In some problems the unknowns or their gradients decay fast enough in space, so that imposing the same boundary condition of Γ_f on Γ and choosing Ω sufficiently large is

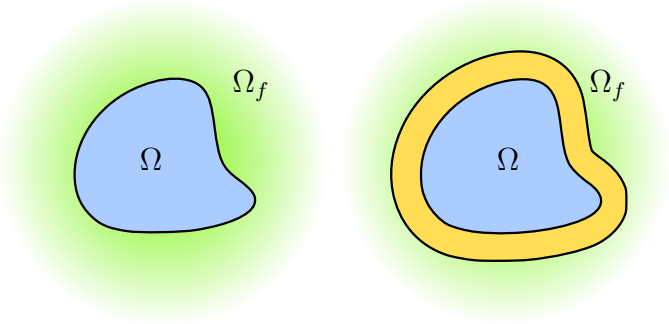

Figure 1.3: NRB families: NRBC and NRBL

good enough. But, some other problems such as wave propagation problems in which the unknown decays with distance r as $r^{-\frac{(d-1)}{2}}$ can require prohibitively big spatial domains in order that the imposition of the same boundary condition of Γ_f on Γ is good enough.

Furthermore, energy will bounce back when it reflects on Γ and it will remain inside Ω perturbing the solution thereafter. The boundary solution is obvious but not trivial: not imposing the same condition of Γ_f on Γ. The ideal non reflecting boundary condition should be such that the solution in Ω_f restricted to Ω is the same as the solution obtained in Ω.

This leads to the introduction of Non-Reflecting Boundary Conditions (NRBC) and Non-Reflecting Boundary Layers (NRBL). We will refer to NRBC and NRBL simply as Non-Reflecting Boundaries (NRB).

Throughout this document, we denote as NRBC to boundary conditions applied on Γ and as NRBL to an added layer of material after Γ (see Fig. 1.3).

NRBC are also known as Absorbing Boundary Conditions (ABC), Artificial Boundary Conditions (ABC) or Open Boundary Conditions (OBC).

Acoustic wave propagation problems often involve the calculation of acoustic intensity at a given point due to a given set of acoustic sources. Using a perfect NRB we obtain an intensity $\boldsymbol{i}_f$ at each spatial point. Using an approximate NRB we obtain an intensity $\boldsymbol{i}$. A good NRB will lead to an intensity $\boldsymbol{i}$ close to $\boldsymbol{i}_f$.

In what follows, we will describe the Sommerfeld boundary condition (a type of NRBC), some other NRBCs and finally the Perfectly Matched Layer (PML) which is a type of NRBL. But first let us start with some basic concepts of impedance, reflection and refraction.

1.4.2 Impedance

Let us consider an harmonic force (perfect sine or cosine variation in time). The ratio of the complex amplitude of the force to the complex amplitude of the velocity at a given point on a surface is called mechanical impedance at the point:

$$Z = \frac{\hat{p}}{\hat{u}_n}, \tag{1.33}$$

where Z is the mechanical impedance and $\hat{u}_n$ is the normal component of $\hat{\boldsymbol{u}}$ in the direction towards the surface (pointing outside of the fluid). Obviously, Z is a complex number

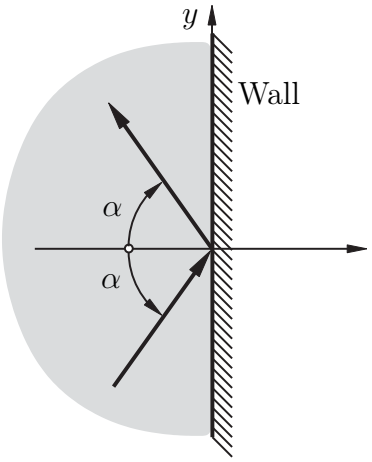

Figure 1.4: Plane Wave Reflection

since $\hat{p}$ and $\hat{\boldsymbol{u}}$ are complex. The real part of Z is called Resistance and its imaginary part Reactance. The inverse $1/Z$ is known as Admittance.

In acoustics the definition of characteristic impedance is:

$$Z_{\text{char}} = \left(\frac{\mu_u}{\mu_p}\right)^{\frac{1}{2}}. \tag{1.34}$$

The characteristic impedance is inherent to the propagation media. Let us assume we divide a domain with an artificial boundary of impedance Z. Now we require that the artificial boundary has no effect on the wave field on both sides of the boundary. Then, the impedance needed for this artificial boundary is the characteristic impedance.

The power per unit surface through a surface of impedance Z is:

$$\boldsymbol{i}_Z = \Re(Z)|\boldsymbol{n} \cdot \hat{\boldsymbol{u}}|^2, \tag{1.35}$$

where $\boldsymbol{n}$ is the unit outward normal to the surface. Notice that when $\Re(Z) > 0$ the surface is passive and absorbs energy, but when $\Re(Z) < 0$ the surface is active and produces energy.

1.4.3 Reflection and Refraction

Before describing NRB, let us first describe the reflection and refraction phenomena.

Wave Reflection

Let us consider a plane wave in the $x - y$ plane incident in the $y - z$ plane (see Fig. 1.4). Assuming a perfect reflection (zero absorption), the reflected wave will have identical wavenumber and angle α as the incident wave [8].

Now, let us consider the surface has a finite impedance Z and that the incident wave has the following form:

$$\hat{p}_{\text{in}} = \hat{A}\mathrm{e}^{\mathrm{i}(k_x x + k_y y)}, \tag{1.36}$$

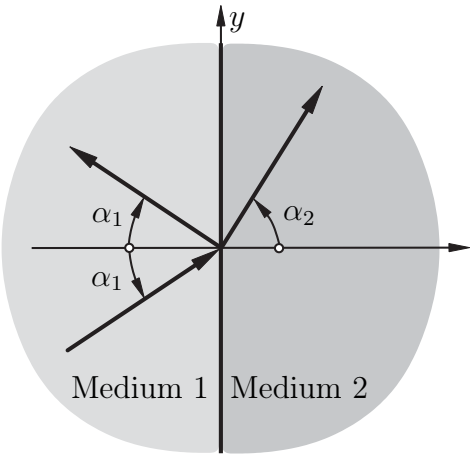

Figure 1.5: Plane Wave Refraction

where k_x and k_y are the wavenumber components in the x and y direction respectively and $\hat{A}$ is the complex amplitude of the incident wave.

The reflected wave will have the following form:

$$\hat{p}_{\text{re}} = \mathcal{R}\hat{A}\mathrm{e}^{\mathrm{i}(-k_x x + k_y y)}, \tag{1.37}$$

where $\mathcal{R}$ is the reflection coefficient that can be computed as:

$$\mathcal{R} = \frac{\xi\cos(\alpha) - 1}{\xi\cos(\alpha) + 1}, \tag{1.38}$$

with

$$\xi = \frac{Z}{Z_{\text{char}}}. \tag{1.39}$$

In the wave equation in mixed form, the condition of perfect reflection on a segment Γ_u of the boundary Γ can be modeled imposing $\boldsymbol{n}\cdot\boldsymbol{u}' = 0$. On the other hand, the boundary condition $p' = 0$ on a segment Γ_p of the boundary Γ represents a pressure released surface. This is an idealization of the interface water-air when considering wave propagation in the water [9].

Wave Refraction

Now, let us consider a wave impacting at the interface between two fluids with wave velocities c_1 and c_2 (see Fig. 1.5). The compatibility condition required in this case is that the trace velocity at the interface of both mediums match. This is known as the *trace velocity matching* [10]. The trace velocity is the tangent component of the velocity at the interface.

There are two cases: the trace velocity is higher than c_2 or lower than c_2. Let us consider the first case (trace velocity higher than c_2):

$$c_2 < \frac{c_1}{\sin\alpha_1}. \tag{1.40}$$

There is a transmitted wave in medium 2 with the form:

$$\hat{p}_{\text{tr}} = \mathcal{T}\hat{A}\mathrm{e}^{\mathrm{i}(k_x x + k_2 y \cos\alpha_2)}, \tag{1.41}$$

where k_2 is the wavenumber in the second medium and α_2 is the refraction or transmission angle.

The requirement that the pressure is continuous at the interface yields:

$$1 + \mathcal{R} = \mathcal{T}, \tag{1.42}$$

and the trace velocity matching yields:

$$\frac{\cos\alpha_1}{Z_{\text{char},1}}(1 - \mathcal{R}) = \frac{\cos\alpha_2}{Z_{\text{char},2}}\mathcal{T}. \tag{1.43}$$

In the second case, when the wave speed at the second medium c_2 is greater than the trace velocity at the interface, the transmission depends on the incidence angle. Obviously, it can only occur when $c_2 > c_1$. Let us define the critical angle as:

$$\alpha_{\text{cr}} = \arcsin\frac{c_1}{c_2}. \tag{1.44}$$

If the incidence angle α_1 is greater than the critical angle α_{cr}, all the energy is reflected in the interface. If the incidence angle α_1 is less than the critical angle α_{cr}, there is a wave transmitted and a wave reflected [8].

1.4.4 Sommerfeld Boundary Condition

The Sommerfeld boundary condition is a type of NRBC and gets its name from Arnold Sommerfeld who was a German theoretical physicist. Sommerfeld mentions it in [11] as:

> "The sources must be sources, not sinks, of energy. The energy which is radiated from the sources must scatter to infinity; no energy may be radiated from infinity into the prescribed singularities of the field".

The Sommerfeld radiation condition is applicable when the sources are concentrated in a region of space and the exterior boundary is a sphere surrounding it and centered at the source region. Additionally, the spherical surface has to be sufficiently far away to the sources in order that the impinging waves only have radial component.

In spherical coordinates and for the Helmholtz equation in 3D, the Sommerfeld radiation condition can be expressed as:

$$\lim_{r\to\infty}\left(r\left(\partial_r\hat{p} - \mathrm{i}k\hat{p}\right)\right) = 0, \tag{1.45}$$

where r is radial component in the spherical coordinate system. Some authors write the Sommerfeld radiation condition with a + sign, but that depends on the time variation assumption. Throughout this document we have assumed a time variation $e^{-\mathrm{i}\omega t}$ which gives the minus sign.

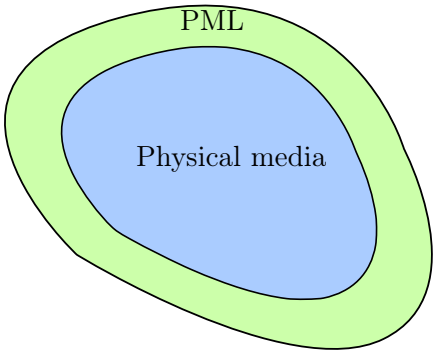

Figure 1.6: PML concept

In 2D or 3D ($d = 2, 3$) the Sommerfeld radiation condition can be expressed as:

$$\lim_{r\to\infty}\left(r^{\frac{d-1}{2}}\left(\partial_r\hat{p} - \mathrm{i}k\hat{p}\right)\right) = 0. \tag{1.46}$$

In time domain and for the scalar wave equation in 3D the Sommerfeld radiation condition can be written as:

$$\lim_{r\to\infty}\left(r\left(\partial_r p' + \frac{1}{c}\partial_t p'\right)\right) = 0. \tag{1.47}$$

1.4.5 Other NRBC

NRBCs impose a boundary condition that mimics a non-reflecting boundary without needing to add an absorbing boundary layer. From the computational cost point of view NRBC do not add extra degrees of freedom to the problem being solved and that is a very appealing feature.

Before, we described the Sommerfeld Radiation condition, which is a well known NRBC, but there are many other NRBC. Some authors have proposed Dirichlet-to Neumann mappings [12, 13] from domain decomposition methods, others proposed High Order Boundary Conditions [14–17] while others proposed simpler approaches [18–20].

NRBC formulations have been formulated for the irreducible form of the wave equation in [14–16, 21–28], for the scalar Helmholtz equation in [12, 13, 29, 30], for the wave equation in mixed form in [17–20] and for flow problems in [31–33].

1.4.6 Perfectly Matched Layer

The concept of perfectly matched layer (PML) was first developed by Berenger in 1994 for electromagnetic waves [34]. It consists in an artificial absorbing boundary layer placed next to the wave propagating media with the property of absorbing waves incident to it. A graphical representation of the absorbing layer can be seen in Fig. 1.6. PML has been used since its appearance in many problems such as the scalar wave equation in irreducible form [35–37], scalar Helmholtz equation [38–40], mixed form of the wave equation [41–44] and electromagnetic waves [34, 45–47].

Theoretically, PML absorbs waves at any angle of incidence but since we are not solving the exact problem (continuous) its absorptivity properties are not perfect. Therefore, in

practical terms, PML has the ability to absorb incident waves in a wide range of angles of incidence. Another feature is that absorbing properties are good for a wide range of frequencies. When comparing PML with the Sommerfeld Radiation condition, the main advantage of PML is the absorptivity in a wide range of angles of incidence because the Sommerfeld radiation condition assumes (or requires) a normal angle of incidence in order to be accurate.

The original Berenger's formulation of PML is called split field PML because he split the solution into two artificial fields whose sum is the physical field. Nowadays, it is more popular the Uniaxial PML formulation (UPML) in which the wave equation is expressed as the combination of artificial anisotropic absorbing materials. Anyway, both PML and UPML are equivalent and can be derived from complex coordinate stretching.

Let us now refer to Fig. 1.6. The wave equation (in time or frequency domain) is solved in the Physical media and the PML equations are solved in the PML absorbing layer.

Now, let us describe the formulation of PML applied to the wave equation in mixed form. For simplicity we will consider the 2D case, but the extension to 3D is straightforward. The formulation we describe here appears in [42] and was implemented and tested using the finite difference method.

Let us split p such that:

$$p = p_a + p_b, \tag{1.48}$$

then, the governing equations in the PML layer are:

$$\partial_t u_1 + q_1 u_1 + \partial_1 (p_a + p_b) = 0, \tag{1.49}$$
$$\partial_t u_2 + q_2 u_2 + \partial_2 (p_a + p_b) = 0, \tag{1.50}$$
$$\partial_t p_a + q_1 p_a + \partial_1 u_1 = 0, \tag{1.51}$$
$$\partial_t p_b + q_2 p_b + \partial_2 u_2 = 0, \tag{1.52}$$

with the following boundary condition on the boundary Γ of the PML layer:

$$p = 0 \quad \text{on } \Gamma. \tag{1.53}$$

The attenuation parameters q_i can be taken as constant or variable. Linear and quadratic profiles have been tested, for instance:

$$q_i = q_\delta \left(\frac{r_{\text{PML}}}{\delta_{\text{PML}}} \right)^{n_{\text{PML}}}, \tag{1.54}$$

where δ_{PML} is the thickness of the PML layer, q_δ is the attenuation factor and r_{PML} is a normal coordinate with value zero on the boundary of the physical media and value δ_{PML} at the end of the PML layer. The exponent n_{PML} can be taken as 1 or 2 to obtain a linear or quadratic attenuation parameter.

Notice that the PML formulation presented increases the number of unknowns of the problem. The cost increase is not so big since it is only an extra scalar unknown. For the scalar wave equation in irreducible form the relative cost increase is higher for obvious reasons.

Later, in 2001, Hu presented a stable and well-posed PML formulation in unsplit physical variables [48]. The avoidance of splitting facilitates the implementation. But still there is an auxiliary variable and thus the number of unknowns in the PML region is increased.

PML features exponential decay of waves propagating inside the absorbing layer. Commonly, a hard wall condition is applied on the exterior boundary of the PML layer, that means energy can still reflect on that boundary and go back to the physical domain. In the way back, the PML layer still absorbs energy of the wave, so the effective attenuation of the PML layer is $2\delta_{\text{PML}}$. The exponential decay inside the PML layer is governed by the attenuation parameters q_i. Higher attenuation parameters mean faster decay.

The design of a PML layer for a given problem involves setting the thickness δ_{PML} and the parameters q_i. We might be tempted to choose the attenuation parameters as high as possible and a small PML thickness but it is not that simple. An abrupt change of properties from physical media to PML media might induce reflection on the PML media/physical media interface. So we cannot choose the attenuation parameters so high. Additionally, a good practice is to choose the attenuation parameters as zero in the interior of the PML layer and maximum in the exterior of the PML layer so that the change of properties from physical media to PML media is smooth. A common practice is to choose δ_{PML} as a fraction of the wavelength. Cohen [49] recommends choosing δ_{PML} as one third of the wavelength for acoustic problems, meanwhile the study of Oskooi [50] in photonics suggests choosing it as one half of the wavelength. This half-wavelength thickness criteria for acoustic waves in air means thicknesses ranging from 8 to 0.01 m for the range of audible frequencies 20 - 20000 Hz.

1.4.7 Other NRBL

PML is a very popular NRBL but there are other NRBL. Richards et al proposes in [51] a NRBL based on damping the solution in time with a factor σ to a desired target value. In that publication they claim better performance than PML.

1.4.8 NRB performance evaluation

Many benchmark problems have been devised in order to evaluate the performance of NRBC and NRBL.

Some procedures compare an analytical solution with the numerical solution in the truncated domain using the NRB. For example Problems 1 and 2 in Category 3 of [52]. Another example are the Parts 1, 2 and 3 of Problem 3 in Category 1 of [53].

Other procedures involve solving the problem in a truncated domain and in a bigger domain and comparing the solution of the big domain restricted to the truncated domain with the solution obtained in the truncated domain with the NRB [54, 55].

Let us describe in more detail the problem 1 in category 3 proposed in [52]. The 2D ($d = 2$) spatial domain is taken as $\Omega = (-100, 100) \times (-100, 100)$. In all the boundary Γ of the domain NRB are imposed. The problem is solved with a Mach number $(M, 0)$ (mean

flow in the x direction). The initial condition is:

$$p = \exp\left[-(\ln 2)\left(\frac{x^2+y^2}{9}\right)\right], \tag{1.55}$$

$$u_1 = 0.04y \exp\left[-(\ln 2)\left(\frac{(x-67)^2+y^2}{25}\right)\right], \tag{1.56}$$

$$u_2 = -0.04(x-67) \exp\left[-(\ln 2)\left(\frac{(x-67)^2+y^2}{25}\right)\right]. \tag{1.57}$$

The problem consists in finding the unknowns at $t = 30, 40, 50, 60, 70, 80, 100, 100$ and 600.

The analytical solution to that problem is the following. Let $\alpha_1 = \frac{\ln 2}{9}$, $\alpha_2 = \frac{\ln 2}{25}$ and $\eta = \sqrt{(x-Mt)^2+y^2}$. The exact solution is:

$$p = \frac{1}{2\alpha_1}\int_0^\infty \mathrm{e}^{\frac{-\xi^2}{4\alpha_1}} \cos(\xi t) J_0(\xi\eta)\xi \,\mathrm{d}\xi, \tag{1.58}$$

$$u_1 = \frac{x-Mt}{2\alpha_1\eta}\int_0^\infty \mathrm{e}^{\frac{-\xi^2}{4\alpha_1}} \sin(\xi t) J_1(\xi\eta)\xi \,\mathrm{d}\xi + 0.04y\mathrm{e}^{-\alpha_2\left[(x-67-Mt)^2+y^2\right]}, \tag{1.59}$$

$$u_2 = \frac{y}{2\alpha_1\eta}\int_0^\infty \mathrm{e}^{\frac{-\xi^2}{4\alpha_1}} \sin(\xi t) J_1(\xi\eta)\xi \,\mathrm{d}\xi - 0.04(x-67-Mt)\mathrm{e}^{-\alpha_2\left[(x-67-Mt)^2+y^2\right]}, \tag{1.60}$$

where J_α are the Bessel functions of order α.

One problem with this benchmark is that it does not specify the mesh to use. Another problem are the benchmark results in the original document, as they are quite old, the document is not clear to read.

The benchmark problem 3 in category 1 of [53] is more specific and specifies the mesh to use. It involves periodic boundary conditions and the results can be easily compared through the error at each time step. The unsuitability of this benchmark is that the error results are not purely due to the non-reflective properties of the NRB used, but include propagation error (due to temporal and spatial discretization).

In my opinion, the best NRB benchmark should only include the non-reflective properties of the NRB. So, the big domain/small domain seems the most appropriate method in the time domain. I have no idea what would be the equivalent in the frequency domain. The big domain benchmark is sketched in Fig. 1.7. The red zone represents the initial wave pulse. The time interval used in the big and small domain is the same. The time interval is chosen such that the initial pulse has touched all the surrounding NRB. The big domain is chosen such that along the previously selected time interval, the initial pulse does not reach the big boundary.

The comparison criteria in the Big Domain Benchmark is multiple and it has two components. The first component is the time domain norm and the second component is the spatial domain norm.

For the time domain norm we have many options An instant of time $t_c \in (0,T)$ can be chosen for comparison. Other option can be comparing in the whole time interval $(0,T)$ with an $L^\infty(0,T)$ norm or with an $L^2(0,T)$ norm.

The spatial domain norm has many options too. A point $\boldsymbol{x}_c \in \Omega$ or the whole domain Ω can be chosen for computing the norm. Additionally, the quantity of interest together with

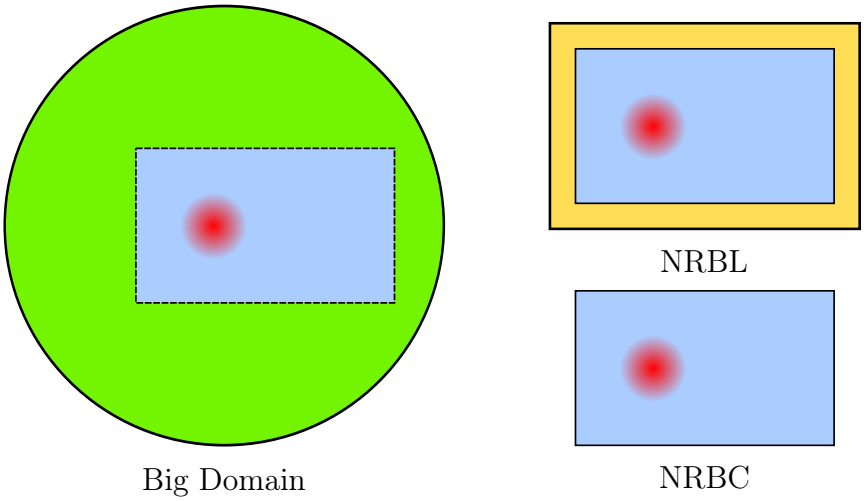

Figure 1.7: Big Domain Benchmark

its norm has multiple options. Among the options we have the energy $\|e\|_{L^2}$, the potential energy $\|e_p\|_{L^2}$, the kinetic energy $\|e_k\|_{L^2}$, the $H^1(\Omega)$ norm of the pressure fluctuation $\|p'\|_{H^1(\Omega)}$, the $H(\mathrm{div},\Omega)$ norm of the velocity fluctuation $\|\boldsymbol{u}'\|_{H(\mathrm{div},\Omega)}$ and a composite norm combining some or all the norms of the above in space and time $|||\cdot|||$. Obviously, the choice of a point $\boldsymbol{x}_c$ does not make any sense in variational formulations.

The comparison criteria (see Chapter 2 or Chapter 3) can be taken as:

$$|||[p',\boldsymbol{u}']|||_A^2 := \mu_p\|p'\|^2_{L^\infty(\Upsilon,L^2(\Omega))} + \mu_u\|\boldsymbol{u}'\|^2_{L^\infty(\Upsilon,L^2(\Omega))}, \tag{1.61}$$

or

$$|||[p',\boldsymbol{u}']|||_B^2 := |||[p',\boldsymbol{u}']|||_A^2 + \tau_p\|\nabla p'\|^2_{L^2(\Upsilon,L^2(\Omega))} + \tau_u\|\nabla\cdot\boldsymbol{u}'\|^2_{L^2(\Upsilon,L^2(\Omega))}, \tag{1.62}$$

where τ_p and τ_u are the stabilization parameters containing length scales of the wave problem.

A typical plot of the total energy in Ω versus time for the Big Domain Benchmark should look like 1.8. In that plot the big domain solution is plotted in black and the small domain solution is plotted in blue. The imperfection of the NRB is seen because the curves do not match exactly.

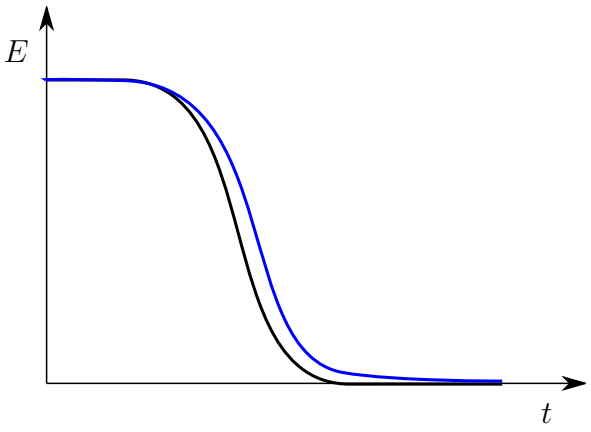

Figure 1.8: Big Domain Benchmark Energy Evolution

1.5 Aeroacoustics

1.5.1 Overview

Acoustic waves can be produced from the unsteady motion of a solid boundary in contact with a fluid (See Fig. 1.9). This field is known as simply Acoustics and it is not the main concern of Aeroacoustics. Aeroacoustics is the study of sound generation by turbulent flow or aerodynamic forces interacting with surfaces and the subsequent propagation of sound through the fluid (See Fig. 1.10). Aerodynamic forces interacting with surfaces can be regarded as Aeroelasticity. Computational Aeroacoustics is the use of numerical methods to solve aeroacoustics problems [7].

Aeroacoustics problems can be approached in two forms: direct computation and indirect or hybrid approach. The first approach consist in solving the flow problem at the same time as the acoustic problem. The advantage of the direct approach is the avoidance approximations in the model. The disadvantage is its high computational cost because a fine enough mesh and time step has to be used [56].

On the other hand, the hybrid approach solves first the flow problem, then uses the information from the flow in order to predict the sound sources (using acoustic analogies) and finally solves the acoustic problem. The main assumption of the hybrid approach is that the flow produces sound and the sound propagating does not affect in any way the

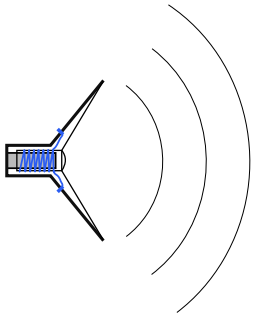

Figure 1.9: Speaker generating sound

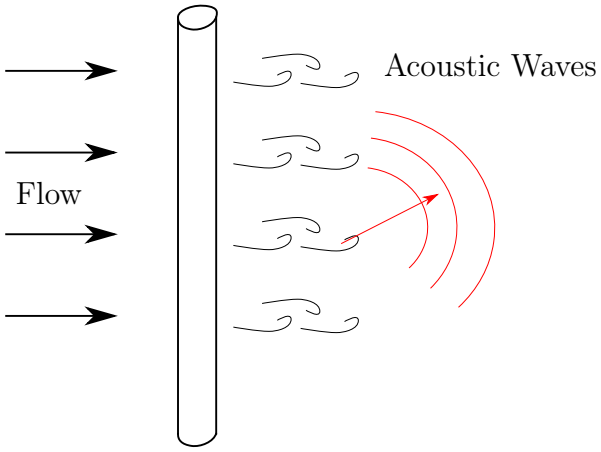

Figure 1.10: Acoustic Waves Generation

flow (there is not two way coupling). This assumption is valid because the propagation of sound involves small pressure fluctuations while fluid flow involves big pressure fluctuations. Additionally, at low Mach numbers, the fluid can be considered incompressible for the flow calculation and the acoustic sources will be accurate enough for the acoustic calculation.

For the hybrid approach the type of fluid dynamics simulation used can be Reynolds-Averaged Navier-Stokes (RANS), Large Eddy Simulation (LES) or Direct Numerical Simulation (DNS). When RANS is used, the approach is known as stochastic. The stochastic approach uses RANS, which is not computationally expensive, and from that information constructs the sound sources.

Aeroacoustics is very challenging from the computational point of view because it requires solving a unsteady flow problem with a fine enough spatial and temporal discretization in order to capture all the flow details responsible of generating sound which is very costly.

Additionally, there is an enormous disparity between the flow velocity/pressure and the acoustic velocity/pressure because for low Mach numbers the energy generated as sound waves is of order Ma^4 [57]. In the case of sound generated by a turbulent jet, the ratio between the power of the waves generated and the power of the jet is of order Ma^5. This disparity makes the direct approach very challenging because the simulation has to be able to detect the small perturbations with enough accuracy. For the hybrid approach, the disparity is less important because the acoustic problem is solved separately.

1.5.2 Concepts

The time-average value $\bar{p}$ of a given property p is defined as [58]:

$$\bar{p}(\boldsymbol{x}) = \frac{1}{T}\int_0^T p(\boldsymbol{x}, t)\,\mathrm{d}t, \tag{1.63}$$

and its fluctuation p' is defined as:

$$p(\boldsymbol{x}, t) = \bar{p}(\boldsymbol{x}) + p'(\boldsymbol{x}, t). \tag{1.64}$$

The root mean square value RMS is defined as:

$$p_{\text{rms}}(\boldsymbol{x}) = \left(\frac{1}{T} \int_0^T (p'(\boldsymbol{x}, t))^2 \mathrm{d}t \right)^{\frac{1}{2}}. \tag{1.65}$$

For a cosinusoidal wave of amplitude A described as $A\cos(\omega t - \phi)$ the RMS value can be calculated as:

$$p_{\text{rms}} = \frac{A}{\sqrt{2}}. \tag{1.66}$$

In acoustics in general and in aeroacoustics in particular we need a way of measuring the loudness of sound in a given point. Thus, the Sound Pressure level SPL is introduced. Sound pressure level is a measure of the deviation of the pressure around the ambient pressure. It is commonly measured in decibels (dB). A dB is a tenth of a Bel. A Bel is a rarely used unit named after Alexander G. Bell. The sound pressure level in dB is calculated as:

$$\text{SPL} = 10 \log_{10} \frac{p_{\text{rms}}^2}{p_{\text{ref}}^2}, \tag{1.67}$$

where p_{ref} is the reference pressure and is taken as $p_{\text{ref}} = 20 \times 10^{-6}$ Pa for air and $p_{\text{ref}} = 1 \times 10^{-6}$ Pa for water.

The pressure fluctuations p_{rms} contain all the frequency spectrum. Sometimes it can be advantageous to split the spectrum and consider the contribution of a given frequency to the total. Assuming the frequency spectrum is discrete and has N frequency contributions (the idea readily extends to continuum frequency spectrum), the pressure fluctuations can be split as:

$$p'(\boldsymbol{x}, t) = \sum_{n=1}^{N} p'_n(\boldsymbol{x}, t), \tag{1.68}$$

where p'_n is the pressure component with angular frequency ω_n. Its complex amplitude $\hat{p}_n$ is defined as:

$$p'_n(\boldsymbol{x}, t) = \Re \left(\hat{p}_n(\boldsymbol{x}) \mathrm{e}^{-\mathrm{i}\omega_n t} \right), \tag{1.69}$$

and the pressure level at the angular frequency ω_n is defined as:

$$\text{SPL}_n = 10 \log_{10} \frac{\frac{1}{2}|\hat{p}_n|^2}{p_{\text{ref}}^2}. \tag{1.70}$$

1.5.3 Navier-Stokes Equations

The Navier-Stokes equations describe the movement of a fluid and are named after Claude-Louis Navier and George Gabriel Stokes. The equations are:

$$\partial_t \rho + \nabla \cdot (\rho \boldsymbol{u}) = 0, \tag{1.71}$$

$$\rho\left(\partial_t \boldsymbol{u} + (\boldsymbol{u}\cdot\nabla)\boldsymbol{u}\right) - \nabla\cdot\boldsymbol{\sigma} = \boldsymbol{f}_{\text{mom}}, \tag{1.72}$$

where ρ is the fluid density, $\boldsymbol{u}$ is the fluid velocity, $\boldsymbol{\sigma}$ is the stress tensor and $\boldsymbol{f}_{\text{mom}}$ is the body force per unit volume. Obviously, we need to add to the Navier-Stokes equations the constitutive equation of the fluid, the state equation and the energy equation in order to be able to solve the problem.

The equations are solved in a spatial domain $\Omega \in \mathbb{R}^d$ $(d = 1, 2, 3)$ with boundary Γ and in a time interval $(0, T)$ with appropriate boundary and initial conditions.

Equation (1.71) is known as mass conservation equation or continuity equation. Equation (1.72) is known as the momentum equation because it is a momentum conservation statement.

The range of applicability of the equations presented includes: compressible or incompressible flows, laminar or turbulent flows and viscous or inviscid flows.

Newtonian fluids are fluids that behave according to the following equation:

$$\sigma_{ij} = -p\,\delta_{ij} + \tau_{ij}, \tag{1.73}$$

$$\tau_{ij} = \mu\left(\partial_j u_i + \partial_i u_j\right) + \left(\lambda - \frac{2}{3}\mu\right)\delta_{ij}\partial_k u_k, \tag{1.74}$$

where p is the pressure (thermodynamic pressure), δ is the Kronecker delta, τ_{ij} is the deviatoric part of the stress tensor, μ is the dynamic viscosity of the fluid and λ is the bulk viscosity (also known as volume viscosity or second viscosity expansion viscosity). Thermodynamics second-law arguments show that λ must be positive. The effect of the term involving $\nabla\cdot\boldsymbol{u}$ is very small even in compressible flows and it is usual to assume $\lambda = 0$ or $\lambda - \frac{2}{3}\mu = 0$.

Recall that:

$$(\nabla\cdot\boldsymbol{\sigma})_i = \partial_j\sigma_{ji} = \partial_j\sigma_{ij}, \tag{1.75}$$

as $\boldsymbol{\sigma}$ is symmetric.

Navier-Stokes equations can be written in conservative form as:

$$\partial_t\rho + \nabla\cdot(\rho\boldsymbol{u}) = 0, \tag{1.76}$$

$$\partial_t(\rho\boldsymbol{u}) + \nabla\cdot(\rho\boldsymbol{u}\boldsymbol{u}) - \nabla\cdot\boldsymbol{\sigma} = \boldsymbol{f}_{\text{mom}}. \tag{1.77}$$

1.5.4 Acoustic Analogy

In the hybrid approach to aeroacoustics, an acoustic analogy is needed in order to translate the flow results into acoustic sources. The first to develop this concept was Lighthill in 1952 [59, 60], then Curle considered solid walls in 1955 [61], afterwards Phillips in 1960 studied sound generated at high Mach numbers [62]. In 1969 Williams and Hawkings [63] proposed a new acoustic analogy in order to consider solid surfaces moving arbitrarily. Recently, in 2003 Goldstein proposed a generalized acoustic analogy [64].

Lighthill Acoustic Analogy

It was proposed by Michael James Lighthill who was a British applied mathematician. He published his results in two famous papers in 1952 and 1954 [59, 60]. The sound generated

is represented by quadrupole volume sources. It assumes the medium is stationary and it does not consider solid walls. The reference density is taken as ρ_0 and the density fluctuation is defined as:

$$\rho' = \rho - \rho_0 \tag{1.78}$$

The Lighthill acoustic analogy can be obtained from the Navier-Stokes equations in conservative form with $\boldsymbol{f}_{\text{mom}} = \mathbf{0}$ differentiating with respect to time the mass conservation equation and subtracting the divergence of the momentum conservation equation:

$$\partial_{tt}\rho + \partial_t(\nabla\cdot(\rho\boldsymbol{u})) - \nabla\cdot(\partial_t(\rho\boldsymbol{u})) - \nabla\cdot(\nabla\cdot(\rho\boldsymbol{u}\boldsymbol{u} - \boldsymbol{\sigma})) = 0, \tag{1.79}$$

then subtracting $c^2\Delta\rho'$ to both sides we get:

$$\partial_{tt}\rho - c^2\Delta\rho' = \nabla\cdot(\nabla\cdot(\rho\boldsymbol{u}\boldsymbol{u} - \boldsymbol{\sigma})) - c^2\Delta\rho', \tag{1.80}$$

finally, as time derivatives only see ρ':

$$\partial_{tt}\rho' - c^2\Delta\rho' = \partial_i\partial_j T_{ij}, \tag{1.81}$$

where $\partial_i\partial_j T_{ij}$ is the acoustic source. T_{ij} is known as the Lighthill stress tensor and is defined as:

$$T_{ij} = \rho u_i u_j + \delta_{ij}\left[(p - p_0) - c^2(\rho - \rho_0)\right] - \tau_{ij}, \tag{1.82}$$

where δ_{ij} is the Kronecker delta, p_0 is the reference pressure, ρ_0 is the reference density, c is the speed of sound at the reference density and pressure and τ_{ij} is the deviatoric part of the stress tensor.

The Lighthill tensor can be neglected in the far field region, because the sound is generated in the near field region. In the near field region, the Lighthill tensor can be approximated by neglecting τ_{ij} because viscosity is known to cause a small damping due to the conversion of acoustic energy into heat.

Another approximation can be made to the Lighthill tensor for isentropic flows and the term $(p - p_0) - c^2(\rho - \rho_0)$ can be neglected, thus:

$$\boldsymbol{T} \approx \rho\boldsymbol{u} \otimes \boldsymbol{u}. \tag{1.83}$$

The Lighthill stress tensor can be calculated from a computational fluid dynamics simulation and then serve as input for the wave equation in the propagation stage.

Before we have written the density fluctuation scalar wave equation in irreducible form. We can write an equivalent equation in terms of pressure as:

$$\frac{1}{c^2}\partial_{tt}p' - \Delta p' = \partial_i\partial_j T_{ij}. \tag{1.84}$$

In the case of the wave equation in mixed form (1.4)-(1.5), we can take the forcing terms from the Lighthill acoustic analogy as:

$$f_p = 0\,, \tag{1.85}$$

$$\boldsymbol{f}_u = -\nabla\cdot\boldsymbol{T} = -\partial_j T_{ji} = -\partial_j T_{ij}. \tag{1.86}$$

Curle Acoustic Analogy

It was developed by Curle in 1955 [61]. It is an extension to the Lighthill analogy taking into account solid boundaries. It considers sound sources in the form of dipoles and quadrupoles. The influence of solid boundaries has to be considered because of reflection, diffraction and the resultant dipole field at the solid boundaries (as the limit of Lighthill quadrupole distribution).

According to Curle, the dipoles are more efficient sound sources than quadrupoles for small enough Mach numbers and must be considered. Additionally, it is shown that the frequency of the dipole sources is half of the frequency of the quadrupole sources.

Phillips Acoustic Analogy

It was developed by Phillips in 1960 [62]. The main advance respect to Lighthill analogy is to consider the movement of the mean flow. This analogy focuses in high Mach numbers.

Phillips mentions that for large Mach numbers the fluctuation of the pressure squared $(p'^2)$is of order $\mathrm{Ma}^{3/2}$ for $\mathrm{Ma} \gg 1$ contrasting with the Lighthill's prediction of Ma^8 for $\mathrm{Ma} \ll 1$. The acoustic efficiency thus varies as $\mathrm{Ma}^{-3/2}$ for $\mathrm{Ma} \gg 1$, and as Ma^5 for $\mathrm{Ma} \ll 1$, indicating a maximum acoustic efficiency for Mach numbers near 1.

Ffowcs Williams-Hawkings Acoustic Analogy (FWH)

It was developed by J.E. Ffowcs Williams and D.L. Hawkings in 1969 [63]. It extends the Lighthill and Curle analogies considering solid surfaces in arbitrary motion. The sound generated is represented by quadrupole, dipole and and monopole sources. The monopole and dipole sources are surface sources associated with the motion of the solid surface and the quadrupole sources are volume sources associated with the fluid flow.

Each type of source term can be given a physical explanation [65]. The monopole source term is the thickness noise and is determined completely by the thickness and kinematics of the body. The dipole source term is the loading noise and is generated by the force that acts on the fluid as a result of the presence of the body. Finally, the quadrupole source term is the non-linear noise source and takes into account shocks, vorticity and turbulence in the flow field.

In certain applications it is possible to neglect some source terms. For example, for rotating blades with low speed flow the quadrupole source term may be neglected [65].Some methods, like boundary integral methods, try to avoid the volume source (quadrupole) approximating it by a surface source.

Some formulations of the FWH embed the exterior flow problem in unbounded space using generalized functions. For Finite Element Formulations we will probably not need to perform that embedding unless we want to use fixed mesh methods.

Now let us describe the derivation of the FWH analogy taken from [66]. Let Ω be the fluid spatial domain with boundary $\partial\Omega$. Let us define the surface defining the solid boundaries as $\Gamma_s(\boldsymbol{x}, t) = 0$. Thus $\Gamma_s \subseteq \partial\Omega$. Additionally, let us define $\Gamma_s > 0$ inside the fluid and $\Gamma_s < 0$ inside the solid in such a way that the outward pointing normal to the boundary is:

$$\boldsymbol{n} = -\nabla\Gamma_s. \tag{1.87}$$

The time dependence means that solid boundaries can move arbitrarily (rigid or flexible body motion). The mass and momentum equations can be written as:

$$\partial_t \rho + \partial_i(\rho u_i) = \rho_0 u_i \delta(\Gamma_s)\partial_i \Gamma_s, \tag{1.88}$$
$$\partial_t(\rho u_i) + \partial_j(\rho u_i u_j + \tau_{ij}) = \tau_{ij}\delta(\Gamma_s)\partial_j \Gamma_s, \tag{1.89}$$

where $\delta(\cdot)$ is the Dirac delta function. For a static surface the source term in the mass conservation equation vanishes.

Then, the wave equation in irreducible form is:

$$\partial_{tt}\rho' - c^2\nabla\rho' = \partial_{ij}T_{ij} - \partial_i\left(\tau_{ij}\delta(\Gamma_s)\partial_j\Gamma_s\right) + \partial_t\left(\rho_o u_i \delta(\Gamma_s)\partial_i\Gamma_s\right), \tag{1.90}$$

where T_{ij} is the Lighthill stress tensor. The first term of the right hand side of the equation represents a quadrupole volume source. The second term represents a dipole surface source. Finally, the third term represents a monopole surface source.

Goldstein Acoustic Analogy

It was developed by Goldstein in 2003 [64]. His contribution was to rewrite Navier-Stokes equations (in conservative form) as inhomogeneous linearized Euler equations. The sound source terms are a result of shear stress and energy flux perturbations.

1.6 Structure

The document is organized as follows: in Chapter 2 the wave equation is discretized in space using stabilized finite element methods. Additionally, stability and convergence of the semi-discrete schemes is analyzed. In Chapter 3 a non-reflecting boundary condition is added to the stabilized finite element formulation of the wave equation in mixed form. Stability and convergence is analyzed as well as the non-reflective properties of the non-reflective boundary condition. In Chapter 4 time marching schemes for the mixed wave equation are analyzed, with emphasis in stability, convergence, dissipation and dispersion. In Chapter 5 various wave propagation problems are solved and some of them are compared with experimental results. Finally, in Chapter 6 conclusions are drawn and future research lines are mentioned.

1.7 Research diffusion

The research work contained in this thesis has been disseminated in the format of articles in peer-reviewed scientific journals and in the form of oral presentations in scientific conferences and congresses.

1.7.1 Publications

Some chapters of this thesis are based on or include the following publications:

Chapter 2:

Santiago Badia, Ramon Codina, and Hector Espinoza. "Stability, Convergence, and Accuracy of Stabilized Finite Element Methods for the Wave Equation in Mixed Form". In: *SIAM Journal on Numerical Analysis* 52.4 (May 2014), pp. 1729–1752. DOI: 10.1137/130918708

Chapter 3:

Hector Espinoza, Ramon Codina, and Santiago Badia. "A Sommerfeld non-reflecting boundary condition for the wave equation in mixed form". In: *Computer Methods in Applied Mechanics and Engineering* 276 (July 2014), pp. 122–148. ISSN: 0045-7825. DOI: 10.1016/j.cma.2014.03.015. URL: http://www.sciencedirect.com/science/article/pii/S0045782514001017

Chapter 4:

Hector Espinoza, Ramon Codina, and Santiago Badia. "On some time marching schemes for the stabilized finite element approximation of the mixed wave equation". In: *Computer Methods in Applied Mechanics and Engineering* (Dec. 2014). Submitted.

Chapter 5:

Oriol Guasch, Marc Arnela, Ramon Codina, and Hector Espinoza. "A stabilized finite element method for the mixed wave equation in an ALE framework with application to diphthong production". In: *Journal of Computational Physics* (Oct. 2014). Submitted.

1.7.2 Conferences

Research results had been presented in the following conferences:

Ramon Codina, Hector Espinoza, and Santiago Badia. "Linear waves in mixed form: functional settings and stabilized finite element approximation". In: *6th Scientific Computing Seminar / VMS 2012*. Christian-Albrechts-Universität zu Kiel. June 2012. URL: http://www.math.uni-kiel.de/numerik/braack/conf/vms2012/

Hector Espinoza, Ramon Codina, and Santiago Badia. "Wave Equation in Mixed Form: Stability and Convergence Estimates using Stabilized Finite Element Methods". In: *Congress on Numerical Methods in Engineering CNM 2013*. Sociedad Española de Métodos Numéricos en Ingeniería (SEMNI). June 2013. URL: http://congress.cimne.com/metnum2013/

Oriol Guasch, Marc Arnela, Ramon Codina, and Hector Espinoza. "A stabilized arbitrary Lagrangian Eulerian finite element method for the mixed wave equation with application to diphthong production". In: *WCCM XI*. IACM and ECCOMAS. July 2014. URL: http://www.wccm-eccm-ecfd2014.org/

Hector Espinoza, Ramon Codina, and Santiago Badia. "Numerical analysis and benchmarking of a Sommerfeld-type non-reflecting boundary condition for the wave equation in mixed form". In: *WCCM XI*. IACM and ECCOMAS. July 2014. URL: http://www.wccm-eccm-ecfd2014.org/

Marc Arnela, Oriol Guasch, Ramon Codina, and Hector Espinoza. "Finite element computation of diphthong sounds using tuned two-dimensional vocal tracts". In: *7th Forum Acusticum*. Polish Acoustics Society and European Acoustics Association. Sept. 2014. URL: http://www.fa2014.pl/

Oriol Guasch, Marc Arnela, Ramon Codina, and Hector Espinoza. "Stabilized finite element formulation for the mixed convected wave equation in domains with driven flex-

ible boundaries". In: *NOVEM 2015*. INSA. Apr. 2015. URL: http://novem2015.sciencesconf.org/

Ramon Codina, Marc Arnela, Oriol Guasch, and Hector Espinoza. "Waves in time dependent domains". In: *10th International Workshop on Variational Multiscale and Stabilized Finite Elements (VMS2015)*. German Association for Computational Mechanics (GACM). Garching, Germany, Feb. 2015. URL: http://www.lnm.mw.tum.de/vms2015/

Ramon Codina, Oriol Guasch, Marc Arnela, and Hector Espinoza. "Approximation of waves written in mixed form in time dependent domains". In: *Congresso de Métodos Numéricos em Engenharia*. Instituto Superior Técnico. June 2015. URL: http://www.dem.ist.utl.pt/cmn2015/

Chapter 2

Stability, Convergence and Accuracy of Stabilized Finite Element Methods for the Wave Equation in Mixed Form

This chapter is based on the material in:
Santiago Badia, Ramon Codina, and Hector Espinoza. "Stability, Convergence, and Accuracy of Stabilized Finite Element Methods for the Wave Equation in Mixed Form". In: *SIAM Journal on Numerical Analysis* 52.4 (May 2014), pp. 1729–1752. DOI: 10.1137/130918708
with the notation modified to make it fit with the other chapters.

In this chapter we propose two stabilized finite element methods for different functional frameworks of the wave equation in mixed form. These stabilized finite element methods are stable for any pair of interpolation spaces of the unknowns. The variational forms corresponding to different functional settings are treated in an unified manner through the introduction of length scales related to the unknowns. Stability and convergence analysis is performed together with numerical experiments. It is shown that modifying the length scales allows one to mimic at the discrete level the different functional settings of the continuous problem and influence the stability and accuracy of the resulting methods.

2.1 Introduction

When applied to approximate differential equations with several unknowns, and particularly saddle point problems, standard Galerkin mixed finite element (FE) formulations often require the use of inf-sup stable interpolations for the unknowns in order to be stable [78]. Inf-sup stable FE formulations have been formulated for several mixed problems, e.g. [79] for the Stokes problem, [80] for the Darcy problem, [81] for the Maxwell problem, [82, 83] for the Stokes-Darcy problem, [84] for the wave equation and [85, 86] for elastodynamics.

On the contrary, stabilized FE methods [87] allow one to avoid inf-sup compatibility constraints. As a result, we can deal with different saddle-point problems by using the same equal interpolation for all the unknowns; see e.g. the unified framework for Stokes, Darcy and Maxwell problems in [88]. This way, we can certainly ease implementation issues,

specially for multiphysics simulations. Stabilized FE methods can nicely be motivated in the Variational Multi-Scale (VMS) framework, as shown in [89].

This work is a follow-up of [90] for the wave equation in mixed form. The mixed wave equation is approximated in [90] using the Orthogonal Sub-scale Stabilization (OSS) method. In the present work, the OSS method is extended and the Algebraic Sub-Grid Scale Method (ASGS) is also considered. Additionally, length scales associated to the unknowns are introduced, allowing one to treat different functional settings in a unified manner. A similar approach for the stationary Stokes-Darcy problem can be found in [91].

We focus on three variational forms of the mixed wave equation and the functional setting for each case. We obtain the different functional settings by *transferring* regularity from the scalar to the vector unknowns or vice-versa. More about functional settings for wave propagation problems of first and second order can be found in [92].

A priori error estimates for the mixed wave equation can be found in the literature. Some only bound L^2 norms of the error of the unknowns [93, 94], whereas others, such as [84], take into account the divergence of the vector unknown too. In this work we bound both the the gradient of the scalar unknown and the divergence of the vector unknown using stabilized FEs.

Several stability and convergence analysis have been done so far for the irreducible form of the wave equation (second order space and time derivatives) [95, 96] but not much attention has been paid to the first order in time and space wave equation. As far as the authors are aware, the present work is the first to analyze the convergence properties of stabilized FEs applied to the mixed form of the wave equation.

The organization of the chapter is as follows. In Section 2.2 we describe the continuous problem and its variational forms. In Section 2.3 we describe the stabilized discrete problem using the ASGS and the OSS methods. In Section 2.4 we state and prove the stability of the discrete formulations. In Section 2.5 we state and prove the convergence of the discrete formulations, including numerical tests. Finally, in Section 2.6 the conclusions of the work are presented.

2.2 Problem Statement

2.2.1 Initial and Boundary Value Problem

The problem we consider is an initial and boundary value problem posed in a time interval $(0, T)$ and in a spatial domain $\Omega \subset \mathbb{R}^d$, ($d = 1,\ 2$ or 3). The long term behavior $T \to \infty$ will not be considered in this work.

Let Γ be the boundary of the domain Ω. We split this boundary into two disjoint sets denoted as Γ_p and Γ_u, where the boundary conditions corresponding to the unknowns p and $\boldsymbol{u}$ will be respectively enforced.

The problem consists in finding $p : \Omega \times (0, T) \longrightarrow \mathbb{R}$ and $\boldsymbol{u} : \Omega \times (0, T) \longrightarrow \mathbb{R}^d$ such that:

$$\mu_p \partial_t p + \nabla \cdot \boldsymbol{u} = f_p \,, \tag{2.1}$$

$$\mu_u \partial_t \boldsymbol{u} + \nabla p = \boldsymbol{f}_u \,, \tag{2.2}$$

with the following initial conditions:

$$p\left(\boldsymbol{x},0\right)=0,\quad \boldsymbol{u}\left(\boldsymbol{x},0\right)=\boldsymbol{0},\quad \boldsymbol{x}\in\Omega, \tag{2.3}$$

and with the following boundary conditions:

$$p=0\ \text{ on }\Gamma_p,\quad \boldsymbol{n}\cdot\boldsymbol{u}=0\ \text{ on }\Gamma_u,\quad t\in(0,T), \tag{2.4}$$

where $\mu_p>0$ and $\mu_u>0$ are coefficients such that $c^2=\left(\mu_p\mu_u\right)^{-1}$, c is the wave speed, f_p and $\boldsymbol{f}_u$ are forcing terms and $\boldsymbol{n}$ is the unit outward normal to the boundary of the domain. Notice that any general problem with non-homogeneous initial and boundary conditions can be cast in the form (2.1)-(2.4) properly modifying the forcing terms.

In the previous equations and in what follows, we use the following convention: bold face italic letters represent vectors in $\mathbb{R}^d$, ($d=1,\ 2$ or 3), bold face regular upper-case letters represent matrices, and non-bold letters represent scalars.

Let $L^2(\Omega)$ be the space of square integrable functions defined on the domain Ω, $L^2(\Omega)^d$ the space of vector valued functions with components in $L^2(\Omega)$, $H^1(\Omega)$ the space of functions in $L^2(\Omega)$ with derivatives in $L^2(\Omega)$, $H^1(\Omega)^d$ the space of vector valued functions with components in $H^1(\Omega)$, and $H(\mathrm{div},\Omega)$ the space of vector functions with components and divergence in $L^2(\Omega)$. Any of the spaces defined previously will be denoted generically as X. Additionally, given X, a space of (scalar or vector) functions defined over Ω, its spatial norm will be denoted as $\|\cdot\|_X$ and the space of functions whose X-norm is C^k continuous in the time interval $[0,T]$ will be denoted by $C^k\left([0,T];X\right)$. We will only be interested in the cases $k=0$, $k=1$ and $k=2$. In the case of $L^2(\Omega)$ or $L^2(\Omega)^d$ the L^2-norm will be simply denoted as $\|\cdot\|$. Functions whose X-norm is L^p in $[0,T]$ will be denoted by $L^p(0,T;X)$; when $X=L^2(\Omega)$ or $X=L^2(\Omega)^d$, the simplification $L^p(L^2)$ will be sometimes used.

Furthermore, let V_p, V_u be spaces associated with p and $\boldsymbol{u}$ respectively. These spaces will be defined afterwards because they depend on the functional setting. Additionally, let us define $V:=V_p\times V_u$ and $L:=L^2(\Omega)\times L^2(\Omega)^d$.

Problem (2.1)-(2.2) will be well posed for

$$p\in C^1\big([0,T];L^2(\Omega)\big)\cap C^0\big([0,T];V_p\big), \tag{2.5}$$

$$\boldsymbol{u}\in C^1\big([0,T];L^2(\Omega)^d\big)\cap C^0\big([0,T];V_u\big), \tag{2.6}$$

with f_p and $\boldsymbol{f}_u$ in regular enough spaces.

2.2.2 Variational Problem

The variational form of problem (2.1)-(2.4) can be expressed in three different ways. Each one requires a certain regularity on the unknowns p and $\boldsymbol{u}$, which is equivalent to say that p and $\boldsymbol{u}$ should belong to a particular space of functions.

The problem reads: find $[p,\boldsymbol{u}]\in C^1\left([0,T];L\right)\cap C^0\left([0,T];V\right)$ such that

$$\mathcal{B}\left([p,\boldsymbol{u}],[q,\boldsymbol{v}]\right)=\mathcal{L}\left([q,\boldsymbol{v}]\right), \tag{2.7}$$

for all test functions $[q,\boldsymbol{v}]\in C^0\left([0,T];V\right)$ and the respective initial conditions. Here, we require that $p(\boldsymbol{x},0)=q(\boldsymbol{x},0)=0$ and $\boldsymbol{u}(\boldsymbol{x},0)=\boldsymbol{v}(\boldsymbol{x},0)=\boldsymbol{0}$. The bilinear form $\mathcal{B}$,

the linear form $\mathcal{L}$ and the space V are defined in three different ways depending on the variational form into consideration.

Let us denote as $(\,\cdot\,,\cdot\,)$ the $L^2(\Omega)$ inner product. For simplicity, we will assume that the forcing terms f_p and $\boldsymbol{f}_u$ are square integrable, although we could relax the this regularity requirement and assume they belong to the dual space of V_p and V_u, respectively.

The variational formulation of problem (2.1)-(2.4) can be posed in three different forms, essentially differing in the way integration by parts from the strong form of the problem is performed and in the regularity required for the unknowns. In the problem statement given below, variational form I (2.8)-(2.11) is obtained not integrating by parts any term. Variational form II (2.12)-(2.15) is obtained integrating by parts the term $(\nabla p, \boldsymbol{v})$. Finally, variational form III (2.16)-(2.19) is obtained integrating by parts the term $(\nabla\cdot\boldsymbol{u}, q)$. Notice that integration by parts leads to a boundary term. The treatment of the boundary term is explained in each case.

Variational Form I

$$V_p = \left\{q \in H^1(\Omega)|\ q = 0 \text{ on } \Gamma_p\right\}, \quad V_u = \{\boldsymbol{v} \in H(\mathrm{div}, \Omega)|\ \boldsymbol{n}\cdot\boldsymbol{v} = 0 \text{ on } \Gamma_u\}$$

$$\mathcal{B}\left([p, \boldsymbol{u}], [q, \boldsymbol{v}]\right) = \mu_p\left(\partial_t p, q\right) + \left(\nabla\cdot\boldsymbol{u}, q\right) + \mu_u\left(\partial_t \boldsymbol{u}, \boldsymbol{v}\right) + \left(\nabla p, \boldsymbol{v}\right) \tag{2.8}$$

$$\mathcal{L}\left([q, \boldsymbol{v}]\right) = \left(f_p, q\right) + \left(\boldsymbol{f}_u, \boldsymbol{v}\right) \tag{2.9}$$

$$p = 0 \text{ on } \Gamma_p, \qquad \text{Strongly imposed} \tag{2.10}$$

$$\boldsymbol{n}\cdot\boldsymbol{u} = 0 \text{ on } \Gamma_u, \qquad \text{Strongly imposed} \tag{2.11}$$

Variational Form II

$$V_p = L^2(\Omega), \quad V_u = \{\boldsymbol{v} \in H(\mathrm{div}, \Omega)|\ \boldsymbol{n}\cdot\boldsymbol{v} = 0 \text{ on } \Gamma_u\}$$

$$\mathcal{B}\left([p, \boldsymbol{u}], [q, \boldsymbol{v}]\right) = \mu_p\left(\partial_t p, q\right) + \left(\nabla\cdot\boldsymbol{u}, q\right) + \mu_u\left(\partial_t \boldsymbol{u}, \boldsymbol{v}\right) - \left(p, \nabla\cdot\boldsymbol{v}\right) \tag{2.12}$$

$$\mathcal{L}\left([q, \boldsymbol{v}]\right) = \left(f_p, q\right) + \left(\boldsymbol{f}_u, \boldsymbol{v}\right) \tag{2.13}$$

$$p = 0 \text{ on } \Gamma_p, \qquad \text{Weakly imposed} \tag{2.14}$$

$$\boldsymbol{n}\cdot\boldsymbol{u} = 0 \text{ on } \Gamma_u, \qquad \text{Strongly imposed} \tag{2.15}$$

Notice that the boundary integral that appears after integration by parts of $(\nabla p, \boldsymbol{v})$ vanishes due to (2.14)-(2.15).

Variational Form III

$$V_p = \left\{q \in H^1(\Omega)|\ q = 0 \text{ on } \Gamma_p\right\}, \quad V_u = L^2(\Omega)^d$$

$$\mathcal{B}\left([p, \boldsymbol{u}], [q, \boldsymbol{v}]\right) = \mu_p\left(\partial_t p, q\right) - \left(\boldsymbol{u}, \nabla q\right) + \mu_u\left(\partial_t \boldsymbol{u}, \boldsymbol{v}\right) + \left(\nabla p, \boldsymbol{v}\right) \tag{2.16}$$

$$\mathcal{L}\left([q, \boldsymbol{v}]\right) = (f_p, q) + (\boldsymbol{f}_u, \boldsymbol{v}) \tag{2.17}$$

$$p = 0 \text{ on } \Gamma_p, \qquad \text{Strongly imposed} \tag{2.18}$$

$$\boldsymbol{n} \cdot \boldsymbol{u} = 0 \text{ on } \Gamma_u, \qquad \text{Weakly imposed} \tag{2.19}$$

Notice that the boundary integral that appears after integration by parts of $(\nabla \cdot \boldsymbol{u}, q)$ vanishes due to (2.18)-(2.19).

2.3 Stabilized Finite Element Methods

In this section, we present two stabilized FE methods, which we will denote by the acronyms ASGS and OSS, aimed to overcome the instability problems of the standard Galerkin method. In general, stabilized FE methods can be used with any type of interpolation for p and $\boldsymbol{u}$. In particular, we focus on equal and continuous interpolations for p and $\boldsymbol{u}$ and therefore conforming FE spaces. For conciseness we will consider quasi-uniform FE partitions of size h. For stabilized formulations in general non-uniform non-degenerate cases, see [97].

Let $V_{p,h}$ and $V_{u,h}$ be the FE spaces to approximate p and $\boldsymbol{u}$, respectively, with $V_{p,h} \subset V_p$ and $V_{u,h} \subset V_u$. Additionally, let us define $V_h = V_{p,h} \times V_{u,h}$. For any of these spaces we will make frequent use of the classical inverse inequality $\|\nabla v_h\| \leq C_{\text{inv}} h^{-1} \|v_h\|$, with C_{inv} a constant independent of the FE function v_h and the mesh size h.

2.3.1 The Variational Multiscale Framework

It is not our purpose here to describe in detail the heuristic design of the stabilized finite element methods we will consider, for which [90] can be consulted. We shall only sketch the idea of how the method can be motivated.

Let us write the wave equation as

$$M\partial_t U + AU = F, \tag{2.20}$$

where M is a diagonal matrix with entries μ_p, μ_u, $U = [p, \boldsymbol{u}]$ is the unknown, A is the differential operator of the problem and F groups the forcing terms. The weak form of the problem can now be written as

$$\langle AU, V \rangle = \mathcal{B}(U, V) = (F, V), \tag{2.21}$$

where $\langle \cdot, \cdot \rangle$ is an appropriate duality depending on the functional setting being chosen.

The idea of the Variational Multiscale (VMS) framework to approximate problem (2.21) is as follows [89]. Let X be the space where U belongs, and consider $X = X_h \oplus \tilde{X}$, where X_h is a finite element approximation space and $\tilde{X}$ a complement to be specified. It can be thought as the space where the components of U which cannot be reproduced by the finite element mesh live. Functions $\tilde{U} \in \tilde{X}$ will be called *sub-grid scales* or *sub-scales*. As a first approximation, we assume that all terms involving $\tilde{U}$ evaluated on inter element boundaries vanish.

Using the splitting $U = U_h + \tilde{U}$ in (2.21), taking first the test function as $V_h \in X_h$ and then considering the test function in $\tilde{X}$ yields:

$$\mathcal{B}(U_h, V_h) + \langle \tilde{U}, A^* V_h \rangle = (F, V_h), \tag{2.22}$$

$$\tilde{P}(M\partial_t \tilde{U} + A\tilde{U}) = \tilde{P}(F - M\partial_t U_h - AU_h), \tag{2.23}$$

where A^* is the adjoint operator of A and $\tilde{P}$ stands for the L^2 projection onto $\tilde{X}$. We shall introduce now two approximations. The first is that $\tilde{P}(M\partial_t \tilde{U}) \approx 0$. This is not crucial, and in fact it can be relaxed, yielding what we call *dynamic* sub-scales [98]. The second approximation is to replace $\tilde{P}A$ by a diagonal algebraic operator τ^{-1}, with entries τ_p^{-1}, τ_u^{-1}. Using these approximations in (2.23) yields

$$\tilde{U} = \tau \tilde{P}(F - M\partial_t U_h - AU_h).$$

When introduced in (2.22) we obtain the stabilized finite element method we were seeking. When applied to our problem, this method will be of the form: Find a pair $[p_h, \boldsymbol{u}_h] \in \mathcal{C}^1([0,T]; V_h)$ satisfying the initial conditions $p_h(\boldsymbol{x}, 0) = 0$, $\boldsymbol{u}_h(\boldsymbol{x}, 0) = \boldsymbol{0}$ and such that

$$\mathcal{B}_s\left([p_h, \boldsymbol{u}_h], [q_h, \boldsymbol{v}_h]\right) = \mathcal{L}_s\left([q_h, \boldsymbol{v}_h]\right), \tag{2.24}$$

for all test functions $[q_h, \boldsymbol{v}_h] \in C^0([0,T]; V_h)$ such that $q_h(\boldsymbol{x}, 0) = 0$, $\boldsymbol{v}_h(\boldsymbol{x}, 0) = \boldsymbol{0}$, where it can be readily checked that the bilinear form $\mathcal{B}_s$ and the linear form $\mathcal{L}_s$ are given by

$$\begin{aligned}
\mathcal{B}_s\left([p_h, \boldsymbol{u}_h], [q_h, \boldsymbol{v}_h]\right) &= \mathcal{B}\left([p_h, \boldsymbol{u}_h], [q_h, \boldsymbol{v}_h]\right) + (\tilde{P}(\mu_p \partial_t p_h + \nabla \cdot \boldsymbol{u}_h), \tau_p \nabla \cdot \boldsymbol{v}_h) \\
&\quad + (\tilde{P}(\mu_u \partial_t \boldsymbol{u}_h + \nabla p_h), \tau_u \nabla q_h), \\
\mathcal{L}_s\left([q_h, \boldsymbol{v}_h]\right) &= \mathcal{L}\left([q_h, \boldsymbol{v}_h]\right) + (\tilde{P}(f_p), \tau_p \nabla \cdot \boldsymbol{v}_h) + (\tilde{P}(\boldsymbol{f}_u), \tau_u \nabla q_h).
\end{aligned} \tag{2.25}$$

Depending on the choice of $\tilde{X}$ or, equivalently, on the projection $\tilde{P}$, different stabilized methods arise. The two analyzed in this chapter are described in the following.

2.3.2 Algebraic Sub-Grid Scale Method (ASGS)

In this case we take $\tilde{X}$ as the space of finite element residuals, so that $\tilde{P}$ is the identity when acting on those residuals. Thus, the problem consists in solving (2.24) with

$$\begin{aligned}
\mathcal{B}_s\left([p_h, \boldsymbol{u}_h], [q_h, \boldsymbol{v}_h]\right) &= \mathcal{B}\left([p_h, \boldsymbol{u}_h], [q_h, \boldsymbol{v}_h]\right) + (\mu_p \partial_t p_h + \nabla \cdot \boldsymbol{u}_h, \tau_p \nabla \cdot \boldsymbol{v}_h) \\
&\quad + (\mu_u \partial_t \boldsymbol{u}_h + \nabla p_h, \tau_u \nabla q_h), \qquad (2.26) \\
\mathcal{L}_s\left([q_h, \boldsymbol{v}_h]\right) &= \mathcal{L}\left([q_h, \boldsymbol{v}_h]\right) + (f_p, \tau_p \nabla \cdot \boldsymbol{v}_h) + (\boldsymbol{f}_u, \tau_u \nabla q_h). \qquad (2.27)
\end{aligned}$$

2.3.3 Orthogonal Sub-scale Stabilization Method (OSS)

This method is an extension to the wave equation in mixed form of the method proposed in [98, 99]. Space $\tilde{X}$ is taking as the orthogonal in the L^2 sense to X_h. Thus, the problem consists in solving problem (2.24) and taking the bilinear form $\mathcal{B}_s$ and the linear form $\mathcal{L}_s$ as:

$$\mathcal{B}_s\left([p_h, \boldsymbol{u}_h], [q_h, \boldsymbol{v}_h]\right) = \mathcal{B}\left([p_h, \boldsymbol{u}_h], [q_h, \boldsymbol{v}_h]\right) + \left(P_p^{\perp}\left(\nabla \cdot \boldsymbol{u}_h\right), \tau_p \nabla \cdot \boldsymbol{v}_h\right)$$

$$+ \left(P_u^{\perp}\left(\nabla p_h\right), \tau_u \nabla q_h\right), \tag{2.28}$$

$$\mathcal{L}_s\left([q_h, \boldsymbol{v}_h]\right) = \mathcal{L}\left([q_h, \boldsymbol{v}_h]\right) + \left(P_p^{\perp}\left(f_p\right), \tau_p \nabla\cdot\boldsymbol{v}_h\right) + \left(P_u^{\perp}\left(\boldsymbol{f}_u\right), \tau_u \nabla q_h\right), \tag{2.29}$$

where $P_p^{\perp}(\cdot) = I(\cdot) - P_p(\cdot)$ and $P_u^{\perp}(\cdot) = I(\cdot) - P_u(\cdot)$, $P_p(\cdot)$ being the $L^2(\Omega)$ projection on $V_{p,h}$ and $P_u(\cdot)$ the $L^2(\Omega)$ projection on $V_{u,h}$. This in particular implies that $P_p(\cdot) = 0$ on Γ_p for variational forms I and III and that $\boldsymbol{n} \cdot P_u(\cdot) = 0$ on Γ_u for variational forms I and II.

From the implementation point of view, the terms $P_p^{\perp}\left(\nabla\cdot\boldsymbol{u}_h\right)$ and $P_u^{\perp}\left(\nabla p_h\right)$ obviously imply an augmented stencil in the matrix of the final algebraic system of equations to be solved. However, using iterative methods it is possible to deal with this without increasing the memory storage and at a very low computation cost, as shown in [97]. In the time discrete problem, it is also possible to approximate $P_p^{\perp}\left(\nabla\cdot\boldsymbol{u}_h^n\right) \approx \nabla\cdot\boldsymbol{u}_h^n - P_p\left(\nabla\cdot\boldsymbol{u}_h^{n-1}\right)$ (and likewise for $P_u^{\perp}\left(\nabla p_h^n\right)$), where the superscript denotes the time step counter. Other possibilities are discussed in [100], and a modified projection with lower sparsity is proposed in [101]. In any case, the increase in computational effort because of the projections can be made very low.

2.3.4 The Stabilization Parameters

An important component of stabilized formulations are the stabilization parameters. Following the motivation presented in Subsection 3.1, they appear when trying to approximate $\tilde{P}A\tilde{U} \approx \tau^{-1}\tilde{U}$ in a certain sense, which in our case is $[\nabla\cdot\tilde{\boldsymbol{u}}, \nabla\tilde{p}] \approx [\tau_p^{-1}\tilde{p}, \tau_u^{-1}\tilde{\boldsymbol{u}}]$. Again, the details of the arguments for this approximation can be found in [90, 102], and here we will only describe the essential ideas.

Consider equation (2.20). In general, the dimensions of the components of F are heterogeneous. Let S be a positive-definite scaling matrix such that the product $F^{\mathrm{t}}SF =: |F|_S^2$ is dimensionally well defined. Within each element K of the finite element partition, we assume that the Fourier transform of $\tilde{U}$ is dominated by wave numbers of the form $h^{-1}\tilde{\boldsymbol{k}}$, with h the diameter of K and $\tilde{\boldsymbol{k}}$ dimensionless and of order one. We may then take the Fourier transform $\mathcal{F}$ of $\tilde{P}A\tilde{U}$ and get $\mathcal{F}(\tilde{P}A\tilde{U}) = h^{-1}\mathcal{S}(\tilde{\boldsymbol{k}})\mathcal{F}(\tilde{U})$, where $\mathcal{S}(\tilde{\boldsymbol{k}})$ is a complex matrix.

Let $\|F\|_{K,S}$ be the $L^2(K)$-norm of $|F|_S$. The way we propose to approximate $\tilde{P}A\tilde{U} \approx \tau^{-1}\tilde{U}$ is to choose τ^{-1} such that $\|h^{-1}\mathcal{S}(\tilde{\boldsymbol{k}})\mathcal{F}(\tilde{U})\|_{K,S} = \|\tau^{-1}\tilde{U}\|_{K,S}$. This in particular can be accomplished by imposing that the spectrum of $h^{-1}\mathcal{S}(\tilde{\boldsymbol{k}})\mathcal{F}(\tilde{U})$ and of $\tau^{-1}\tilde{U}$ with respect to the scaling matrix S coincide. Choosing S as diagonal, with entries

$$S_p = \mu_u \ell_p, \qquad S_u = \mu_p \ell_u,$$

with ℓ_p, ℓ_u length scales corresponding to p and $\boldsymbol{u}$, respectively, it can be shown that

$$\tau_p = C_\tau \sqrt{\frac{\mu_u}{\mu_p}} h \sqrt{\frac{\ell_p}{\ell_u}}, \qquad \tau_u = C_\tau \sqrt{\frac{\mu_p}{\mu_u}} h \sqrt{\frac{\ell_u}{\ell_p}}, \tag{2.30}$$

where C_τ is a dimensionless algorithmic constant that corresponds to the norm of $\mathcal{S}(\tilde{\boldsymbol{k}})$ evaluated at a certain wave number $\tilde{\boldsymbol{k}}$. See [90, 102] for the details of the derivation.

Table 2.1: Stabilization Parameters Order and Length Scales Definition

Variational Form	I	II	III
τ_p	$\mathcal{O}(h)$	$\mathcal{O}(1)$	$\mathcal{O}(h^2)$
τ_u	$\mathcal{O}(h)$	$\mathcal{O}(h^2)$	$\mathcal{O}(1)$
ℓ_p	$\ell_p = \ell_u$	L_0^2/h	h
ℓ_u	$\ell_p = \ell_u$	h	L_0^2/h

As it will be shown in the analysis to be presented, in order to mimic at the discrete level the proper functional setting of the continuous problem the length scales ℓ_p and ℓ_u should be taken as shown in Table 2.1, where L_0 is a fixed length scale of the problem that can be fixed a priori. The motivation for designing the stabilization parameters can be found in [90, 91].

2.4 Stability Analysis

In this section, we state and prove stability for the ASGS and the OSS methods. Firstly, we use the concept of Λ-Coercivity, which will aid us in the proof of stability and later in the convergence analysis.

2.4.1 Λ-Coercivity

In this section, we state and prove Λ-coercivity in the same sense as in [103] for the ASGS method and with some modifications for the OSS method. The results obtained apply to any of the variational forms defined in (2.8)-(2.19). We only prove Λ-coercivity for the variational form I (2.8)-(2.11) because variational forms II and III only differ in two of the Galerkin terms, namely $(\nabla p_h, \boldsymbol{v}_h)$ and $(\nabla \cdot \boldsymbol{u}_h, q_h)$. That difference makes the proof just slightly different among the three variational forms. Therefore we only include the proof for the variational form I.

In what follows, C denotes a positive constant, independent of μ_p, μ_u, ℓ_p and ℓ_u, but which might depend on the computational domain Ω. In the discrete formulation C will be independent of the mesh size h. The value of C may be different at different occurrences. Additionally, we will use the notation $A \gtrsim B$ and $A \lesssim B$ to indicate that $A \geq CB$ and $A \leq CB$ respectively, where A and B are two quantities that might depend on the solution or mesh size.

The previous methods are not coercive in the norms of interest. The well-posedness is proved via an inf-sup condition. Let $\mathcal{V}$ be a normed space with norm $|\cdot|_{\mathcal{V}}$ and $\zeta : \mathcal{V} \times \mathcal{V} \longrightarrow \mathbb{R}$ a bilinear form. The inf-sup condition implies that $\forall u \in \mathcal{V}\ \exists\, v \in \mathcal{V}$ such that $\zeta(u, v) \gtrsim |u|_{\mathcal{V}}|v|_{\mathcal{V}}$ with $|v|_{\mathcal{V}} \lesssim |u|_{\mathcal{V}}$.

For the subsequent analysis we want to prove a more descriptive property than the inf-sup condition. We will define an operator $\Lambda : \mathcal{V} \longrightarrow \mathcal{V}$ such that $\zeta(u, \Lambda(u)) \gtrsim |u|_{\mathcal{V}}|\Lambda(u)|_{\mathcal{V}}\ \forall u \in \mathcal{V}$, with $|\Lambda(u)|_{\mathcal{V}} \lesssim |u|_{\mathcal{V}}$. This property has been defined as Λ-Coercivity in [103]. It implies the inf-sup condition for a particular definition of norms but it also provides additional information on how to choose a v such that the inf-sup condition holds.

Definition 2.4.1. *Let us define the following norm in* $\mathcal{C}^1([0,T];V_h)$*:*

$$\begin{aligned}\|\!|\, [q_h, \boldsymbol{v}_h] \,|\!\|^2_{W,h} := \mu_p \|q_h\|^2_{L^\infty(\Upsilon,L^2(\Omega))} + \mu_u \|\boldsymbol{v}_h\|^2_{L^\infty(\Upsilon,L^2(\Omega))} \\ + \tau_p \|\mu_p \partial_t q_h + \nabla\cdot \boldsymbol{v}_h\|^2_{L^2(\Upsilon,L^2(\Omega))} + \tau_u \|\mu_u \partial_t \boldsymbol{v}_h + \nabla q_h\|^2_{L^2(\Upsilon,L^2(\Omega))}.\end{aligned} \tag{2.31}$$

The way the norm $|\!|\!| \cdot |\!|\!|_{W,h}$ is written and the spaces to which $[p_h, \boldsymbol{u}_h]$ belong allow us to determine the expression of the length scales ℓ_p and ℓ_u. In particular, the terms that contain ∇p_h and $\nabla\cdot\boldsymbol{u}_h$ are the ones that allow us to define the length scales. For instance, in the case of Variational Form II, as $p_h \in L^2(\Omega)$, the term containing the ∇p_h should include a factor h^2, that means we choose $\tau_u = \mathcal{O}(h^2)$. Following the same reasoning, for $\nabla\cdot\boldsymbol{u}_h \in L^2(\Omega)$ we arrive to $\tau_p = \mathcal{O}(1)$. In Table 2.1 we have summarized this reasoning and extended it to the remaining variational forms.

Note that some of the results to be presented hold even in the case $\tau_p = 0$, $\tau_u = 0$. However, in this case the norm in (2.31) only contains $L^\infty(\Upsilon, L^2(\Omega))$ norms, and this is not enough to avoid point-to-point oscillations. This stability would be found in most first-order-in-time problems using the standard Galerkin method, even if the spatial approximation is completely unstable.

ASGS Method

Here we state and prove Λ-Coercivity for the ASGS method.

Lemma 2.4.1. *(Weak* Λ*-Coercivity, ASGS) The bilinear form* (2.26) *satisfies*

$$|\!|\!| \, [q_h, \boldsymbol{v}_h] \, |\!|\!|^2_{W,h} \lesssim \int_0^T \mathcal{B}_s\left([q_h, \boldsymbol{v}_h], \Lambda\left([q_h, \boldsymbol{v}_h]\right)\right) \mathrm{d}t \quad \forall\, [q_h, \boldsymbol{v}_h]\,, \tag{2.32}$$

where the norm $|\!|\!| \cdot |\!|\!|_{W,h}$ *is defined in* (2.31) *and*

$$\Lambda\left([q_h, \boldsymbol{v}_h]\right) := [q_h + \tau_p \mu_p \partial_t q_h, \boldsymbol{v}_h + \tau_u \mu_u \partial_t \boldsymbol{v}_h]\,. \tag{2.33}$$

Proof. Let us test (2.26) with (2.33):

$$\begin{aligned}&\mathcal{B}_s\left([q_h, \boldsymbol{v}_h], \Lambda\left([q_h, \boldsymbol{v}_h]\right)\right) \\ &= (\mu_p \partial_t q_h + \nabla\cdot\boldsymbol{v}_h, q_h) + (\mu_p \partial_t q_h + \nabla\cdot\boldsymbol{v}_h, \tau_p \mu_p \partial_t q_h + \tau_p \nabla\cdot\boldsymbol{v}_h) \\ &\quad + (\mu_u \partial_t \boldsymbol{v}_h + \nabla q_h, \boldsymbol{v}_h) + (\mu_u \partial_t \boldsymbol{v}_h + \nabla q_h, \tau_u \mu_u \partial_t \boldsymbol{v}_h + \tau_u \nabla q_h) \\ &\quad + (\mu_p \partial_t q_h + \nabla\cdot\boldsymbol{v}_h, \tau_p \nabla\cdot(\tau_u \mu_u \partial_t \boldsymbol{v}_h)) + (\mu_u \partial_t \boldsymbol{v}_h + \nabla q_h, \tau_u \nabla\left(\tau_p \mu_p \partial_t q_h\right))\,,\end{aligned} \tag{2.34}$$

using the divergence theorem, recalling that $q_h(\boldsymbol{n}\cdot\boldsymbol{v}_h) = 0$ and $\partial_t q_h \partial_t(\boldsymbol{n}\cdot\boldsymbol{v}_h) = 0$ on Γ due to (2.4), we get:

$$\begin{aligned}\mathcal{B}_s\left([q_h, \boldsymbol{v}_h], \Lambda\left([q_h, \boldsymbol{v}_h]\right)\right) &= \frac{1}{2}\mu_p \frac{\mathrm{d}}{\mathrm{d}t}\|q_h\|^2 + \frac{1}{2}\mu_u \frac{\mathrm{d}}{\mathrm{d}t}\|\boldsymbol{v}_h\|^2 + \frac{1}{2}\mu_p \tau_p \tau_u \frac{\mathrm{d}}{\mathrm{d}t}\|\nabla q_h\|^2 \\ &+ \frac{1}{2}\mu_u \tau_p \tau_u \frac{\mathrm{d}}{\mathrm{d}t}\|\nabla\cdot\boldsymbol{v}_h\|^2 + \tau_p \|\mu_p \partial_t q_h + \nabla\cdot\boldsymbol{v}_h\|^2 + \tau_u \|\mu_u \partial_t \boldsymbol{v}_h + \nabla q_h\|^2,\end{aligned} \tag{2.35}$$

and integrating (2.35) from $t = 0$ up to any $t = t^* \leq T$ we get:

$$\int_0^{t^*} \mathcal{B}_s\left([q_h, \boldsymbol{v}_h], \Lambda\left([q_h, \boldsymbol{v}_h]\right)\right) \mathrm{d}t$$

$$
\begin{aligned}
=&\frac{1}{2}\mu_p\|q_h(t^*)\|^2+\frac{1}{2}\mu_u\|\boldsymbol{v}_h(t^*)\|^2+\frac{1}{2}\tau_p\tau_u\mu_p\|\nabla q_h(t^*)\|^2+\frac{1}{2}\tau_p\tau_u\mu_u\|\nabla\cdot\boldsymbol{v}_h(t^*)\|^2\\
&+\tau_p\int_0^{t^*}\|\mu_p\partial_t q_h(t)+\nabla\cdot\boldsymbol{v}_h(t)\|^2\,\mathrm{d}t+\tau_u\int_0^{t^*}\|\mu_u\partial_t\boldsymbol{v}_h(t)+\nabla q_h(t)\|^2\,\mathrm{d}t,
\end{aligned}
$$

from where $L^\infty(\Upsilon,L^2(\Omega))$ stability follows. Choosing $t^*=T$ we complete the proof. □

OSS Method

Here we state and prove Λ-Coercivity for the OSS method. In this case we express Λ-Coercivity in two norms: a weak norm defined in (2.31) and a stronger norm defined in (2.42) below. The norm in (2.42) is stronger, since it provides full control over ∇p_h and $\nabla\cdot\boldsymbol{u}_h$.

Lemma 2.4.2. *(Weak Λ-Coercivity, OSS) The bilinear form* (2.28) *satisfies:*

$$
|\!|\!|\,[q_h,\boldsymbol{v}_h]\,|\!|\!|^2_{W,h}\lesssim\int_0^T\mathcal{B}_s\left([q_h,\boldsymbol{v}_h],\Lambda\left([q_h,\boldsymbol{v}_h]\right)\right)\mathrm{d}t\quad\forall\,[q_h,\boldsymbol{v}_h]\,, \tag{2.36}
$$

where the norm $|\!|\!|\cdot|\!|\!|_{W,h}$ *is defined in* (2.31) *and*

$$
\Lambda\left([q_h,\boldsymbol{v}_h]\right)=[q_h,\boldsymbol{v}_h]+\beta\left[\tau_p(\mu_p\partial_t q_h+P_p(\nabla\cdot\boldsymbol{v}_h)),\tau_u(\mu_u\partial_t\boldsymbol{v}_h+P_u(\nabla q_h))\right], \tag{2.37}
$$

with a small enough $\beta>0$.

Proof. Let us test (2.28) against $\Lambda_a([q_h,\boldsymbol{v}_h])=[q_h,\boldsymbol{v}_h]$. Using the divergence theorem, the boundary condition $q_h(\boldsymbol{n}\cdot\boldsymbol{v}_h)=0$ and integrating from $t=0$ to $t=T$, we can readily get:

$$
\begin{aligned}
\int_0^T\mathcal{B}_s\left([q_h,\boldsymbol{v}_h],\Lambda_a\left([q_h,\boldsymbol{v}_h]\right)\right)\,\mathrm{d}t\geq&\frac{1}{2}\mu_p\|q_h\|^2_{L^\infty(L^2)}+\frac{1}{2}\mu_u\|\boldsymbol{v}_h\|^2_{L^\infty(L^2)}\\
&+\tau_p\|P_p^\perp\left(\nabla\cdot\boldsymbol{v}_h\right)\|^2_{L^2(L^2)}+\tau_u\|P_u^\perp\left(\nabla q_h\right)\|^2_{L^2(L^2)}.
\end{aligned} \tag{2.38}
$$

Now, let $\Lambda_b([q_h,\boldsymbol{v}_h])=\left[\tau_p(\mu_p\partial_t q_h+P_p\left(\nabla\cdot\boldsymbol{v}_h\right)),\tau_u(\mu_u\partial_t\boldsymbol{v}_h+P_u\left(\nabla q_h\right))\right]$ and let us test (2.28) against $\Lambda_b([q_h,\boldsymbol{v}_h])$:

$$
\begin{aligned}
\mathcal{B}_s\left([q_h,\boldsymbol{v}_h],\Lambda_b\left([q_h,\boldsymbol{v}_h]\right)\right)=&\left(\mu_p\partial_t q_h+\nabla\cdot\boldsymbol{v}_h,\tau_p(\mu_p\partial_t q_h+P_p\left(\nabla\cdot\boldsymbol{v}_h\right))\right)\\
&+\left(\mu_u\partial_t\boldsymbol{v}_h+\nabla q_h,\tau_u(\mu_u\partial_t\boldsymbol{v}_h+P_u\left(\nabla q_h\right))\right)\\
&+\left(P_p^\perp(\nabla\cdot\boldsymbol{v}_h),\tau_p\nabla\cdot(\tau_u(\mu_u\partial_t\boldsymbol{v}_h+P_u\left(\nabla q_h\right)))\right)\\
&+\left(P_u^\perp(\nabla q_h),\tau_u\nabla\left(\tau_p(\mu_p\partial_t q_h+P_p\left(\nabla\cdot\boldsymbol{v}_h\right))\right)\right).
\end{aligned} \tag{2.39}
$$

Using the Cauchy-Schwarz inequality, the inverse inequality, the fact that $\tau_p\tau_u=C_\tau^2h^2$ and Young's inequality, we get:

$$
\begin{aligned}
&\mathcal{B}_s\left([q_h,\boldsymbol{v}_h],\Lambda_b\left([q_h,\boldsymbol{v}_h]\right)\right)\\
&\quad\geq\tau_p\|\mu_p\partial_t q_h+P_p\left(\nabla\cdot\boldsymbol{v}_h\right)\|^2+\tau_u\|\mu_u\partial_t\boldsymbol{v}_h+P_u\left(\nabla q_h\right)\|^2\\
&\qquad-\frac{1}{2\alpha_1}\tau_p\|\mu_p\partial_t q_h+P_p\left(\nabla\cdot\boldsymbol{v}_h\right)\|^2-\frac{\alpha_1}{2}C_\tau^2C_{\mathrm{inv}}^2\tau_u\|P_u^\perp(\nabla q_h)\|^2
\end{aligned}
$$

$$- \frac{1}{2\alpha_2}\tau_u\|\mu_u\partial_t\boldsymbol{v}_h + P_u\left(\nabla q_h\right)\|^2 - \frac{\alpha_2}{2}C_\tau^2 C_{\text{inv}}^2\tau_p\|P_p^\perp(\nabla\cdot\boldsymbol{v}_h)\|^2, \tag{2.40}$$

for any $\alpha_1, \alpha_2 > 0$. Next, we integrate (2.40) in time from 0 to T and multiply it by a positive constant β. The resulting inequality is added to (2.38). Taking β small enough and α_i large enough, we prove the lemma. □

As was explained before, now we introduce a norm stronger than (2.31). Using this norm we establish a new Λ-coercivity result.

Lemma 2.4.3. *(Strong Λ-Coercivity, OSS) The bilinear form* (2.28) *satisfies:*

$$\begin{aligned}\|\!|\left[q_h, \boldsymbol{v}_h\right]|\!\|_{S,h}^2 \lesssim &\int_0^T \mathcal{B}_s\left(\left[q_h, \boldsymbol{v}_h\right], \Lambda_1\left(\left[q_h, \boldsymbol{v}_h\right]\right)\right)\mathrm{d}t \\ &+ \int_0^T \mathcal{B}_s\left(\left[\partial_t q_h, \partial_t\boldsymbol{v}_h\right], \Lambda_2\left(\left[q_h, \boldsymbol{v}_h\right]\right)\right)\mathrm{d}t \\ &+ \mathcal{B}_s\left(\left[q_h, \boldsymbol{v}_h\right], \Lambda_2\left(\left[q_h, \boldsymbol{v}_h\right]\right)\right)\big|_{t=0},\end{aligned} \tag{2.41}$$

$\forall\left[q_h, \boldsymbol{v}_h\right]$, *where*

$$\begin{aligned}\|\!|\left[q_h, \boldsymbol{v}_h\right]|\!\|_{S,h}^2 := &\,\mu_p\|q_h\|_{L^\infty(\Upsilon,L^2(\Omega))}^2 + \mu_u\|\boldsymbol{v}_h\|_{L^\infty(\Upsilon,L^2(\Omega))}^2 \\ &+ \tau_p\|\nabla\cdot\boldsymbol{v}_h\|_{L^2(\Upsilon,L^2(\Omega))}^2 + \tau_u\|\nabla q_h\|_{L^2(\Upsilon,L^2(\Omega))}^2,\end{aligned} \tag{2.42}$$

and

$$\Lambda_1\left(\left[q_h, \boldsymbol{v}_h\right]\right) = \left[q_h + \beta_1\tau_p P_p(\nabla\cdot\boldsymbol{v}_h), \boldsymbol{v}_h + \beta_1\tau_u P_u(\nabla q_h)\right], \tag{2.43}$$

$$\Lambda_2\left(\left[q_h, \boldsymbol{v}_h\right]\right) = \beta_2\left[\partial_t q_h, \partial_t\boldsymbol{v}_h\right], \tag{2.44}$$

with $\beta_1 > 0$ small enough,

$$\beta_2 = \mu_p\gamma_p + \mu_u\gamma_u, \quad \gamma_p = \frac{\alpha}{2}T\left(\tau_p + \tau_u\frac{\mu_u}{\mu_p}\right), \quad \gamma_u = \frac{\alpha}{2}T\left(\tau_u + \tau_p\frac{\mu_p}{\mu_u}\right), \tag{2.45}$$

and $\alpha > 0$ large enough.

Proof. Let us test (2.28) with (2.43):

$$\begin{aligned}&\mathcal{B}_s\left(\left[q_h, \boldsymbol{v}_h\right], \Lambda_1\left(\left[q_h, \boldsymbol{v}_h\right]\right)\right) \\ &= \left(\mu_p\partial_t q_h + \nabla\cdot\boldsymbol{v}_h, q_h + \beta_1\tau_p P_p(\nabla\cdot\boldsymbol{v}_h)\right) + \left(\mu_u\partial_t\boldsymbol{v}_h + \nabla q_h, \boldsymbol{v}_h + \beta_1\tau_u P_u(\nabla q_h)\right) \\ &\quad + \left(P_p^\perp(\nabla\cdot\boldsymbol{v}_h), \tau_p\nabla\cdot(\boldsymbol{v}_h + \beta_1\tau_u P_u(\nabla q_h))\right) \\ &\quad + \left(P_u^\perp(\nabla q_h), \tau_u\nabla(q_h + \beta_1\tau_p P_p(\nabla\cdot\boldsymbol{v}_h))\right).\end{aligned} \tag{2.46}$$

Using the divergence theorem, the fact that $q_h(\boldsymbol{n}\cdot\boldsymbol{v}_h) = 0$ on the boundary, the Cauchy-Schwarz inequality, Young's inequality and integrating in time from 0 to T, we readily get:

$$\int_0^T \mathcal{B}_s\left(\left[q_h, \boldsymbol{v}_h\right], \Lambda_1\left(\left[q_h, \boldsymbol{v}_h\right]\right)\right)\,\mathrm{d}t \geq \frac{1}{2}\mu_p\|q_h\|_{L^\infty(L^2)}^2 + \frac{1}{2}\mu_u\|\boldsymbol{v}_h\|_{L^\infty(L^2)}^2$$

$$+ \beta_3\tau_p\|\nabla\cdot\boldsymbol{v}_h\|^2_{L^2(L^2)} - \frac{\alpha_1}{2}\tau_p\|\mu_p\partial_t q_h\|^2_{L^2(L^2)}$$
$$+ \beta_3\tau_u\|\nabla q_h\|^2_{L^2(L^2)} - \frac{\alpha_1}{2}\tau_u\|\mu_u\partial_t\boldsymbol{v}_h\|^2_{L^2(L^2)}, \tag{2.47}$$

with

$$\beta_3 = \min\left\{\beta_1\left(1 - \frac{\beta_1}{2\alpha_1} - \frac{\beta_1 C_\tau^2 C_{\text{inv}}^2}{2}\right), \frac{1}{2}\right\}. \tag{2.48}$$

and β_1 small enough, so that β_3 is positive.

Now, let us take Λ_2 as defined in (2.44). Using the fact that $\partial_t q_h \partial_t(\boldsymbol{n}\cdot\boldsymbol{v}_h) = 0$ on the boundary and integrating in time, we get:

$$\int_0^T \mathcal{B}_s\left([\partial_t q_h, \partial_t\boldsymbol{v}_h], \Lambda_2\left([q_h,\boldsymbol{v}_h]\right)\right)\,\mathrm{d}t \geq \gamma_p\left(\|\mu_p\partial_t q_h\|^2_{L^\infty(L^2)} - \|\mu_p\partial_t q_h(0)\|^2\right)$$
$$+ \gamma_u\left(\|\mu_u\partial_t\boldsymbol{v}_h\|^2_{L^\infty(L^2)} - \|\mu_u\partial_t\boldsymbol{v}_h(0)\|^2\right). \tag{2.49}$$

Additionally, we take α large enough so that γ_p and γ_u are large enough and the combination of (2.47) and (2.49) results in a positive factor multiplying both $\|\mu_p\partial_t q_h\|_{L^\infty(L^2)}$ and $\|\mu_u\partial_t\boldsymbol{u}_h\|_{L^\infty(L^2)}$.

Now, let us test (2.28) with (2.44) and evaluate it at $t = 0$:

$$\begin{aligned}&\mathcal{B}_s\left([q_h,\boldsymbol{v}_h], \Lambda_2\left([q_h,\boldsymbol{v}_h]\right)\right)\big|_{t=0}\\ &= (\mu_p\partial_t q_h(0) + \nabla\cdot\boldsymbol{v}_h(0), \beta_2\partial_t q_h(0)) + (\mu_u\partial_t\boldsymbol{v}_h(0) + \nabla q_h(0), \beta_2\partial_t\boldsymbol{v}_h(0))\\ &\quad + \left(P_p^\perp(\nabla\cdot\boldsymbol{v}_h(0)), \tau_p\nabla\cdot(\beta_2\partial_t\boldsymbol{v}_h(0))\right) + \left(P_u^\perp(\nabla q_h(0)), \tau_u\nabla(\beta_2\partial_t q_h(0))\right).\end{aligned} \tag{2.50}$$

Noticing that $\nabla q_h(0) = \boldsymbol{0}$ and $\nabla\cdot\boldsymbol{v}_h(0) = 0$, we get:

$$\mathcal{B}_s\left([q_h,\boldsymbol{v}_h], \Lambda_2\left([q_h,\boldsymbol{v}_h]\right)\right)\big|_{t=0} \geq 2\gamma_p\|\mu_p\partial_t q_h(0)\|^2 + 2\gamma_u\|\mu_u\partial_t\boldsymbol{v}_h(0)\|^2. \tag{2.51}$$

Combining (2.47), (2.49) and (2.51) the proof is complete. □

2.4.2 Stability

Here, using the previous Λ-coercivity lemmata, we state and prove stability for the ASGS and the OSS methods, i.e. we prove that the solution is bounded by the initial conditions and forcing terms. The results obtained apply to any of the variational forms defined in (2.8)-(2.19).

ASGS Method

In this section we define the external forces norm and prove stability for the ASGS method.

Theorem 2.4.1. *(ASGS Stability) The solution* $[p_h, \boldsymbol{u}_h]$ *of* (2.24) *obtained with the ASGS method* (2.26) - (2.27) *satisfies*

$$|\!|\!|\,[p_h,\boldsymbol{u}_h]\,|\!|\!|^2_{W,h} \lesssim |\!|\,[f_p,\boldsymbol{f}_u]\,|\!|^2_{W,h}, \tag{2.52}$$

with the norm $\|\!|\!| \cdot |\!|\!|_{W,h}$ *defined in* (2.31) *and with*

$$\begin{aligned}\|\!|\!| [f_p, \boldsymbol{f}_u] |\!|\!|^2_{W,h} :=& \frac{1}{\mu_p}\|f_p\|^2_{L^1(\Upsilon,L^2(\Omega))} + \frac{1}{\mu_u}\|\boldsymbol{f}_u\|^2_{L^1(\Upsilon,L^2(\Omega))} \\ &+ \tau_p\|f_p\|^2_{L^2(\Upsilon,L^2(\Omega))} + \tau_u\|\boldsymbol{f}_u\|^2_{L^2(\Upsilon,L^2(\Omega))} \\ &+ \tau_p\tau_u\mu_u\|\partial_t f_p\|^2_{L^1(\Upsilon,L^2(\Omega))} + \tau_p\tau_u\mu_p\|\partial_t \boldsymbol{f}_u\|^2_{L^1(\Upsilon,L^2(\Omega))} \\ &+ \tau_p\tau_u\mu_u\|f_p\|^2_{L^\infty(\Upsilon,L^2(\Omega))} + \tau_p\tau_u\mu_p\|\boldsymbol{f}_u\|^2_{L^\infty(\Upsilon,L^2(\Omega))}. \end{aligned} \tag{2.53}$$

Proof. Using weak Λ-Coercivity for the ASGS method (2.32) and the definition of the operator Λ in (2.33) we arrive to:

$$\begin{aligned}|\!|\!| [p_h, \boldsymbol{u}_h] |\!|\!|^2_{W,h} \lesssim \int_0^T \Big[& (f_p, p_h + \tau_p\mu_p\partial_t p_h) + \tau_p\left(f_p, \nabla\cdot(\boldsymbol{u}_h + \tau_u\mu_u\partial_t\boldsymbol{u}_h)\right) \\ & + (\boldsymbol{f}_u, \boldsymbol{u}_h + \tau_u\mu_u\partial_t\boldsymbol{u}_h) + \tau_u\left(\boldsymbol{f}_u, \nabla\left(p_h + \tau_p\mu_p\partial_t p_h\right)\right)\Big]\,\mathrm{d}t. \end{aligned} \tag{2.54}$$

Combining some terms and using Cauchy-Schwarz inequality, we get

$$\begin{aligned}|\!|\!| [p_h, \boldsymbol{u}_h] |\!|\!|^2_{W,h} \lesssim \int_0^T \Big[& \|f_p\|\|p_h\| + \tau_p\|f_p\|\|\mu_p\partial_t p_h + \nabla\cdot\boldsymbol{u}_h\| \\ & + (f_p, \tau_p\tau_u\mu_u\nabla\cdot\partial_t\boldsymbol{u}_h) + (\boldsymbol{f}_u, \tau_p\tau_u\mu_p\nabla\partial_t p_h) \\ & + \|\boldsymbol{f}_u\|\|\boldsymbol{u}_h\| + \tau_u\|\boldsymbol{f}_u\|\|\mu_u\partial_t\boldsymbol{u}_h + \nabla p_h\|\Big]\,\mathrm{d}t. \end{aligned} \tag{2.55}$$

Most of the terms of (2.55) are easy to bound, the only ones that require special treatment are the ones containing $\nabla\cdot\partial_t\boldsymbol{u}_h$ and $\nabla\partial_t p_h$. Those terms can be bounded as:

$$\begin{aligned} & (f_p, \tau_p\tau_u\mu_u\nabla\cdot\partial_t\boldsymbol{u}_h) + (\boldsymbol{f}_u, \tau_p\tau_u\mu_p\nabla\partial_t p_h) \\ & = -\int_0^T (\partial_t f_p, \tau_p\tau_u\mu_u\nabla\cdot\boldsymbol{u}_h)\,\mathrm{d}t + \left(f_p(T), \tau_p\tau_u\mu_u\nabla\cdot\boldsymbol{u}_h(T)\right) \\ & \quad - \int_0^T (\partial_t\boldsymbol{f}_u, \tau_p\tau_u\mu_p\nabla p_h)\,\mathrm{d}t + \left(\boldsymbol{f}_u(T), \tau_p\tau_u\mu_p\nabla p_h(T)\right) \\ & \leq \frac{\alpha_1}{2}\tau_p\tau_u\mu_u\|\partial_t f_p\|^2_{L^1(L^2)} + \frac{1}{2\alpha_1}\tau_p\tau_u\mu_u\|\nabla\cdot\boldsymbol{u}_h\|^2_{L^\infty(L^2)} \\ & \quad + \frac{\alpha_2}{2}\tau_p\tau_u\mu_u\|f_p\|^2_{L^\infty(L^2)} + \frac{1}{2\alpha_2}\tau_p\tau_u\mu_u\|\nabla\cdot\boldsymbol{u}_h\|^2_{L^\infty(L^2)} \\ & \quad + \frac{\alpha_3}{2}\tau_p\tau_u\mu_p\|\partial_t\boldsymbol{f}_u\|^2_{L^1(L^2)} + \frac{1}{2\alpha_3}\tau_p\tau_u\mu_p\|\nabla p_h\|^2_{L^\infty(L^2)} \\ & \quad + \frac{\alpha_4}{2}\tau_p\tau_u\mu_p\|\boldsymbol{f}_u\|^2_{L^\infty(L^2)} + \frac{1}{2\alpha_4}\tau_p\tau_u\mu_p\|\nabla p_h\|^2_{L^\infty(L^2)}. \end{aligned} \tag{2.56}$$

Finally, taking α_i sufficiently large in (2.56) and replacing it in (2.55), it is easy to arrive to (2.52), which is what we wanted to prove. □

OSS Method

In this section we define the external forces norm and prove stability for the OSS method.

Theorem 2.4.2. *(Weak OSS Stability) The solution* $[p_h, \boldsymbol{u}_h]$ *of* (2.24) *obtained with the OSS method* (2.28)-(2.29) *satisfies*

$$|\!|\!| [p_h, \boldsymbol{u}_h] |\!|\!|^2_{W,h} \lesssim |\!| [f_p, \boldsymbol{f}_u] |\!|^2_{W,h}, \tag{2.57}$$

with the norm $|\!|\!| \cdot |\!|\!|_{W,h}$ *defined in* (2.31) *and with*

$$\begin{aligned} |\!| [f_p, \boldsymbol{f}_u] |\!|^2_{W,h} :=& \frac{1}{\mu_p}\|f_p\|^2_{L^1(\Upsilon,L^2(\Omega))} + \frac{1}{\mu_u}\|\boldsymbol{f}_u\|^2_{L^2(\Upsilon,L^2(\Omega))} \\ &+ \tau_p\|f_p\|^2_{L^2(\Upsilon,L^2(\Omega))} + \tau_u\|\boldsymbol{f}_u\|^2_{L^2(\Upsilon,L^2(\Omega))}. \end{aligned} \tag{2.58}$$

Proof. Using the weak Λ-Coercivity for the OSS method (2.36) with Λ as in (2.37) we arrive to:

$$\begin{aligned} |\!|\!| [p_h, \boldsymbol{u}_h] |\!|\!|^2_{W,h} \lesssim& \int_0^T \Big[(f_p, p_h + \beta\tau_p (\mu_p\partial_t p_h + P_p(\nabla\cdot\boldsymbol{u}_h))) \\ &+ (\boldsymbol{f}_u, \boldsymbol{u}_h + \beta\tau_u (\mu_u\partial_t\boldsymbol{u}_h + P_u(\nabla p_h))) \\ &+ \big(P_p^\perp(f_p), \tau_p\nabla\cdot(\boldsymbol{u}_h + \beta\tau_u (\mu_u\partial_t\boldsymbol{u}_h + P_u(\nabla p_h)))\big) \\ &+ \big(P_u^\perp(\boldsymbol{f}_u), \tau_u\nabla (p_h + \beta\tau_p (\mu_p\partial_t p_h + P_p(\nabla\cdot\boldsymbol{u}_h)))\big) \Big] \mathrm{d}t \\ \lesssim& \frac{\alpha_1}{2}\frac{1}{\mu_p}\|f_p\|^2_{L^1(L^2)} + \frac{1}{2\alpha_1}\mu_p\|p_h\|^2_{L^\infty(L^2)} \\ &+ \frac{\alpha_2}{2}\tau_p\|f_p\|^2_{L^2(L^2)} + \frac{\beta^2}{2\alpha_2}\tau_p\|\mu_p\partial_t p_h + \nabla\cdot\boldsymbol{u}_h\|^2_{L^2(L^2)} \\ &+ \frac{\alpha_3}{2}\frac{1}{\mu_u}\|\boldsymbol{f}_u\|^2_{L^1(L^2)} + \frac{1}{2\alpha_3}\mu_u\|\boldsymbol{u}_h\|^2_{L^\infty(L^2)} \\ &+ \frac{\alpha_4}{2}\tau_u\|\boldsymbol{f}_u\|^2_{L^2(L^2)} + \frac{\beta^2}{2\alpha_4}\tau_u\|\mu_u\partial_t\boldsymbol{u}_h + \nabla p_h\|^2_{L^2(L^2)} \\ &+ \frac{\alpha_5}{2}\tau_p\|P_p^\perp(f_p)\|^2_{L^2(L^2)} + \frac{\beta^2}{2\alpha_5}\tau_p\|P_p^\perp(\nabla\cdot\boldsymbol{u}_h)\|^2_{L^2(L^2)} \\ &+ \frac{\alpha_6}{2}\tau_p\|P_p^\perp(f_p)\|^2_{L^2(L^2)} + \frac{\beta^2 C_\tau^2 C_{\text{inv}}^2}{2\alpha_6}\tau_u\|\mu_u\partial_t\boldsymbol{u}_h + P_u(\nabla p_h)\|^2_{L^2(L^2)} \\ &+ \frac{\alpha_7}{2}\tau_u\|P_u^\perp(\boldsymbol{f}_u)\|^2_{L^2(L^2)} + \frac{\beta^2}{2\alpha_7}\tau_u\|P_u^\perp(\nabla p_h)\|^2_{L^2(L^2)} \\ &+ \frac{\alpha_8}{2}\tau_u\|P_u^\perp(\boldsymbol{f}_u)\|^2_{L^2(L^2)} + \frac{\beta^2 C_\tau^2 C_{\text{inv}}^2}{2\alpha_8}\tau_p\|\mu_p\partial_t p_h + P_p(\nabla\cdot\boldsymbol{u}_h)\|^2_{L^2(L^2)}. \end{aligned}$$

We complete the proof choosing α_i large enough. □

Theorem 2.4.3. *(Strong OSS Stability) The solution* $[p_h, \boldsymbol{u}_h]$ *of* (2.24) *obtained with the OSS method* (2.28)-(2.29) *satisfies*

$$|\!|\!| [p_h, \boldsymbol{u}_h] |\!|\!|^2_{S,h} \lesssim |\!| [f_p, \boldsymbol{f}_u] |\!|^2_{S,h}, \tag{2.59}$$

with the norm $|\!|\!| \cdot |\!|\!|_{S,h}$ *defined in* (2.42) *and with*

$$|\!| [f_p, \boldsymbol{f}_u] |\!|^2_{S} := \frac{1}{\mu_p}\|f_p\|^2_{L^1(\Upsilon,L^2(\Omega))} + \frac{1}{\mu_u}\|\boldsymbol{f}_u\|^2_{L^1(\Upsilon,L^2(\Omega))}$$

$$
\begin{aligned}
&+ \tau_p \|f_p\|^2_{L^2(\Upsilon,L^2(\Omega))} + \tau_u \|\boldsymbol{f}_u\|^2_{L^2(\Upsilon,L^2(\Omega))} \\
&+ \gamma_p \left(\|\partial_t f_p\|^2_{L^1(\Upsilon,L^2(\Omega))} + \|f_p(0)\|^2 \right) \\
&+ \gamma_u \left(\|\partial_t \boldsymbol{f}_u\|^2_{L^1(\Upsilon,L^2(\Omega))} + \|\boldsymbol{f}_u(0)\|^2 \right) \\
&+ \frac{\gamma_u}{\mu_u} \tau_p \|\partial_t f_p\|^2_{L^2(\Upsilon,L^2(\Omega))} + \frac{\gamma_p}{\mu_p} \tau_u \|\partial_t \boldsymbol{f}_u\|^2_{L^2(\Upsilon,L^2(\Omega))} \\
&+ \gamma_u \tau_p \|f_p(0)\| + \gamma_p \tau_u \|\boldsymbol{f}_u(0)\|, \qquad (2.60)
\end{aligned}
$$

and the parameters γ_p and γ_u are given in (2.45).

Proof. Using the strong Λ-Coercivity for the OSS method (2.41) and the definitions of Λ_i from (2.43)-(2.44), we arrive to:

$$
\begin{aligned}
\| [p_h, \boldsymbol{u}_h] \|^2_{S,h} \lesssim & \int_0^T \mathcal{L}_s \left(\Lambda_1 \left([p_h, \boldsymbol{u}_h] \right) \right) \mathrm{d}t + \int_0^T \mathcal{L}_t \left(\Lambda_2 \left([p_h, \boldsymbol{u}_h] \right) \right) \mathrm{d}t \\
& + \mathcal{L}_s \left(\Lambda_2 \left([p_h, \boldsymbol{u}_h] \right) \right) \big|_{t=0}, \qquad (2.61)
\end{aligned}
$$

where $\mathcal{L}_t$ is $\mathcal{L}_s$ with the time derivative of the forces. The first term of (2.61) can be written and bounded as follows:

$$
\begin{aligned}
&\int_0^T \mathcal{L}_s \left(\Lambda_1 \left([p_h, \boldsymbol{u}_h] \right) \right) \mathrm{d}t \\
&\quad = \int_0^T \Big[(f_p, p_h + \beta_1 \tau_p P_p(\nabla \cdot \boldsymbol{u}_h)) + (\boldsymbol{f}_u, \boldsymbol{u}_h + \beta_1 \tau_u P_u(\nabla p_h)) \Big] \mathrm{d}t \\
&\qquad + \int_0^T \left(P_p^{\perp}(f_p), \tau_p \nabla \cdot (\boldsymbol{u}_h + \beta_1 \tau_u P_u(\nabla p_h)) \right) \mathrm{d}t \\
&\qquad + \int_0^T \left(P_u^{\perp}(\boldsymbol{f}_u), \tau_u \nabla \left(p_h + \beta_1 \tau_p P_p(\nabla \cdot \boldsymbol{u}_h) \right) \right) \mathrm{d}t \\
&\quad \leq \frac{\alpha_1}{2} \frac{1}{\mu_p} \|f_p\|^2_{L^1(L^2)} + \Big(\frac{\beta_1^2}{2\alpha_2} + \frac{1}{2\alpha_5} + \frac{\beta_1^2 C_\tau^2 C_{\mathrm{inv}}^2}{2\alpha_8} \Big) \tau_p \|\nabla \cdot \boldsymbol{u}_h\|^2_{L^2(L^2)} \\
&\qquad + \frac{\alpha_2 + \alpha_5 + \alpha_6}{2} \tau_p \|f_p\|^2_{L^2(L^2)} + \frac{1}{2\alpha_1} \mu_p \|p_h\|^2_{L^\infty(L^2)} \\
&\qquad + \frac{\alpha_3}{2} \frac{1}{\mu_u} \|\boldsymbol{f}_u\|^2_{L^1(L^2)} + \Big(\frac{\beta_1^2}{2\alpha_4} + \frac{1}{2\alpha_7} + \frac{\beta_1^2 C_\tau^2 C_{\mathrm{inv}}^2}{2\alpha_6} \Big) \tau_u \|\nabla p_h\|^2_{L^2(L^2)} \\
&\qquad + \frac{\alpha_4 + \alpha_7 + \alpha_8}{2} \tau_u \|\boldsymbol{f}_u\|^2_{L^2(L^2)} + \frac{1}{2\alpha_3} \mu_u \|\boldsymbol{u}_h\|^2_{L^\infty(L^2)}. \qquad (2.62)
\end{aligned}
$$

The second term of (2.61) can be written and bounded as follows:

$$
\begin{aligned}
&\int_0^T \mathcal{L}_t \left(\Lambda_2 \left([p_h, \boldsymbol{u}_h] \right) \right) \mathrm{d}t \\
&\quad = \int_0^T \Big[(\partial_t f_p, \beta_2 \partial_t p_h) + \left(P_p^{\perp}(\partial_t f_p), \tau_p \nabla \cdot (\beta_2 \partial_t \boldsymbol{u}_h) \right) \Big] \mathrm{d}t \\
&\qquad + \int_0^T \Big[(\partial_t \boldsymbol{f}_u, \beta_2 \partial_t \boldsymbol{u}_h) + \left(P_u^{\perp}(\partial_t \boldsymbol{f}_u), \tau_u \nabla \left(\beta_2 \partial_t p_h \right) \right) \Big] \mathrm{d}t
\end{aligned}
$$

$$
\begin{aligned}
&\leq \alpha_9\gamma_p\|\partial_t f_p\|^2_{L^1(L^2)} + \frac{\gamma_p}{\alpha_9}\|\mu_p\partial_t p_h\|^2_{L^\infty(L^2)} \\
&\quad + \frac{\alpha_{10}\gamma_u}{\mu_u}\tau_p\|\partial_t f_p\|^2_{L^2(L^2)} + \frac{\gamma_u}{\alpha_{10}\mu_u}\tau_p\|P_p^\perp(\nabla\cdot\mu_u\partial_t\boldsymbol{u}_h)\|^2_{L^2(L^2)} \\
&\quad + \alpha_{11}\gamma_u\|\partial_t\boldsymbol{f}_u\|^2_{L^1(L^2)} + \frac{\gamma_u}{\alpha_{11}}\|\mu_u\partial_t\boldsymbol{u}_h\|^2_{L^\infty(L^2)} \\
&\quad + \frac{\alpha_{12}\gamma_p}{\mu_p}\tau_u\|\partial_t\boldsymbol{f}_u\|^2_{L^2(L^2)} + \frac{\gamma_p}{\alpha_{12}\mu_p}\tau_u\|P_u^\perp(\nabla\mu_p\partial_t p_h)\|^2_{L^2(L^2)}.
\end{aligned} \tag{2.63}
$$

The third term of (2.61) can be written and bounded as follows:

$$
\begin{aligned}
&\mathcal{L}_s\left(\Lambda_2\left([p_h,\boldsymbol{u}_h]\right)\right)\big|_{t=0} = (f_p(0),\beta_2\partial_t p_h(0)) + (\boldsymbol{f}_u(0),\beta_2\partial_t\boldsymbol{u}_h(0)) \\
&\quad + \left(P_p^\perp(f_p(0)),\tau_p\nabla\cdot\beta_2\partial_t\boldsymbol{u}_h(0)\right) + \left(P_u^\perp(\boldsymbol{f}_u(0)),\tau_u\nabla\beta_2\partial_t p_h(0)\right) \\
&\leq \alpha_{13}\gamma_p\|f_p(0)\|^2 + \frac{\gamma_p}{\alpha_{13}}\|\mu_p\partial_t p_h(0)\|^2 + \alpha_{15}\gamma_u\tau_p\|f_p(0)\|^2 \\
&\quad + \alpha_{14}\gamma_u\|\boldsymbol{f}_u(0)\|^2 + \frac{\gamma_u}{\alpha_{14}}\|\mu_u\partial_t\boldsymbol{u}_h(0)\|^2 + \alpha_{16}\gamma_p\tau_u\|\boldsymbol{f}_u(0)\|^2 \\
&\quad + \frac{\gamma_u}{\alpha_{15}}\tau_p\|P_p^\perp(\nabla\cdot\mu_u\partial_t\boldsymbol{u}_h)(0)\|^2 + \frac{\gamma_p}{\alpha_{16}}\tau_u\|P_u^\perp(\nabla\mu_p\partial_t p_h)(0)\|^2.
\end{aligned} \tag{2.64}
$$

Finally, combining (2.62), (2.63) and (2.64) and taking α_i large enough, the proof is complete. □

Remark 2.4.1. *From Theorems 4.5, 4.6 and 4.7, two conclusions can be drawn. First, in the case of the weaker norm* (2.31) *both the ASGS and the OSS methods are stable, but the latter requires less regularity on the forcing terms than the former. But, secondly, the OSS method allows one to obtain convergence in the stronger norm* (2.42) *(at the expense of more regularity on the forcing terms), and thus to control all the gradient of p_h and all the divergence of $\boldsymbol{u}_h$, not in combination with temporal derivatives.*

2.5 Convergence Analysis

In this section we state and prove convergence of the stabilized finite element methods proposed: ASGS and OSS. The results obtained apply to any of the variational forms defined in (2.8)-(2.19). We only prove convergence for the variational form I because variational forms II and III only differ in two of the Galerkin terms $(\nabla p_h,\boldsymbol{v}_h)$ and $(\nabla\cdot\boldsymbol{u}_h,q_h)$ with respect to the variational form I.

Let us define p_I as the P_p projection of the exact solution p on $V_{p,h}$ and $\boldsymbol{u}_I$ as the P_u projection of the exact solution $\boldsymbol{u}$ on $V_{u,h}$.

Lemma 2.5.1. *(Optimality of P_p and P_u) Let $P_p : V_p \longrightarrow V_{p,h}$ and $P_u : V_u \longrightarrow V_{u,h}$ be two projections defined as:*

$$(P_p(q),\chi_h) = (q,\chi_h) \quad \forall\chi_h \in V_{p,h}, \tag{2.65}$$

$$P_p(q) = 0 \quad \text{on } \Gamma_p, \tag{2.66}$$

$$(P_u(\boldsymbol{v}),\boldsymbol{w}_h) = (\boldsymbol{v},\boldsymbol{w}_h) \quad \forall\boldsymbol{w}_h \in V_{u,h}, \tag{2.67}$$

$$\boldsymbol{n}\cdot P_u(\boldsymbol{v}) = 0 \quad \text{on } \Gamma_u. \tag{2.68}$$

Let k and l be the polynomial interpolation order for $V_{p,h}$ and $V_{u,h}$ respectively. Then, P_p and P_u are optimal in $L^2(\Omega)$ and $H^1(\Omega)$. That is:

$$\|q - P_p(q)\|_0 \lesssim h^{k+1}|q|_{k+1}, \qquad \|q - P_p(q)\|_1 \lesssim h^{k}|q|_{k+1}, \tag{2.69}$$

$$\|\boldsymbol{v} - P_u(\boldsymbol{v})\|_0 \lesssim h^{l+1}|\boldsymbol{v}|_{l+1}, \qquad \|\boldsymbol{v} - P_u(\boldsymbol{v})\|_1 \lesssim h^{l}|\boldsymbol{v}|_{l+1}. \tag{2.70}$$

for smooth enough $q \in V_p$ and $\boldsymbol{v} \in V_u$.

Proof. Let $Z_{p,h}$ and $Z_{u,h}$ be the Scott-Zhang projection operators that satisfy the boundary conditions of V_p and V_u, respectively [104]. By the definition of P_p in (2.65) we have:

$$(q - P_p(q), q - P_p(q)) = (q - P_p(q), q - Z_{p,h}(q)), \tag{2.71}$$

$$\|q - P_p(q)\| \leq \|q - Z_{p,h}(q)\| \lesssim h^{k+1}|q|_{k+1}. \tag{2.72}$$

Now, let us consider the approximation error in the H^1 norm:

$$\|q - P_p(q)\|_1 \leq \|q - Z_{p,h}(q)\|_1 + \|Z_{p,h}(q) - P_p(q)\|_1 \tag{2.73}$$

$$\leq \|q - Z_{p,h}(q)\|_1 + C_{\text{inv}}h^{-1}\|Z_{p,h}(q) - P_p(q)\|_0 \tag{2.74}$$

$$\leq \|q - Z_{p,h}(q)\|_1 + C_{\text{inv}}h^{-1}\left(\|Z_{p,h}(q) - q\|_0 + \|q - P_p(q)\|_0\right) \tag{2.75}$$

$$\lesssim h^{k}|q|_{k+1}, \tag{2.76}$$

where we have used the inverse inequality. The proof for P_u is similar to the proof for P_p and we omit it. □

Let us define two types of error. The error of the approximate solution (obtained using ASGS or OSS) with respect to the projected exact solution is defined as:

$$e_p := p_h - p_I\,, \quad \boldsymbol{e}_u := \boldsymbol{u}_h - \boldsymbol{u}_I, \tag{2.77}$$

and the error of the exact solution with respect to the projected exact solution is defined as:

$$\varepsilon_p := p - p_I, \quad \boldsymbol{\varepsilon}_u := \boldsymbol{u} - \boldsymbol{u}_I. \tag{2.78}$$

Notice that $[e_p, \boldsymbol{e}_u]$ belongs to the FE space and $[\varepsilon_p, \boldsymbol{\varepsilon}_u]$ is orthogonal to the FE space with respect to the $L^2(\Omega)$ inner product. We shall make frequent use of this orthogonality property.

Additionally, let us define the projection error in the $H^i(\Omega)$ norm:

$$\varepsilon_i(p) = \|\varepsilon_p\|_{H^i(\Omega)}, \quad \varepsilon_i(\boldsymbol{u}) = \|\boldsymbol{\varepsilon}_u\|_{H^i(\Omega)}, \quad i = 0, 1. \tag{2.79}$$

2.5.1 ASGS Method

Let us consider problem (2.24) with $\mathcal{B}_s$ and $\mathcal{L}_s$ defined in (2.26) and (2.27), respectively. The approximate solution to that problem converges as stated in the following result:

Theorem 2.5.1. *(ASGS Convergence) Let $[p, \boldsymbol{u}]$ be the solution of the continuous problem (2.7) and let $[p_h, \boldsymbol{u}_h]$ be the solution of the stabilized discrete problem (2.24) using the ASGS method. Then*

$$\| [p - p_h, \boldsymbol{u} - \boldsymbol{u}_h] \|_{W,h} \lesssim E_W(h), \tag{2.80}$$

with the norm $\| \cdot \|_{W,h}$ defined in (2.31) and

$$\begin{aligned} E_W^2(h) := & \mu_p \|\varepsilon_p\|^2_{L^\infty(\Upsilon,L^2(\Omega))} + \mu_u \|\boldsymbol{\varepsilon}_u\|^2_{L^\infty(\Upsilon,L^2(\Omega))} \\ & + \tau_p \|\mu_p \partial_t \varepsilon_p\|^2_{L^2(\Upsilon,L^2(\Omega))} + \tau_u \|\mu_u \partial_t \boldsymbol{\varepsilon}_u\|^2_{L^2(\Upsilon,L^2(\Omega))} \\ & + \mu_u \tau_p \tau_u \|\mu_p \partial_t \varepsilon_p\|^2_{L^\infty(\Upsilon,L^2(\Omega))} + \mu_p \tau_p \tau_u \|\mu_u \partial_t \boldsymbol{\varepsilon}_u\|^2_{L^\infty(\Upsilon,L^2(\Omega))} \\ & + \mu_u \tau_p \tau_u \|\mu_p \partial_{tt} \varepsilon_p\|^2_{L^1(\Upsilon,L^2(\Omega))} + \mu_p \tau_p \tau_u \|\mu_u \partial_{tt} \boldsymbol{\varepsilon}_u\|^2_{L^1(\Upsilon,L^2(\Omega))} \\ & + \frac{1}{\tau_p} \|\varepsilon_p\|^2_{L^2(\Upsilon,L^2(\Omega))} + \frac{1}{\tau_u} \|\boldsymbol{\varepsilon}_u\|^2_{L^2(\Upsilon,L^2(\Omega))} \\ & + \tau_u \|\nabla \varepsilon_p\|^2_{L^2(\Upsilon,L^2(\Omega))} + \tau_p \|\nabla \cdot \boldsymbol{\varepsilon}_u\|^2_{L^2(\Upsilon,L^2(\Omega))} \\ & + \mu_p \tau_p \tau_u \|\nabla \varepsilon_p\|^2_{L^\infty(\Upsilon,L^2(\Omega))} + \mu_u \tau_p \tau_u \|\nabla \cdot \boldsymbol{\varepsilon}_u\|^2_{L^\infty(\Upsilon,L^2(\Omega))} \\ & + \mu_p \tau_p \tau_u \|\nabla \partial_t \varepsilon_p\|^2_{L^1(\Upsilon,L^2(\Omega))} + \mu_u \tau_p \tau_u \|\nabla \cdot \partial_t \boldsymbol{\varepsilon}_u\|^2_{L^1(\Upsilon,L^2(\Omega))}. \end{aligned} \tag{2.81}$$

Proof. Since the ASGS method is consistent (in the sense that the exact solution is solution of the discrete problem) and using (2.32) with Λ given in (2.33) we have:

$$\begin{aligned} \| [e_p, \boldsymbol{e}_u] \|^2_{W,h} \lesssim & \int_0^T \mathcal{B}_s \left([e_p, \boldsymbol{e}_u], \Lambda([e_p, \boldsymbol{e}_u]) \right) \mathrm{d}t = \int_0^T \mathcal{B}_s \left([\varepsilon_p, \boldsymbol{\varepsilon}_u], \Lambda([e_p, \boldsymbol{e}_u]) \right) \mathrm{d}t \\ \lesssim & \int_0^T \left(\mu_p \partial_t \varepsilon_p, e_p + \tau_p \left(\mu_p \partial_t e_p + \nabla \cdot \boldsymbol{e}_u \right) + \mu_u \tau_p \tau_u \nabla \cdot \partial_t \boldsymbol{e}_u \right) \mathrm{d}t \\ & + \int_0^T \left(\mu_u \partial_t \boldsymbol{\varepsilon}_u, \boldsymbol{e}_u + \tau_u \left(\mu_u \partial_t \boldsymbol{e}_u + \nabla e_p \right) + \mu_p \tau_p \tau_u \nabla \partial_t e_p \right) \mathrm{d}t \\ & + \int_0^T \left(\nabla \cdot \boldsymbol{\varepsilon}_u, e_p + \tau_p \left(\mu_p \partial_t e_p + \nabla \cdot \boldsymbol{e}_u \right) + \mu_u \tau_p \tau_u \nabla \cdot \partial_t \boldsymbol{e}_u \right) \mathrm{d}t \\ & + \int_0^T \left(\nabla \varepsilon_p, \boldsymbol{e}_u + \tau_u \left(\mu_u \partial_t \boldsymbol{e}_u + \nabla e_p \right) + \mu_p \tau_p \tau_u \nabla \partial_t e_p \right) \mathrm{d}t. \end{aligned} \tag{2.82}$$

Now we can bound $\| [e_p, \boldsymbol{e}_u] \|_{W,h}$ in terms of the projection error $[\varepsilon_p, \boldsymbol{\varepsilon}_u]$. We will show parts of the right hand side of (2.82) and how they are bounded. The first term of this expression can be bounded as:

$$\begin{aligned} & \int_0^T \left(\mu_p \partial_t \varepsilon_p, e_p + \tau_p \left(\mu_p \partial_t e_p + \nabla \cdot \boldsymbol{e}_u \right) + \mu_u \tau_p \tau_u \nabla \cdot \partial_t \boldsymbol{e}_u \right) \mathrm{d}t \\ \leq & \frac{\alpha_1}{2} \tau_p \|\mu_p \partial_t \varepsilon_p\|^2_{L^2(L^2)} + \frac{1}{2\alpha_1} \tau_p \|\mu_p \partial_t e_p + \nabla \cdot \boldsymbol{e}_u\|^2_{L^2(L^2)} \\ & + \frac{\alpha_2}{2} \mu_u \tau_p \tau_u \|\mu_p \partial_t \varepsilon_p\|^2_{L^\infty(L^2)} + \frac{1}{2\alpha_2} \mu_u \tau_p \tau_u \|\nabla \cdot \boldsymbol{e}_u\|^2_{L^\infty(L^2)} \\ & + \frac{\alpha_3}{2} \mu_u \tau_p \tau_u \|\mu_p \partial_{tt} \varepsilon_p\|^2_{L^1(L^2)} + \frac{1}{2\alpha_3} \mu_u \tau_p \tau_u \|\nabla \cdot \boldsymbol{e}_u\|^2_{L^\infty(L^2)}. \end{aligned} \tag{2.83}$$

The third term of (2.82) can be bounded as:

$$\begin{aligned}
&\int_0^T \left(\nabla\cdot\boldsymbol{\varepsilon}_u, e_p + \tau_p\left(\mu_p\partial_t e_p + \nabla\cdot\boldsymbol{e}_u\right) + \mu_u\tau_p\tau_u\nabla\cdot\partial_t\boldsymbol{e}_u\right)\mathrm{d}t \\
&\leq \frac{\alpha_4}{2}\tau_u^{-1}\|\boldsymbol{\varepsilon}_u\|^2_{L^2(L^2)} + \frac{1}{2\alpha_4}\tau_u\|\mu_u\partial_t\boldsymbol{e}_u + \nabla e_p\|^2_{L^2(L^2)} \\
&\quad + \frac{\alpha_5}{2}\tau_p\|\nabla\cdot\boldsymbol{\varepsilon}_u\|^2_{L^2(L^2)} + \frac{1}{2\alpha_5}\tau_p\|\mu_p\partial_t e_p + \nabla\cdot\boldsymbol{e}_u\|^2_{L^2(L^2)} \\
&\quad + \frac{\alpha_6}{2}\mu_u\tau_p\tau_u\|\nabla\cdot\boldsymbol{\varepsilon}_u\|^2_{L^\infty(L^2)} + \frac{1}{2\alpha_6}\mu_u\tau_p\tau_u\|\nabla\cdot\boldsymbol{e}_u\|^2_{L^\infty(L^2)} \\
&\quad + \frac{\alpha_7}{2}\mu_u\tau_p\tau_u\|\nabla\cdot\partial_t\boldsymbol{\varepsilon}_u\|^2_{L^1(L^2)} + \frac{1}{2\alpha_7}\mu_u\tau_p\tau_u\|\nabla\cdot\boldsymbol{e}_u\|^2_{L^\infty(L^2)}. \qquad (2.84)
\end{aligned}$$

The second and fourth terms of (2.82) can be bounded similarly as the first and third terms as shown in (2.83)-(2.84). Taking α_i big enough, it follows that $|\!|\!|\left[e_p, \boldsymbol{e}_u\right]|\!|\!|^2_{W,h} \lesssim E^2_W(h)$. Additionally, $|\!|\!|\left[p-p_h, \boldsymbol{u}-\boldsymbol{u}_h\right]|\!|\!|^2_{W,h} \lesssim |\!|\!|\left[e_p, \boldsymbol{e}_u\right]|\!|\!|^2_{W,h} + |\!|\!|\left[\varepsilon_p, \boldsymbol{\varepsilon}_u\right]|\!|\!|^2_{W,h}$. Furthermore, by definition $|\!|\!|\left[\varepsilon_p, \boldsymbol{\varepsilon}_u\right]|\!|\!|^2_{W,h} \lesssim E^2_W(h)$, which completes the proof. □

The inequality $|\!|\!|\left[\varepsilon_p, \boldsymbol{\varepsilon}_u\right]|\!|\!|^2_{W,h} \lesssim E^2_W(h)$ is precisely the way of determining $E^2_W(h)$.

2.5.2 OSS Method

As we have defined two norms for the OSS method, one weaker than the other, we will prove convergence in both, starting with the weaker one.

Theorem 2.5.2. *(OSS Convergence in the weak norm) Let $[p, \boldsymbol{u}]$ be the solution of the continuous problem (2.7) and let $[p_h, \boldsymbol{u}_h]$ be the solution of the stabilized discrete problem (2.24) using the OSS method. Then*

$$|\!|\!|\left[p-p_h, \boldsymbol{u}-\boldsymbol{u}_h\right]|\!|\!|_{W,h} \lesssim E_W\left(h\right), \qquad (2.85)$$

with the norm $|\!|\!|\cdot|\!|\!|_{W,h}$ defined in (2.31) and

$$\begin{aligned}
E^2_W(h) :=& \mu_p\|\varepsilon_p\|^2_{L^\infty(\Upsilon,L^2(\Omega))} + \mu_u\|\boldsymbol{\varepsilon}_u\|^2_{L^\infty(\Upsilon,L^2(\Omega))} \\
&+ \tau_p\|\mu_p\partial_t\varepsilon_p\|^2_{L^2(\Upsilon,L^2(\Omega))} + \tau_u\|\mu_u\partial_t\boldsymbol{\varepsilon}_u\|^2_{L^2(\Upsilon,L^2(\Omega))} \\
&+ \frac{1}{\tau_p}\|\varepsilon_p\|^2_{L^2(\Upsilon,L^2(\Omega))} + \frac{1}{\tau_u}\|\boldsymbol{\varepsilon}_u\|^2_{L^2(\Upsilon,L^2(\Omega))} \\
&+ \tau_u\|\nabla\varepsilon_p\|^2_{L^2(\Upsilon,L^2(\Omega))} + \tau_p\|\nabla\cdot\boldsymbol{\varepsilon}_u\|^2_{L^2(\Upsilon,L^2(\Omega))}. \qquad (2.86)
\end{aligned}$$

Proof. Since the OSS method is consistent (in the sense that the exact solution is solution of the discrete problem) because the OSS method uses the projections P_p and P_u, we can use the weak Λ-coercivity of the OSS method (2.36) with Λ given in (2.37) and we get:

$$\begin{aligned}
|\!|\!|\left[e_p, \boldsymbol{e}_u\right]|\!|\!|^2_{W,h} \lesssim& \int_0^T \left(\mu_p\partial_t\varepsilon_p + \nabla\cdot\boldsymbol{\varepsilon}_u, e_p + \beta\tau_p\left(\mu_p\partial_t e_p + P_p\left(\nabla\cdot\boldsymbol{e}_u\right)\right)\right)\mathrm{d}t \\
&+ \int_0^T \left(\mu_u\partial_t\boldsymbol{\varepsilon}_u + \nabla\varepsilon_p, \boldsymbol{e}_u + \beta\tau_u\left(\mu_u\partial_t\boldsymbol{e}_u + P_u\left(\nabla e_p\right)\right)\right)\mathrm{d}t
\end{aligned}$$

$$+\int_0^T \left(\tau_p P_p^{\perp}(\nabla\cdot\boldsymbol{\varepsilon}_u), \nabla\cdot(\boldsymbol{e}_u + \beta\tau_u\left(\mu_u\partial_t\boldsymbol{e}_u + P_u\left(\nabla e_p\right)\right))\right)\mathrm{d}t$$
$$+\int_0^T \left(\tau_u P_u^{\perp}(\nabla\varepsilon_p), \nabla\left(e_p + \beta\tau_p\left(\mu_p\partial_t e_p + P_p\left(\nabla\cdot\boldsymbol{e}_u\right)\right)\right)\right)\mathrm{d}t. \tag{2.87}$$

Now we can bound $|\!|\!| [e_p, \boldsymbol{e}_u] |\!|\!|_{W,h}$ in terms of the projection error $[\varepsilon_p, \boldsymbol{\varepsilon}_u]$. We will show parts of the right hand side of (2.87) and how they are bounded. The first term of this expression can be bounded as:

$$\begin{aligned}
&\int_0^T \left(\mu_p\partial_t\varepsilon_p + \nabla\cdot\boldsymbol{\varepsilon}_u, e_p + \beta\tau_p\left(\mu_p\partial_t e_p + P_p\left(\nabla\cdot\boldsymbol{e}_u\right)\right)\right)\mathrm{d}t \\
&\leq \frac{\alpha_1}{2}\tau_p\|\mu_p\partial_t\varepsilon_p + P_p(\nabla\cdot\boldsymbol{\varepsilon}_u)\|^2_{L^2(L^2)} + \frac{\alpha_2}{2}\tau_u^{-1}\|\boldsymbol{\varepsilon}_u\|^2_{L^2(L^2)} \\
&\quad + \frac{\beta^2}{2\alpha_1}\tau_p\|\mu_p\partial_t e_p + P_p(\nabla\cdot\boldsymbol{e}_u)\|^2_{L^2(L^2)} + \frac{\tau_u}{2\alpha_2}\|\mu_u\partial_t\boldsymbol{e}_u + P_u(\nabla e_p)\|^2_{L^2(L^2)}.
\end{aligned} \tag{2.88}$$

The third term of (2.87) can be bounded as:

$$\begin{aligned}
&\int_0^T \left(\tau_p P_p^{\perp}(\nabla\cdot\boldsymbol{\varepsilon}_u), \nabla\cdot(\boldsymbol{e}_u + \beta\tau_u\left(\mu_u\partial_t\boldsymbol{e}_u + P_u\left(\nabla e_p\right)\right))\right)\mathrm{d}t \\
&\leq \frac{\alpha_3}{2}\tau_p\|P_p^{\perp}(\nabla\cdot\boldsymbol{\varepsilon}_u)\|^2_{L^2(L^2)} + \frac{1}{2\alpha_3}\tau_p\|P_p^{\perp}(\nabla\cdot\boldsymbol{e}_u)\|^2_{L^2(L^2)} \\
&\quad + \frac{\beta^2}{2\alpha_3}\tau_u C_\tau^2 C_{\mathrm{inv}}^2\|\mu_u\partial_t\boldsymbol{e}_u + P_u(\nabla e_p)\|^2_{L^2(L^2)}.
\end{aligned} \tag{2.89}$$

The second and fourth terms of (2.87) can be bounded similarly as we did for the first and third terms in (2.88)-(2.89). Taking α_i big enough, it follows that $|\!|\!| [e_p, \boldsymbol{e}_u] |\!|\!|^2_{W,h} \lesssim E^2_W(h)$. Using the same reasoning as for the ASGS method, we complete the proof for the OSS method. □

Let us examine each term of $E^2_{W,h}$ from (2.86) with respect to $\|p - p_h\|^2_{L^\infty(\Upsilon,L^2(\Omega))}$ (or the equivalent norm for $\boldsymbol{u}$). The first and second terms are optimal for any of the variational forms I, II and III (2.8)-(2.17). The third and fourth terms are at least optimal for I, II or III. The fifth and seventh terms are quasi-optimal for I, optimal for II and sub-optimal for III. The sixth and eighth terms are quasi-optimal for I, sub-optimal for II and optimal for III. A similar analysis can be carried out for the error of ∇p_h and $\nabla\cdot\boldsymbol{u}_h$. Results are summarized in Table 2.2.

Now, let us examine the convergence of the OSS method in the strong norm (2.42).

Theorem 2.5.3. *(OSS Convergence in the strong norm) Let $[p, \boldsymbol{u}]$ be the solution of the continuous problem (2.7) and let $[p_h, \boldsymbol{u}_h]$ be the solution of the stabilized discrete problem (2.24) using the OSS method. Then*

$$|\!|\!| [p - p_h, \boldsymbol{u} - \boldsymbol{u}_h] |\!|\!|_{S,h} \lesssim E_S\left(h\right), \tag{2.90}$$

with the norm $|\!|\!| \cdot |\!|\!|_{S,h}$ defined in (2.42) and

$$E^2_S(h) := \mu_p\|\varepsilon_p\|^2_{L^\infty(\Upsilon,L^2(\Omega))} + \mu_u\|\boldsymbol{\varepsilon}_u\|^2_{L^\infty(\Upsilon,L^2(\Omega))}$$

$$
\begin{aligned}
&+ \tau_u \|\nabla \varepsilon_p\|_{L^2(\Upsilon,L^2(\Omega))} + \tau_p \|\nabla\cdot\boldsymbol{\varepsilon}_u\|_{L^2(\Upsilon,L^2(\Omega))} \\
&+ \tau_p \|\mu_p \partial_t \varepsilon_p\|^2_{L^2(\Upsilon,L^2(\Omega))} + \tau_u \|\mu_u \partial_t \boldsymbol{\varepsilon}_u\|^2_{L^2(\Upsilon,L^2(\Omega))} \\
&+ \frac{1}{\tau_p}\|\varepsilon_p\|^2_{L^2(\Upsilon,L^2(\Omega))} + \frac{1}{\tau_u}\|\boldsymbol{\varepsilon}_u\|^2_{L^2(\Upsilon,L^2(\Omega))} \\
&+ \gamma_p \|\mu_p \partial_{tt}\varepsilon_p + \nabla\cdot\partial_t \boldsymbol{\varepsilon}_u\|^2_{L^1(\Upsilon,L^2(\Omega))} + \gamma_u \|\mu_u \partial_{tt}\boldsymbol{\varepsilon}_u + \nabla \partial_t \varepsilon_p\|^2_{L^1(\Upsilon,L^2(\Omega))} \\
&+ \beta_2 \tau_p \|\nabla\cdot\partial_t \boldsymbol{\varepsilon}_u\|^2_{L^2(\Upsilon,L^2(\Omega))} + \beta_2 \tau_u \|\nabla \partial_t \varepsilon_p\|^2_{L^2(\Upsilon,L^2(\Omega))} \\
&+ \gamma_p \|\mu_p \partial_t \varepsilon_p(0)\|^2 + \gamma_u \|\mu_u \partial_t \boldsymbol{\varepsilon}_u(0)\|^2. \qquad (2.91)
\end{aligned}
$$

Proof. Since the OSS method is consistent (in the sense that the exact solution is solution of the discrete problem) , using the strong Λ-coercivity (2.41) with Λ_i given in (2.43)-(2.44), $i = 1, 2$, we get:

$$
\begin{aligned}
|\!|\!| [e_p, \boldsymbol{e}_u] |\!|\!|^2_{W,h} \lesssim & \int_0^T \mathcal{B}_s \left([\varepsilon_p, \boldsymbol{\varepsilon}_u], \Lambda_1 ([e_p, \boldsymbol{e}_u])\right) \mathrm{d}t \\
&+ \int_0^T \mathcal{B}_s \left([\partial_t \varepsilon_p, \partial_t \boldsymbol{\varepsilon}_u], \Lambda_2 ([e_p, \boldsymbol{e}_u])\right) \mathrm{d}t \\
&+ \mathcal{B}_s \left([\varepsilon_p, \boldsymbol{\varepsilon}_u], \Lambda_2 ([e_p, \boldsymbol{e}_u])\right)\big|_{t=0}. \qquad (2.92)
\end{aligned}
$$

Now we can bound each term of (2.92) in terms of the interpolation error $[\varepsilon_p, \boldsymbol{\varepsilon}_u]$. The first term of (2.92) can be written as:

$$
\begin{aligned}
\int_0^T \mathcal{B}_s \left([\varepsilon_p, \boldsymbol{\varepsilon}_u], \Lambda_1 ([e_p, \boldsymbol{e}_u])\right) \mathrm{d}t = & \int_0^T (\mu_p \partial_t \varepsilon_p + \nabla\cdot\boldsymbol{\varepsilon}_u, e_p + \beta_1 \tau_p P_p(\nabla\cdot\boldsymbol{e}_u)) \, \mathrm{d}t \\
&+ \int_0^T (\mu_u \partial_t \boldsymbol{\varepsilon}_u + \nabla \varepsilon_p, \boldsymbol{e}_u + \beta_1 \tau_u P_u(\nabla e_p)) \, \mathrm{d}t \\
&+ \int_0^T \left(P_p^{\perp}(\nabla\cdot\boldsymbol{\varepsilon}_u), \tau_p \nabla\cdot(\boldsymbol{e}_u + \beta_1 \tau_u P_u(\nabla e_p))\right) \mathrm{d}t \\
&+ \int_0^T \left(P_u^{\perp}(\nabla \varepsilon_p), \tau_u \nabla(e_p + \beta_1 \tau_p P_p(\nabla\cdot\boldsymbol{e}_u))\right) \mathrm{d}t. \qquad (2.93)
\end{aligned}
$$

The first term (and similarly the second term) of (2.93) can be bounded as:

$$
\begin{aligned}
&\int_0^T (\mu_p \partial_t \varepsilon_p + \nabla\cdot\boldsymbol{\varepsilon}_u, e_p + \beta_1 \tau_p P_p(\nabla\cdot\boldsymbol{e}_u)) \, \mathrm{d}t \\
&\leq \frac{\alpha_1}{2} \tau_u^{-1} \|\boldsymbol{\varepsilon}_u\|^2_{L^2(L^2)} + \frac{1}{2\alpha_1} \tau_u \|\nabla e_p\|^2_{L^2(L^2)} \\
&\quad + \frac{\alpha_2}{2} \tau_p \|\mu_p \partial_t \varepsilon_p + \nabla\cdot\boldsymbol{\varepsilon}_u\|^2_{L^2(L^2)} + \frac{\beta_1^2}{2\alpha_2} \tau_p \|\nabla\cdot\boldsymbol{e}_u\|^2_{L^2(L^2)}. \qquad (2.94)
\end{aligned}
$$

The third term (and similarly the fourth term) of (2.93) can be bounded as:

$$
\int_0^T \left(P_p^{\perp}(\nabla\cdot\boldsymbol{\varepsilon}_u), \tau_p \nabla\cdot(\boldsymbol{e}_u + \beta_1 \tau_u P_u(\nabla e_p))\right) \mathrm{d}t
$$

$$\leq \frac{\alpha_3}{2}\tau_p\|\nabla\cdot\boldsymbol{\varepsilon}_u\|^2_{L^2(L^2)} + \frac{1}{2\alpha_3}\tau_p\|\nabla\cdot\boldsymbol{e}_u\|^2_{L^2(L^2)} + \frac{\beta_1^2}{2\alpha_3}C_\tau^2 C_{\text{inv}}^2\tau_u\|\nabla e_p\|^2_{L^2(L^2)}. \tag{2.95}$$

The second term of (2.92) can be written and bounded as:

$$\begin{aligned}
&\int_0^T \mathcal{B}_s\left([\partial_t\varepsilon_p, \partial_t\boldsymbol{\varepsilon}_u], \Lambda_2\left([e_p, \boldsymbol{e}_u]\right)\right)\mathrm{d}t \\
&= \int_0^T \Big[\left(\mu_p\partial_{tt}\varepsilon_p + \nabla\cdot\partial_t\boldsymbol{\varepsilon}_u, \beta_2\partial_t e_p\right) + \left(\mu_u\partial_{tt}\boldsymbol{\varepsilon}_u + \nabla\partial_t\varepsilon_p, \beta_2\partial_t\boldsymbol{e}_u\right)\Big]\mathrm{d}t \\
&\quad + \int_0^T \Big[\left(P_p^\perp(\nabla\cdot\partial_t\boldsymbol{\varepsilon}_u), \tau_p\nabla\cdot(\beta_2\partial_t\boldsymbol{e}_u)\right) + \left(P_u^\perp(\nabla\partial_t\varepsilon_p), \tau_u\nabla(\beta_2\partial_t e_p)\right)\Big]\mathrm{d}t \\
&\leq \alpha_4\Big(\gamma_p\|\mu_p\partial_{tt}\varepsilon_p + \nabla\cdot\partial_t\boldsymbol{\varepsilon}_u\|^2_{L^1(L^2)} + \gamma_u\|\mu_u\partial_{tt}\boldsymbol{\varepsilon}_u + \nabla\partial_t\varepsilon_p\|^2_{L^1(L^2)}\Big) \\
&\quad + \frac{1}{\alpha_4}\Big(\gamma_p\|\mu_p\partial_t e_p\|^2_{L^\infty(L^2)} + \gamma_u\|\mu_u\partial_t\boldsymbol{e}_u\|^2_{L^\infty(L^2)}\Big) \\
&\quad + \frac{\alpha_5}{2}\Big(\beta_2\tau_p\|\nabla\cdot\partial_t\boldsymbol{\varepsilon}_u\|^2_{L^2(L^2)} + \beta_2\tau_u\|\nabla\partial_t\varepsilon_p\|^2_{L^2(L^2)}\Big) \\
&\quad + \frac{1}{2\alpha_5}\Big(\beta_2\tau_p\|P_p^\perp(\nabla\cdot\partial_t\boldsymbol{e}_u)\|^2_{L^2(L^2)} + \beta_2\tau_u\|P_u^\perp(\nabla\partial_t e_p)\|^2_{L^2(L^2)}\Big).
\end{aligned} \tag{2.96}$$

The third term of (2.92) can be written and bounded as:

$$\begin{aligned}
&\mathcal{B}_s\left([\varepsilon_p, \boldsymbol{\varepsilon}_u], \Lambda_2\left([e_p, \boldsymbol{e}_u]\right)\right)\big|_{t=0} \\
&= \left(\mu_p\partial_t\varepsilon_p(0) + \nabla\cdot\boldsymbol{\varepsilon}_u(0), \beta_2\partial_t e_p(0)\right) + \left(\mu_u\partial_t\boldsymbol{\varepsilon}_u(0) + \nabla\varepsilon_p(0), \beta_2\partial_t\boldsymbol{e}_u(0)\right) \\
&\quad + \left(P_p^\perp(\nabla\cdot\boldsymbol{\varepsilon}_u(0)), \tau_p\nabla\cdot(\beta_2\partial_t\boldsymbol{e}_u(0))\right) + \left(P_u^\perp(\nabla\varepsilon_p(0)), \tau_u\nabla(\beta_2\partial_t e_p(0))\right) \\
&\leq \frac{\alpha_6}{2}\left(\gamma_p\|\mu_p\partial_t\varepsilon_p(0)\|^2 + \gamma_u\|\mu_u\partial_t\boldsymbol{\varepsilon}_u(0)\|^2\right) \\
&\quad + \frac{1}{2\alpha_6}\left(\gamma_p\|\mu_p\partial_t e_p(0)\|^2 + \gamma_u\|\mu_u\partial_t\boldsymbol{e}_u(0)\|^2\right).
\end{aligned} \tag{2.97}$$

Combining all bounds (2.94) - (2.97) and taking α_i big enough, it follows that $\|\!|\, [e_p, \boldsymbol{e}_u] \,|\!\|_h^2 \lesssim E_S^2(h)$. Using the same reasoning as for the ASGS method, we complete the proof for the OSS method. □

2.5.3 Accuracy of ASGS and OSS Methods

Let us define as k the order of p-interpolation and as l the order of $\boldsymbol{u}$-interpolation. Analyzing the a priori error estimates for the ASGS and the OSS methods from (2.80) and (2.85) and assuming regular enough solutions we can summarize the convergence rates of the formulations as shown in Table 2.2. When the convergence rate is the same as that of the interpolation error we call it *optimal*, when the gap is 1/2 *quasi-optimal* and when the gap is 1 *suboptimal*.

Now, let us just consider the OSS method and the error estimate in the strong norm from (2.90). The convergence rates of each of the variational forms in the strong norm can be summarized as shown in Table 2.3

Table 2.2: Convergence rates according to the variational forms for the ASGS and OSS methods in the weak norm

Variational Form	I	II	III
$\|p-p_h\|_{L^\infty(\Upsilon,L^2(\Omega))}$	$h^{k+1/2}+h^{l+1/2}$ Quasi-optimal	$h^{k+1}+h^l$ Suboptimal	h^k+h^{l+1} Suboptimal
$\|\boldsymbol{u}-\boldsymbol{u}_h\|_{L^\infty(\Upsilon,L^2(\Omega))}$	$h^{k+1/2}+h^{l+1/2}$ Quasi-optimal	$h^{k+1}+h^l$ Suboptimal	h^k+h^{l+1} Suboptimal
$\|\mu_u\partial_t(\boldsymbol{u}-\boldsymbol{u}_h)+\nabla(p-p_h)\|_{L^2(\Upsilon,L^2(\Omega))}$	h^k+h^l Optimal	h^k+h^{l-1} Suboptimal	h^k+h^{l+1} Optimal
$\|\mu_p\partial_t(p-p_h)+\nabla\cdot(\boldsymbol{u}-\boldsymbol{u}_h)\|_{L^2(\Upsilon,L^2(\Omega))}$	h^k+h^l Optimal	$h^{k+1}+h^l$ Optimal	$h^{k-1}+h^l$ Suboptimal
k, l Optimal	$k=l$	$k+1=l$	$k=l+1$

Table 2.3: Convergence rates according to the variational forms for the OSS method in the strong norm

Variational Form	I	II	III
$\|\nabla(p-p_h)\|_{L^2(\Upsilon,L^2(\Omega))}$	h^k+h^l Optimal	$h^{k-1}+h^{l-1}$ Suboptimal	h^k+h^l Optimal
$\|\nabla\cdot(\boldsymbol{u}-\boldsymbol{u}_h)\|_{L^2(\Upsilon,L^2(\Omega))}$	h^k+h^l Optimal	h^k+h^l Optimal	$h^{k-1}+h^{l-1}$ Suboptimal
k, l Optimal	$k=l$	$k=l$	$k=l$

2.5.4 Numerical Tests

Let us consider a two dimensional transient problem with analytical solution to investigate the convergence properties of the stabilized FE formulations proposed. We take Ω as the unit square $(0,1)\times(0,1)$, the time interval is taken as $[0,0.01]$, the physical properties are taken as $\mu_p=10.0$ and $\mu_u=10.0$, and the forcing terms f_p and $\boldsymbol{f}_u$ are taken such that the exact solution is:

$$p=\sin(3\pi x)\sin(3\pi y)\sin(2\pi t),\quad \boldsymbol{u}=[p,p]\,. \tag{2.98}$$

This exact solution is zero on the boundary Γ, so the boundary conditions of the problem are satisfied. We denote as BC1 the imposition (weak or strong) of $p=0$ on Γ. Additionally, we denote as BC2 the imposition of $\boldsymbol{n}\cdot\boldsymbol{u}=0$ on Γ.

For the spatial discretization, we have used four uniform FE meshes with $h=0.010$, $h=0.005$, $h=0.002$ and $h=0.001$. The elements used are $P1$ (three-node triangular elements) and $P2$ (six-node triangular elements).

Fig. 2.1 shows the mesh for $h=0.10$. The other meshes are isotropic refinements of that one. Anisotropic meshes are not encompassed in the analysis presented. This would require the use of the analysis techniques introduced in [97].

The stabilization parameters are computed with the algorithmic constant $C_\tau=0.01$ for $P1$ and with $C_\tau=0.4$ for $P2$. The characteristic domain length was taken as $\mathrm{L}_0=\sqrt[d]{\mathrm{meas}(\Omega)}=1$. The time integration scheme is Crank-Nicolson with a time step

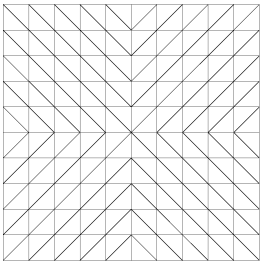

Figure 2.1: Mesh Sample

Table 2.4: Experimental convergence rates for the ASGS method using $P1/P1$ interpolation.

Variational Form	I			II			III		
Boundary Cond.	BC1	BC2	min	BC1	BC2	min	BC1	BC2	min
$\|p - p_h\|_{L^\infty(\Upsilon,L^2(\Omega))}$	2.15	2.38	1.5	1.99	1.79	1	2.13	2.20	1
$\|\boldsymbol{u} - \boldsymbol{u}_h\|_{L^\infty(\Upsilon,L^2(\Omega))}$	2.19	2.09	1.5	1.43	1.59	1	1.84	1.79	1
$\|\nabla(p - p_h)\|_{L^2(\Upsilon,L^2(\Omega))}$	1.03	1.18	1	0.99	0.84	0	1.04	1.07	1
$\|\nabla\cdot(\boldsymbol{u} - \boldsymbol{u}_h)\|_{L^2(\Upsilon,L^2(\Omega))}$	1.48	1.10	1	1.10	1.13	1	0.81	0.71	0

size of 10^{-5}. We have used a very small time step to avoid any interference of the time marching algorithm into the spatial error since we are only interested in this spatial error. With that time step size the difference between the error of the scalar unknown in the norm $\|\cdot\|_{L^\infty(\Upsilon,L^2(\Omega))}$ and the error in the same norm with a time step size twice as big was less than 1% in the finest mesh. This of course depends on the time interval chosen ($T = 0.01$), which has been taken small enough to avoid long term effects which would require a carefully designed time integration scheme, but large enough to obtain significant spatial errors.

In Tables 2.4 to 2.7 the experimental convergence rates for the ASGS and the OSS methods are shown. BC1 and BC2 are the results obtained using BC1 and BC2 as boundary conditions and min stands for the minimum expected convergence rate based on theoretical analysis. All these numerical results match with the convergence rates predicted theoretically, in the sense that the convergence rate is always at least as fast as the worst predicted by the analysis. It would be perhaps possible to improve the convergence rates obtained using some sort of duality arguments, although we have not pursued this in this work (see [91]). It is noteworthy that the convergence rates for both the ASGS and the OSS method are surprisingly similar, although the absolute errors are not. For example, for BC1 and the Variational Form III using linear elements, the slope of the convergence curve of p_h in $L^\infty(\Upsilon, L^2(\Omega))$ is 2.13 for both the ASGS and the OSS methods, but the absolute errors are different. For $h = 0.1$, 0.05 and 0.025 the errors for the ASGS method are 2.92×10^{-2}, 6.60×10^{-3} and 1.38×10^{-3}, respectively, whereas for the OSS method these are 2.61×10^{-2}, 6.15×10^{-3} and 1.36×10^{-3}.

Table 2.5: Experimental convergence rates for the OSS method using $P1/P1$ interpolation.

Variational Form	I			II			III		
Boundary Cond.	BC1	BC2	min	BC1	BC2	min	BC1	BC2	min
$\|p - p_h\|_{L^\infty(\Upsilon,L^2(\Omega))}$	2.16	2.43	1.5	1.99	1.79	1	2.13	2.20	1
$\|\boldsymbol{u} - \boldsymbol{u}_h\|_{L^\infty(\Upsilon,L^2(\Omega))}$	2.18	2.18	1.5	1.41	1.59	1	1.84	1.79	1
$\|\nabla(p - p_h)\|_{L^2(\Upsilon,L^2(\Omega))}$	1.04	1.18	1	0.99	0.84	0	1.04	1.07	1
$\|\nabla\cdot(\boldsymbol{u} - \boldsymbol{u}_h)\|_{L^2(\Upsilon,L^2(\Omega))}$	1.48	1.10	1	1.10	1.13	1	0.81	0.71	0

Table 2.6: Experimental convergence rates for the ASGS method using $P2/P2$ interpolation.

Variational Form	I			II			III		
Boundary Cond.	BC1	BC2	min	BC1	BC2	min	BC1	BC2	min
$\|p - p_h\|_{L^\infty(\Upsilon,L^2(\Omega))}$	3.03	3.03	2.5	2.67	2.67	2	3.41	3.40	2
$\|\boldsymbol{u} - \boldsymbol{u}_h\|_{L^\infty(\Upsilon,L^2(\Omega))}$	3.01	3.01	2.5	2.50	2.54	2	2.76	2.76	2
$\|\nabla(p - p_h)\|_{L^2(\Upsilon,L^2(\Omega))}$	2.06	2.07	2	1.79	1.79	1	2.54	2.54	2
$\|\nabla\cdot(\boldsymbol{u} - \boldsymbol{u}_h)\|_{L^2(\Upsilon,L^2(\Omega))}$	2.07	2.06	2	2.55	2.55	2	1.79	1.79	1

Table 2.7: Experimental convergence rates for the OSS method using $P2/P2$ interpolation.

Variational Form	I			II			III		
Boundary Cond.	BC1	BC2	min	BC1	BC2	min	BC1	BC2	min
$\|p - p_h\|_{L^\infty(\Upsilon,L^2(\Omega))}$	3.03	3.02	2.5	2.66	2.66	2	3.30	3.29	2
$\|\boldsymbol{u} - \boldsymbol{u}_h\|_{L^\infty(\Upsilon,L^2(\Omega))}$	2.99	3.00	2.5	2.48	2.52	2	2.76	2.76	2
$\|\nabla(p - p_h)\|_{L^2(\Upsilon,L^2(\Omega))}$	2.06	2.06	2	1.79	1.79	1	2.53	2.53	2
$\|\nabla\cdot(\boldsymbol{u} - \boldsymbol{u}_h)\|_{L^2(\Upsilon,L^2(\Omega))}$	2.06	2.06	2	2.55	2.54	2	1.79	1.79	1

2.6 Conclusions

In the present work, we have presented two stabilized FE methods (ASGS and OSS) for the wave equation in mixed form. Additionally, these stabilized methods have been applied to three variational forms of the problem. We normally use the stabilized FE formulations for equal interpolation of the unknowns, but the analysis is not restricted to that and allows any continuous interpolation pair. Extension to discontinuous approximations would be easy to analyze, but this would require the introduction of terms evaluated on the inter element boundaries.

Length scales related to the unknowns were introduced in order to treat all variational forms in a unified manner. The way length scales are computed is determined by the norm $|||\cdot|||$ in order to have control over the gradient of the scalar unknown or the divergence of the vector unknown if it is the case. Furthermore, length scales obviously influence the stability and accuracy of the methods.

Stability was proven for both the ASGS and the OSS methods applied to the wave equation in mixed form. According to those results, we have control over the L^2-norm of these unknowns. Moreover, depending on the variational form into consideration, additional control over the gradient of the scalar unknown and/or over the divergence of the vector unknown is attained, and therefore we can guarantee that no numerical point-to-point oscillations will occur.

Theoretical convergence rates were found for both the ASGS and the OSS methods, and for all the variational forms analyzed. Both stabilization methods exhibit at least the same convergence properties based on theoretical analysis. Additionally, there is no numerical evidence that the ASGS method has convergence superiority over the OSS method or vice-versa. One interesting feature of the convergence analysis applied to the three variational forms of the wave equation in mixed form is the guideline given to which variational form to use. That said, for a balanced accuracy for both unknowns and equal interpolation, variational form I is the best choice.

Chapter 3

A Sommerfeld non-reflecting boundary condition for the wave equation in mixed form

This chapter is based on the material in:
Hector Espinoza, Ramon Codina, and Santiago Badia. "A Sommerfeld non-reflecting boundary condition for the wave equation in mixed form". In: *Computer Methods in Applied Mechanics and Engineering* 276 (July 2014), pp. 122–148. ISSN: 0045-7825. DOI: 10.1016/j.cma.2014.03.015. URL: http://www.sciencedirect.com/science/article/pii/S0045782514001017
with the notation modified to make it fit with the other chapters. Some content is repeated from Chapter 1 and Chapter 2 so it is self-contained.

In this chapter we develop numerical approximations of the wave equation in mixed form supplemented with non-reflecting boundary conditions (NRBCs) of Sommerfeld-type on artificial boundaries for truncated domains. We consider three different variational forms for this problem, depending on the functional space for the solution, in particular, in what refers to the regularity required on artificial boundaries. Then, stabilized finite element methods that can mimic these three functional settings are described. Stability and convergence analyses of these stabilized formulations including the NRBC are presented. Additionally, numerical convergence tests are evaluated for various polynomial interpolations, stabilization methods and variational forms. Finally, several benchmark problems are solved to determine the accuracy of these methods in 2D and 3D.

3.1 Introduction

Many engineering problems dealing with waves involve infinite domains. Usually, the infinite domain is truncated for computational purposes and the wave problem is solved in a finite domain [105, 106]. Non-reflecting boundaries (NRBs) have to be considered, which must allow the waves to leave the truncated domain avoiding spurious reflections that may pollute the solution in the interior of the computational domain of interest. There are many types of NRBs, which can be classified into two groups, namely, Non-Reflecting Boundary Conditions (NRBCs) and Non-Reflecting Boundary Layers (NRBLs). NRBCs

are boundary conditions on the artificial boundary that absorb impinging waves. On the other hand, NRBLs have the property of absorbing waves that are traveling inside the layer.

NRBL techniques have been applied to the time-domain wave equation in irreducible [35, 36, 107] and mixed form [42, 43, 51], and to the linearized Euler equations [108–110]. Perhaps the most popular among the NRBL techniques is the Perfectly Matched Layer (PML). The PML concept was developed by Berenger in 1994 for electromagnetic scattering [34]. The idea is to add an absorbing layer to the domain designed to have zero reflection for any plane wave and to make the solution decay exponentially inside the layer [111].

A classical example of NRBC is the so-called Sommerfeld boundary (or radiation) condition [11]. It relates the temporal derivative and the normal derivative of the unknown in the case of boundaries far away from sources and normal to the propagating wave. Thus, it is inexact for non-perpendicular wave incidence and boundaries close to sources, and therefore it has to be understood as an approximate boundary condition to avoid wave reflection in these cases. NRBCs have also been applied to the time-domain wave equation in irreducible [16, 112–114] and mixed form [20], as well as for the linearized Euler equations in [17, 20].

The error $\mathcal{E}$ introduced by a NRBC is the difference between the exact solution in the unbounded domain and the solution in the truncated domain with the artificial boundary. Let J be the order of the NRBC, R the distance of the artificial boundary to the wave source, k_t the tangential wave number and ω the wave angular frequency. The error $\mathcal{E}$ introduced by a NRBC of order J [106] behaves as

$$\mathcal{E} = \mathcal{O}\left(\frac{k_t^2}{\omega^2}\right)^J = \mathcal{O}\left(\frac{1}{R^2}\right)^J. \tag{3.1}$$

For a fixed location of the artificial boundary, increasing the order J reduces the error introduced by the NRBC. If the error approaches zero as J increases the NRBC is exact, whereas if the error does not approach zero the NRBC is asymptotic [105].

Many NRBCs have been developed and can be classified as classical, exact non-local and local high-order. Among classical NRBCs we have those proposed by Engquist-Majda [14], Bayliss-Turkel [115] and Higdon [116]. Classical NRBCs appeared as an improvement of Sommerfeld NRBC and can be high-order in theory, but in practice only low-order versions are used because of the presence of high-order derivatives which are difficult to handle numerically [111]. Among exact non-local NRBCs we have Dirichlet-to-Neumann formulations [117] and the Difference Potential Method [118]. Exact non-local NRBCs involve a boundary integral operator which couples all the points on the boundary [111]. Among local high-order NRBCs we have those due to Collino [119], Grote-Keller [23], Rowley-Colonius [120], Guddati-Tassoulas [121], Givoli-Neta [16] and Hagstrom-Warburton [122]. Local high-order NRBCs are high-order in theory and can be implemented up to any desired order in practice, which can be achieved introducing auxiliary variables [111].

The wave equations can be posed in irreducible form, leading to a second-order (in space and time) scalar partial differential equation. Many applications require the vector-valued unknown of the problem, which can be computed by the solution of the irreducible form plus a post-processing step, but leads to a poor approximation of it. In order to improve

the convergence rate for the vector field, we can consider the problem as a first-order (in space and time) hyperbolic system, that involves both the scalar and vector unknowns. The wave equation in mixed form is in fact mandatory for some applications in solid mechanics or in nonlinear waves in shallow waters.

The finite element (FE) approximation in space of this hyperbolic problem is not straightforward, since its well-posedness relies on an inf-sup condition. Thus, Galerkin FE schemes require mixed interpolations that satisfy a discrete version of this compatibility condition [78]. Inf-sup stable FE formulations have been developed for several mixed problems, e.g., [79] for the Stokes problem, [80] for the Darcy problem, [81] for the Maxwell problem, [82, 83] for the Stokes-Darcy problem, [84] for the wave equation, and [85, 86] for elastodynamics. As an alternative to inf-sup stable formulations, we can consider stabilized FE formulations [90]. Stabilized FEs add new terms to the Galerkin formulation, which provide the required stability for well-posedness (without the need to rely on a discrete inf-sup condition) keeping optimal convergence properties. This way, we are able to use equal interpolation for the scalar and vector unknowns of the wave equation in mixed form.

In this work, we develop novel stabilized FE formulations for wave scattering problems on unbounded domains truncated via Sommerfeld-type boundary conditions as the simplest example of NRBC. Our starting point is the formulation recently presented and analyzed in [67]. It is a stabilized FE method with the important feature of allowing for different functional settings. This is accomplished by *transferring* regularity from the scalar to the vector unknowns or vice-versa [67] through an appropriate integration by parts and design of the stabilization parameters. Summarizing, the main contributions are:

- Statement of the mixed form of the wave equation with Sommerfeld artificial boundary conditions in three different functional settings. It is an extension of the work in [67], in which the functional setting has to be properly modified in order to give sense to the Sommerfeld terms; extra regularity is required on the artificial boundary for the vector unknown. One of the resulting formulations has already been proposed in [20], whereas the other two problem settings are new. We observe that the new functional spaces are in fact complete.

- Extension of the stabilized FE formulations in [67] to deal with Sommerfeld boundary conditions. We design stabilized FE formulations that can mimic the three functional settings proposed at the continuous level. Stability and convergence results are presented, and their proof is sketched. A set of numerical experiments is performed to check the convergence of the formulations, as well as the error introduced by the Sommerfeld boundary condition.

The organization of the chapter is as follows. In Section 3.2, we present the wave equation in irreducible and mixed form and in time and frequency domain. Additionally, we describe the Sommerfeld boundary condition applied to the wave equation. We also propose three different functional settings for the time-domain wave problem in mixed form truncated with Sommerfeld boundary conditions. In Section 3.3, we describe the spatial discretization we propose, which is a stabilized FE method (in two different versions), and show how to mimic the three functional settings by properly integrating by parts and choosing the stabilization parameters. Section 3.4 is devoted to the stability and

convergence analysis of these formulations, respectively. In all these sections, time is left continuous, concentrating the exposition only in the spatial approximation. In Section 3.5 we carry out convergence tests and evaluate the performance of the NRBC through various benchmark problems in 2D and 3D. Finally, we draw some conclusions in Section 3.6.

3.2 Problem statement

In this section, we state the wave equation in mixed form in time and frequency domain. Further, we state the Sommerfeld artificial boundary conditions in both cases. The use of Sommerfeld-type boundary conditions for the mixed form of the wave equation has been used in [20] (without using this terminology). Waves are commonly found in many physical phenomena such as acoustic and electromagnetic scattering, fluid dynamics, and elastodynamics. To fix ideas, we will use the terminology of waves propagating in fluids, although our approach is obviously general.

3.2.1 Wave equation in time and frequency domain

Waves can be described in time domain or frequency domain. In both cases, the problem involves a spatial domain $\Omega \subset \mathbb{R}^d$, where d is the space dimension ($d = 1, 2, 3$). Let Γ be its boundary and $\boldsymbol{x} \in \Omega$ any spatial point. From hereafter, we will refer to vectors in $\mathbb{R}^d$ simply as vectors. Further, we use the following convention: lower-case bold italic letters represent vectors in $\mathbb{R}^d$, and non-bold letters represent scalars. Both complex and real numbers are used in this section. We implicitly assume real numbers unless otherwise specified.

In the time domain, the problem is posed in $\Xi := \Omega \times \Upsilon$, where $t \in \Upsilon := (0, T)$ denotes a time value. The long term behavior, i.e. $T \to \infty$, will not be considered in this work. The time-domain wave equation in its irreducible form reads as:

$$\frac{1}{c^2}\partial_{tt}p' - \Delta p' = f', \tag{3.2}$$

where $p'(\boldsymbol{x}, t)$ is the unknown (real-valued scalar function), f' is a forcing term and c is the wave speed. Alternatively, we can consider the wave equation in mixed form:

$$\mu_p \partial_t p' + \nabla \cdot \boldsymbol{u}' = f_p, \tag{3.3}$$

$$\mu_u \partial_t \boldsymbol{u}' + \nabla p' = \boldsymbol{f}_u, \tag{3.4}$$

where the unknowns $p'(\boldsymbol{x}, t)$ and $\boldsymbol{u}'(\boldsymbol{x}, t)$ are real-valued scalar and vector functions, respectively, $\mu_p > 0$ and $\mu_u > 0$ are the physical parameters of the equation and $[f_p, \boldsymbol{f}_u]$ are forcing terms. The coefficients μ_p and μ_u that characterize the mixed wave equation (3.3)-(3.4) are related to the wave speed c appearing in irreducible form of the scalar wave equation (3.2) as follows:

$$c^2 = (\mu_p \mu_u)^{-1}.$$

Time domain analysis solves the wave problem for the full range of frequencies involved. The only limit for the frequencies captured at time-discrete level is the size of the time

step used for the time discretization. Frequency domain analysis results from a Fourier transform in time of the time-domain problem and solves the wave problem for one angular frequency ω. In the irreducible case, it leads to the scalar Helmholtz equation:

$$\Delta\hat{p} + k^2\hat{p} = \hat{f}_k, \tag{3.5}$$

where $\hat{p}(\boldsymbol{x})$ is now the unknown (complex-valued scalar function), and $k = \omega/c$ is the wavenumber corresponding to a certain angular frequency ω. As in the time domain case, we can also make use of the Helmholtz equation in mixed form:

$$-\mathrm{i}\mu_p\omega\hat{p} + \nabla\cdot\hat{\boldsymbol{u}} = \hat{f}_p, \tag{3.6}$$

$$-\mathrm{i}\mu_u\omega\hat{\boldsymbol{u}} + \nabla\hat{p} = \hat{\boldsymbol{f}}_u, \tag{3.7}$$

where $\hat{p}(\boldsymbol{x})$ and $\hat{\boldsymbol{u}}(\boldsymbol{x})$ are complex unknowns, ω is the angular frequency, $\hat{f}_p$ and $\hat{\boldsymbol{f}}_u$ are forcing terms and $\mathrm{i} = \sqrt{-1}$.

Notice that the number of unknowns in the wave equation in mixed form (both in the time and frequency domain) is $d+1$ times the ones in irreducible form, but the regularity requirements in space and time can be made less stringent for p'. In all cases, the wave equation has to be supplemented with appropriate initial and boundary conditions. In the case of the mixed form, boundary conditions also depend on the functional setting of the problem.

3.2.2 Sommerfeld Boundary Condition

The Sommerfeld boundary condition is a type of NRBC, that takes its name from the German theoretical physicist Arnold Sommerfeld, applicable when the sources are concentrated in a region of the space and the exterior boundary is a sphere surrounding it and centered at the source region. Additionally, the spherical surface has to be far away from the source, so that one can assume that the impinging waves only have radial component when they reach the artificial boundary. In spherical coordinates and for the scalar Helmholtz equation in 3D (frequency domain), the Sommerfeld radiation condition can be expressed as:

$$\lim_{r\to\infty}\left(r\left(\partial_r\hat{p} - \mathrm{i}k\hat{p}\right)\right) = 0,$$

where r is radial component in the spherical coordinate system and ∂_r is the derivative in the radial direction.[1] In spherical coordinates and for the scalar wave equation in irreducible form in 3D (time domain) the Sommerfeld radiation condition can be written as:

$$\lim_{r\to\infty}\left(r\left(\partial_r p' + \frac{1}{c}\partial_t p'\right)\right) = 0.$$

[1]Some authors write the Sommerfeld radiation condition with a + sign, but that depends on the time variation assumption. In this work, we have assumed a harmonic time variation with harmonics of the form $\mathrm{e}^{-\mathrm{i}\omega t}$, which gives the minus sign.

On the other hand, when considering the mixed form of these equations, the Sommerfeld radiation condition can be written in two different ways:

$$\begin{aligned}\lim_{r\to\infty}\left(r\left(\sqrt{\mu_p}\,\partial_r p' - \sqrt{\mu_u}\,\nabla\cdot\boldsymbol{u}'\right)\right) &= 0,\\ \lim_{r\to\infty}\left(r\left(\sqrt{\mu_p}\,\partial_t p' - \sqrt{\mu_u}\,\partial_t u_r'\right)\right) &= 0.\end{aligned} \tag{3.8}$$

In the frequency domain, these Sommerfeld boundary conditions lead to:

$$\begin{aligned}\lim_{r\to\infty}\left(r\left(\sqrt{\mu_p}\,\partial_r \hat{p} - \sqrt{\mu_u}\,\nabla\cdot\hat{\boldsymbol{u}}\right)\right) &= 0,\\ \lim_{r\to\infty}\left(r\left(\sqrt{\mu_p}\,\hat{p} - \sqrt{\mu_u}\;\hat{u}_r\right)\right) &= 0.\end{aligned}$$

Condition (3.8) can be simplified taking out the temporal derivative, which yields

$$\lim_{r\to\infty}\left(r\left(\sqrt{\mu_p}\,p' - \sqrt{\mu_u}\,u_r' + C(\boldsymbol{x})\right)\right) = 0.$$

$C(\boldsymbol{x})$ is a time-independent function defined on Γ, which can be determined from initial conditions. Assuming that $\sqrt{\mu_p}\,p'(\boldsymbol{x},0) - \sqrt{\mu_u}\,u_r'(\boldsymbol{x},0) = 0$ holds on the artificial boundary, we get $C(\boldsymbol{x}) = 0$. It leads to the final expression

$$\lim_{r\to\infty}\left(r\left(\sqrt{\mu_p}\,p' - \sqrt{\mu_u}\,u_r'\right)\right) = 0.$$

This Sommerfeld radiation condition is a limit for $r \to \infty$, and establishes a fast decay of $\sqrt{\mu_p}\,p' - \sqrt{\mu_u}\,u_r'$. If $R < \infty$, the *approximation* that we may consider is $\sqrt{\mu_p}\,p' - \sqrt{\mu_u}\,u_r' = 0$ at $r = R$. Moreover, if the boundary is not a sphere, we may replace u_r' by $\boldsymbol{n}\cdot\boldsymbol{u}'$, $\boldsymbol{n}$ being the unit normal exterior to the boundary. Thus, we may consider the approximation

$$\sqrt{\mu_p}\,p' - \sqrt{\mu_u}\,\boldsymbol{n}\cdot\boldsymbol{u}' = 0. \tag{3.9}$$

Because of its simplicity, this is the boundary condition we propose to enforce on the artificial boundary for the mixed wave equation in time domain. In the following sections, we show that this boundary condition has good non-reflecting properties and is stable, in spite of having been superseded in accuracy by high order NRBCs. The analysis of its performance in combination with the FE method we propose is the subject of this chapter.

3.2.3 Initial and Boundary Value Problem

Let us split Γ into three disjoint sets denoted as Γ_p, Γ_u and Γ_{o}. The scalar unknown p is enforced on Γ_p, the normal trace of the vector unknown $\gamma_n\boldsymbol{u}$ on Γ_u (γ_n denotes the normal trace operator), and the NRBC we wish to analyze on Γ_{o} (the artificial boundary). The problem consists in finding $p : \Xi \longrightarrow \mathbb{R}$ and $\boldsymbol{u} : \Xi \longrightarrow \mathbb{R}^d$ such that:

$$\mu_p\partial_t p + \nabla\cdot\boldsymbol{u} = f_p\,, \tag{3.10}$$

$$\mu_u\partial_t\boldsymbol{u} + \nabla p = \boldsymbol{f}_u\,, \tag{3.11}$$

with the initial conditions

$$p(\boldsymbol{x},0) = 0, \quad \boldsymbol{u}\,(\boldsymbol{x},0) = \boldsymbol{0}, \tag{3.12}$$

and with the boundary conditions

$$p = 0 \;\text{ on } \Gamma_p, \quad \gamma_n \boldsymbol{u} := \boldsymbol{n} \cdot \boldsymbol{u} = 0 \;\text{ on } \Gamma_u, \quad \mu_p^{\frac{1}{2}} p = \mu_u^{\frac{1}{2}} \gamma_n \boldsymbol{u} \;\text{ on } \Gamma_o. \tag{3.13}$$

Let us define two auxiliary variables denoted as κ_p and κ_u defined as:

$$\kappa_p := \left(\frac{\mu_p}{\mu_u}\right)^{\frac{1}{2}}, \quad \kappa_u := \left(\frac{\mu_u}{\mu_p}\right)^{\frac{1}{2}}.$$

Let Ψ be a generic spatial domain, i.e., Ω or Γ or part of them. Let $L^2(\Psi)$ be the space of square integrable functions defined on Ψ, and $L^2(\Psi)^d$ the space of vector functions with components in $L^2(\Psi)$. $H^1(\Psi)$ is the space of functions in $L^2(\Psi)$ with derivatives in $L^2(\Psi)$, $H(\mathrm{div}, \Psi)$ the space of vector functions with components and divergence in $L^2(\Psi)$. Any of the spaces defined previously will be denoted generically as $\mathtt{X}$. Additionally, for an arbitrary functional space $\mathtt{X}$, its norm will be denoted as $\|\cdot\|_{\mathtt{X}}$. In the case of $L^2(\Omega)$ or $L^2(\Omega)^d$, the L^2-norm will simply be denoted as $\|\cdot\|$ and the L^2-inner-product as $(\cdot\,,\cdot)$. Furthermore, the space of functions whose $\mathtt{X}$-norm is C^r continuous in the time interval Υ will be denoted by $C^r(\Upsilon; \mathtt{X})$. (We will only be interested in the cases $r = 0$ and $r = 1$.) Functions whose $\mathtt{X}$-norm is L^p in Υ will be denoted by $L^p(\Upsilon; \mathtt{X})$.

Furthermore, let V_p, V_u be the functional spaces associated with p and $\boldsymbol{u}$, respectively. These spaces will be defined afterwards because they depend on the functional setting. Additionally, let us define $V := V_p \times V_u$ and $L := L^2(\Omega) \times L^2(\Omega)^d$.

Problem (3.10)-(3.11) with appropriate initial and boundary conditions will be stated for

$$p \in C^1\big(\Upsilon; L^2(\Omega)\big) \cap C^0\big(\Upsilon; V_p\big),$$
$$\boldsymbol{u} \in C^1\big(\Upsilon; L^2(\Omega)^d\big) \cap C^0\big(\Upsilon; V_u\big),$$

with f_p and $\boldsymbol{f}_u$ in regular enough spaces.

3.2.4 Internal energy and power flux

Let us multiply (3.10) against p, (3.11) against $\boldsymbol{u}$, add the resulting equations and integrate over Ω. Applying the divergence theorem, we get the energy balance equation:

$$\frac{1}{2}\mu_p \frac{\mathrm{d}}{\mathrm{d}t}\|p\|^2 + \frac{1}{2}\mu_u \frac{\mathrm{d}}{\mathrm{d}t}\|\boldsymbol{u}\|^2 = -\int_\Gamma \boldsymbol{n} \cdot p\boldsymbol{u} \;\mathrm{d}\Gamma + (f_p, p) + (\boldsymbol{f}_u, \boldsymbol{u})\,.$$

The *total internal energy* E is defined as:

$$E := \frac{1}{2}\left(\mu_p \|p\|^2 + \mu_u \|\boldsymbol{u}\|^2\right),$$

which contains the *potential energy* $\frac{1}{2}\mu_p\|p\|^2$ and the *kinetic energy* $\frac{1}{2}\mu_u\|\boldsymbol{u}\|^2$. The energy per unit time, i.e. the power added through the boundary, is defined as:

$$P_b := -\int_\Gamma \boldsymbol{n} \cdot p\boldsymbol{u} \;\mathrm{d}\Gamma,$$

whereas the power of the external forces is defined as:

$$P_f := (f_p, p) + (\boldsymbol{f}_u, \boldsymbol{u}) .$$

The power flux (energy per unit time per unit surface) at any given point of the boundary is $\boldsymbol{n} \cdot p\boldsymbol{u}$. The Sommerfeld boundary condition prescribed on Γ_{o} is the one that ensures that energy always flows out of the boundary because $\boldsymbol{n} \cdot p\boldsymbol{u} \geq 0$ everywhere at any instant of time, i.e., $P_b \leq 0$. It makes the problem well-posed, since the solution is bounded by the data. With these definitions we can write the energy balance equation as:

$$\frac{\mathrm{d}E}{\mathrm{d}t} = P_b + P_f. \tag{3.14}$$

Our interest in equation (3.14) relies in the fact that it represents the power balance of the system and it reveals the interaction of the forces and boundaries with the domain.

3.2.5 Variational Problem

The variational form of problem (3.10)-(3.13) can be expressed in three different ways. Each one requires a certain regularity on the unknowns p and $\boldsymbol{u}$, which amounts to say that p and $\boldsymbol{u}$ should belong to a particular space of functions. In all cases the problem reads: find $[p, \boldsymbol{u}] \in C^1(\Upsilon; L) \cap C^0(\Upsilon; V)$ such that

$$\mathcal{B}([p, \boldsymbol{u}], [q, \boldsymbol{v}]) = \mathcal{L}([q, \boldsymbol{v}]), \tag{3.15}$$

for all test functions $[q, \boldsymbol{v}] \in V$ and the respective initial conditions. The bilinear form $\mathcal{B}$, the linear form $\mathcal{L}$ and the space V are defined in three different ways depending on the variational form into consideration. For simplicity, we will assume that the forcing terms f_p and $\boldsymbol{f}_u$ are square integrable, although we could relax this regularity requirement and assume they belong to the dual space of V_p and V_u, respectively.

The three different variational formulations of problem (3.10)-(3.13) essentially differ in the way integration-by-parts from the strong form of the problem is performed and in the regularity required for the unknowns. In the problem statement given below, variational form I (3.16)-(3.20) is obtained without integrating by parts any term. Thus, boundary conditions on both scalar and vector quantities have to be imposed strongly. Pressures in $H^1(\Omega)$ have well-defined traces in $L^2(\Gamma)$, and the pressure boundary condition on Γ_p has sense. The velocity space $H(\mathrm{div}, \Omega)$ does not have a continuous γ_n operator onto $L^2(\Gamma)$. Thus, in order for the Sommerfeld condition $p = \kappa_u \gamma_n u$ to have sense in $L^2(\Omega)$ (which is required for $p \in H^1(\Omega)$), we consider a more regular velocity space, viz., the space of $H(\mathrm{div}, \Omega)$ with normal traces in $L^2(\Omega)$. We can easily check that the resulting bilinear/linear forms in (3.16)-(3.17) are continuous in this functional setting.

The introduction of the NRBC motivated a slight modification of the functional framework and working norms with respect to Chapter 2. The modifications are reflected below.

Variational Form I

$$V_p = \left\{ q \in H^1(\Omega) |\ q = 0 \text{ on } \Gamma_p \right\},$$

$$V_u = \left\{ \boldsymbol{v} \in H(\mathrm{div}, \Omega) |\ \gamma_n \boldsymbol{v} = 0 \text{ on } \Gamma_u \text{ and } \gamma_n \boldsymbol{v} \in L^2(\Gamma_o) \right\},$$

$$\mathcal{B}\left([p, \boldsymbol{u}], [q, \boldsymbol{v}]\right) = \mu_p \left(\partial_t p, q\right) + \left(\nabla \cdot \boldsymbol{u}, q\right) + \mu_u \left(\partial_t \boldsymbol{u}, \boldsymbol{v}\right) + \left(\nabla p, \boldsymbol{v}\right), \tag{3.16}$$

$$\mathcal{L}\left([q, \boldsymbol{v}]\right) = \left(f_p, q\right) + \left(\boldsymbol{f}_u, \boldsymbol{v}\right), \tag{3.17}$$

$$p = 0 \text{ on } \Gamma_p, \qquad \text{strongly imposed}, \tag{3.18}$$

$$\gamma_n \boldsymbol{u} = 0 \text{ on } \Gamma_u, \qquad \text{strongly imposed}, \tag{3.19}$$

$$\mu_p^{\frac{1}{2}} p = \mu_u^{\frac{1}{2}} \gamma_n \boldsymbol{u} \text{ on } \Gamma_o, \qquad \text{strongly imposed}. \tag{3.20}$$

The variational form II (3.21)-(3.25) is obtained integrating by parts the term $(\nabla p, \boldsymbol{v})$, and using the Sommerfeld condition (3.9) on Γ_o:

$$(\nabla p, \boldsymbol{v}) = -(p, \nabla \cdot \boldsymbol{v}) + \int_{\Gamma_o} \gamma_n \boldsymbol{v} p = -(p, \nabla \cdot \boldsymbol{v}) + \kappa_u \int_{\Gamma_o} \gamma_n \boldsymbol{u} \gamma_n \boldsymbol{v}.$$

The boundary integral on $\Gamma_p \cup \Gamma_u$ vanishes due to (3.23)-(3.24) below; the pressure condition on Γ_p is weakly enforced and the velocity condition on Γ_u is strongly enforced. In this case, pressures only need to be in $L^2(\Omega)$, whereas velocities should belong to the same space as in the previous variational form. We observe that the normal trace γ_n of velocity functions have to be in $L^2(\Gamma_o)$ in order to give sense to the Sommerfeld term on Γ_o. In this functional setting, the bilinear/linear forms (3.21)-(3.22) are continuous. [2]

Variational Form II

$V_p = L^2(\Omega)$,
$V_u = \left\{ \boldsymbol{v} \in H(\mathrm{div}, \Omega) |\ \gamma_n \boldsymbol{v} = 0 \text{ on } \Gamma_u \text{ and } \gamma_n \boldsymbol{v} \in L^2(\Gamma_o) \right\},$

$$\mathcal{B}\left([p, \boldsymbol{u}], [q, \boldsymbol{v}]\right) = \mu_p \left(\partial_t p, q\right) + \left(\nabla \cdot \boldsymbol{u}, q\right) + \mu_u \left(\partial_t \boldsymbol{u}, \boldsymbol{v}\right) - (p, \nabla \cdot \boldsymbol{v}) + \kappa_u \int_{\Gamma_o} \gamma_n \boldsymbol{v} \gamma_n \boldsymbol{u} \, \mathrm{d}\Gamma, \tag{3.21}$$

$$\mathcal{L}\left([q, \boldsymbol{v}]\right) = \left(f_p, q\right) + \left(\boldsymbol{f}_u, \boldsymbol{v}\right), \tag{3.22}$$

$$p = 0 \text{ on } \Gamma_p, \qquad \text{weakly imposed}, \tag{3.23}$$

$$\gamma_n \boldsymbol{u} = 0 \text{ on } \Gamma_u, \qquad \text{strongly imposed}, \tag{3.24}$$

$$\mu_p^{\frac{1}{2}} p = \mu_u^{\frac{1}{2}} \gamma_n \boldsymbol{u} \text{ on } \Gamma_o, \qquad \text{weakly imposed}. \tag{3.25}$$

Finally, the variational form III (3.26)-(3.30) is obtained integrating by parts the term $(\nabla \cdot \boldsymbol{u}, q)$ and proceeding analogously on the boundary:

$$(\nabla \cdot \boldsymbol{u}, q) = -(\boldsymbol{u}, \nabla q) + \int_{\Gamma_o} \gamma_n \boldsymbol{u} q = -(\boldsymbol{u}, \nabla q) + \kappa_p \int_{\Gamma_o} p q.$$

[2] This formulation has already been proposed in [20], but the functional setting was incorrect; only $H(\mathrm{div}, \Omega)$ regularity was assumed for the vector unknowns and the Sommerfeld terms were ill-posed. In any case, the authors explicitly say that this is not the goal of their paper.

In this case, the velocity condition on Γ_u is weakly enforced, whereas the pressure condition on Γ_p is strongly enforced. The functional setting in this third case is standard.

Variational Form III

$$V_p = \left\{ q \in H^1(\Omega) |\ q = 0 \text{ on } \Gamma_p \right\}, \quad V_u = L^2(\Omega)^d,$$

$$\mathcal{B}\left([p, \boldsymbol{u}], [q, \boldsymbol{v}]\right) = \mu_p \left(\partial_t p, q\right) - \left(\boldsymbol{u}, \nabla q\right) + \mu_u \left(\partial_t \boldsymbol{u}, \boldsymbol{v}\right) + \left(\nabla p, \boldsymbol{v}\right) + \kappa_p \int_{\Gamma_o} pq \, \mathrm{d}\Gamma, \tag{3.26}$$

$$\mathcal{L}\left([q, \boldsymbol{v}]\right) = \left(f_p, q\right) + \left(\boldsymbol{f}_u, \boldsymbol{v}\right), \tag{3.27}$$

$$p = 0 \text{ on } \Gamma_p, \qquad \text{strongly imposed}, \tag{3.28}$$

$$\gamma_n \boldsymbol{u} = 0 \text{ on } \Gamma_u, \qquad \text{weakly imposed}, \tag{3.29}$$

$$\mu_p^{\frac{1}{2}} p = \mu_u^{\frac{1}{2}} \gamma_n \boldsymbol{u} \text{ on } \Gamma_o, \qquad \text{weakly imposed}. \tag{3.30}$$

Let us note that the Sommerfeld condition on Γ_o is strongly enforced for the first variational form, whereas it is weakly enforced in the other two cases. On the other hand, the introduction of the Sommerfeld boundary conditions requires a more regular functional setting (see [67] for comparison).

Notice the way we have defined V_u for variational forms I and II. When we move from the continuous level to the discrete level we have to ensure the spaces we are working with are complete. The completeness of V_u is proved in the following lemma. A similar result with a similar proof but involving $\boldsymbol{u} \in H(\mathrm{curl}, \Omega)$ and $\boldsymbol{u} \times \boldsymbol{n} \in L^2(\Gamma)$ can be found in [123, p. 69, p. 84].

Lemma 3.2.1. *(Completeness of V_u) The space V_u for the variational forms I and II is complete when it is endowed with the following norm:*

$$|||\boldsymbol{u}|||_{V_u}^2 := \frac{1}{L_0^2} \|\boldsymbol{u}\|^2 + \|\nabla \cdot \boldsymbol{u}\|^2 + \frac{1}{L_0} \|\gamma_n \boldsymbol{u}\|_{L^2(\Gamma_o)}^2. \tag{3.31}$$

Proof. Let $\{\boldsymbol{u}_n\}$ be a Cauchy sequence in V_u. Since $H(\mathrm{div}, \Omega)$ is complete, $\boldsymbol{u}_n \longrightarrow \boldsymbol{w}$ in $H(\mathrm{div}, \Omega)$. Additionally, $\gamma_n \boldsymbol{u}_n \longrightarrow v$ in $L^2(\Gamma_o)$ since $L^2(\Gamma_o)$ is complete. Furthermore, $\gamma_n \boldsymbol{u}_n \longrightarrow \gamma_n \boldsymbol{w}$ in $H^{-1/2}(\Gamma)$ since the normal trace operator γ_n goes from $H(\mathrm{div}, \Omega)$ to $H^{-1/2}(\Gamma)$. Since the limits must be the same, we conclude that $\gamma_n \boldsymbol{w} = v$ in $L^2(\Gamma_o)$ and therefore V_u is complete. □

3.3 Stabilized Finite Element Methods

In this section, we present two stabilized FE methods, which we will denote by the acronyms ASGS and OSS, aimed to overcome the instability problems of the standard Galerkin method. In general, the stabilized FE methods we propose can be used with any type of continuous interpolation for p and $\boldsymbol{u}$. In particular, we focus on equal order continuous interpolations. For conciseness, we consider quasi-uniform FE partitions of size h. For stabilized formulations in general non-uniform non-degenerate cases, see [97].

Let $V_{p,h}$ and $V_{u,h}$ be the FE spaces to approximate p and $\boldsymbol{u}$, respectively, with $V_{p,h} \subset V_p$ and $V_{u,h} \subset V_u$. Additionally, let us define $V_h = V_{p,h} \times V_{u,h}$. For any of these spaces we will make frequent use of the classical inverse inequality $\|\nabla v_h\| \leq C_{\text{inv}} h^{-1} \|v_h\|$, with C_{inv} a constant independent of the FE function v_h and the mesh size h.

Stabilized FE methods deal with the following problem: Find a pair $[p_h, \boldsymbol{u}_h] \in \mathcal{C}^1(\Upsilon; V_h)$ satisfying the initial conditions $p_h(\boldsymbol{x}, 0) = 0$, $\boldsymbol{u}_h(\boldsymbol{x}, 0) = \boldsymbol{0}$ and such that

$$\mathcal{B}_s\left([p_h, \boldsymbol{u}_h], [q_h, \boldsymbol{v}_h]\right) = \mathcal{L}_s\left([q_h, \boldsymbol{v}_h]\right), \tag{3.32}$$

for all test functions $[q_h, \boldsymbol{v}_h] \in V_h$, where the bilinear form $\mathcal{B}_s$ and the linear form $\mathcal{L}_s$ include the Galerkin terms and additional stabilization terms. Depending on how the stabilization part is designed, a different stabilization method arises. Below, we propose two different types of methods, namely ASGS and OSS. The stabilization terms depend on the choice of the so-called stabilization parameters τ_p and τ_u.

3.3.1 Algebraic Sub-Grid Scale (ASGS) method

The ASGS-type stabilization was originally proposed in [87, 89]. The ASGS stabilization terms have the same expression for the three variational forms introduced above. For the wave equation in mixed form, the ASGS stabilized problem (3.32) is obtained by taking $\mathcal{B}_s$ and $\mathcal{L}_s$ as:

$$\begin{aligned}\mathcal{B}_s\left([p_h, \boldsymbol{u}_h], [q_h, \boldsymbol{v}_h]\right) &= \mathcal{B}\left([p_h, \boldsymbol{u}_h], [q_h, \boldsymbol{v}_h]\right) \\ &\quad + \left(\mu_p \partial_t p_h + \nabla\cdot\boldsymbol{u}_h, \tau_p \nabla\cdot\boldsymbol{v}_h\right) + \left(\mu_u \partial_t \boldsymbol{u}_h + \nabla p_h, \tau_u \nabla q_h\right), \qquad (3.33)\\ \mathcal{L}_s\left([q_h, \boldsymbol{v}_h]\right) &= \mathcal{L}\left([q_h, \boldsymbol{v}_h]\right) + \left(f_p, \tau_p \nabla\cdot\boldsymbol{v}_h\right) + \left(\boldsymbol{f}_u, \tau_u \nabla q_h\right). \qquad (3.34)\end{aligned}$$

It consists in subtracting to the Galerkin terms the integral of the residual of the equation times the adjoint of the spatial differential operator and a stabilization parameter. (τ_u, τ_p) are the stabilization parameters, which will be different for every variational formulation. The additional terms provide stability without harming consistency and a priori error estimates.

3.3.2 Orthogonal Sub-scale Stabilization (OSS) method

The OSS stabilization technique was designed in [98, 99]. Instead of considering the whole residual (as in ASGS), it only includes quantities that provide stabilization. However, since it would spoil accuracy, the FE projection of these quantities is subtracted, recovering optimal convergence. It consists in solving problem (3.32) taking $\mathcal{B}_s$ and $\mathcal{L}_s$ as:

$$\begin{aligned}\mathcal{B}_s\left([p_h, \boldsymbol{u}_h], [q_h, \boldsymbol{v}_h]\right) &= \mathcal{B}\left([p_h, \boldsymbol{u}_h], [q_h, \boldsymbol{v}_h]\right) \\ &\quad + \left(P_p^{\perp}\left(\nabla\cdot\boldsymbol{u}_h\right), \tau_p \nabla\cdot\boldsymbol{v}_h\right) + \left(P_u^{\perp}\left(\nabla p_h\right), \tau_u \nabla q_h\right), \qquad (3.35)\\ \mathcal{L}_s\left([q_h, \boldsymbol{v}_h]\right) &= \mathcal{L}\left([q_h, \boldsymbol{v}_h]\right) + \left(P_p^{\perp}\left(f_p\right), \tau_p \nabla\cdot\boldsymbol{v}_h\right) + \left(P_u^{\perp}\left(\boldsymbol{f}_u\right), \tau_u \nabla q_h\right), \qquad (3.36)\end{aligned}$$

where $P_p^{\perp}(\cdot) = I(\cdot) - P_p(\cdot)$ and $P_u^{\perp}(\cdot) = I(\cdot) - P_u(\cdot)$, $P_p(\cdot)$ being the $L^2(\Omega)$ projection on $V_{p,h}$ and $P_u(\cdot)$ the $L^2(\Omega)$ projection on $V_{u,h}$. This in particular implies that $P_p(\cdot) = 0$ on Γ_p for variational forms I and III and that $\boldsymbol{n} \cdot P_u(\cdot) = 0$ on Γ_u for variational forms I and II.

Table 3.1: Stabilization Parameters Order and Length Scales Definition

Variational Form	I	II	III
τ_p	$\mathcal{O}(h)$	$\mathcal{O}(1)$	$\mathcal{O}(h^2)$
τ_u	$\mathcal{O}(h)$	$\mathcal{O}(h^2)$	$\mathcal{O}(1)$
ℓ_p	$\ell_p = \ell_u$	L_0^2/h	h
ℓ_u	$\ell_p = \ell_u$	h	L_0^2/h

3.3.3 The stabilization parameters

An important component of stabilized formulations are the stabilization parameters. In our case, we compute them in all formulations as:

$$\tau_p = C_\tau \sqrt{\frac{\mu_u}{\mu_p}} h \sqrt{\frac{\ell_p}{\ell_u}}, \qquad \tau_u = C_\tau \sqrt{\frac{\mu_p}{\mu_u}} h \sqrt{\frac{\ell_u}{\ell_p}}, \tag{3.37}$$

where C_τ is a dimensionless algorithmic constant and ℓ_p, ℓ_u are length scales corresponding to p and $\boldsymbol{u}$ respectively. As it was shown in the analysis presented in [67], in order to mimic at the discrete level the proper functional setting of the continuous problem, the length scales ℓ_p and ℓ_u should be taken as shown in Table 3.1, where L_0 is a fixed length scale of the problem that can be fixed a priori. The motivation for designing the stabilization parameters can be found in [90, 91].

3.4 Numerical analysis

3.4.1 Stability analysis

In this section, we present stability results for the ASGS and the OSS methods. We use the concept of Λ-coercivity, originally introduced in [103], which aids us in the proof of stability and convergence analyses. The proofs of the stability lemmata and theorems are very similar to the proofs shown in [67], the only difference being the new terms on Γ_o, due to the Sommerfeld artificial boundary condition. Since these terms have required a more regular functional setting than the one in [67], the working norms now contain the new terms $\kappa_p \|q_h\|^2_{L^2(\Upsilon, L^2(\Gamma_\mathrm{o}))}$ and $\kappa_u \|\gamma_n \boldsymbol{v}_h\|^2_{L^2(\Upsilon, L^2(\Gamma_\mathrm{o}))}$. These working norms are defined next:

Definition 3.4.1 (Working norms)**.** *Let*

$$\begin{aligned} |||[q_h, \boldsymbol{v}_h]|||^2_{0,h} := \mu_p \|q_h\|^2_{L^\infty(\Upsilon; L^2(\Omega))} + \mu_u \|\boldsymbol{v}_h\|^2_{L^\infty(\Upsilon; L^2(\Omega))} \\ + (1+\sigma)\kappa_p \|q_h\|^2_{L^2(\Upsilon, L^2(\Gamma_\mathrm{o}))} + (1-\sigma)\kappa_u \|\gamma_n \boldsymbol{v}_h\|^2_{L^2(\Upsilon, L^2(\Gamma_\mathrm{o}))}, \end{aligned}$$

with $\sigma = 0, -1, 1$ for variational forms I, II and III, respectively. We define:

i) Weak norm:

$$\begin{aligned} |||[q_h, \boldsymbol{v}_h]|||^2_{W,h} := |||[q_h, \boldsymbol{v}_h]|||^2_{0,h} + \tau_p \|\mu_p \partial_t q_h + \nabla \cdot \boldsymbol{v}_h\|^2_{L^2(\Upsilon; L^2(\Omega))} \\ + \tau_u \|\mu_u \partial_t \boldsymbol{v}_h + \nabla q_h\|^2_{L^2(\Upsilon; L^2(\Omega))}. \end{aligned} \tag{3.38}$$

ii) Strong norm:

$$|||[q_h, \boldsymbol{v}_h]|||^2_{S,h} := |||[q_h, \boldsymbol{v}_h]|||^2_{0,h} + \tau_p \|\nabla\cdot\boldsymbol{v}_h\|^2_{L^2(\Upsilon,L^2(\Omega))} + \tau_u \|\nabla q_h\|^2_{L^2(\Upsilon,L^2(\Omega))}. \tag{3.39}$$

We state a first stability result in the form of Λ-coercivity. This concept is used here in the same sense as in [67, 103] for the ASGS and OSS methods. The results obtained apply to any of the variational forms, defined in (3.16), (3.21), and (3.26).

In what follows, C denotes a positive constant, independent of μ_p, μ_u, ℓ_p and ℓ_u. In the discrete formulation C will be independent of the mesh size h. The value of C may be different at different occurrences. Additionally, we will use the notation $A \gtrsim B$ and $A \lesssim B$ to indicate that $A \geq CB$ and $A \leq CB$ respectively, where A and B are two quantities that might depend on the solution or mesh size.

The ASGS and OSS methods are not coercive in the norms of interest and therefore their well-posedness needs to be proved via an inf-sup condition. For the subsequent analysis we use a more descriptive property than the inf-sup condition. This property has been defined as Λ-coercivity in [103].

Definition 3.4.2 (Λ-coercivity)**.** *Let $\mathcal{V}$ be a normed space and $\zeta : \mathcal{V} \times \mathcal{V} \longrightarrow \mathbb{R}$ a bilinear form. ζ is Λ-coercive if we can define a continuous operator $\Lambda : \mathcal{V} \longrightarrow \mathcal{V}$, i.e., $\|\Lambda(u)\|_{\mathcal{V}} \lesssim \|u\|_{\mathcal{V}}\ \forall u \in \mathcal{V}$, such that*

$$\zeta(u, \Lambda(u)) \gtrsim \|u\|_{\mathcal{V}} \|\Lambda(u)\|_{\mathcal{V}}\ \forall u \in \mathcal{V}.$$

Let us recall that the inf-sup condition for ζ implies that $\forall u \in \mathcal{V}\ \exists\, v \in \mathcal{V}$ such that $\zeta(u, v) \gtrsim \|u\|_{\mathcal{V}}\|v\|_{\mathcal{V}}$ with $\|v\|_{\mathcal{V}} \lesssim \|u\|_{\mathcal{V}}$. Thus, Λ-coercivity implies the inf-sup condition for a particular definition of norms but it is stronger, since it also provides a continuous operator Λ that for every function u in $\mathcal{V}$ gives a function $v = \Lambda(u)$ such that the inf-sup condition holds.

In the case of the OSS method we can state Λ-coercivity in two norms: the weak norm defined in (3.38) and the strong norm defined in (3.39); ASGS stability can only be proved with the weak norm. The norm in (3.39) is stronger, since it provides full control over ∇p_h and $\nabla\cdot\boldsymbol{u}_h$. The proof is just a slight modification of the one in [67] to account for the boundary terms and we omit it. We detail the expressions of Λ that allow us to prove Λ-coercivity because they in fact provide information about the stabilization mechanism of every method.

Lemma 3.4.1 (Λ-coercivity)**.** *Both the ASGS and the OSS methods are Λ-coercive in the norm defined in* (3.38)*, i.e., their associated bilinear form satisfies*

$$|||[q_h, \boldsymbol{v}_h]|||^2_{W,h} \lesssim \int_\Upsilon \mathcal{B}_s\left([q_h, \boldsymbol{v}_h], \Lambda\left([q_h, \boldsymbol{v}_h]\right)\right) \mathrm{d}t \quad \forall\, [q_h, \boldsymbol{v}_h],$$

whit the following choices of $\Lambda(\cdot)$:

i) ASGS method:

$$\Lambda\left([q_h, \boldsymbol{v}_h]\right) := [q_h + \tau_p\mu_p\partial_t q_h, \boldsymbol{v}_h + \tau_u\mu_u\partial_t\boldsymbol{v}_h],$$

ii) OSS method:

$$\Lambda\left([q_h, \boldsymbol{v}_h]\right) := [q_h, \boldsymbol{v}_h] + \beta\big[\tau_p(\mu_p\partial_t q_h + P_p(\nabla\cdot\boldsymbol{v}_h)), \tau_u(\mu_u\partial_t\boldsymbol{v}_h + P_u(\nabla q_h))\big],$$

with a small enough $\beta > 0$. Moreover, the OSS method is also Λ-coercive in the norm defined in (3.39)*, i.e., its bilinear form satisfies*

$$|||[q_h, \boldsymbol{v}_h]|||^2_{S,h} \lesssim \int_\Upsilon \mathcal{B}_s\left([q_h, \boldsymbol{v}_h], \Lambda_1([q_h, \boldsymbol{v}_h])\right) \mathrm{d}t + \int_\Upsilon \mathcal{B}_s\left([\partial_t q_h, \partial_t \boldsymbol{v}_h], \Lambda_2([q_h, \boldsymbol{v}_h])\right) \mathrm{d}t + \mathcal{B}_s\left([q_h, \boldsymbol{v}_h], \Lambda_2([q_h, \boldsymbol{v}_h])\right)\big|_{t=0},$$

for all $[q_h, \boldsymbol{v}_h]$, where

$$\Lambda_1([q_h, \boldsymbol{v}_h]) = [q_h + \beta_1 \tau_p P_p(\nabla \cdot \boldsymbol{v}_h), \boldsymbol{v}_h + \beta_1 \tau_u P_u(\nabla q_h)],$$
$$\Lambda_2([q_h, \boldsymbol{v}_h]) = \beta_2 [\partial_t q_h, \partial_t \boldsymbol{v}_h],$$

with $\beta_1 > 0$ small enough, $\beta_2 = \mu_p \gamma_p + \mu_u \gamma_u$,

$$\gamma_p = \frac{\alpha}{2} T \left(\tau_p + \tau_u \frac{\mu_u}{\mu_p}\right), \quad \gamma_u = \frac{\alpha}{2} T \left(\tau_u + \tau_p \frac{\mu_p}{\mu_u}\right), \tag{3.40}$$

and $\alpha > 0$ large enough.

Now, we state stability of the ASGS and the OSS methods. The results obtained apply to any of the variational forms defined in (3.16)-(3.30). We start defining the norms in which the external forces need to be bounded in order to obtain stability. Again, it provides information about the behavior of the two formulations considered and, obviously, the regularity requirements on the data in order to have well-posedness.

Definition 3.4.3 (External Forces Norms)**.** *Let us consider the following norms of the data:*

i) External forces weak norm for the OSS method:

$$\|[f_p, \boldsymbol{f}_u]\|^2_{W\text{-}OSS,h} := \frac{1}{\mu_p}\|f_p\|^2_{L^1(\Upsilon,L^2(\Omega))} + \frac{1}{\mu_u}\|\boldsymbol{f}_u\|^2_{L^1(\Upsilon,L^2(\Omega))} + \tau_p\|f_p\|^2_{L^2(\Upsilon,L^2(\Omega))} + \tau_u\|\boldsymbol{f}_u\|^2_{L^2(\Upsilon,L^2(\Omega))}. \tag{3.41}$$

ii) External forces weak norm for the ASGS method:

$$\|[f_p, \boldsymbol{f}_u]\|^2_{W\text{-}ASGS,h} := \|[f_p, \boldsymbol{f}_u]\|^2_{W\text{-}OSS,h} + \tau_p\tau_u\mu_u\|\partial_t f_p\|^2_{L^1(\Upsilon,L^2(\Omega))} + \tau_p\tau_u\mu_p\|\partial_t \boldsymbol{f}_u\|^2_{L^1(\Upsilon,L^2(\Omega))} + \tau_p\tau_u\mu_u\|f_p\|^2_{L^\infty(\Upsilon,L^2(\Omega))} + \tau_p\tau_u\mu_p\|\boldsymbol{f}_u\|^2_{L^\infty(\Upsilon,L^2(\Omega))}. \tag{3.42}$$

iii) External forces strong norm for the OSS method:

$$\|[f_p, \boldsymbol{f}_u]\|^2_{S\text{-}OSS,h} := \|[f_p, \boldsymbol{f}_u]\|^2_{W\text{-}OSS,h} + \gamma_p\left(\|\partial_t f_p\|^2_{L^1(\Upsilon,L^2(\Omega))} + \|f_p(0)\|^2\right) + \gamma_u\left(\|\partial_t \boldsymbol{f}_u\|^2_{L^1(\Upsilon,L^2(\Omega))} + \|\boldsymbol{f}_u(0)\|^2\right) + \beta_2\tau_p\|\partial_t f_p\|^2_{L^2(\Upsilon,L^2(\Omega))} + \beta_2\tau_u\|\partial_t \boldsymbol{f}_u\|^2_{L^2(\Upsilon,L^2(\Omega))}, \tag{3.43}$$

with γ_p and γ_u given in (3.40)*.*

Next, we state the stability properties of the different methods. Their proof is very similar to the ones in [67], the only modification being the boundary terms arising from the Sommerfeld boundary condition.

Theorem 3.4.1 (Stability)**.** *The solution* $[p_h, \boldsymbol{u}_h]$ *of the ASGS-stabilized FE formulation* (3.32) *with* (3.33)-(3.34) *satisfies*

$$|||[p_h, \boldsymbol{u}_h]|||^2_{W,h} \lesssim \|[f_p, \boldsymbol{f}_u]\|^2_{W\text{-}ASGS,h}, \tag{3.44}$$

with the norms defined in (3.38) *and* (3.42)*. On the other hand, the solution of the OSS-stabilized FE formulation* (3.32) *with* (3.35)-(3.36) *satisfies*

$$|||[p_h, \boldsymbol{u}_h]|||^2_{W,h} \lesssim \|[f_p, \boldsymbol{f}_u]\|^2_{W\text{-}OSS,h}, \tag{3.45}$$

with the (weak) norms defined in (3.38) *and* (3.41)*, as well as*

$$|||[p_h, \boldsymbol{u}_h]|||^2_{S,h} \lesssim \|[f_p, \boldsymbol{f}_u]\|^2_{S\text{-}OSS,h}, \tag{3.46}$$

with the (strong) norms defined in (3.39) *and* (3.43)*.*

3.4.2 Convergence Analysis

In this section we present convergence results for the stabilized FE methods proposed. The results obtained apply to any of the variational forms defined in (3.16)-(3.30). Once again, the proof is omitted because it is very similar to the proofs presented in [67], the only difference being the treatment of the boundary terms arising from the Sommerfeld condition. The way to deal with them is shown in the following lemma.

Let us define p_I as the P_p projection of the exact solution p on $V_{p,h}$ and $\boldsymbol{u}_I$ as the P_u projection of the exact solution $\boldsymbol{u}$ on $V_{u,h}$. This projection, which, contrary to the classical L^2 projection, incorporates boundary conditions, turns out to be optimal:

Lemma 3.4.2 (Optimality of P_p and $P_{u,h}$)**.** *Let* $P_p : V_p \longrightarrow V_{p,h}$ *and* $P_u : V_u \longrightarrow V_{u,h}$ *be two projections defined as:*

$$\begin{aligned} (P_p(q), \chi_h) &= (q, \chi_h) \quad \forall \chi_h \in V_{p,h}, \quad P_p(q) = 0 \text{ on } \Gamma_p, \\ (P_u(\boldsymbol{v}), \boldsymbol{w}_h) &= (\boldsymbol{v}, \boldsymbol{w}_h) \quad \forall \boldsymbol{w}_h \in V_{u,h}, \quad \boldsymbol{n} \cdot P_u(\boldsymbol{v}) = 0 \text{ on } \Gamma_u. \end{aligned}$$

Let k *and* l *be the polynomial interpolation order for* $V_{p,h}$ *and* $V_{u,h}$ *respectively. Then,* P_p *and* P_u *are optimal in* $L^2(\Omega)$*,* $H^1(\Omega)$ *and* $L^2(\Gamma)$*, that is to say:*

$$\begin{aligned} &\|q - P_p(q)\|_{L^2(\Omega)} \lesssim h^{k+1}|q|_{H^{k+1}(\Omega)}, && \|\boldsymbol{v} - P_u(\boldsymbol{v})\|_{L^2(\Omega)} \lesssim h^{l+1}|\boldsymbol{v}|_{H^{l+1}(\Omega)}, \\ &\|q - P_p(q)\|_{H^1(\Omega)} \lesssim h^{k}|q|_{H^{k+1}(\Omega)}, && \|\boldsymbol{v} - P_u(\boldsymbol{v})\|_{H^1(\Omega)} \lesssim h^{l}|\boldsymbol{v}|_{H^{l+1}(\Omega)}, \\ &\|q - P_p(q)\|_{L^2(\Gamma)} \lesssim h^{k+\frac{1}{2}}|q|_{H^{k+\frac{1}{2}}(\Gamma)}, && \|\gamma_n \boldsymbol{v} - \gamma_n P_u(\boldsymbol{v})\|_{L^2(\Gamma)} \lesssim h^{l+\frac{1}{2}}|\boldsymbol{v}|_{H^{l+\frac{1}{2}}(\Gamma)}, \end{aligned}$$

for smooth enough $q \in V_p$ *and* $\boldsymbol{v} \in V_u$*.*

Proof. The proof follows the one in [67]. The additional ingredient is the error estimate for the boundary terms, whose proof is a straightforward consequence of the classical interpolation estimates for traces of functions on boundaries. Note that $P_p(q) = q$ on Γ_p and $\gamma_n P_u(\boldsymbol{v}) = \gamma_n \boldsymbol{v}$ on Γ_u. □

Let us define two types of error functions. The error of the approximate solution (obtained using the ASGS or the OSS methods) with respect to the projected exact solution is defined as:

$$e_p := p_h - p_I\,, \quad \boldsymbol{e}_u := \boldsymbol{u}_h - \boldsymbol{u}_I,$$

whereas the error of the exact solution with respect to the projected exact solution is defined as:

$$\varepsilon_p := p - p_I\,, \quad \boldsymbol{\varepsilon}_u := \boldsymbol{u} - \boldsymbol{u}_I.$$

Notice that $[e_p, \boldsymbol{e}_u]$ belongs to the FE space and $[\varepsilon_p, \boldsymbol{\varepsilon}_u]$ is orthogonal to the FE space with respect to the $L^2(\Omega)$ inner product.

Definition 3.4.4 (Error Functions)**.** *Let us define the following error functions:*

i) OSS weak error function:

$$\begin{aligned}
E^2_{\text{W-OSS}}(h) :=& \mu_p \|\varepsilon_p\|^2_{L^\infty(\Upsilon,L^2(\Omega))} + \mu_u \|\boldsymbol{\varepsilon}_u\|^2_{L^\infty(\Upsilon,L^2(\Omega))} \\
&+ \tau_u \|\nabla\varepsilon_p\|^2_{L^2(\Upsilon,L^2(\Omega))} + \tau_p \|\nabla\cdot\boldsymbol{\varepsilon}_u\|^2_{L^2(\Upsilon,L^2(\Omega))} \\
&+ \tau_p \|\mu_p \partial_t \varepsilon_p\|^2_{L^2(\Upsilon,L^2(\Omega))} + \tau_u \|\mu_u \partial_t \boldsymbol{\varepsilon}_u\|^2_{L^2(\Upsilon,L^2(\Omega))} \\
&+ \frac{1}{\tau_p} \|\varepsilon_p\|^2_{L^2(\Upsilon,L^2(\Omega))} + \frac{1}{\tau_u} \|\boldsymbol{\varepsilon}_u\|^2_{L^2(\Upsilon,L^2(\Omega))} \\
&+ (1+\sigma)\kappa_p \|\varepsilon_p\|^2_{L^2(\Upsilon,L^2(\Gamma_o))} + (1-\sigma)\kappa_u \|\gamma_n \boldsymbol{\varepsilon}_u\|^2_{L^2(\Upsilon,L^2(\Gamma_o))}.
\end{aligned} \tag{3.47}$$

ii) ASGS error function:

$$\begin{aligned}
E^2_{\text{W-ASGS}}(h) :=& E^2_{\text{W-OSS}}(h) \\
&+ \mu_u \tau_p \tau_u \|\mu_p \partial_t \varepsilon_p\|^2_{L^\infty(\Upsilon,L^2(\Omega))} + \mu_p \tau_p \tau_u \|\mu_u \partial_t \boldsymbol{\varepsilon}_u\|^2_{L^\infty(\Upsilon,L^2(\Omega))} \\
&+ \mu_u \tau_p \tau_u \|\mu_p \partial_{tt} \varepsilon_p\|^2_{L^1(\Upsilon,L^2(\Omega))} + \mu_p \tau_p \tau_u \|\mu_u \partial_{tt} \boldsymbol{\varepsilon}_u\|^2_{L^1(\Upsilon,L^2(\Omega))} \\
&+ \mu_p \tau_p \tau_u \|\nabla\varepsilon_p\|^2_{L^\infty(\Upsilon,L^2(\Omega))} + \mu_u \tau_p \tau_u \|\nabla\cdot\boldsymbol{\varepsilon}_u\|^2_{L^\infty(\Upsilon,L^2(\Omega))} \\
&+ \mu_p \tau_p \tau_u \|\nabla\partial_t \varepsilon_p\|^2_{L^1(\Upsilon,L^2(\Omega))} + \mu_u \tau_p \tau_u \|\nabla\cdot\partial_t \boldsymbol{\varepsilon}_u\|^2_{L^1(\Upsilon,L^2(\Omega))}.
\end{aligned} \tag{3.48}$$

iii) OSS strong error function:

$$\begin{aligned}
E^2_{\text{S-OSS}}(h) :=& E^2_{\text{W-OSS}}(h) \\
&+ \gamma_p \|\mu_p \partial_{tt} \varepsilon_p + \nabla\cdot\partial_t \boldsymbol{\varepsilon}_u\|^2_{L^1(\Upsilon,L^2(\Omega))} + \gamma_u \|\mu_u \partial_{tt} \boldsymbol{\varepsilon}_u + \nabla\partial_t \varepsilon_p\|^2_{L^1(\Upsilon,L^2(\Omega))} \\
&+ \beta_2 \tau_p \|\nabla\cdot\partial_t \boldsymbol{\varepsilon}_u\|^2_{L^2(\Upsilon,L^2(\Omega))} + \beta_2 \tau_u \|\nabla\partial_t \varepsilon_p\|^2_{L^2(\Upsilon,L^2(\Omega))} \\
&+ \gamma_p \|\mu_p \partial_t \varepsilon_p(0)\|^2 + \gamma_u \|\mu_u \partial_t \boldsymbol{\varepsilon}_u(0)\|^2.
\end{aligned} \tag{3.49}$$

The following theorem shows that the previous error functions are in fact the upper bounds for the error of the methods we consider. The proof follows the same lines as in [67].

Table 3.2: Convergence rates according to the variational forms for the ASGS and OSS methods in the weak norm

Variational Form	I	II	III
$\|p-p_h\|_{L^\infty(\Upsilon,L^2(\Omega))}$	$h^{k+1/2}+h^{l+1/2}$ Quasi-optimal	$h^{k+1/2}+h^{l}$ Suboptimal	$h^{k}+h^{l+1/2}$ Suboptimal
$\|\boldsymbol{u}-\boldsymbol{u}_h\|_{L^\infty(\Upsilon,L^2(\Omega))}$	$h^{k+1/2}+h^{l+1/2}$ Quasi-optimal	$h^{k+1/2}+h^{l}$ Suboptimal	$h^{k}+h^{l+1/2}$ Suboptimal
$\|\mu_u\partial_t(\boldsymbol{u}-\boldsymbol{u}_h)+\nabla(p-p_h)\|_{L^2(\Upsilon,L^2(\Omega))}$	$h^{k}+h^{l}$ Optimal	$h^{k-1/2}+h^{l-1}$ Suboptimal	$h^{k}+h^{l+1/2}$ Optimal
$\|\mu_p\partial_t(p-p_h)+\nabla\cdot(\boldsymbol{u}-\boldsymbol{u}_h)\|_{L^2(\Upsilon,L^2(\Omega))}$	$h^{k}+h^{l}$ Optimal	$h^{k+1/2}+h^{l}$ Optimal	$h^{k-1}+h^{l-1/2}$ Suboptimal
k, l Optimal	$k=l$	$k+1/2=l$	$k=l+1/2$

Theorem 3.4.2 (Convergence)**.** *Let $[p,\boldsymbol{u}]$ be the solution of the continuous problem* (3.15) *and let $[p_h,\boldsymbol{u}_h]$ be the solution of the stabilized discrete problem* (3.32)*. For the ASGS formulation* (3.33)-(3.34)*, the discrete solution satisfies the following error estimate:*

$$|||[p-p_h,\boldsymbol{u}-\boldsymbol{u}_h]|||_{W,h}\lesssim E_{W\text{-}ASGS}(h)\,, \tag{3.50}$$

with the norm defined in (3.38) *and the error function* (3.48)*. On the other hand, the OSS formulation* (3.35)-(3.36) *satisfies*

$$|||[p-p_h,\boldsymbol{u}-\boldsymbol{u}_h]|||_{W,h}\lesssim E_{W\text{-}OSS}(h)\,, \tag{3.51}$$

with the norm defined in (3.38) *and the error function* (3.47)*, as well as*

$$|||[p-p_h,\boldsymbol{u}-\boldsymbol{u}_h]|||_{S,h}\lesssim E_{S\text{-}OSS}(h)\,, \tag{3.52}$$

with the norm (3.39) *and the error function* (3.49)*.*

3.4.3 Accuracy of ASGS and OSS Methods

Let k be the order of p-interpolation and l the order of $\boldsymbol{u}$-interpolation. Analyzing the a priori error estimates for the ASGS and the OSS methods from (3.50) and (3.51) and assuming regular enough solutions, we can summarize the convergence rates of the formulations as shown in Table 3.2. Further, the OSS method also satisfies the error estimate in the strong norm (3.52), summarized in Table 3.3. We stress the fact that the convergence rates do depend on the choice of the stabilization parameters, and different convergence orders are obtained for the three discrete variational formulations above. We note that the introduction of Sommerfeld artificial boundary conditions does not spoil the convergence rates in [67].

Table 3.3: Convergence rates according to the variational forms for the OSS method in the strong norm

Variational Form	I	II	III
$\|\nabla(p-p_h)\|_{L^2(\Upsilon,L^2(\Omega))}$	h^k+h^l Optimal	$h^{k-1}+h^{l-1}$ Suboptimal	h^k+h^l Optimal
$\|\nabla\cdot(\boldsymbol{u}-\boldsymbol{u}_h)\|_{L^2(\Upsilon,L^2(\Omega))}$	h^k+h^l Optimal	h^k+h^l Optimal	$h^{k-1}+h^{l-1}$ Suboptimal
k, l Optimal	$k=l$	$k=l$	$k=l$

3.5 Numerical experiments

In this section we perform numerical experiments with the finite element formulations presented. First, in Section 3.5.1, we test convergence in h. To achieve that, we choose an analytical solution that *satisfies* the boundary conditions. This experiment shows the convergence of the discrete solution to the analytical solution. The intention of this experiment is just to check the convergence in h of the stabilization methods for all variational forms. Additionally, the intention is not to evaluate the accuracy of the NRBC because that is done later on in Section 3.5.2.

Then, in Section 3.5.2, we evaluate the accuracy of the NRBC. The main objective is to evaluate how good is the NRBC compared to the solution obtained in an unbounded domain. As the NRBC is not exact, we show that the error of the discrete solution using the NRBC with respect to the solution in the unbounded domain does not approach zero as we refine the mesh. This is the error introduced by the NRBC. Additionally, in Section 3.5.2, we evaluate the error as a function of the NRBC location.

3.5.1 Convergence tests

Let us consider a two-dimensional transient problem with analytical solution to investigate the convergence properties of the stabilized FE formulations proposed. We take $\Omega = (0,1)\times(0,1)$, the time interval $[0, 0.01]$, physical properties $\mu_p = 10.0$ and $\mu_u = 10.0$, and the forcing terms f_p and $\boldsymbol{f}_u$ such that the exact solution is:

$$p = \sin\Big(\frac{3}{2}\pi x\Big)\sin(3\pi y)\sin(2\pi t), \quad \boldsymbol{u} = [p, p]\,.$$

We impose $p = 0$ on $x = 0$, $y = 0$ and $y = 1$. The NRBC is imposed on $x = 1$.

For the spatial discretization, we have used four uniform FE meshes with $h = 0.010$, $h = 0.005$, $h = 0.002$ and $h = 0.001$. The elements used are $P1$ (three-node triangular elements) and $P2$ (six-node triangular elements). Fig. 3.1 shows the mesh for $h = 0.10$. The other meshes are isotropic refinements of that one.

The stabilization parameters are computed with the algorithmic constant $C_\tau = 0.01$ for $P1$ elements and with $C_\tau = 0.4$ for $P2$ elements. The characteristic domain length was taken as $\mathrm{L}_0 = \sqrt[d]{\mathrm{meas}(\Omega)} = 1$. The time integration scheme is Crank-Nicolson with a time step size of 10^{-5}. We have used a very small time step to avoid any interference of the time marching algorithm into the spatial error since we are only interested in the spatial

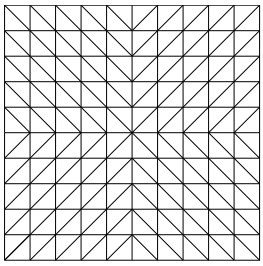

Figure 3.1: Mesh Sample

Table 3.4: Experimental convergence rates for the ASGS method using $P1/P1$ interpolation.

Variational Form	I		II		III	
Boundary Cond.	Num	Min	Num	Min	Num	Min
$\|p - p_h\|_{L^\infty(\Upsilon,L^2(\Omega))}$	2.01	1.5	1.97	1	1.98	1
$\|\boldsymbol{u} - \boldsymbol{u}_h\|_{L^\infty(\Upsilon,L^2(\Omega))}$	2.01	1.5	1.99	1	2.01	1
$\|\nabla(p - p_h)\|_{L^2(\Upsilon,L^2(\Omega))}$	1.00	1	1.00	0	1.00	1
$\|\nabla\cdot(\boldsymbol{u} - \boldsymbol{u}_h)\|_{L^2(\Upsilon,L^2(\Omega))}$	1.00	1	1.00	1	1.00	0

error. With that time step size, the difference between the error of the scalar unknown in the norm $\|\cdot\|_{L^\infty(\Upsilon,L^2(\Omega))}$ and the error in the same norm with a time step size twice as big was less than 1% in the finest mesh.

In Tables 3.4 to 3.7 the experimental convergence rates for the ASGS and the OSS methods are shown. In the tables, the word Num stands for the numerical result and the word Min stands for the minimum expected convergence rate based on theoretical analysis. All these numerical results match or are better than the convergence rates predicted theoretically.

3.5.2 NRB Performance Evaluation

Many benchmark problems have been devised in order to evaluate the performance of NRBC and NRBL formulations. Some procedures compare an analytical solution with the numerical solution in the truncated domain using the NRB, e.g., Problems 1 and 2 in

Table 3.5: Experimental convergence rates for the OSS method using $P1/P1$ interpolation.

Variational Form	I		II		III	
Boundary Cond.	Num	Min	Num	Min	Num	Min
$\|p - p_h\|_{L^\infty(\Upsilon,L^2(\Omega))}$	2.01	1.5	1.97	1	1.98	1
$\|\boldsymbol{u} - \boldsymbol{u}_h\|_{L^\infty(\Upsilon,L^2(\Omega))}$	2.01	1.5	1.99	1	2.01	1
$\|\nabla(p - p_h)\|_{L^2(\Upsilon,L^2(\Omega))}$	1.00	1	1.00	0	1.00	1
$\|\nabla\cdot(\boldsymbol{u} - \boldsymbol{u}_h)\|_{L^2(\Upsilon,L^2(\Omega))}$	1.00	1	1.00	1	1.00	0

Table 3.6: Experimental convergence rates for the ASGS method using $P2/P2$ interpolation.

Variational Form	I		II		III	
Boundary Cond.	Num	Min	Num	Min	Num	Min
$\|p-p_h\|_{L^\infty(\Upsilon,L^2(\Omega))}$	3.04	2.5	2.67	2	3.41	2
$\|\boldsymbol{u}-\boldsymbol{u}_h\|_{L^\infty(\Upsilon,L^2(\Omega))}$	3.01	2.5	2.62	2	2.77	2
$\|\nabla(p-p_h)\|_{L^2(\Upsilon,L^2(\Omega))}$	2.07	2	1.78	1	2.56	2
$\|\nabla\cdot(\boldsymbol{u}-\boldsymbol{u}_h)\|_{L^2(\Upsilon,L^2(\Omega))}$	2.08	2	2.57	2	1.78	1

Table 3.7: Experimental convergence rates for the OSS method using $P2/P2$ interpolation.

Variational Form	I		II		III	
Boundary Cond.	Num	Min	Num	Min	Num	Min
$\|p-p_h\|_{L^\infty(\Upsilon,L^2(\Omega))}$	3.00	2.5	2.64	2	3.17	2
$\|\boldsymbol{u}-\boldsymbol{u}_h\|_{L^\infty(\Upsilon,L^2(\Omega))}$	3.00	2.5	2.48	2	2.75	2
$\|\nabla(p-p_h)\|_{L^2(\Upsilon,L^2(\Omega))}$	2.06	2	1.78	1	2.54	2
$\|\nabla\cdot(\boldsymbol{u}-\boldsymbol{u}_h)\|_{L^2(\Upsilon,L^2(\Omega))}$	2.06	2	2.53	2	1.78	1

Category 3 of [52]. Other examples are the Parts 1, 2 and 3 of Problem 3 in Category 1 of [53]. Other procedures involve solving the problem in a truncated domain and in a bigger domain, and compare the solution of the big domain restricted to the truncated domain with the solution obtained in the truncated domain with the NRB [17, 42].

Benchmark problem with analytical solution

Let us consider Problem 1-Category 3 proposed in [52]. This problem has also appeared in [110]. The 2D ($d = 2$) spatial domain is taken as $\Omega = (-100, 100) \times (-100, 100)$ The physical parameters are taken as $\mu_u = 1$, $\mu_p = 1$. In all the boundary Γ of the domain NRBCs are imposed. In the references mentioned, the problem is solved with a Mach number $(M, 0)$ (mean flow in the x direction). In this work we have considered the non-convected wave equation and therefore we take $M = 0$ (zero mean flow). The simulation time is $T = 150$. The time step is taken as 1.0 and the time integration scheme used is BDF2. The initial condition is:

$$p = \exp\left[-(\ln 2)\left(\frac{x^2+y^2}{\delta_a^2}\right)\right], \qquad u_1 = 0, \qquad u_2 = 0,$$

where $\delta_a = 20$ is the radius of the acoustic pulse. The problem consists in finding the unknowns at various instants of time.

Let $\alpha_1 = \frac{\ln 2}{\delta_a^2}$ and $\eta = \sqrt{x^2+y^2}$. The exact solution is:

$$p = \frac{1}{2\alpha_1}\int_0^\infty \mathrm{e}^{\frac{-\xi^2}{4\alpha_1}}\cos(\xi t)J_0(\xi\eta)\xi\,\mathrm{d}\xi,$$

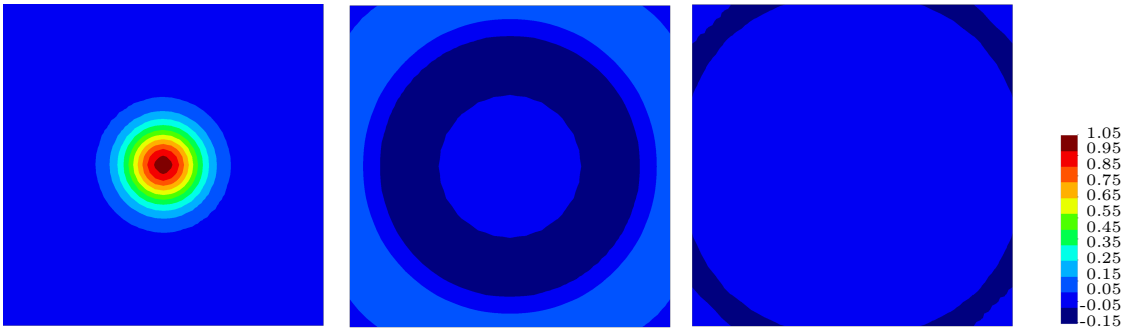

Figure 3.2: Contours of p_h for the benchmark problem with analytical solution (ASGS method, VF I, $h = 5$)

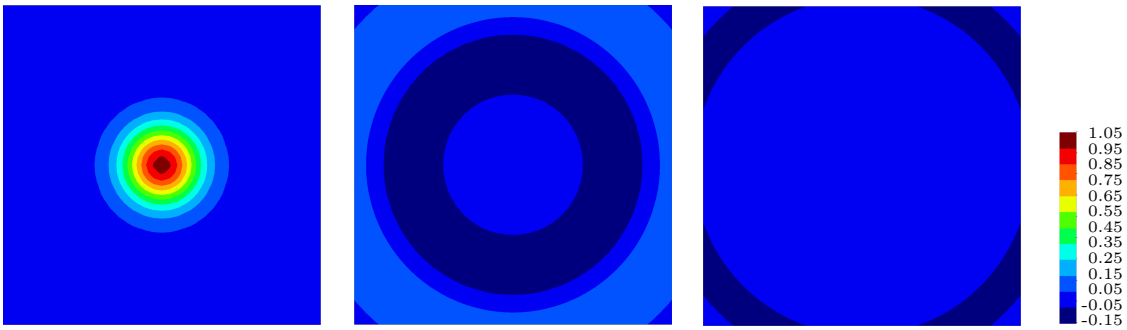

Figure 3.3: Contours of the exact p for the benchmark problem with analytical solution

$$u_1 = \frac{x}{2\alpha_1\eta}\int_0^\infty \mathrm{e}^{\frac{-\xi^2}{4\alpha_1}}\sin(\xi t)J_1(\xi\eta)\xi\,\mathrm{d}\xi,$$
$$u_2 = \frac{y}{2\alpha_1\eta}\int_0^\infty \mathrm{e}^{\frac{-\xi^2}{4\alpha_1}}\sin(\xi t)J_1(\xi\eta)\xi\,\mathrm{d}\xi,$$

where J_α are the Bessel functions of first kind of order α.

The mesh used to solve the problem was a structured mesh of various element sizes, ranging from $h = 20$ (10 elements per direction) to $h = 2$ (100 elements per direction). Fig. 3.2 shows the contours of the discrete solution p_h at $t = 0$, $t = 50$ and $t = 150$, computed using variational form I (VF I) and the ASGS method on the mesh with $h = 5$. Fig. 3.3 shows the contours of the exact solution p at $t = 0$, 50 and 150. These figures are only intended to illustrate the type of solution of this problem and how the numerical solution behaves. Approximate solutions obtained with other variational forms or with the OSS method are qualitatively very similar.

Fig. 3.4 shows a cut along $y = 0$ from $x = 0$ to $x = 100$ of p_h, and compares it with the analytical solution at $t = 50$, 100 and 150. Fig. 3.5 shows a cut along $x = y$ from $(x, y) = 0$ to $(x, y) = (100, 100)$ of p_h and compares it with the analytical solution at the same time instants. Once again, the discrete solution corresponds to the ASGS method, VF I and $h = 5$.

In Table 3.8 the results obtained are shown for various mesh sizes, polynomial interpolations, stabilization methods and variational forms. The error is computed as the $L^\infty(\Upsilon, L^2(\Omega))$-norm of the numerical solution respect to the exact solution and it is normal-

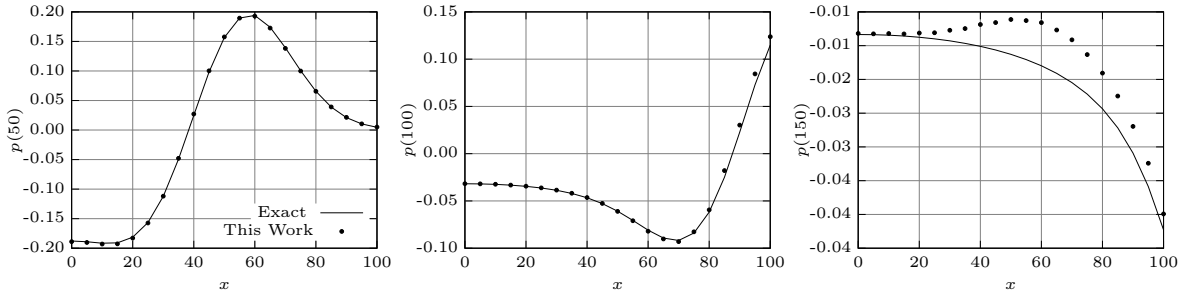

Figure 3.4: Cut at $y = 0$ of p for the benchmark problem with analytical solution (ASGS method, VF I, $h = 5$, Q1 elements, $C_\tau = 0.05$). Results shown at $t = 50$, 100 and 150.

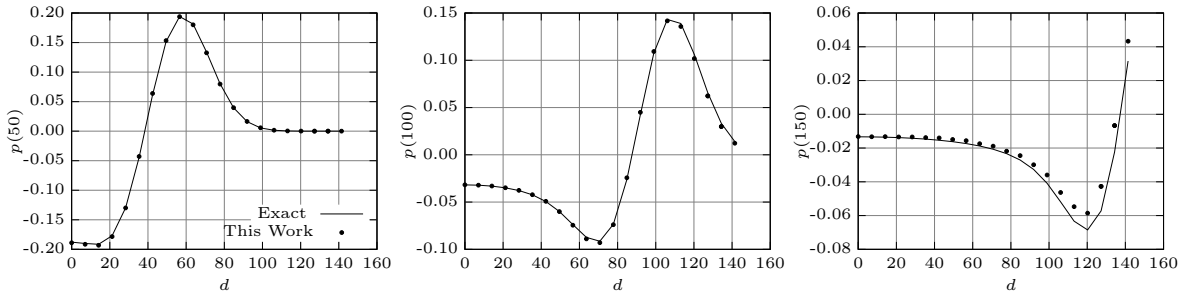

Figure 3.5: Cut at $x = y$ of p for the benchmark problem with analytical solution (ASGS method, VF I, $h = 5$, Q1 elements, $C_\tau = 0.05$). Results shown at $t = 50$, 100 and 150.

ized by the $L^\infty(\Upsilon, L^2(\Omega))$-norm of the exact solution. For VF II and III, the characteristic length is taken as $\mathrm{L}_0 = 100$. The algorithmic constant is taken as $C_\tau = 0.05$ for linear elements and $C_\tau = 0.1$ for quadratic elements in 2D and $C_\tau = 0.1$ for linear elements in 3D. We have found experimentally that these values yield good results, and are the values used in all the examples. Note that in all cases the error behaves as expected. When the error does not decrease as the mesh is refined or the polynomial order is increased, it is because of the error introduced by the NRBC.

Table 3.8: Error of the NRBC for the benchmark problem with analytical solution

h	Element	Method	VF	Error in p	Error in $\boldsymbol{u}$
20	Q1	ASGS	I	0.2166	0.2571
20	Q2	ASGS	I	0.1120	0.1398
5	Q1	ASGS	I	0.0385	0.0894
5	Q2	ASGS	I	0.0379	0.0903
2	Q1	ASGS	I	0.0383	0.0912
2	Q2	ASGS	I	0.0384	0.0916
5	Q1	ASGS	II	0.0439	0.0934
5	Q1	ASGS	III	0.0443	0.0935
5	Q1	OSS	I	0.0386	0.0897

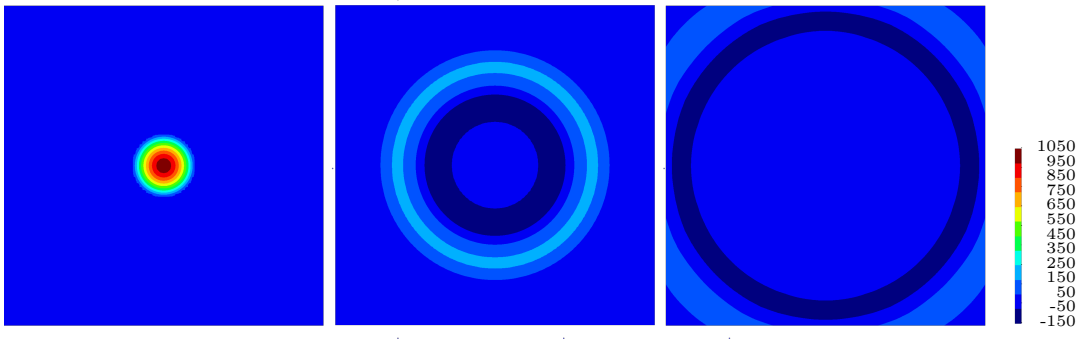

Figure 3.6: Contours of p_h in the small domain for the big/small domain benchmark problem in 2D. From the left to the right: $t = 8$, $t = 16$ and $t = 24$.

Big/small domain benchmark problem in 2D

A very interesting NRB performance test appeared in [17]. Using SI units throughout, the problem proposed is defined on a square domain of side 10 000 centered at the origin of coordinates and divided into 100×100 Q1 elements, with the NRB condition on the four sides. The reference state properties are density $\rho_0 = 1.2$, pressure $p_0 = 1.01 \times 10^5$ and heat capacity ratio $\gamma = 1.4$. We take $\mu_p = \frac{1}{\gamma p_0}$, $\mu_u = \rho_0$ and the initial condition is

$$p(\boldsymbol{x}, 0) = \begin{cases} 0.01\, p_0 \cos\left(\frac{\pi r}{2R}\right) & \text{if } r < R, \\ 0 & \text{otherwise,} \end{cases}$$

with $R = 1\,000$ and $r = \sqrt{x^2 + y^2}$. The simulation time is $T = 24$.

For comparison, a reference solution is obtained in a bigger domain, namely, a square of side 30 000 with the region of interest in its center. The boundary condition used in the big domain is $p = 0$ everywhere. The big domain is discretized with a mesh of 300×300 Q1 elements.

Let us denote as $[p_h, \boldsymbol{u}_h]$ the solution in the small domain and as $[p_{R,h}, \boldsymbol{u}_{R,h}]$ the solution in the big domain. The error is computed as:

$$e_p = \left(\max_t \sqrt{\sum_{n=1}^{N} \left(p_{R,h}(\boldsymbol{x}_n, t) - p_h(\boldsymbol{x}_n, t)\right)^2} \right) \left(\max_t \sqrt{\sum_{n=1}^{N} \left(p_{R,h}(\boldsymbol{x}_n, t)\right)^2} \right)^{-1}, \qquad (3.53)$$

where N is the number of nodes of the problem in the small domain, with coordinates $\boldsymbol{x}_n$, $n = 1, ..., N$. The error for the x-component and y-component of $\boldsymbol{u}$ (e_u and e_v, respectively) is computed similarly.

To get an qualitative impression of the type of solution we are looking for and how the NRBC behaves, Fig. 3.6 shows the contours of p_h in the small domain at $t = 0$, 8 and 16, whereas Fig. 3.7 shows the contours of $p_{R,h}$ in the same region and at the same time instants. As in the previous example, these solutions have been computed using VF I and the ASGS method.

Fig. 3.8 shows a cut at $y = 0$ for $0 \leq x \leq 5000$ of p_h and compares it with the solution $p_{R,h}$ obtained in the big domain at $t = 8$, 16 and 24. Fig. 3.9 shows a similar cut and at

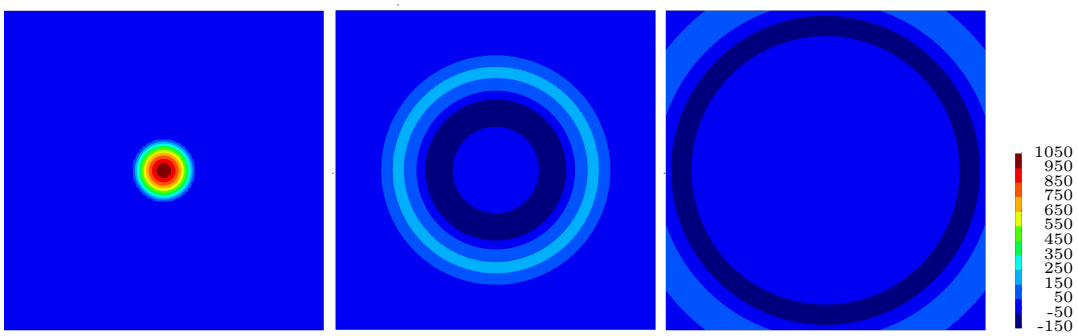

Figure 3.7: Contours of $p_{R,h}$ in the big domain for the big/small domain benchmark problem in 2D. From the left to the right: $t = 8$, $t = 16$ and $t = 24$.

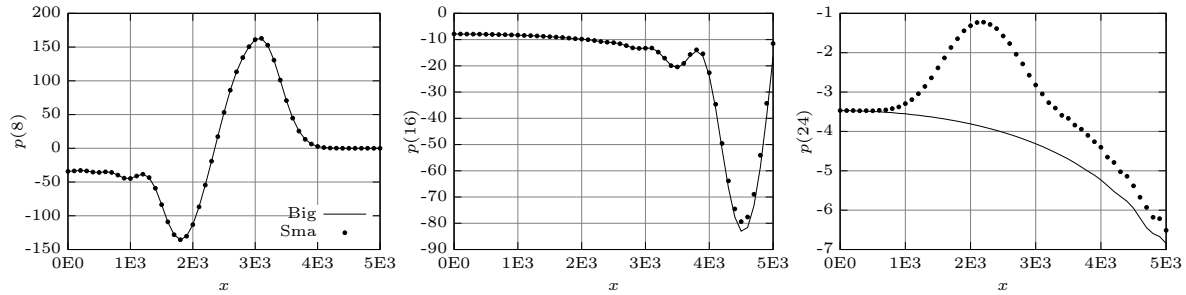

Figure 3.8: Cut at $y = 0$ of p_h and $p_{R,h}$ for the big/small domain benchmark problem in 2D. From the left to the right: $t = 8$, $t = 16$ and $t = 24$.

the same time instants, but along $x = y$ from $(x, y) = (0, 0)$ to $(x, y) = (5000, 5000)$. It is observed that the solutions in the big and small domains only differ significantly at $t = 24$, where a certain reflection is observed in spite of using the Sommerfeld boundary condition. However, these reflections are very small. To see this, Fig. 3.10 shows the evolution in time of the energy E in the region of interest. It can be seen that the solution in the small domain with the NRBC behaves as the big domain solution.

The results obtained with the NRBC are presented in Table 3.9 for various mesh sizes (100 and 50), polynomial order (P1 and P2), stabilization methods (ASGS and OSS),

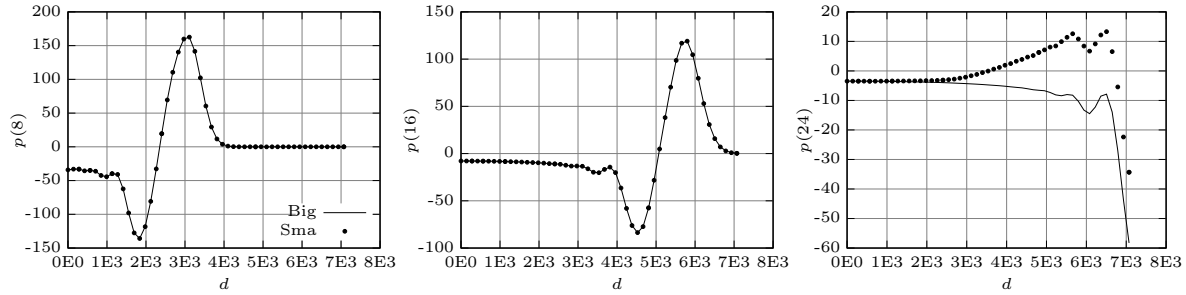

Figure 3.9: Cut at $x = y$ of p_h and $p_{R,h}$ for the big/small domain benchmark problem in 2D. From the left to the right: $t = 8$, $t = 16$ and $t = 24$.

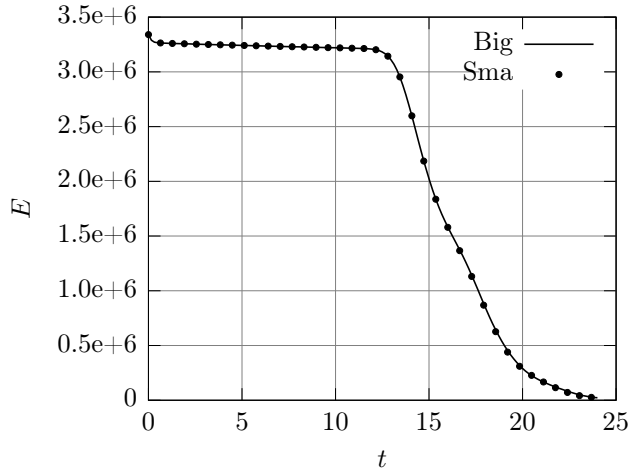

Figure 3.10: Evolution of total energy E for the big/small domain benchmark problem in 2D.

Table 3.9: Error of the NRBC for the big/small domain benchmark problem in 2D

h	Element	Method	VF	L_0	tsche	δt	e_p	e_u	e_v
100	P1	ASGS	I	-	CN	0.16	0.057	0.081	0.081
100	P1	ASGS	I	-	BDF2	0.16	0.058	0.081	0.081
100	P2	ASGS	I	-	BDF2	0.16	0.058	0.081	0.081
100	P1	OSS	I	-	BDF2	0.16	0.058	0.081	0.081
100	P1	ASGS	I	-	BDF2	0.08	0.057	0.081	0.081
50	P1	ASGS	I	-	BDF2	0.08	0.056	0.081	0.081
100	P1	ASGS	II	100	BDF2	0.16	0.058	0.082	0.082
100	P1	ASGS	II	1000	BDF2	0.16	0.058	0.082	0.082
100	P1	ASGS	II	10	BDF2	0.16	0.058	0.082	0.082
100	P1	ASGS	III	100	BDF2	0.16	0.058	0.082	0.082

variational forms (I, II and III), domain length scales (10, 100 and 1000), time marching schemes (Crank Nicolson and 2nd order BDF) and time step sizes ($\delta t = 0.16$ and 0.08). It can be seen that the error for p is around 5.8% and the error for $\boldsymbol{u}$ is around 8.2% for all cases, independently of the numerical strategy. It can therefore be concluded that this error comes exclusively from the truncation of the domain with the NRBC. In [17] the errors reported are $e_p = 2.9\%$ and $e_u = e_v = 6.2\%$ for a NRBC of order $J = 10$, slightly smaller than those we have found. Additionally, the errors obtained with our formulation are similar to the ones obtained with $J = 7$. A second order finite difference formulation with a node spacing of 100 per direction and a second order explicit time integration scheme is used in this reference, with a time step size equal to the critical time step needed for stability multiplied by 0.9.

Big/small domain benchmark problem in 3D

To test the NRBC in 3D, we solve a similar problem to the one in [17] extended to 3D. We choose the small domain as a cube of side 10 000 centered at the origin. The small domain

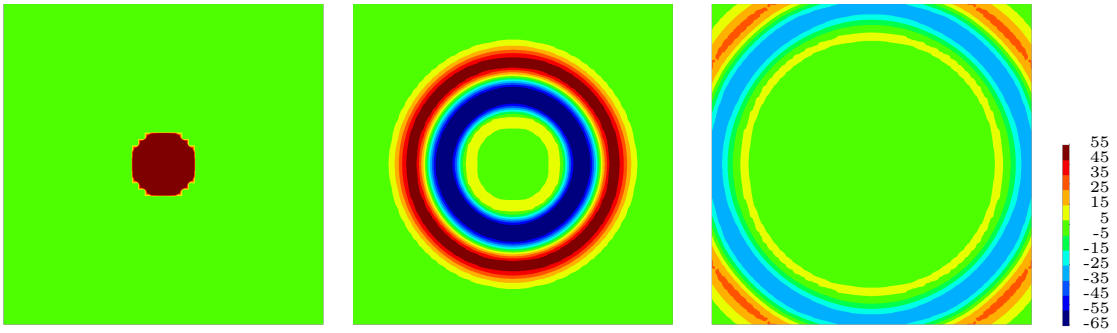

Figure 3.11: Contours of p_h in the small domain for the big/small domain benchmark problem in 3D. From the left to the right: $t = 0$, 8 and 16 (ASGS method, VF I, $h = 200$, Q1 elements).

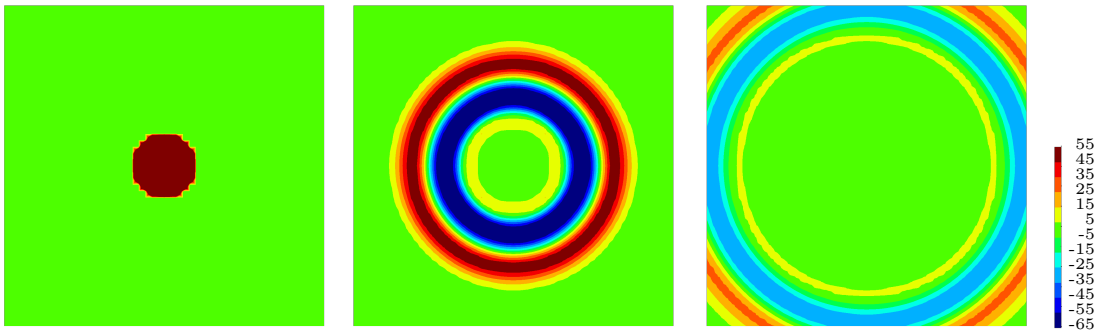

Figure 3.12: Contours of $p_{R,h}$ in the big domain for the big/small domain benchmark problem in 3D. From the left to the right: $t = 0$, 8 and 16 (ASGS method, VF I, $h = 200$, Q1 elements).

is divided in $50 \times 50 \times 50$ Q1 elements ($h = 200$) with the NRBC applied on the whole boundary. The simulation time is $T = 24$, the time step size is taken as 0.16 and the time scheme used is BDF2. The equation coefficients μ_p and μ_u, as well as the initial condition, are chosen to be the same as before, in the 2D case. The only change is that the initial condition is in a sphere of radius R, so now r is computed as $r = \sqrt{x^2 + y^2 + z^2}$.

For comparison, a reference solution $p_{R,h}$ is obtained in a bigger domain, namely, a cube of side 20 000 with the region of interest in its center. The big domain is divided in $100 \times 100 \times 100$ Q1 elements and the boundary condition $p_{R,h} = 0$ is imposed. The error is computed as in the 2D version of the case with equation (3.53). Fig. 3.11 shows the contours of p in the plane $z = 0$ for the small domain at $t = 0$, $t = 8$ and $t = 16$, whereas Fig. 3.12 shows the contours of p in the plane $z = 0$ for the big domain at the same instants. A good qualitative agreement is observed.

Fig. 3.13 shows a cut at $y = z = 0$ for $0 \leq x \leq 5000$ of p_h and $p_{R,h}$ at $t = 8$, 16 and 24. Significant discrepancies are only observed at $t = 24$. However, they have small energy, as shown below.

The results obtained with our NRBC are presented in Table 3.10 for various mesh sizes (500, 250 and 200), polynomial order (Q1 and Q2), stabilization methods (ASGS and OSS), variational forms (I, II and III) and domain length scales (25, 250 and 2500). It can

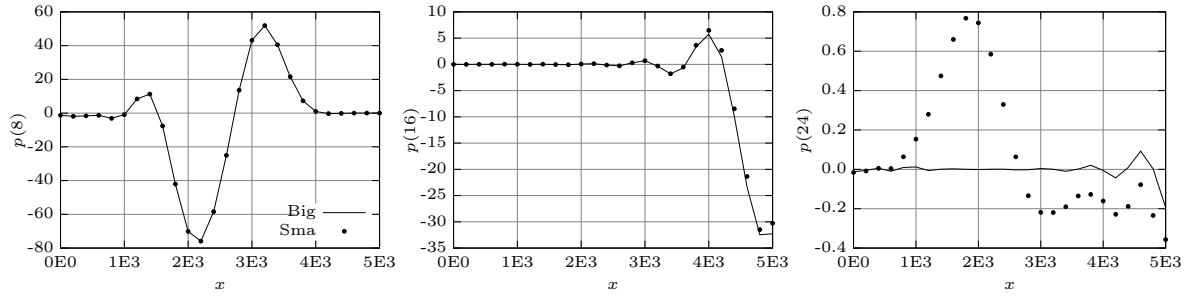

Figure 3.13: Cut at $y = 0$ of p for the big/small domain benchmark problem in 3D (ASGS method, VF I, $h = 200$, Q1 elements). From the left to the right: $t = 8$, 16 and 24.

Table 3.10: Error of the NRBC for the big/small domain benchmark problem in 3D

h	Element	Method	VF	L_0	e_p	e_u
500	Q1	ASGS	I	-	0.077	0.084
250	Q1	ASGS	I	-	0.078	0.085
200	Q1	ASGS	I	-	0.077	0.085
250	Q2	ASGS	I	-	0.081	0.090
250	Q1	OSS	I	-	0.078	0.086
250	Q1	ASGS	II	100	0.081	0.090
250	Q1	ASGS	III	100	0.081	0.090
250	Q1	ASGS	II	25	0.081	0.090
250	Q1	ASGS	II	2500	0.081	0.090

be seen that the error for p is around 7.9% and the error for $\boldsymbol{u}$ is around 8.6% for all cases.

Fig. 3.14 shows the evolution in time of the energy E in the region of interest for the case with mesh size 250 m, the ASGS method, Q1 elements and VF I. It can be seen that the solution obtained with the NRBC behaves as the big domain solution.

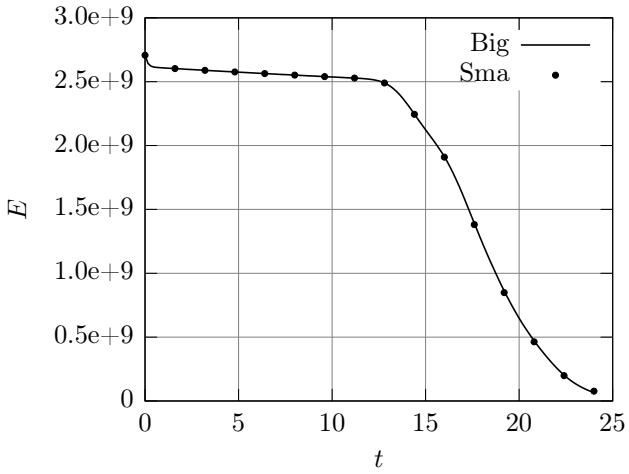

Figure 3.14: Evolution of total energy E for the big/small domain benchmark problem in 3D

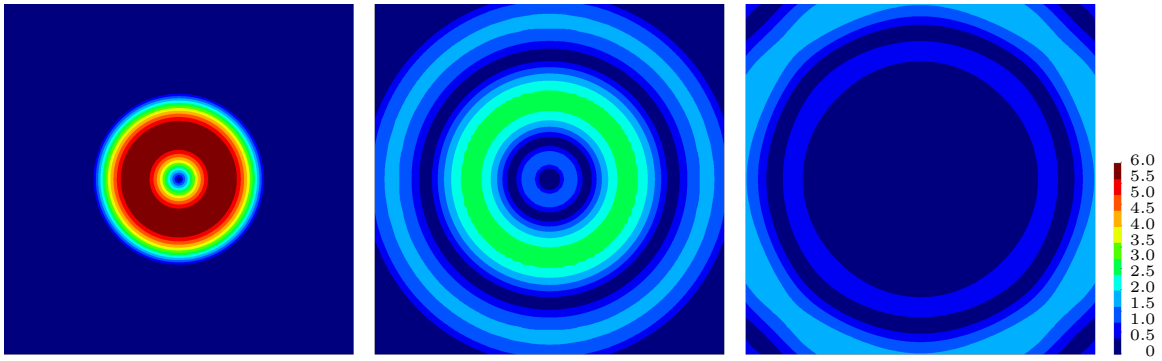

Figure 3.15: Contours of $|\boldsymbol{u}_h|$ in the small domain for the showcase problem with NRBC. From the left to the right: $t = 0$, $t = 0.3$ and $t = 0.6$.

Showcase problem with NRBC in 2D

An illustrative NRBC showcase appeared in [20] by Glowinski et al. Although it is not a benchmark of the NRBC, a plot of the evolution in time of the total energy of the system illustrates that the energy goes out of the region of interest and never enters again because the total energy decreases monotonically. The problem is defined in a square domain $\Omega = (-0.5, 0.5) \times (-0.5, 0.5)$, with $\mu_p = 1$ and $\mu_u = 1$. The simulation time is $T = 1$. The initial solution is $p(\boldsymbol{x}, 0) = 0$ and

$$\boldsymbol{u}(\boldsymbol{x}, 0) = \begin{cases} -\frac{4\pi}{r}\sin(2\pi r)\cos(2\pi r)\begin{bmatrix} x \\ y \end{bmatrix} & r \leq R, \\ \mathbf{0} & \text{otherwise}, \end{cases}$$

with $r = \sqrt{x^2 + y^2}$, $R = 0.25$. In all the boundary the NRBC is applied. The problem is solved with a mesh size $h = 0.01$, a time step of $\delta t = 0.002$ and the time integration scheme is BDF2.

Additionally, we have defined a big domain to compare the results of the NRBC in the small domain. The big domain is taken as $\Omega = (-1.5, 1.5) \times (-1.5, 1.5)$. Fig. 3.15 shows the contours of $|\boldsymbol{u}_h|$ computed in the small domain at $t = 0$, $t = 0.3$ and $t = 0.6$. Fig. 3.16 shows the contours of $|\boldsymbol{u}_{R,h}|$, the solution computed in the big domain, at the same instants. It is observed that there is a certain distortion of the wave at $t = 0.6$ close to the boundary in the small domain case, which is not observed in the solution computed in the big domain.

The evolution of total energy inside the domain of interest is shown in Fig. 3.17. The agreement between the energy computed in both the big and the small domains is very good, indicating that the wave distortion close to the boundary of the solution computed in the small domain has low energy.

The error of the small domain with respect to the big domain in $L^\infty(\Upsilon, L^2(\Omega))$ norm for VF I, the ASGS method and P1 elements was 6.8% for p and 5.3% for $\boldsymbol{u}$.

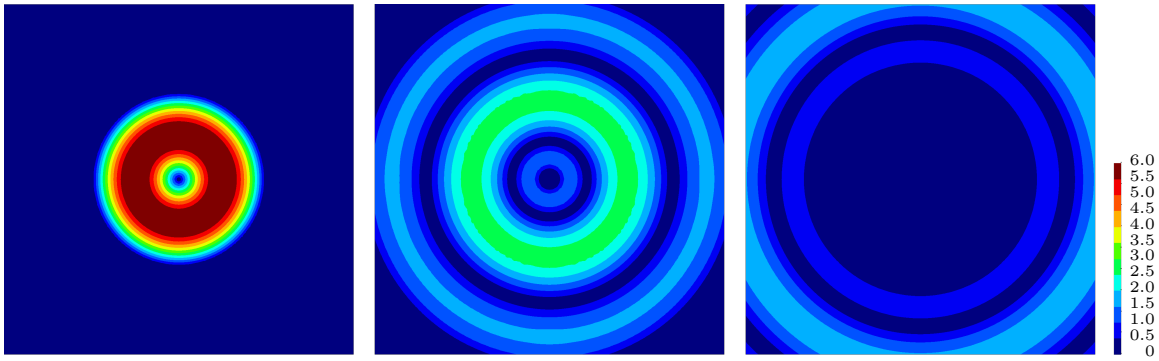

Figure 3.16: Contours of $|\boldsymbol{u}_{R,h}|$ in the big domain for the showcase problem with NRBC. From the left to the right: $t = 0$, $t = 0.3$ and $t = 0.6$.

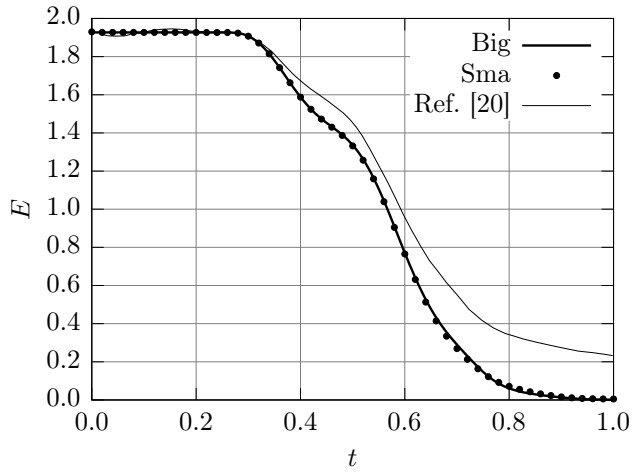

Figure 3.17: Evolution of total energy E for the showcase problem with NRBC

Showcase problem with NRBL in 2D

A NRBL example appeared in [42] by Qi et al. It uses PML as NRBL. We solve the same example using our NRBC and compare the results. The domain is a hollow cylinder that extends from $r = 1$ to $r = 1 + H$, with $H = 1$. The mesh size is $h = 0.01$ in the radial direction and has 720 divisions in the circumferential direction. The coefficients of the equation are taken as $\mu_p = 1$ and $\mu_u = 1$. The simulation time is $T = 4$, the time step size is $\delta t = 0.005$ and the time integration algorithm is BDF2. The initial condition is zero for both p and $\boldsymbol{u}$. The boundary condition at $r = 1$ changes from a prescription in p to a prescription in $\gamma_n \boldsymbol{u}$, and is given by:

$$\begin{aligned} p &= \cos(2\pi t) && 0 < t \leq 1,\ r = 1, \\ \gamma_n \boldsymbol{u} &= 0 && 1 < t < 4,\ r = 1. \end{aligned}$$

At $r = 1 + H$ the NRB is prescribed. In the case of [42], as a PML strategy is used, the domains extends from $r = 1 + H$ to $r = 1 + H + \delta$ to include the absorbing PML. The case with $\delta = 2$ from [42] was chosen as it is the one that provides less reflection according to their results. In Fig. 3.18 it is shown the evolution of p at $r = 1$ with our method and the comparison with the results obtained using PML by [42].

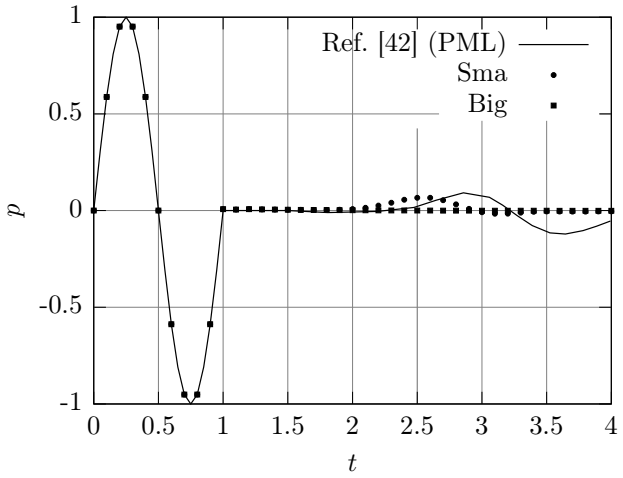

Figure 3.18: Evolution of p_h at $r = 1$ for the showcase problem with NRBL.

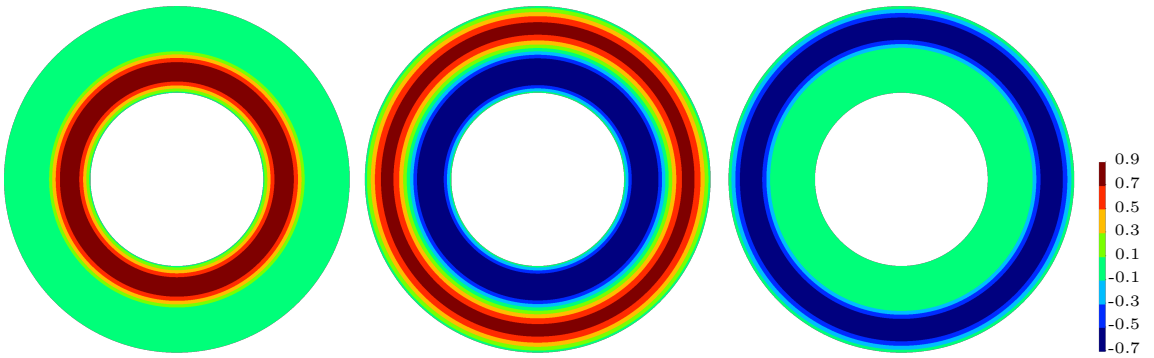

Figure 3.19: Contours of p_h in the small domain for the the showcase problem with NRBL. From the left to the right: $t = 0$, $t = 0.5$ and $t = 1.0$.

In addition to the results presented in [42], we followed the big/small domain approach as in the previous examples, taking $1 < r < 2(1 + H)$ as the big domain. Fig. 3.19 shows the contours of p_h in the small domain at $t = 0$, 0.5 and 1.0, whereas Fig. 3.20 shows the contours of the solution computed in the big domain, $p_{R,h}$, at the same time instants.

Fig. 3.21 shows the energy evolution inside the domain of interest. As in the previous examples, the differences between the solutions in the small and the big domains have low energy.

The error of the small domain with NRBC respect to the big domain in $L^\infty(\Upsilon, L^2(\Omega))$ norm for VF I, the ASGS method and Q1 elements was 5.3% for p and 3.8% for $\boldsymbol{u}$.

In addition to the Big/Small domain analysis, we performed a Big/Medium/Small domain analysis. The idea is to compare the solutions in the medium and small domains with respect to the solution in the big domain. The medium domain was taken with $H = 1.83$ and the error in the medium domain with respect to the big domain in $L^\infty(\Upsilon, L^2(\Omega))$ norm for VF I, the ASGS method and Q1 elements was 3.4% for p and 2.3% for $\boldsymbol{u}$. The small domain corresponds to a location of the NRBC of $R = 2$, whereas the medium domain has $R = 2.83$. With the errors obtained we can infer that the error is proportional to $(1/R^2)^J$ with $J \approx 0.66$.

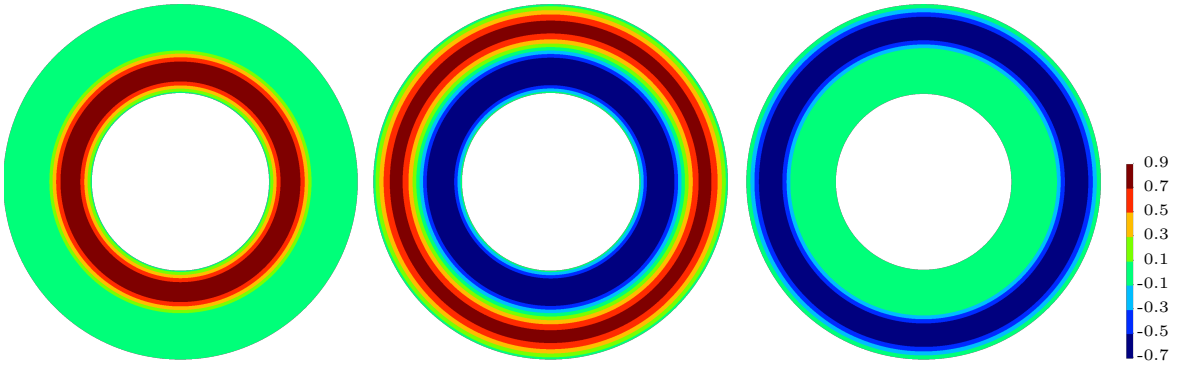

Figure 3.20: Contours of $p_{R,h}$ in the big domain for the the showcase problem with NRBL. From the left to the right: $t = 0$, $t = 0.5$ and $t = 1.0$.

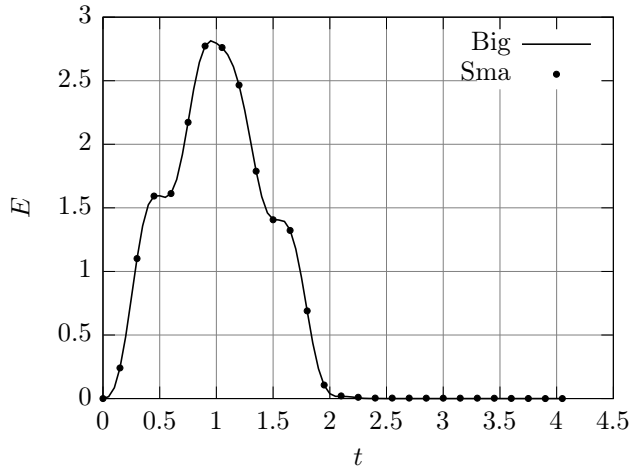

Figure 3.21: Evolution of total energy E for the showcase problem with NRBL.

3.6 Conclusions

In this work, we have described a NRBC for the wave equation in mixed form in time domain. In particular, we have considered Sommerfeld-type artificial boundary conditions. The resulting system of equations has been stated in three different functional settings, based on the regularity required for the scalar and vector unknowns. The introduction of the NRBC terms require to increase the regularity of the functional setting for problems in bounded domains [67]. The extra regularity required is somehow small because the set of functions in $H(\mathrm{div}, \Omega)$ with normal trace in $L^2(\Gamma_o)$ is *close* to $H(\mathrm{div}, \Omega)$, considering that $H^{\frac{1}{2}+\epsilon}(\Omega)$ has trace in $L^2(\Gamma)$ for any $\epsilon > 0$ and that $H^1(\Omega)$ has trace in $H^{\frac{1}{2}}(\Gamma)$.

We have presented two stabilized FE methods (ASGS and OSS) including the NRBC. Additionally, the stabilized methods can mimic the three variational forms of the problem, which require different regularity of the unknowns, via a proper design of the stabilization parameters. Stability and convergence results have been presented for these stabilized FE formulations. The NRBC does not affect previous results proved in [67] for Dirichlet-type boundary conditions, although it requires extra regularity on the boundary for the vector unknown in variational forms I and II. We normally use the stabilized FE formulations for

equal interpolation of the unknowns, but the analysis is not restricted to that and allows any continuous interpolation pair.

Numerical experiments have been carried out to check the accuracy of the methods and the results obtained are in agreement with the accuracy predicted theoretically. Benchmark problems have been solved using the NRBCs proposed and good results have been obtained when compared with other NRBCs or NRBLs. The main practical advantage of the NRBC described over other NRBCs is its simplicity and the fact that no nonlinear or iterative methods are required. Further, for NRBC schemes, the truncated domain does not need to be extended with an absorbing layer. Additionally, when compared to PML techniques, it avoids extra degrees of freedom per node and avoids the solution of other governing equations in the absorbing layer.

Chapter 4

On some time marching schemes for the stabilized finite element approximation of the mixed wave equation

This chapter is based on the material in:
Hector Espinoza, Ramon Codina, and Santiago Badia. "On some time marching schemes for the stabilized finite element approximation of the mixed wave equation". In: *Computer Methods in Applied Mechanics and Engineering* (Dec. 2014). Submitted
Some content is repeated from Chapter 1 and Chapter 3 so it is self-contained.

In this chapter we analyze time marching schemes for the wave equation in mixed form. The problem is discretized in space using stabilized finite elements. On the one hand, stability and convergence analyses of the fully discrete numerical schemes are presented. On the other hand, we use Fourier techniques (also known as von Neumann analysis) in order to analyze stability, dispersion and dissipation. Additionally, numerical convergence tests are presented for various time integration schemes, polynomial interpolations (for the spatial discretization), stabilization methods, and variational forms. Finally, a 1D example is solved to analyze the behavior of the different schemes considered.

4.1 Introduction

Finite difference time marching schemes are mostly used for the time integration of evolution problems because of their efficiency and ease of implementation. In the case of partial differential equations (PDEs) in space and time, even if a given finite difference scheme has some general properties regarding stability and accuracy, the precise behavior of the scheme needs to be analyzed together with the spatial discretization employed. In this chapter we aim at analyzing classical first and second order schemes for the hyperbolic wave equation, with the particularity that we write it in mixed form and discretize in space using stabilized finite element (FE) methods.

For the analysis of time discretization schemes for wave propagation problems it is customary to split the total discretization error into two parts: dispersion error and dissipation error. Dispersion is the dependency of the phase velocity on the frequency and the dispersion error is the deviation of the phase velocity with respect to the expected one for

a given frequency. On the other hand, dissipation error is the decrease in amplitude with respect to the expected one. In general, dispersion and dissipation errors are higher for poorly resolved frequencies, which occurs mainly for small frequencies. The wave equation we aim to analyze is non-dispersive and non-dissipative. Therefore, it would be desirable to have non-dispersive and non-dissipative discretization schemes. This sometimes cannot be achieved, thus one just aims to have low-dispersion low-dissipation schemes [124, 125]. Dispersion and/or dissipation of numerical schemes can be evaluated using Fourier techniques (see [126, 127]), energy methods (see [128]), or modified equation analysis (see [127, 129]). Fourier analysis can be carried out for semi-discretizations or full discretizations. Dispersion/dissipation analysis methods have been used to optimize numerical schemes [126, 129]. Other properties of the continuous wave equation, such as the preservation of symplecticity, some invariants or some symmetries are even more difficult to inherit for discrete schemes. This is the motivation of the so-called geometric numerical integrators, which we will not consider in this chapter (see [130], for example).

Contrary to the irreducible hyperbolic wave equation, which is of second order in space and time, the mixed wave equation is of first order in space and time. We will consider the case of a single scalar unknown, which in the mixed format unfolds into two unknowns, namely, this scalar field and a vector unknown. With regard to the space approximation, the Galerkin FE discretization of this mixed wave equation requires to satisfy a compatibility condition between the spaces of the two unknowns (scalar and vector), i.e., to use so-called inf-sup compatible interpolations. Alternatively, we can consider stabilized FE methods, which provide much more flexibility when choosing the interpolation spaces [67, 68, 90]. In particular, we can consider equal interpolation for the unknowns. Stability and convergence of the stabilized FE spatial semi-discretization of the mixed wave equation has been presented in [67, 68]. Stability and convergence of fully discrete schemes has also been analyzed for the convection-diffusion equation and the Stokes equations in [103, 131, 132] using spatial and temporal approximations related to those used in the present work.

In this work, we analyze the stability and convergence properties for the mixed wave equation, after time semi-discretization, space semi-discretization, and full discretization, and perform their Fourier analyses. For the time discretization, we consider backward Euler (BE), Crank-Nicolson[1] (CN) and the second order backward differentiation formula (BDF2). We will see how a symplectic time integrator (CN) compares to non-symplectic time integrators (BE and BDF2). Dispersion and dissipation of discretization methods will be evaluated through numerical experiments. This consists in solving a given problem and evaluating the solution obtained [126, 134, 135]. We will solve a 1D wave propagation problem to show qualitatively dispersion and dissipation of the proposed numerical schemes.

The organization of the chapter is as follows. In Section 4.2 we present the problem statement and its space-time discretization. In Section 4.3 we present stability and con-

[1]The original CN discretization scheme was devised to solve numerically PDEs of heat-conduction type; it is a space-time discretization based on finite differences. Sometimes CN is used to refer to the implicit midpoint method or the (implicit) trapezoidal rule and there is no agreement in the literature [133]. We have to mention that for linear operators (which is the the case of the mixed wave equation) the trapezoidal rule and the implicit midpoint method are equivalent.

vergence results of the fully discrete problem obtained using variational techniques. We provide results for all the methods considered, even though we only present one sample of the proofs of these results. In Section 4.4 we present a complete Fourier analysis for the 1D wave equation in mixed form, from which precise information on the behavior of the different schemes can be drawn. Numerical results are presented in Section 4.5 and, finally, in Section 4.6 the conclusions of the work are summarized. This chapter is a continuation of our work on the approximation of the mixed form of the wave equation presented in [67, 68] which correspond to Chapter 2 and Chapter 3 respectively. Frequent reference is made to these two papers/chapters, to which the reader is addressed for details.

4.2 Problem statement and numerical approximation

4.2.1 Initial and boundary value problem

The problem we consider is an initial and boundary value problem posed in a time interval $\Upsilon := (0, T)$ and in a spatial domain $\Omega \subset \mathbb{R}^d$, ($d = 1,\ 2$ or 3). Let $t \in \Upsilon$ be a given time instant in the temporal domain and $\boldsymbol{x} \in \Omega$ a given point in the spatial domain. We define the space-time domain as $\Xi := \Omega \times \Upsilon$. Let Γ be the boundary of the domain Ω. We split Γ into three disjoint sets denoted as Γ_p, Γ_u and Γ_{o}. The scalar unknown p is enforced on Γ_p, the normal trace of the vector unknown $\gamma_n \boldsymbol{u}$ on Γ_u, and a simple non reflecting boundary condition (NRBC) on Γ_{o}. Although the boundary conditions are irrelevant for the von Neumann analysis, we just mention them for completeness.

The problem consists in finding $p : \Xi \longrightarrow \mathbb{R}$ and $\boldsymbol{u} : \Xi \longrightarrow \mathbb{R}^d$ such that

$$\mu_p \partial_t p + \nabla \cdot \boldsymbol{u} = f_p \,, \tag{4.1}$$

$$\mu_u \partial_t \boldsymbol{u} + \nabla p = \boldsymbol{f}_u \,, \tag{4.2}$$

with the following initial conditions

$$p(\boldsymbol{x}, 0) = 0, \quad \boldsymbol{u}\,(\boldsymbol{x}, 0) = \boldsymbol{0}, \tag{4.3}$$

and with the following boundary conditions

$$p = 0 \ \text{ on } \Gamma_p, \quad \gamma_n \boldsymbol{u} := \boldsymbol{n} \cdot \boldsymbol{u} = 0 \ \text{ on } \Gamma_u, \quad \mu_p^{\frac{1}{2}} p = \mu_u^{\frac{1}{2}} \gamma_n \boldsymbol{u} \ \text{ on } \Gamma_{\mathrm{o}}, \tag{4.4}$$

where $\mu_p > 0$ and $\mu_u > 0$ are physical coefficients such that $c^2 = (\mu_p \mu_u)^{-1}$, c is the wave speed, f_p and $\boldsymbol{f}_u$ are forcing terms, $\boldsymbol{n}$ is the unit outward normal to the boundary of the domain and γ_n is the normal trace operator. In the previous equations and in what follows, we use the following convention: lower-case bold italic letters represent vectors in $\mathbb{R}^d$, lower-case non-bold italic letters represent scalars, whereas upper-case non-bold italic letters may be arrays or matrices.

Let Ψ be a generic spatial domain, i.e. Ω or Γ or part of them. Whenever they are well defined, we denote by $L^2(\Psi)$ the space of square integrable functions defined on Ψ, by $H^1(\Psi)$ the space of functions in $L^2(\Psi)$ with derivatives in $L^2(\Psi)$, by $H(\mathrm{div}, \Psi)$ the space of vector functions with components and divergence in $L^2(\Psi)$, and by $L^2(\Psi)^d$ the space of vector functions with components in $L^2(\Psi)$. Additionally, for an arbitrary normed

functional space $\mathtt{X}$, its norm will be denoted as $\|\cdot\|_{\mathtt{X}}$. In the case of $L^2(\Omega)$ or $L^2(\Omega)^d$ the L^2-norm will simply be denoted as $\|\cdot\|$ and the L^2-inner-product as $(\cdot\,,\cdot)$ Furthermore, the space of functions whose $\mathtt{X}$-norm is C^r continuous in the time interval Υ will be denoted by $C^r(\Upsilon;\mathtt{X})$. We will only be interested in the cases $r=0$ and $r=1$. Functions whose $\mathtt{X}$-norm is L^p in Υ will be denoted by $L^p(\Upsilon;\mathtt{X})$; when $\mathtt{X}=L^2(\Omega)$ or $\mathtt{X}=L^2(\Omega)^d$, the compact notation $L^p(L^2)$ will sometimes be used. Furthermore, let $\mathtt{V}_p, \mathtt{V}_u$ be spaces associated with p and $\boldsymbol{u}$ respectively. These spaces will be defined afterwards because they depend on the functional setting. Additionally, let us define $\mathtt{V} := \mathtt{V}_p \times \mathtt{V}_u$ and $\mathtt{L} := L^2(\Omega) \times L^2(\Omega)^d$.

Problem (4.1)-(4.2) with appropriate initial and boundary conditions will be well-posed for:

$$p \in C^1\big(\Upsilon; L^2(\Omega)\big) \cap C^0\big(\Upsilon; \mathtt{V}_p\big), \quad \boldsymbol{u} \in C^1\big(\Upsilon; L^2(\Omega)^d\big) \cap C^0\big(\Upsilon; \mathtt{V}_u\big),$$

with f_p and $\boldsymbol{f}_u$ regular enough.

4.2.2 Variational problem

The variational form of problem (4.1)-(4.4) can be expressed in three different ways. Each one requires a certain regularity on the unknowns p and $\boldsymbol{u}$. The problem reads: find $[p,\boldsymbol{u}] \in C^1(\Upsilon;\mathtt{L}) \cap C^0(\Upsilon;\mathtt{V})$ such that

$$\mathcal{B}\left([p,\boldsymbol{u}],[q,\boldsymbol{v}]\right) = \mathcal{L}\left([q,\boldsymbol{v}]\right),$$

for all test functions $[q,\boldsymbol{v}] \in \mathtt{V}$, and satisfying the initial conditions. The bilinear form $\mathcal{B}$, the linear form $\mathcal{L}$ and the space $\mathtt{V}$ are defined in three different ways depending on the variational form into consideration. For simplicity, we will assume that the forcing terms f_p and $\boldsymbol{f}_u$ are square integrable, although we could relax this regularity requirement and assume they belong to the dual space of $\mathtt{V}_p$ and $\mathtt{V}_u$, respectively. Let us also define two auxiliary variables denoted as κ_p and κ_u:

$$\kappa_p := \left(\frac{\mu_p}{\mu_u}\right)^{\frac{1}{2}}, \quad \kappa_u := \left(\frac{\mu_u}{\mu_p}\right)^{\frac{1}{2}}.$$

The possible variational formulations of the problem are the following [67, 68]:

Variational Form I

$$\begin{aligned}
&\mathtt{V}_p = \left\{q \in H^1(\Omega) |\ q = 0 \text{ on } \Gamma_p\right\},\\
&\mathtt{V}_u = \left\{\boldsymbol{v} \in H(\mathrm{div},\Omega) |\ \gamma_n\boldsymbol{v} = 0 \text{ on } \Gamma_u \text{ and } \gamma_n\boldsymbol{v} \in L^2(\Gamma_{\mathrm{o}})\right\}\\
&\mathcal{B}\left([p,\boldsymbol{u}],[q,\boldsymbol{v}]\right) = \mu_p\left(\partial_t p, q\right) + \left(\nabla\cdot\boldsymbol{u}, q\right) + \mu_u\left(\partial_t\boldsymbol{u},\boldsymbol{v}\right) + \left(\nabla p,\boldsymbol{v}\right) && (4.5)\\
&\mathcal{L}\left([q,\boldsymbol{v}]\right) = \left(f_p, q\right) + \left(\boldsymbol{f}_u,\boldsymbol{v}\right) && (4.6)\\
&p = 0 \text{ on } \Gamma_p, \qquad \text{Strongly imposed} && (4.7)\\
&\gamma_n\boldsymbol{u} = 0 \text{ on } \Gamma_u, \qquad \text{Strongly imposed} && (4.8)\\
&\mu_p^{\frac{1}{2}} p = \mu_u^{\frac{1}{2}}\gamma_n\boldsymbol{u} \text{ on } \Gamma_{\mathrm{o}}, \qquad \text{Strongly imposed} && (4.9)
\end{aligned}$$

Variational Form II

$$\mathtt{V}_p = L^2(\Omega), \quad \mathtt{V}_u = \left\{\boldsymbol{v} \in H(\mathrm{div},\Omega) |\ \gamma_n \boldsymbol{v} = 0 \text{ on } \Gamma_u \text{ and } \gamma_n \boldsymbol{v} \in L^2(\Gamma_\mathrm{o})\right\}$$

$$\mathcal{B}\left([p,\boldsymbol{u}],[q,\boldsymbol{v}]\right) = \mu_p\left(\partial_t p, q\right) + \left(\nabla\cdot\boldsymbol{u}, q\right) + \mu_u\left(\partial_t \boldsymbol{u}, \boldsymbol{v}\right) - \left(p, \nabla\cdot\boldsymbol{v}\right) + \kappa_u \int_{\Gamma_\mathrm{o}} (\gamma_n \boldsymbol{v})(\gamma_n \boldsymbol{u})\,\mathrm{d}\Gamma \tag{4.10}$$

$$\mathcal{L}\left([q,\boldsymbol{v}]\right) = \left(f_p, q\right) + \left(\boldsymbol{f}_u, \boldsymbol{v}\right) \tag{4.11}$$

$$p = 0 \text{ on } \Gamma_p, \qquad \text{Weakly imposed} \tag{4.12}$$

$$\gamma_n \boldsymbol{u} = 0 \text{ on } \Gamma_u, \qquad \text{Strongly imposed} \tag{4.13}$$

$$\mu_p^{\frac{1}{2}} p = \mu_u^{\frac{1}{2}} \gamma_n \boldsymbol{u} \text{ on } \Gamma_\mathrm{o}, \qquad \text{Weakly imposed} \tag{4.14}$$

Variational Form III

$$\mathtt{V}_p = \left\{q \in H^1(\Omega) |\ q = 0 \text{ on } \Gamma_p\right\}, \quad \mathtt{V}_u = L^2(\Omega)^d$$

$$\mathcal{B}\left([p,\boldsymbol{u}],[q,\boldsymbol{v}]\right) = \mu_p\left(\partial_t p, q\right) - \left(\boldsymbol{u}, \nabla q\right) + \mu_u\left(\partial_t \boldsymbol{u}, \boldsymbol{v}\right) + \left(\nabla p, \boldsymbol{v}\right) + \kappa_p \int_{\Gamma_\mathrm{o}} pq\,\mathrm{d}\Gamma \tag{4.15}$$

$$\mathcal{L}\left([q,\boldsymbol{v}]\right) = \left(f_p, q\right) + \left(\boldsymbol{f}_u, \boldsymbol{v}\right) \tag{4.16}$$

$$p = 0 \text{ on } \Gamma_p, \qquad \text{Strongly imposed} \tag{4.17}$$

$$\gamma_n \boldsymbol{u} = 0 \text{ on } \Gamma_u, \qquad \text{Weakly imposed} \tag{4.18}$$

$$\mu_p^{\frac{1}{2}} p = \mu_u^{\frac{1}{2}} \gamma_n \boldsymbol{u} \text{ on } \Gamma_\mathrm{o}, \qquad \text{Weakly imposed} \tag{4.19}$$

4.2.3 Stabilized finite element formulations

Here we present two stabilized FE methods, which we will denote by the acronyms ASGS (Algebraic Sub-Grid Scales) and OSS (Orthogonal Sub-grid Scales), aimed to overcome the instability problems of the standard Galerkin method found when the interpolating spaces do not satisfy an appropriate inf-sup condition. We focus on equal and continuous interpolations for p and $\boldsymbol{u}$ and therefore, conforming FE spaces. For conciseness, we will consider quasi-uniform FE partitions $\{K\}$ of size h. For stabilized formulations in general non-uniform non-degenerate cases, see [97].

Let $\mathtt{V}_{p,h}$ and $\mathtt{V}_{u,h}$ be the FE spaces constructed from the FE partition $\{K\}$ to approximate p and $\boldsymbol{u}$, respectively, with $\mathtt{V}_{p,h} \subset \mathtt{V}_p$ and $\mathtt{V}_{u,h} \subset \mathtt{V}_u$. Additionally, let us define $\mathtt{V}_h = \mathtt{V}_{p,h} \times \mathtt{V}_{u,h}$. Stabilized FE methods deal with the following problem: find a pair $[p_h, \boldsymbol{u}_h] \in \mathcal{C}^1(\Upsilon; \mathtt{V}_h)$ with initial conditions $p_h(\boldsymbol{x}, 0) = 0$, $\boldsymbol{u}_h(\boldsymbol{x}, 0) = \boldsymbol{0}$ such that

$$\mathcal{B}_s\left([p_h,\boldsymbol{u}_h],[q_h,\boldsymbol{v}_h]\right) = \mathcal{L}_s\left([q_h,\boldsymbol{v}_h]\right), \tag{4.20}$$

for all test functions $[q_h, \boldsymbol{v}_h] \in \mathtt{V}_h$, where the bilinear form $\mathcal{B}_s$ and the linear form $\mathcal{L}_s$ include the Galerkin terms and additional stabilization terms. Depending on how the stabilization part is designed, a different stabilization method arises. Below, we present two methods, namely ASGS and OSS. The stabilization terms depend on the choice of the so-called stabilization parameters τ_p and τ_u.

Table 4.1: Stabilization Parameters Order and Length Scales Definition

Variational Form	I	II	III
ℓ_p	$\ell_p = \ell_u$	L_0^2/h	h
ℓ_u	$\ell_p = \ell_u$	h	L_0^2/h
τ_p	$\mathcal{O}(h)$	$\mathcal{O}(1)$	$\mathcal{O}(h^2)$
τ_u	$\mathcal{O}(h)$	$\mathcal{O}(h^2)$	$\mathcal{O}(1)$

The ASGS method is an extension to the mixed form of the wave equation of the method proposed in [87, 89]. It consists in solving problem (4.20) and taking the bilinear form $\mathcal{B}_s$ and the linear form $\mathcal{L}_s$ as:

$$\begin{aligned}\mathcal{B}_s\left([p_h, \boldsymbol{u}_h], [q_h, \boldsymbol{v}_h]\right) &= \mathcal{B}\left([p_h, \boldsymbol{u}_h], [q_h, \boldsymbol{v}_h]\right) + \left(\mu_p \partial_t p_h + \nabla\cdot\boldsymbol{u}_h, \tau_p \nabla\cdot\boldsymbol{v}_h\right) \\ &\quad + \left(\mu_u \partial_t \boldsymbol{u}_h + \nabla p_h, \tau_u \nabla q_h\right), \qquad (4.21)\\ \mathcal{L}_s\left([q_h, \boldsymbol{v}_h]\right) &= \mathcal{L}\left([q_h, \boldsymbol{v}_h]\right) + \left(f_p, \tau_p \nabla\cdot\boldsymbol{v}_h\right) + \left(\boldsymbol{f}_u, \tau_u \nabla q_h\right). \qquad (4.22)\end{aligned}$$

The OSS method is an extension to the wave equation in mixed form of the method proposed in [98, 99]. It consists in solving problem (4.20) and taking the bilinear form $\mathcal{B}_s$ and the linear form $\mathcal{L}_s$ as:

$$\begin{aligned}\mathcal{B}_s\left([p_h, \boldsymbol{u}_h], [q_h, \boldsymbol{v}_h]\right) &= \mathcal{B}\left([p_h, \boldsymbol{u}_h], [q_h, \boldsymbol{v}_h]\right) + \left(P_p^{\perp}\left(\nabla\cdot\boldsymbol{u}_h\right), \tau_p \nabla\cdot\boldsymbol{v}_h\right) \\ &\quad + \left(P_u^{\perp}\left(\nabla p_h\right), \tau_u \nabla q_h\right), \qquad (4.23)\\ \mathcal{L}_s\left([q_h, \boldsymbol{v}_h]\right) &= \mathcal{L}\left([q_h, \boldsymbol{v}_h]\right) + \left(P_p^{\perp}\left(f_p\right), \tau_p \nabla\cdot\boldsymbol{v}_h\right) + \left(P_u^{\perp}\left(\boldsymbol{f}_u\right), \tau_u \nabla q_h\right), \qquad (4.24)\end{aligned}$$

where $P_p^{\perp}(\cdot) = I(\cdot) - P_p(\cdot)$ and $P_u^{\perp}(\cdot) = I(\cdot) - P_u(\cdot)$, $P_p(\cdot)$ being the $L^2(\Omega)$ projection on $\mathtt{V}_{p,h}$ and $P_u(\cdot)$ the $L^2(\Omega)$ projection on $\mathtt{V}_{u,h}$. This in particular implies that $P_p(\cdot) = 0$ on Γ_p for variational forms I and III and that $\boldsymbol{n}\cdot P_u(\cdot) = 0$ on Γ_u for variational forms I and II. Let us remark that for the sake of conciseness we will not consider in this chapter the so-called dynamic subscales introduced in [98], even if we favor them and their use is crucial in the case of very small time steps (see also [136, 137]).

An important ingredient of stabilized formulations are the stabilization parameters. In our case, we compute them in all formulations as:

$$\tau_p = C_\tau h \sqrt{\frac{\mu_u}{\mu_p}} \sqrt{\frac{\ell_p}{\ell_u}}, \qquad \tau_u = C_\tau h \sqrt{\frac{\mu_p}{\mu_u}} \sqrt{\frac{\ell_u}{\ell_p}}, \qquad (4.25)$$

where C_τ is a dimensionless algorithmic constant and ℓ_p, ℓ_u are length scales corresponding to p and $\boldsymbol{u}$, respectively. As it was shown in the analysis presented in [67], in order to mimic at the discrete level the proper functional setting of the continuous problem the length scales ℓ_p and ℓ_u should be taken as shown in Table 4.1, where L_0 is a fixed length scale of the problem that can be fixed a priori. The motivation for designing the stabilization parameters can be found in [90, 91].

4.2.4 Full discretization

To discretize in time we will use standard finite difference schemes of first and second order, namely, the BE, the CN and the BDF2 schemes. Let $0 = t^0 < \ldots < t^n < \ldots t^N = T$ be a

finite difference partition of Υ of size δt, , that we take constant for the sake of simplicity. Let U be the sequence of exact solutions $U := \{U^n\}_{n=0}^N := \{[p(\boldsymbol{x}, t^n), \boldsymbol{u}(\boldsymbol{x}, t^n)]\}_{n=0}^N$. We will often abbreviate $p^n := p(\boldsymbol{x}, t^n)$ and $\boldsymbol{u}^n := \boldsymbol{u}(\boldsymbol{x}, t^n)$; the same symbol will be used for a time approximation to these unknowns. Let U_h be the sequence of approximate solutions of the fully discrete problem, that is $U_h := \{U_h^n\}_{n=0}^N := \{[p_h^n, \boldsymbol{u}_h^n]\}_{n=0}^N$. This fully discrete problem reads: find the sequence U_h such that

$$\mathcal{B}_h\left(U_h, V_h\right) = \mathcal{L}_h\left(V_h\right), \tag{4.26}$$

for all V_h. The definitions of $\mathcal{B}_h$ and $\mathcal{L}_h$ depend on the combination of space and time discretization and will be given in the next section, where the stability and convergence properties of the fully discrete methods are presented.

To simplify notation we will use the backward ($D^r_{\mathrm{B},q,s}$) central ($D^r_{\mathrm{C},q,s}$) and forward ($D^r_{\mathrm{F},q,s}$) difference operators for the r-th derivative, of order q and in a time interval of size $s\delta t$. For instance, the BE and BDF2 approximations of the time derivative for the scalar unknown will be

$$D^1_{\mathrm{B},1,1}p^n = \frac{p^n - p^{n-1}}{\delta t}, \quad D^1_{\mathrm{B},2,1}p^n = \frac{3p^n - 4p^{n-1} + p^{n-2}}{2\delta t}.$$

4.3 Stability and convergence results

4.3.1 Preliminaries

We present here the results of stability and convergence of the fully discrete methods arising from the combination of time marching schemes (BE, CN and BDF2) and spatial stabilized FE methods (ASGS and OSS). We provide stability and convergence results for each fully discrete method. In order to do that, we use the concept of Λ-coercivity, used for the first time in [103], which aids us in the proof of stability and later in the convergence analysis. The proofs are similar to the ones shown in [67, 68], but considering now the time-discretization also. Only one of such proofs will be developed here, the others following very similar strategies.

As usual, we use C for a generic constant independent of the mesh size h and time step δt. The value of C may be different at different occurrences. Additionally, we will use the notation $A \gtrsim B$ and $A \lesssim B$ to indicate that $A \geq CB$ and $A \leq CB$ for any A and B depending on the solution and the data. All our results are presented in such a way that C is independent of the dimensional system, i.e., C is dimensionless.

Let U_I be the sequence of *projected* solutions $U_I := \{[p_I^n, \boldsymbol{u}_I^n]\}_{n=0}^N$, where $p_I^n := \Pi_p^n\left(p^n\right)$ and $\boldsymbol{u}_I^n := \Pi_u^n\left(\boldsymbol{u}^n\right)$, where $\Pi_p^n\left(\cdot\right)$ and $\Pi_u^n\left(\cdot\right)$ are adequate interpolants onto the FE spaces, taken to be projections. Notice that this notation allows us to take different interpolants at different time steps.

Let us define some auxiliary norms to ease notation in the following:

$$|||V^n|||_0^2 := \mu_p\|q^n\|^2 + \mu_u\|\boldsymbol{v}^n\|^2, \tag{4.27}$$

$$|||V|||_B^2 := (1+\sigma)\kappa_p\|q\|^2_{\ell^2(\Upsilon,L^2(\Gamma_\mathrm{o}))} + (1-\sigma)\kappa_u\|\gamma_n\boldsymbol{v}\|^2_{\ell^2(\Upsilon,L^2(\Gamma_\mathrm{o}))}, \tag{4.28}$$

$$|||F|||_F^2 := \frac{1}{\mu_p}\|f_p\|^2_{\ell^1(\Upsilon,L^2(\Omega))} + \frac{1}{\mu_u}\|\boldsymbol{f}_u\|^2_{\ell^1(\Upsilon,L^2(\Omega))} + \tau_p\|f_p\|^2_{\ell^2(\Upsilon,L^2(\Omega))} + \tau_u\|\boldsymbol{f}_u\|^2_{\ell^2(\Upsilon,L^2(\Omega))}, \tag{4.29}$$

with $\sigma = -1, 0, 1$ for variational forms I, II and III respectively, and $\|\cdot\|_{\ell^p(\Upsilon,\mathtt{X})}$ stands for the ℓ^p-norm of a sequence of $\mathtt{X}$-norms associated to the time discretization of Υ. When $\mathtt{X} = L^q(\Omega)$, we will use the abbreviation $\ell^p(\Upsilon, L^q(\Omega)) \equiv \ell^p(L^q)$.

For the convergence analysis we need to define three types of errors: the projection error, the discretization error, and the total error. The projection error is the error between the exact solution and the projected exact solution and is defined as $\varepsilon := \{\varepsilon^n\}_{n=0}^N := \left\{[\varepsilon_p^n, \boldsymbol{\varepsilon}_u^n]\right\}_{n=0}^N := U - U_I$. The discretization error is the error between the discrete solution and the projected exact solution and is defined as $e := \{e^n\}_{n=0}^N := \left\{[e_p^n, \boldsymbol{e}_u^n]\right\}_{n=0}^N := U_h - U_I$. Finally, the total error is the error between the exact solution and the discrete solution and is defined as $\xi := \{\xi^n\}_{n=0}^N := \left\{[\xi_p^n, \boldsymbol{\xi}_u^n]\right\}_{n=0}^N := U - U_h$.

4.3.2 Analysis strategy

As mentioned above, all the methods considered have the form (4.26). We have proved that all of them (ASGS and OSS for the spatial discretization, considering the three possible variational formulations, and BE, CN and BDF2 for the time integration) are stable and optimally convergent, with the convergence order in space and time that should be expected. However, including all the proofs would be extremely long and tedious. Rather than this, we explain in what follows the analysis strategy that we have employed, give the details of the terms involved for each method in the following subsection and present then the proof of the simplest case.

For all methods we have proved Λ-coercivity, stability and convergence in an appropriate norm $|||\cdot|||$ that depends on the method. More precisely, we have shown that

1. **Λ-coercivity**. If V is a sequence of functions, either continuous or discrete in space, there exist a map $\Lambda(V)$ such that

$$\mathcal{B}_h(V, \Lambda(V)) \gtrsim |||V|||^2, \quad |||\Lambda(V)||| \lesssim |||V|||, \tag{4.30}$$

   for all V. From this property one easily gets stability in the form of an inf-sup condition (see [103]).

2. **Stability**. The discrete solution U_h satisfies

$$|||U_h||| \lesssim |||F|||_*, \tag{4.31}$$

   for an appropriate norm $|||F|||_*$ of the data (the forcing terms).

3. **Convergence**. Of course, the final objective is to provide an estimate for the total error ξ in some norm. We can show that if U is the sequence of continuous solutions and U_h the sequence of discrete solutions, then

$$|||U - U_h||| \lesssim E(h, \delta t), \tag{4.32}$$

for a certain error function $E(h, \delta t)$. At this point, let us remark that convergence is *not* a more or less straightforward consequence of stability, since the discrete problem is not consistent in the variational sense. To prove convergence we need to deal with the consistency error

$$\mathcal{C}(U, V_h) := \mathcal{L}_h(V_h) - \mathcal{B}_h(U, V_h). \tag{4.33}$$

From this definition it is easy to arrive to

$$\mathcal{B}_h(e, V_h) = \mathcal{B}_h(\varepsilon, V_h) + \mathcal{C}(U, V_h). \tag{4.34}$$

4.3.3 Forms, norms and error functions

Recalling that we have taken as zero the initial conditions, all methods are solely defined by the bilinear form $\mathcal{B}_h$ and the linear form $\mathcal{L}_h$. These are given for all methods in Table 4.2. The only comment that needs to be made is that in practice BDF2 can be started either with BE or CN. Numerical experiments show no difference in the convergence rate, even if theoretical error estimates are not optimal for convergence in terms of δt when BDF2 is started with BE for variational forms II and III.

The stability analysis of the different methods relies on the expression of map $\Lambda(V)$ satisfying (4.30), the norm of the unknown $|||V|||$ and the norm of the forcing terms $|||F|||_*$. These are all given in Table 4.3. Note that in this table use is made of abbreviations (4.27)-(4.29). The expressions of $|||F|||_*$ determine the regularity required for the data in each case.

Finally, Tables 4.4 and 4.5 provide the error functions of the error estimates (4.32) for the ASGS and the OSS methods, respectively. There are many terms in these expressions with the same convergence order. However, including all of them gives an indication of the possible sources of error, as well as of the required regularity of the continuous solution to obtain optimal convergence rates.

4.3.4 A sample of the proofs: ASGS-BE method

As an example of how to prove (4.30), (4.31) and (4.32), we present now the proof of these results for the simplest of the six methods considered, namely, ASGS for the space discretization and BE for the time integration. The proof of the rest of methods is more or less involved, but follows the same ideas.

Proof of Λ-coercivity (4.30)

From the definition of $\mathcal{B}_h$ in Table 4.2 and of $\Lambda(V)$ in Table 4.3 for the ASGS-BE method we get

$$\begin{aligned}\mathcal{B}_h\left(V, \Lambda\left(V\right)\right) = &\sum_{n=1}^{N} \delta t \left(\mu_p D^1_{\mathrm{B},1,1} q^n, q^n\right) + \sum_{n=1}^{N} \delta t \left(\mu_u D^1_{\mathrm{B},1,1} \boldsymbol{v}^n, \boldsymbol{v}^n\right) \\ &+ \tau_p \tau_u \mu_u \sum_{n=1}^{N} \delta t \left(\nabla\cdot\boldsymbol{v}^n, \nabla\cdot\left(D^1_{\mathrm{B},1,1}\boldsymbol{v}^n\right)\right) + \tau_p\tau_u\mu_p \sum_{n=1}^{N} \delta t \left(\nabla q^n, \nabla\left(D^1_{\mathrm{B},1,1} q^n\right)\right)\end{aligned}$$

Table 4.2: Forms that define the methods

Method	$\mathcal{B}_h$ and $\mathcal{L}_h$
ASGS-BE	$\mathcal{B}_h\left(U_h,V_h\right)=\sum_{n=1}^{N}\delta t\left[\left(\mu_p D^1_{\mathrm{B},1,1}p_h^n+\nabla\cdot\boldsymbol{u}_h^n,q_h^n+\tau_p\nabla\cdot\boldsymbol{v}_h^n\right)+\left(\mu_u D^1_{\mathrm{B},1,1}\boldsymbol{u}_h^n+\nabla p_h^n,\boldsymbol{v}_h^n+\tau_u\nabla q_h^n\right)\right]$ $\mathcal{L}_h\left(V_h\right)=\sum_{n=1}^{N}\delta t\left({f_p}^n,q_h^n+\tau_p\nabla\cdot\boldsymbol{v}_h^n\right)+\sum_{n=1}^{N}\delta t\left({\boldsymbol{f}_u}^n,\boldsymbol{v}_h^n+\tau_u\nabla q_h^n\right)$
ASGS-CN	$\mathcal{B}_h\left(U_h,V_h\right)=\sum_{n=1}^{N}\delta t\left[\left(\mu_p D^1_{\mathrm{B},1,1}p_h^n+\nabla\cdot{\boldsymbol{u}_h}^{n-\frac{1}{2}},q_h^n+\tau_p\nabla\cdot\boldsymbol{v}_h^n\right)\right.$ $\left.+\left(\mu_u D^1_{\mathrm{B},1,1}\boldsymbol{u}_h^n+\nabla {p_h}^{n-\frac{1}{2}},\boldsymbol{v}_h^n+\tau_u\nabla q_h^n\right)\right]$ $\mathcal{L}_h\left(V_h\right)=\sum_{n=1}^{N}\delta t\left({f_p}^{n-\frac{1}{2}},q_h^n+\tau_p\nabla\cdot\boldsymbol{v}_h^n\right)+\sum_{n=1}^{N}\delta t\left({\boldsymbol{f}_u}^{n-\frac{1}{2}},\boldsymbol{v}_h^n+\tau_u\nabla q_h^n\right)$
ASGS-BDF2	$\mathcal{B}_h\left(U_h,V_h\right)=\delta t\left[\left(\mu_p D^1_{\mathrm{B},1,1}p_h^1+\nabla\cdot{\boldsymbol{u}_h}^{1-\frac{1}{2}},q_h^1+\tau_p\nabla\cdot\boldsymbol{v}_h^1\right)+\left(\mu_u D^1_{\mathrm{B},1,1}\boldsymbol{u}_h^1+\nabla {p_h}^{1-\frac{1}{2}},\boldsymbol{v}_h^1+\tau_u\nabla q_h^1\right)\right]$ $+\sum_{n=2}^{N}\delta t\left[\left(\mu_p D^1_{\mathrm{B},2,1}p_h^n+\nabla\cdot\boldsymbol{u}_h^n,q_h^n+\tau_p\nabla\cdot\boldsymbol{v}_h^n\right)+\left(\mu_u D^1_{\mathrm{B},2,1}\boldsymbol{u}_h^n+\nabla p_h^n,\boldsymbol{v}_h^n+\tau_u\nabla q_h^n\right)\right]$ $\mathcal{L}_h\left(V_h\right)=\delta t\left({f_p}^{1-\frac{1}{2}},q_h^1+\tau_p\nabla\cdot\boldsymbol{v}_h^1\right)+\sum_{n=2}^{N}\delta t\left({f_p}^n,q_h^n+\tau_p\nabla\cdot\boldsymbol{v}_h^n\right)$ $+\delta t\left({\boldsymbol{f}_u}^{1-\frac{1}{2}},\boldsymbol{v}_h^1+\tau_u\nabla q_h^1\right)+\sum_{n=2}^{N}\delta t\left({\boldsymbol{f}_u}^n,\boldsymbol{v}_h^n+\tau_u\nabla q_h^n\right)$
OSS-BE	$\mathcal{B}_h\left(U_h,V_h\right)=\sum_{n=1}^{N}\delta t\left[\left(\mu_p D^1_{\mathrm{B},1,1}p_h^n+\nabla\cdot\boldsymbol{u}_h^n,q_h^n\right)+\tau_p\left(P_p^{\perp}\left(\nabla\cdot\boldsymbol{u}_h^n\right),\nabla\cdot\boldsymbol{v}_h^n\right)\right]$ $+\sum_{n=1}^{N}\delta t\left[\left(\mu_u D^1_{\mathrm{B},1,1}\boldsymbol{u}_h^n+\nabla p_h^n,\boldsymbol{v}_h^n\right)+\tau_u\left(P_u^{\perp}\left(\nabla p_h^n\right),\nabla q_h^n\right)\right]$ $\mathcal{L}_h\left(V_h\right)=\sum_{n=1}^{N}\delta t\left[\left({f_p}^n,q_h^n\right)+\tau_p\left(P_p^{\perp}\left({f_p}^n\right),\nabla\cdot\boldsymbol{v}_h^n\right)\right]+\sum_{n=1}^{N}\delta t\left[\left({\boldsymbol{f}_u}^n,\boldsymbol{v}_h^n\right)+\tau_u\left(P_u^{\perp}\left({\boldsymbol{f}_u}^n\right),\nabla q_h^n\right)\right]$
OSS-CN	$\mathcal{B}_h\left(U_h,V_h\right)=\sum_{n=1}^{N}\delta t\left[\left(\mu_p D^1_{\mathrm{B},1,1}p_h^n+\nabla\cdot{\boldsymbol{u}_h}^{n-\frac{1}{2}},q_h^n\right)+\tau_p\left(P_p^{\perp}\left(\nabla\cdot{\boldsymbol{u}_h}^{n-\frac{1}{2}}\right),\nabla\cdot\boldsymbol{v}_h^n\right)\right]$ $+\sum_{n=1}^{N}\delta t\left[\left(\mu_u D^1_{\mathrm{B},1,1}\boldsymbol{u}_h^n+\nabla {p_h}^{n-\frac{1}{2}},\boldsymbol{v}_h^n\right)+\tau_u\left(P_u^{\perp}\left(\nabla {p_h}^{n-\frac{1}{2}}\right),\nabla q_h^n\right)\right]$ $\mathcal{L}_h\left(V_h\right)=\sum_{n=1}^{N}\delta t\left[\left({f_p}^{n-\frac{1}{2}},q_h^n\right)+\tau_p\left(P_p^{\perp}\left({f_p}^{n-\frac{1}{2}}\right),\nabla\cdot\boldsymbol{v}_h^n\right)\right]$ $+\sum_{n=1}^{N}\delta t\left[\left({\boldsymbol{f}_u}^{n-\frac{1}{2}},\boldsymbol{v}_h^n\right)+\tau_u\left(P_u^{\perp}\left({\boldsymbol{f}_u}^{n-\frac{1}{2}}\right),\nabla q_h^n\right)\right]$
OSS-BDF2	$\mathcal{B}_h\left(U_h,V_h\right)=\delta t\left[\left(\mu_p D^1_{\mathrm{B},1,1}p_h^1+\nabla\cdot\boldsymbol{u}_h^{\frac{1}{2}},q_h^1+\tau_p\nabla\cdot\boldsymbol{v}_h^1\right)+\left(P_p^{\perp}\left(\nabla\cdot\boldsymbol{u}_h^{\frac{1}{2}}\right),\tau_p\nabla\cdot\boldsymbol{v}_h^1\right)\right]$ $+\sum_{n=2}^{N}\delta t\left[\left(\mu_p D^1_{\mathrm{B},2,1}p_h^n+\nabla\cdot\boldsymbol{u}_h^n,q_h^n\right)+\tau_p\left(P_p^{\perp}\left(\nabla\cdot\boldsymbol{u}_h^n\right),\nabla\cdot\boldsymbol{v}_h^n\right)\right]$ $+\delta t\left[\left(\mu_u D^1_{\mathrm{B},1,1}\boldsymbol{u}_h^1+\nabla p_h^{\frac{1}{2}},\boldsymbol{v}_h^1\right)+\left(P_u^{\perp}\left(\nabla p_h^{\frac{1}{2}}\right),\tau_u\nabla q_h^1\right)\right]$ $+\sum_{n=2}^{N}\delta t\left[\left(\mu_u D^1_{\mathrm{B},2,1}\boldsymbol{u}_h^n+\nabla p_h^n,\boldsymbol{v}_h^n\right)+\tau_u\left(P_u^{\perp}\left(\nabla p_h^n\right),\nabla q_h^n\right)\right]$ $\mathcal{L}_h\left(V_h\right)=\delta t\left[\left({f_p}^{\frac{1}{2}},q_h^1\right)+\tau_p\left(P_p^{\perp}\left({f_p}^{\frac{1}{2}}\right),\nabla\cdot\boldsymbol{v}_h^1\right)\right]+\delta t\left[\left({\boldsymbol{f}_u}^{\frac{1}{2}},\boldsymbol{v}_h^1\right)+\tau_u\left(P_u^{\perp}\left({\boldsymbol{f}_u}^{\frac{1}{2}}\right),\nabla q_h^1\right)\right]$ $+\sum_{n=2}^{N}\delta t\left[\left({f_p}^n,q_h^n\right)+\tau_p\left(P_p^{\perp}\left({f_p}^n\right),\nabla\cdot\boldsymbol{v}_h^n\right)\right]+\sum_{n=2}^{N}\delta t\left[\left({\boldsymbol{f}_u}^n,\boldsymbol{v}_h^n\right)+\tau_u\left(P_u^{\perp}\left({\boldsymbol{f}_u}^n\right),\nabla q_h^n\right)\right]$

$$
\begin{aligned}
&+\sum_{n=1}^{N}\delta t\left[\left(\nabla\cdot\boldsymbol{v}^n,q^n\right)+\left(\nabla q^n,\boldsymbol{v}^n\right)\right]\\
&+\sum_{n=1}^{N}\delta t\tau_p\left\|\mu_p D^1_{\mathrm{B},1,1}q^n+\nabla\cdot\boldsymbol{v}^n\right\|^2+\sum_{n=1}^{N}\delta t\tau_u\left\|\mu_u D^1_{\mathrm{B},1,1}\boldsymbol{v}^n+\nabla q^n\right\|^2\\
&+\tau_p\tau_u\mu_p\mu_u\sum_{n=1}^{N}\delta t\left[\left(D^1_{\mathrm{B},1,1}q^n,\nabla\cdot\left(D^1_{\mathrm{B},1,1}\boldsymbol{v}^n\right)\right)+\left(D^1_{\mathrm{B},1,1}\boldsymbol{v}^n,\nabla\left(D^1_{\mathrm{B},1,1}q^n\right)\right)\right].
\end{aligned}
\tag{4.35}
$$

Now we show how each term is bounded. The first four terms of (4.35) can be bounded as

$$
\begin{aligned}
&\sum_{n=1}^{N}\delta t\left(\mu_p D^1_{\mathrm{B},1,1}q^n,q^n\right)+\sum_{n=1}^{N}\delta t\left(\mu_u D^1_{\mathrm{B},1,1}\boldsymbol{v}^n,\boldsymbol{v}^n\right)+\tau_p\tau_u\mu_u\sum_{n=1}^{N}\delta t\left(\nabla\cdot\boldsymbol{v}^n,\nabla\cdot\left(D^1_{\mathrm{B},1,1}\boldsymbol{v}^n\right)\right)\\
&\qquad+\tau_p\tau_u\mu_p\sum_{n=1}^{N}\delta t\left(\nabla q^n,\nabla\left(D^1_{\mathrm{B},1,1}q^n\right)\right)\gtrsim\left|\left|\left|V^N\right|\right|\right|_0^2.
\end{aligned}
\tag{4.36}
$$

Table 4.3: Functions to obtain Λ-coercivity and norms

Method	$\Lambda(V)$, $\|\|\|V\|\|\|$ and $\|\|\|F\|\|\|_*$
ASGS-BE	$\Lambda\left(V\right) := V + \left\{ \left[0, \mathbf{0}\right], \left\{ \left[\tau_p \mu_p D^1_{\mathrm{B},1,1} q^n, \tau_u \mu_u D^1_{\mathrm{B},1,1} \boldsymbol{v}^n\right] \right\}_{n=1}^{N} \right\}$ $\|\|\|V\|\|\|^2 := \|\|\|V^N\|\|\|_0^2 + \|\|\|V\|\|\|_B^2 + \tau_p \left\| \mu_p D^1_{\mathrm{B},1,1} q^n + \nabla\cdot\boldsymbol{v}^n \right\|^2_{\ell^2(\Upsilon, L^2(\Omega))} + \tau_u \left\| \mu_u D^1_{\mathrm{B},1,1} \boldsymbol{v}^n + \nabla q^n \right\|^2_{\ell^2(\Upsilon, L^2(\Omega))}$ $\|\|\|F\|\|\|_*{}^2 := \|\|\|F\|\|\|_F^2 + \tau_p\tau_u\mu_u \left\| D^1_{\mathrm{B},1,1} f_p \right\|^2_{\ell^1(\Upsilon, L^2(\Omega))} + \tau_p\tau_u\mu_p \left\| D^1_{\mathrm{B},1,1} \boldsymbol{f}_u \right\|^2_{\ell^1(\Upsilon, L^2(\Omega))}$ $+\tau_p\tau_u\mu_u \|f_p\|^2_{\ell^\infty(\Upsilon, L^2(\Omega))} + \tau_p\tau_u\mu_p \|\boldsymbol{f}_u\|^2_{\ell^\infty(\Upsilon, L^2(\Omega))}$
ASGS-CN	$\Lambda\left(V\right) := \left\{ \left[p^0, \boldsymbol{u}^0\right], \left\{ \left[p^{n-\frac{1}{2}}, \boldsymbol{u}^{n-\frac{1}{2}}\right] \right\}_{n=1}^{N} \right\} + \left\{ \left[0, \mathbf{0}\right], \left\{ \left[\tau_p \mu_p D^1_{\mathrm{B},1,1} q^n, \tau_u \mu_u D^1_{\mathrm{B},1,1} \boldsymbol{v}^n\right] \right\}_{n=1}^{N} \right\}$ $\|\|\|V\|\|\|^2 := \|\|\|V^N\|\|\|_0^2 + \|\|\|V\|\|\|_B^2 + \tau_p \left\| \mu_p D^1_{\mathrm{B},1,1} q^n + \nabla\cdot\boldsymbol{v}^{n-\frac{1}{2}} \right\|^2_{\ell^2(\Upsilon, L^2(\Omega))}$ $+\tau_u \left\| \mu_u D^1_{\mathrm{B},1,1} \boldsymbol{v}^n + \nabla q^{n-\frac{1}{2}} \right\|^2_{\ell^2(\Upsilon, L^2(\Omega))}$ $\|\|\|F\|\|\|_*{}^2 := \|\|\|F\|\|\|_F^2 + \tau_p\tau_u\mu_u \left\| D^1_{\mathrm{B},1,1} f_p \right\|^2_{\ell^1(\Upsilon, L^2(\Omega))} + \tau_p\tau_u\mu_p \left\| D^1_{\mathrm{B},1,1} \boldsymbol{f}_u \right\|^2_{\ell^1(\Upsilon, L^2(\Omega))}$ $+\tau_p\tau_u\mu_u \|f_p\|^2_{\ell^\infty(\Upsilon, L^2(\Omega))} + \tau_p\tau_u\mu_p \|\boldsymbol{f}_u\|^2_{\ell^\infty(\Upsilon, L^2(\Omega))}$
ASGS-BDF2	$\Lambda\left(V\right) := \left\{ V^0, V^{\frac{1}{2}}, \{V^n\}_{n=2}^{N} \right\}$ $+ \left\{ \left[0, \mathbf{0}\right], \left[\tau_p \mu_p D^1_{\mathrm{B},1,1} q^1, \tau_u \mu_u D^1_{\mathrm{B},1,1} \boldsymbol{v}^1\right], \left\{ \left[\tau_p \mu_p D^1_{\mathrm{B},2,1} q^n, \tau_u \mu_u D^1_{\mathrm{B},2,1} \boldsymbol{v}^n\right] \right\}_{n=2}^{N} \right\}$ $\|\|\|V\|\|\|^2 := \|\|\|V^N\|\|\|_0^2 + \|\|\|V\|\|\|_B^2 + \tau_p \left\| \mu_p D^1_{\mathrm{B},1,1} q^1 + \nabla\cdot\boldsymbol{v}^{\frac{1}{2}} \right\|^2 \delta t + \tau_u \left\| \mu_u D^1_{\mathrm{B},1,1} \boldsymbol{v}^1 + \nabla q^{\frac{1}{2}} \right\|^2 \delta t$ $+\tau_p \left\| \mu_p D^1_{\mathrm{B},2,1} q^n + \nabla\cdot\boldsymbol{v}^n \right\|^2_{\ell^2(\Upsilon, L^2(\Omega))} + \tau_u \left\| \mu_u D^1_{\mathrm{B},2,1} \boldsymbol{v}^n + \nabla q^n \right\|^2_{\ell^2(\Upsilon, L^2(\Omega))}$ $\|\|\|F\|\|\|_*{}^2 := \|\|\|F\|\|\|_F^2 + \tau_p\tau_u\mu_u \left\| D^1_{\mathrm{B},1,1} {f_p}^1 \right\|^2 \delta t^2 + \tau_p\tau_u\mu_u \left\| D^1_{\mathrm{B},2,1} f_p \right\|^2_{\ell^1(\Upsilon, L^2(\Omega))} + \tau_p\tau_u\mu_u \|f_p\|^2_{\ell^\infty(\Upsilon, L^2(\Omega))}$ $+\tau_p\tau_u\mu_p \left\| D^1_{\mathrm{B},1,1} {\boldsymbol{f}_u}^1 \right\|^2 \delta t^2 + \tau_p\tau_u\mu_p \left\| D^1_{\mathrm{B},2,1} \boldsymbol{f}_u \right\|^2_{\ell^1(\Upsilon, L^2(\Omega))} + \tau_p\tau_u\mu_p \|\boldsymbol{f}_u\|^2_{\ell^\infty(\Upsilon, L^2(\Omega))}$
OSS-BE	$\Lambda\left(V\right) := V + \beta\Lambda_b\left(V\right) \quad (\beta \text{ small enough})$ $\Lambda_b\left(V\right) := \left\{ \left[0, \mathbf{0}\right], \left\{ \left[\tau_p \left(\mu_p D^1_{\mathrm{B},1,1} q^n + P_p\left(\nabla\cdot\boldsymbol{v}^n\right)\right), \tau_u \left(\mu_u D^1_{\mathrm{B},1,1} \boldsymbol{v}^n + P_u\left(\nabla q^n\right)\right)\right] \right\}_{n=\frac{1}{2}}^{N} \right\}$ $\|\|\|V\|\|\|^2 := \|\|\|V^N\|\|\|_0^2 + \|\|\|V\|\|\|_B^2 + \tau_p \left\| \mu_p D^1_{\mathrm{B},1,1} q^n + \nabla\cdot\boldsymbol{v}^n \right\|^2_{\ell^2(\Upsilon, L^2(\Omega))} + \tau_u \left\| \mu_u D^1_{\mathrm{B},1,1} \boldsymbol{v}^n + \nabla q^n \right\|^2_{\ell^2(\Upsilon, L^2(\Omega))}$ $\|\|\|F\|\|\|_*{}^2 := \|\|\|F\|\|\|_F^2$
OSS-CN	$\Lambda\left(V\right) := \Lambda_a\left(V\right) + \beta\Lambda_b\left(V\right) \quad (\beta \text{ small enough})$ $\Lambda_a\left(V\right) := \left\{ \left[p^0, \boldsymbol{u}^0\right], \left\{ \left[p^{n-\frac{1}{2}}, \boldsymbol{u}^{n-\frac{1}{2}}\right] \right\}_{n=1}^{N} \right\}$ $\Lambda_b\left(V\right) := \left\{ \left[0, \mathbf{0}\right], \left\{ \left[\tau_p \left(\mu_p D^1_{\mathrm{B},1,1} q^n + P_p\left(\nabla\cdot\boldsymbol{v}^{n-\frac{1}{2}}\right)\right), \tau_u \left(\mu_u D^1_{\mathrm{B},1,1} \boldsymbol{v}^n + P_u\left(\nabla q^{n-\frac{1}{2}}\right)\right)\right] \right\}_{n=1}^{N} \right\}$ $\|\|\|V\|\|\|^2 := \|\|\|V^N\|\|\|_0^2 + \|\|\|V\|\|\|_B^2 + \tau_p \left\| \mu_p D^1_{\mathrm{B},1,1} q^n + \nabla\cdot\boldsymbol{v}^{n-\frac{1}{2}} \right\|^2_{\ell^2(\Upsilon, L^2(\Omega))}$ $+\tau_u \left\| \mu_u D^1_{\mathrm{B},1,1} \boldsymbol{v}^n + \nabla q^{n-\frac{1}{2}} \right\|^2_{\ell^2(\Upsilon, L^2(\Omega))}$ $\|\|\|F\|\|\|_*{}^2 := \|\|\|F\|\|\|_F^2$
OSS-BDF2	$\Lambda\left(V\right) := \Lambda_a\left(V\right) + \beta\Lambda_b\left(V\right) \quad (\beta > 0 \text{ small enough})$ $\Lambda_a\left(V\right) := \left\{ V^0, V^{\frac{1}{2}}, \{V^n\}_{n=2}^{N} \right\}$ $\Lambda_b\left(V\right) := \left\{ \left[0, \mathbf{0}\right], \left[\tau_p \left(\mu_p D^1_{\mathrm{B},1,1} q^1 + P_p\left(\nabla\cdot\boldsymbol{v}^{\frac{1}{2}}\right)\right), \tau_u \left(\mu_u D^1_{\mathrm{B},1,1} \boldsymbol{v}^1 + P_u\left(\nabla q^{\frac{1}{2}}\right)\right)\right] \right.$ $\left. \left\{ \left[\tau_p \left(\mu_p D^1_{\mathrm{B},2,1} q^n + P_p\left(\nabla\cdot\boldsymbol{v}^n\right)\right), \tau_u \left(\mu_u D^1_{\mathrm{B},2,1} \boldsymbol{v}^n + P_u\left(\nabla q^n\right)\right)\right] \right\}_{n=2}^{N} \right\}$ $\|\|\|V\|\|\|^2 := \|\|\|V^N\|\|\|_0^2 + \|\|\|V\|\|\|_B^2 + \tau_p \left\| \mu_p D^1_{\mathrm{B},1,1} q^1 + \nabla\cdot\boldsymbol{v}^{\frac{1}{2}} \right\|^2 \delta t + \tau_u \left\| \mu_u D^1_{\mathrm{B},1,1} \boldsymbol{v}^1 + \nabla q^{\frac{1}{2}} \right\|^2 \delta t$ $+\tau_p \left\| \mu_p D^1_{\mathrm{B},2,1} q^n + \nabla\cdot\boldsymbol{v}^n \right\|^2_{\ell^2(\Upsilon, L^2(\Omega))} + \tau_u \left\| \mu_u D^1_{\mathrm{B},2,1} \boldsymbol{v}^n + \nabla q^n \right\|^2_{\ell^2(\Upsilon, L^2(\Omega))}$ $\|\|\|F\|\|\|_*{}^2 := \|\|\|F\|\|\|_F^2$

Table 4.4: Error functions I: ASGS formulation

Method	$E(h,\delta t)$
BE	$E^2(h,\delta t) := \mu_p\|\varepsilon_p\|^2_{\ell^\infty(L^2)} + \mu_u\|\boldsymbol{\varepsilon}_u\|^2_{\ell^\infty(L^2)} + \tau_p\tau_u\mu_u\|\nabla\cdot\boldsymbol{\varepsilon}_u\|^2_{\ell^\infty(L^2)} + \tau_p\tau_u\mu_p\|\nabla\varepsilon_p\|^2_{\ell^\infty(L^2)}$ $+\frac{1}{\tau_u}\|\boldsymbol{\varepsilon}_u\|^2_{\ell^2(L^2)} + \tau_p\left\|\mu_p D^1_{\mathrm{B},1,1}\varepsilon_p\right\|^2_{\ell^2(L^2)} + \tau_p\|\nabla\cdot\boldsymbol{\varepsilon}_u\|^2_{\ell^2(L^2)} + (1+\sigma)\kappa_p\|\varepsilon_p\|^2_{\ell^2(\Upsilon,L^2(\Gamma_o))}$ $+\frac{1}{\tau_p}\|\varepsilon_p\|^2_{\ell^2(L^2)} + \tau_u\left\|\mu_u D^1_{\mathrm{B},1,1}\boldsymbol{\varepsilon}_u\right\|^2_{\ell^2(L^2)} + \tau_u\|\nabla\varepsilon_p\|^2_{\ell^2(L^2)} + (1-\sigma)\kappa_u\|\boldsymbol{\varepsilon}_u\|^2_{\ell^2(\Upsilon,L^2(\Gamma_o))}$ $+\tau_p\tau_u\mu_u\left\|\mu_p D^1_{\mathrm{B},1,1}\varepsilon_p\right\|^2_{\ell^\infty(L^2)} + \tau_p\tau_u\mu_u\left\|\mu_p D^2_{\mathrm{C},2,1}\varepsilon_p\right\|^2_{\ell^1(L^2)} + \tau_p\tau_u\mu_u\left\|\nabla\cdot D^1_{\mathrm{B},1,1}\boldsymbol{\varepsilon}_u\right\|^2_{\ell^1(L^2)}$ $+\tau_p\tau_u\mu_p\left\|\mu_u D^1_{\mathrm{B},1,1}\boldsymbol{\varepsilon}_u\right\|^2_{\ell^\infty(L^2)} + \tau_p\tau_u\mu_p\left\|\mu_u D^2_{\mathrm{C},2,1}\boldsymbol{\varepsilon}_u\right\|^2_{\ell^1(L^2)} + \tau_p\tau_u\mu_p\left\|\nabla D^1_{\mathrm{B},1,1}\varepsilon_p\right\|^2_{\ell^1(L^2)}$ $+\frac{\delta t^2}{\mu_p}\|\mu_p\partial_{tt}p\|^2_{\ell^1(L^2)} + \delta t^2\tau_p\|\mu_p\partial_{tt}p\|^2_{\ell^2(L^2)} + \tau_p\tau_u\mu_u\delta t^2\left(\|\mu_p\partial_{tt}p\|^2_{\ell^\infty(L^2)} + \|\mu_p\partial_{ttt}p\|^2_{\ell^1(L^2)}\right)$ $+\frac{\delta t^2}{\mu_u}\|\mu_u\partial_{tt}\boldsymbol{u}\|^2_{\ell^1(L^2)} + \delta t^2\tau_u\|\mu_u\partial_{tt}\boldsymbol{u}\|^2_{\ell^2(L^2)} + \tau_p\tau_u\mu_p\delta t^2\left(\|\mu_u\partial_{tt}\boldsymbol{u}\|^2_{\ell^\infty(L^2)} + \|\mu_u\partial_{ttt}\boldsymbol{u}\|^2_{\ell^1(L^2)}\right)$
CN	$E^2(h,\delta t) := \mu_p\|\varepsilon_p\|^2_{\ell^\infty(\Upsilon,L^2(\Omega))} + \mu_u\|\boldsymbol{\varepsilon}_u\|^2_{\ell^\infty(\Upsilon,L^2(\Omega))}$ $+(1+\sigma)\kappa_p\|\varepsilon_p\|^2_{\ell^2(\Upsilon,L^2(\Gamma_o))} + (1-\sigma)\kappa_u\|\boldsymbol{\varepsilon}_u\|^2_{\ell^2(\Upsilon,L^2(\Gamma_o))}$ $+\frac{1}{\tau_u}\|\boldsymbol{\varepsilon}_u\|^2_{\ell^2(L^2)} + \tau_p\left\|\mu_p D^1_{\mathrm{B},1,1}\varepsilon_p\right\|^2_{\ell^2(L^2)} + \tau_p\|\nabla\cdot\boldsymbol{\varepsilon}_u\|^2_{\ell^2(L^2)} + \tau_p\tau_u\mu_u\left\|\nabla\cdot D^1_{\mathrm{B},1,1}\boldsymbol{\varepsilon}_u\right\|^2_{\ell^1(L^2)}$ $+\frac{1}{\tau_p}\|\varepsilon_p\|^2_{\ell^2(L^2)} + \tau_u\left\|\mu_u D^1_{\mathrm{B},1,1}\boldsymbol{\varepsilon}_u\right\|^2_{\ell^2(L^2)} + \tau_u\|\nabla\varepsilon_p\|^2_{\ell^2(L^2)} + \tau_p\tau_u\mu_p\left\|\nabla D^1_{\mathrm{B},1,1}\varepsilon_p\right\|^2_{\ell^1(L^2)}$ $+\tau_p\tau_u\mu_u\left\|\mu_p D^1_{\mathrm{B},1,1}\varepsilon_p\right\|^2_{\ell^\infty(L^2)} + \tau_p\tau_u\mu_u\left\|\mu_p D^2_{\mathrm{C},2,1}\varepsilon_p\right\|^2_{\ell^1(L^2)}$ $+\tau_p\tau_u\mu_p\left\|\mu_u D^1_{\mathrm{B},1,1}\boldsymbol{\varepsilon}_u\right\|^2_{\ell^\infty(L^2)} + \tau_p\tau_u\mu_p\left\|\mu_u D^2_{\mathrm{C},2,1}\boldsymbol{\varepsilon}_u\right\|^2_{\ell^1(L^2)}$ $+\frac{\delta t^4}{\mu_p}\|\mu_p\partial_{ttt}p\|^2_{\ell^1(L^2)} + \delta t^4\tau_p\|\mu_p\partial_{ttt}p\|^2_{\ell^2(L^2)} + \tau_p\tau_u\mu_u\delta t^4\left[\|\mu_p\partial_{ttt}p\|^2_{\ell^\infty(L^2)} + \|\mu_p\partial_{tttt}p\|^2_{\ell^1(L^2)}\right]$ $+\frac{\delta t^4}{\mu_u}\|\mu_u\partial_{ttt}\boldsymbol{u}\|^2_{\ell^1(L^2)} + \delta t^4\tau_u\|\mu_u\partial_{ttt}\boldsymbol{u}\|^2_{\ell^2(L^2)} + \tau_p\tau_u\mu_p\delta t^4\left[\|\mu_u\partial_{ttt}\boldsymbol{u}\|^2_{\ell^\infty(L^2)} + \|\mu_u\partial_{tttt}\boldsymbol{u}\|^2_{\ell^1(L^2)}\right]$
BDF2	$E^2(h,\delta t) := \mu_p\|\varepsilon_p\|^2_{\ell^\infty(L^2)} + \mu_u\|\boldsymbol{\varepsilon}_u\|^2_{\ell^\infty(L^2)}$ $+(1+\sigma)\kappa_p\|\varepsilon_p\|^2_{\ell^2(\Upsilon,L^2(\Gamma_o))} + (1-\sigma)\kappa_u\|\boldsymbol{\varepsilon}_u\|^2_{\ell^2(\Upsilon,L^2(\Gamma_o))}$ $+\frac{1}{\tau_u}\|\boldsymbol{\varepsilon}_u\|^2_{\ell^2(\Upsilon,L^2(\Omega))} + \tau_p\left\|\mu_p D^1_{\mathrm{B},1,1}\varepsilon^1_p\right\|^2\delta t + \tau_p\left\|\mu_p D^1_{\mathrm{B},2,1}\varepsilon_p\right\|^2_{\ell^2(L^2)} + \tau_p\|\nabla\cdot\boldsymbol{\varepsilon}_u\|^2_{\ell^2(L^2)}$ $+\frac{1}{\tau_p}\|\varepsilon_p\|^2_{\ell^2(L^2)} + \tau_u\left\|\mu_u D^1_{\mathrm{B},1,1}\boldsymbol{\varepsilon}^1_u\right\|^2\delta t + \tau_u\left\|\mu_u D^1_{\mathrm{B},2,1}\boldsymbol{\varepsilon}_u\right\|^2_{\ell^2(L^2)} + \tau_u\|\nabla\varepsilon_p\|^2_{\ell^2(\Upsilon,L^2(\Omega))}$ $+\tau_p\tau_u\mu_u\left\|\mu_p D^2_{\mathrm{C},2,\frac{1}{2}}\varepsilon_p^{\frac{1}{2}}\right\|^2\delta t^2 + \tau_p\tau_u\mu_p\left\|\mu_u D^2_{\mathrm{C},2,\frac{1}{2}}\boldsymbol{\varepsilon}_u^{\frac{1}{2}}\right\|^2\delta t^2$ $+\tau_p\tau_u\mu_u\left(\left\|\mu_p D^1_{\mathrm{B},2,1}\varepsilon^2_p\right\|^2 + \left\|\mu_p\left(D^1_{\mathrm{B},2,1}\varepsilon^3_p - 4D^1_{\mathrm{B},2,1}\varepsilon^2_p\right)\right\|^2\right)$ $+\tau_p\tau_u\mu_p\left(\left\|\mu_u D^1_{\mathrm{B},2,1}\boldsymbol{\varepsilon}^2_u\right\|^2 + \left\|\mu_u\left(D^1_{\mathrm{B},2,1}\boldsymbol{\varepsilon}^3_u - 4D^1_{\mathrm{B},2,1}\boldsymbol{\varepsilon}^2_u\right)\right\|^2\right)$ $+\tau_p\tau_u\mu_u\left\|\mu_p(3D^2_{\mathrm{C},4,1} - 2D^2_{\mathrm{C},2,2})\varepsilon^n_p\right\|^2_{\ell^1(L^2)} + \tau_p\tau_u\mu_p\left\|\mu_u(3D^2_{\mathrm{C},4,1} - 2D^2_{\mathrm{C},2,2})\boldsymbol{\varepsilon}^n_u\right\|^2_{\ell^1(L^2)}$ $+\tau_p\tau_u\mu_u\left(\left\|\mu_p D^1_{\mathrm{B},2,1}\varepsilon^N_p\right\|^2 + \left\|\mu_p\left(3D^1_{\mathrm{B},2,1}\varepsilon^{N-1}_p - 4D^1_{\mathrm{B},2,1}\varepsilon^N_p\right)\right\|^2\right)$ $+\tau_p\tau_u\mu_p\left(\left\|\mu_u D^1_{\mathrm{B},2,1}\boldsymbol{\varepsilon}^N_u\right\|^2 + \left\|\mu_u\left(3D^1_{\mathrm{B},2,1}\boldsymbol{\varepsilon}^{N-1}_u - 4D^1_{\mathrm{B},2,1}\boldsymbol{\varepsilon}^N_u\right)\right\|^2\right)$ $+\tau_p\tau_u\mu_u\left(\left\|\nabla\cdot D^1_{\mathrm{B},1,1}\boldsymbol{\varepsilon}^1_u\right\|^2\delta t^2 + \left\|\nabla\cdot D^1_{\mathrm{F},2,1}\boldsymbol{\varepsilon}_u\right\|^2_{\ell^1(L^2)}\right)$ $+\tau_p\tau_u\mu_p\left(\left\|\nabla D^1_{\mathrm{B},1,1}\varepsilon^1_p\right\|^2\delta t^2 + \left\|\nabla D^1_{\mathrm{F},2,1}\varepsilon_p\right\|^2_{\ell^1(L^2)}\right)$ $+\frac{\delta t^4}{\mu_p}\left\|\mu_p\partial_{ttt}p^{\frac{1}{2}}\right\|^2\delta t^2 + \frac{\delta t^4}{\mu_p}\|\mu_p\partial_{ttt}p^n\|^2_{\ell^1(L^2)} + \frac{\delta t^4}{\mu_u}\left\|\mu_u\partial_{ttt}\boldsymbol{u}^{\frac{1}{2}}\right\|^2\delta t^2 + \frac{\delta t^4}{\mu_u}\|\mu_u\partial_{ttt}\boldsymbol{u}^n\|^2_{\ell^1(L^2)}$ $+\delta t^4\tau_p\left\|\mu_p\partial_{ttt}p^{\frac{1}{2}}\right\|^2\delta t + \delta t^4\tau_p\|\mu_p\partial_{ttt}p^n\|^2_{\ell^2(L^2)} + \delta t^4\tau_u\left\|\mu_u\partial_{ttt}\boldsymbol{u}^{\frac{1}{2}}\right\|^2\delta t + \delta t^4\tau_u\|\mu_u\partial_{ttt}\boldsymbol{u}^n\|^2_{\ell^2(L^2)}$ $+\delta t^4\tau_p\tau_u\mu_u\left(\left\|\mu_p\partial_{ttt}p^{\frac{1}{2}}\right\|^2 + \|\mu_p\partial_{tttt}p\|^2_{\ell^1(L^2)} + \|\mu_p\partial_{ttt}p\|^2_{L^\infty(L^2)}\right)$ $+\delta t^4\tau_p\tau_u\mu_p\left(\left\|\mu_u\partial_{ttt}\boldsymbol{u}^{\frac{1}{2}}\right\|^2 + \|\mu_u\partial_{tttt}\boldsymbol{u}\|^2_{\ell^1(L^2)} + \|\mu_u\partial_{ttt}\boldsymbol{u}\|^2_{L^\infty(L^2)}\right)$

Table 4.5: Error functions II: OSS formulation

Method	$E(h,\delta t)$
BE	$E^2(h,\delta t) := \mu_p\|\varepsilon_p\|^2_{\ell^\infty(L^2)} + \frac{1}{\tau_u}\|\boldsymbol{\varepsilon}_u\|^2_{\ell^2(\Upsilon,L^2(\Omega))} + \tau_p\left\|\mu_p D^1_{\mathrm{B},1,1}\varepsilon_p\right\|^2_{\ell^2(L^2)} + \tau_p\|\nabla\cdot\boldsymbol{\varepsilon}_u\|^2_{\ell^2(L^2)}$ $+\mu_u\|\boldsymbol{\varepsilon}_u\|^2_{\ell^\infty(L^2)} + \frac{1}{\tau_p}\|\varepsilon_p\|^2_{\ell^2(L^2)} + \tau_u\left\|\mu_u D^1_{\mathrm{B},1,1}\boldsymbol{\varepsilon}_u\right\|^2_{\ell^2(L^2)} + \tau_u\|\nabla\varepsilon_p\|^2_{\ell^2(L^2)}$ $+(1+\sigma)\kappa_p\|\varepsilon_p\|^2_{\ell^2(\Upsilon,L^2(\Gamma_\circ))} + (1-\sigma)\kappa_u\|\boldsymbol{\varepsilon}_u\|^2_{\ell^2(\Upsilon,L^2(\Gamma_\circ))}$ $+\frac{\delta t^2}{\mu_p}\|\mu_p\partial_{tt}p\|^2_{\ell^1(L^2)} + \frac{\delta t^2}{\mu_u}\|\mu_u\partial_{tt}\boldsymbol{u}\|^2_{\ell^1(L^2)} + \delta t^2\tau_p\|\mu_p\partial_{tt}p\|^2_{\ell^2(L^2)} + \delta t^2\tau_u\|\mu_u\partial_{tt}\boldsymbol{u}\|^2_{\ell^2(L^2)}$
CN	$E^2(h,\delta t) := \mu_p\|\varepsilon_p\|^2_{\ell^\infty(L^2)} + \mu_u\|\boldsymbol{\varepsilon}_u\|^2_{\ell^\infty(L^2)}$ $+(1+\sigma)\kappa_p\|\varepsilon_p\|^2_{\ell^2(\Upsilon,L^2(\Gamma_\circ))} + (1-\sigma)\kappa_u\|\boldsymbol{\varepsilon}_u\|^2_{\ell^2(\Upsilon,L^2(\Gamma_\circ))}$ $+\frac{1}{\tau_u}\|\boldsymbol{\varepsilon}_u\|^2_{\ell^2(L^2)} + \tau_p\left\|\mu_p D^1_{\mathrm{B},1,1}\varepsilon_p\right\|^2_{\ell^2(L^2)} + \tau_p\|\nabla\cdot\boldsymbol{\varepsilon}_u\|^2_{\ell^2(L^2)}$ $+\frac{1}{\tau_p}\|\varepsilon_p\|^2_{\ell^2(L^2)} + \tau_u\left\|\mu_u D^1_{\mathrm{B},1,1}\boldsymbol{\varepsilon}_u\right\|^2_{\ell^2(L^2)} + \tau_u\|\nabla\varepsilon_p\|^2_{\ell^2(L^2)}$ $+\frac{\delta t^4}{\mu_p}\|\mu_p\partial_{ttt}p\|^2_{\ell^1(L^2)} + \delta t^4\tau_p\|\mu_p\partial_{ttt}p\|^2_{\ell^2(L^2)} + \frac{\delta t^4}{\mu_u}\|\mu_u\partial_{ttt}\boldsymbol{u}\|^2_{\ell^1(L^2)} + \delta t^4\tau_u\|\mu_u\partial_{ttt}\boldsymbol{u}\|^2_{\ell^2(L^2)}$
BDF2	$E^2(h,\delta t) := \mu_p\|\varepsilon_p\|^2_{\ell^\infty(L^2)} + \mu_u\|\boldsymbol{\varepsilon}_u\|^2_{\ell^\infty(L^2)} + \frac{1}{\tau_u}\left\|\boldsymbol{\varepsilon}_u^{\frac{1}{2}}\right\|^2\delta t + \frac{1}{\tau_p}\left\|\varepsilon_p^{\frac{1}{2}}\right\|^2\delta t$ $+\frac{1}{\tau_u}\|\boldsymbol{\varepsilon}_u\|^2_{\ell^2(L^2)} + \frac{1}{\tau_p}\|\varepsilon_p\|^2_{\ell^2(L^2)}$ $+(1+\sigma)\kappa_p\|\varepsilon_p\|^2_{\ell^2(\Upsilon,L^2(\Gamma_\circ))} + (1-\sigma)\kappa_u\|\boldsymbol{\varepsilon}_u\|^2_{\ell^2(\Upsilon,L^2(\Gamma_\circ))}$ $+\tau_p\left\|\mu_p D^1_{\mathrm{B},1,1}\varepsilon_p^1\right\|^2\delta t + \tau_p\left\|\nabla\cdot\boldsymbol{\varepsilon}_u^{\frac{1}{2}}\right\|^2\delta t + \tau_p\left\|\mu_p D^1_{\mathrm{B},2,1}\varepsilon_p^n\right\|^2_{\ell^2(L^2)} + \tau_p\|\nabla\cdot\boldsymbol{\varepsilon}_u\|^2_{\ell^2(L^2)}$ $+\tau_u\left\|\mu_u D^1_{\mathrm{B},1,1}\boldsymbol{\varepsilon}_u^1\right\|^2\delta t + \tau_u\left\|\nabla\varepsilon_p^{\frac{1}{2}}\right\|^2\delta t + \tau_u\left\|\mu_u D^1_{\mathrm{B},2,1}\boldsymbol{\varepsilon}_u^n\right\|^2_{\ell^2(L^2)} + \tau_u\|\nabla\varepsilon_p\|^2_{\ell^2(L^2)}$ $+\frac{\delta t^4}{\mu_p}\left\|\mu_p\partial_{ttt}p^{\frac{1}{2}}\right\|^2\delta t^2 + \frac{\delta t^4}{\mu_p}\|\mu_p\partial_{ttt}p^n\|^2_{\ell^1(L^2)} + \frac{\delta t^4}{\mu_u}\left\|\mu_p\partial_{ttt}\boldsymbol{u}^{\frac{1}{2}}\right\|^2\delta t^2 + \frac{\delta t^4}{\mu_u}\|\mu_u\partial_{ttt}\boldsymbol{u}^n\|^2_{\ell^1(L^2)}$ $+\delta t^4\left(\tau_p\left\|\mu_p\partial_{ttt}p^{\frac{1}{2}}\right\|^2\delta t + \tau_p\|\mu_p\partial_{ttt}p^n\|^2_{\ell^2(L^2)} + \tau_u\left\|\mu_u\partial_{ttt}\boldsymbol{u}^{\frac{1}{2}}\right\|^2\delta t + \tau_u\|\mu_u\partial_{ttt}\boldsymbol{u}^n\|^2_{\ell^2(L^2)}\right)$

The 5th term is bounded as

$$\sum_{n=1}^{N}\delta t\left[(\nabla\cdot\boldsymbol{v}^n,q^n)+(\nabla q^n,\boldsymbol{v}^n)\right]\geq|||V|||_B^2. \tag{4.37}$$

The 6th and 7th terms are already what we need. The 8th and 9th terms are greater than zero by boundary conditions. Combining (4.35)-(4.37) the proof is completed.

Proof of stability (4.31)

Recalling the Λ-coercivity result we can write

$$|||U_h|||^2\lesssim\mathcal{B}_h(U_h,\Lambda(U_h))=\mathcal{L}_h(\Lambda(U_h), \tag{4.38}$$

and using the definition of $\mathcal{L}_h$ we can write

$$|||U_h|||^2\lesssim\sum_{n=1}^{N}\delta t\left({f_p}^n,p_h^n+\tau_p\left(\mu_p D^1_{\mathrm{B},1,1}p_h^n+\nabla\cdot\boldsymbol{u}_h^n\right)\right)+\sum_{n=1}^{N}\delta t\left({f_p}^n,\tau_p\nabla\cdot\tau_u\mu_u D^1_{\mathrm{B},1,1}\boldsymbol{u}_h^n\right)$$

$$+\sum_{n=1}^{N}\delta t\left(\boldsymbol{f}_u{}^n,\boldsymbol{u}_h^n+\tau_u\left(\mu_u D^1_{\mathrm{B},1,1}\boldsymbol{u}_h^n+\nabla p_h^n\right)\right)+\sum_{n=1}^{N}\delta t\left(\boldsymbol{f}_u{}^n,\tau_u\nabla\tau_p\mu_p D^1_{\mathrm{B},1,1}p_h^n\right). \tag{4.39}$$

The 1st and 3rd terms can be bounded as

$$\begin{aligned}&\sum_{n=1}^{N}\delta t\left(f_p{}^n,p_h^n+\tau_p\left(\mu_p D^1_{\mathrm{B},1,1}p_h^n+\nabla\cdot\boldsymbol{u}_h^n\right)\right)\\&\quad+\sum_{n=1}^{N}\delta t\left(\boldsymbol{f}_u{}^n,\boldsymbol{u}_h^n+\tau_u\left(\mu_u D^1_{\mathrm{B},1,1}\boldsymbol{u}_h^n+\nabla p_h^n\right)\right)\lesssim\alpha_1|||F|||_F^2+\frac{1}{\alpha_1}|||U_h|||^2,\end{aligned} \tag{4.40}$$

where here and in what follows $\alpha_i>0$ are reals appearing from Young's inequality. The 2nd and 4th terms are bounded in a similar manner and we just show how we bound the 2nd term:

$$\begin{aligned}&\sum_{n=1}^{N}\delta t\left(f_p{}^n,\tau_p\nabla\cdot\tau_u\mu_u D^1_{\mathrm{B},1,1}\boldsymbol{u}_h^n\right)\\&\quad=-\sum_{n=1}^{N}\delta t\left(D^1_{\mathrm{B},1,1}f_p{}^n,\tau_p\tau_u\mu_u\nabla\cdot\boldsymbol{u}_h^{n-1}\right)+\left(f_p{}^N,\tau_p\tau_u\mu_u\nabla\cdot\boldsymbol{u}_h^N\right)\\&\quad\lesssim\alpha_2\tau_p\tau_u\mu_u\left\|D^1_{\mathrm{B},1,1}f_p\right\|^2_{\ell^1(\Upsilon,L^2(\Omega))}+\alpha_3\tau_p\tau_u\mu_u\|f_p\|^2_{\ell^\infty(\Upsilon,L^2(\Omega))}\\&\qquad+\frac{1}{\alpha_2}\tau_p\tau_u\mu_u\|\nabla\cdot\boldsymbol{u}_h\|^2_{\ell^\infty(\Upsilon,L^2(\Omega))}+\frac{1}{\alpha_3}\tau_p\tau_u\mu_u\|\nabla\cdot\boldsymbol{u}_h\|^2_{\ell^\infty(\Upsilon,L^2(\Omega))}.\end{aligned} \tag{4.41}$$

Combining (4.38)-(4.41) and taking α_i large enough the proof is complete.

Proof of convergence (4.32)

Combining Λ-coercivity with $V=e$ and (4.34) we can arrive to

$$|||e|||^2\lesssim\mathcal{B}_h(e,\Lambda(e))=\mathcal{B}_h(\varepsilon,\Lambda(e))+\mathcal{C}(U,\Lambda(e)).$$

The aim is to bound e in terms of ε and U. We first analyze the term containing $\mathcal{B}_h$ and then the term associated to the consistency error (4.33):

$$\begin{aligned}\mathcal{B}_h(\varepsilon,\Lambda(e))=&\sum_{n=1}^{N}\delta t\left(\mu_p D^1_{\mathrm{B},1,1}\varepsilon_p^n+\nabla\cdot\boldsymbol{\varepsilon}_u^n,e_p^n+\tau_p\left(\mu_p D^1_{\mathrm{B},1,1}e_p^n+\nabla\cdot\boldsymbol{e}_u^n\right)+\tau_p\tau_u\mu_u\nabla\cdot D^1_{\mathrm{B},1,1}\boldsymbol{e}_u^n\right)\\&+\sum_{n=1}^{N}\delta t\left(\mu_u D^1_{\mathrm{B},1,1}\boldsymbol{\varepsilon}_u^n+\nabla\varepsilon_p^n,\boldsymbol{e}_u^n+\tau_u\left(\mu_u D^1_{\mathrm{B},1,1}\boldsymbol{e}_u^n+\nabla e_p^n\right)+\tau_p\tau_u\mu_p\nabla D^1_{\mathrm{B},1,1}e_p^n\right)\\\leq&\sum_{n=1}^{N}\delta t\left[\frac{\alpha_1}{2\tau_p}\left\|\varepsilon_p^n\right\|^2+\frac{\tau_p}{2\alpha_1}\left\|\mu_p D^1_{\mathrm{B},1,1}e_p^n+\nabla\cdot\boldsymbol{e}_u^n\right\|^2\right]\\&+\sum_{n=1}^{N}\delta t\left[\frac{\alpha_2}{2\tau_u}\|\boldsymbol{\varepsilon}_u^n\|^2+\frac{\tau_u}{2\alpha_2}\left\|\mu_u D^1_{\mathrm{B},1,1}\boldsymbol{e}_u^n+\nabla e_p^n\right\|^2\right]\end{aligned}$$

$$
\begin{aligned}
&+\sum_{n=1}^{N}\delta t\tau_p\left[\frac{\alpha_3}{2}\left\|\mu_p D^1_{\mathrm{B},1,1}\varepsilon_p^n+\nabla\cdot\boldsymbol{\varepsilon}_u^n\right\|^2+\frac{1}{2\alpha_3}\left\|\mu_p D^1_{\mathrm{B},1,1}e_p^n+\nabla\cdot\boldsymbol{e}_u^n\right\|^2\right]\\
&+\sum_{n=1}^{N}\delta t\tau_u\left[\frac{\alpha_4}{2}\left\|\mu_u D^1_{\mathrm{B},1,1}\boldsymbol{\varepsilon}_u^n+\nabla\varepsilon_p^n\right\|^2+\frac{1}{2\alpha_4}\left\|\mu_u D^1_{\mathrm{B},1,1}\boldsymbol{e}_u^n+\nabla e_p^n\right\|^2\right]\\
&+\sum_{n=1}^{N}\delta t\left(\mu_p D^1_{\mathrm{B},1,1}\varepsilon_p^n+\nabla\cdot\boldsymbol{\varepsilon}_u^n,\tau_p\tau_u\mu_u\nabla\cdot D^1_{\mathrm{B},1,1}\boldsymbol{e}_u^n\right)\\
&+\sum_{n=1}^{N}\delta t\left(\mu_u D^1_{\mathrm{B},1,1}\boldsymbol{\varepsilon}_u^n+\nabla\varepsilon_p^{n+1},\tau_p\tau_u\mu_p\nabla D^1_{\mathrm{B},1,1}e_p^n\right).
\end{aligned}
$$

The only terms missing to bound are the last two ones. Both are bound similarly and we will only show how the first one is bounded. The first part is bounded as

$$
\begin{aligned}
&\sum_{n=1}^{N}\delta t\left(\mu_p D^1_{\mathrm{B},1,1}\varepsilon_p^n,\tau_p\tau_u\mu_u\nabla\cdot D^1_{\mathrm{B},1,1}\boldsymbol{e}_u^n\right)\\
&\quad=\tau_p\tau_u\mu_u\left[\left(\mu_p D^1_{\mathrm{B},1,1}\varepsilon_p^N,\nabla\cdot\boldsymbol{e}_u^N\right)-\left(\mu_p D^1_{\mathrm{B},1,1}\varepsilon_p^1,\nabla\cdot\boldsymbol{e}_u^0\right)\right]-\sum_{n=1}^{N-1}\delta t\tau_p\tau_u\mu_u\left(\mu_p D^2_{\mathrm{C},2,1}\varepsilon_p^n,\nabla\cdot\boldsymbol{e}_u^n\right)\\
&\quad\le\tau_p\tau_u\mu_u\left[\frac{\alpha_5}{2}\left\|\mu_p D^1_{\mathrm{B},1,1}\varepsilon_p^N\right\|^2+\frac{1}{2\alpha_5}\left\|\nabla\cdot\boldsymbol{e}_u^N\right\|^2\right]\\
&\qquad+\tau_p\tau_u\mu_u\left[\frac{\alpha_6}{2}\left\|\mu_p D^2_{\mathrm{C},2,1}\varepsilon_p\right\|^2_{\ell^1(L^2)}+\frac{1}{2\alpha_6}\|\nabla\cdot\boldsymbol{e}_u\|^2_{\ell^\infty(L^2)}\right],
\end{aligned}
$$

and the second part is bounded as

$$
\begin{aligned}
&\sum_{n=1}^{N}\delta t\left(\nabla\cdot\boldsymbol{\varepsilon}_u^n,\tau_p\tau_u\mu_u\nabla\cdot D^1_{\mathrm{B},1,1}\boldsymbol{e}_u^n\right)\\
&\quad=\tau_p\tau_u\mu_u\left[\left(\nabla\cdot\boldsymbol{\varepsilon}_u^N,\nabla\cdot\boldsymbol{e}_u^N\right)-\left(\nabla\cdot\boldsymbol{\varepsilon}_u^0,\nabla\cdot\boldsymbol{e}_u^0\right)\right]-\sum_{n=1}^{N}\delta t\left(\nabla\cdot D^1_{\mathrm{B},1,1}\boldsymbol{\varepsilon}_u^n,\tau_p\tau_u\mu_u\nabla\cdot\boldsymbol{e}_u^n\right)\\
&\quad\le\tau_p\tau_u\mu_u\left[\frac{\alpha_7}{2}\left\|\nabla\cdot\boldsymbol{\varepsilon}_u^N\right\|^2+\frac{1}{2\alpha_7}\left\|\nabla\cdot\boldsymbol{e}_u^N\right\|^2+\frac{\alpha_8}{2}\left\|\nabla\cdot D^1_{\mathrm{B},1,1}\boldsymbol{\varepsilon}_u\right\|^2_{\ell^1(L^2)}+\frac{1}{2\alpha_8}\|\nabla\cdot\boldsymbol{e}_u\|^2_{\ell^\infty(L^2)}\right].
\end{aligned}
$$

This completes the bounding of $\mathcal{B}_h$. Now let us bound the consistency error (4.33):

$$
\begin{aligned}
\mathcal{C}(U,&\Lambda(e))=\mathcal{L}_h(\Lambda(e))-\mathcal{B}_h(U,\Lambda(e))\\
&=-\sum_{n=1}^{N}\delta t\left(\mu_p D^1_{\mathrm{B},1,1}p^n+\nabla\cdot\boldsymbol{u}^n,e_p^n+\tau_p\left(\mu_p D^1_{\mathrm{B},1,1}e_p^n+\nabla\cdot\boldsymbol{e}_u^n\right)+\tau_p\tau_u\mu_u\nabla\cdot D^1_{\mathrm{B},1,1}\boldsymbol{e}_u^n\right)\\
&\quad-\sum_{n=1}^{N}\delta t\left(\mu_u D^1_{\mathrm{B},1,1}\boldsymbol{u}^n+\nabla p^n,\boldsymbol{e}_u^n+\tau_u\left(\mu_u D^1_{\mathrm{B},1,1}\boldsymbol{e}_u^n+\nabla e_p^n\right),+\tau_p\tau_u\mu_p\nabla D^1_{\mathrm{B},1,1}e_p^n\right).
\end{aligned}
$$

Both terms are bounded similarly and we only show how it is bounded the first one. Let us start with its first part

$$\begin{aligned}
-\sum_{n=1}^{N}\delta t\left(\mu_p D^1_{\mathrm{B},1,1}p^n+\nabla\cdot\boldsymbol{u}^n,e_p^n\right)\leq&\frac{\alpha_9}{2}\frac{\delta t^2}{\mu_p}\left[\sum_{n=1}^{N}\left\|\mu_p D^1_{\mathrm{B},1,1}p^n+\nabla\cdot\boldsymbol{u}^n\right\|\right]^2+\frac{1}{2\alpha_9}\mu_p\|e_p\|^2_{\ell^\infty(L^2)}\\
\leq&\frac{\alpha_9}{2}\frac{\delta t^2}{\mu_p}\left[\sum_{n=1}^{N}\left\|\mu_p D^1_{\mathrm{B},1,1}p^n-\mu_p\partial_t p^n\right\|\right]^2+\frac{1}{2\alpha_9}\mu_p\|e_p\|^2_{\ell^\infty(L^2)}\\
\leq&\frac{\alpha_9}{2}\frac{\delta t^2}{\mu_p}\|\mu_p\partial_{tt}p^n\|^2_{\ell^1(L^2)}+\frac{1}{2\alpha_9}\mu_p\|e_p\|^2_{\ell^\infty(L^2)}.
\end{aligned}$$

The second part can be bounded as

$$\begin{aligned}
&-\sum_{n=1}^{N}\delta t\left(\mu_p D^1_{\mathrm{B},1,1}p^n+\nabla\cdot\boldsymbol{u}^n,\tau_p\left(\mu_p D^1_{\mathrm{B},1,1}e_p^n+\nabla\cdot\boldsymbol{e}_u^n\right)\right)\\
&\quad\leq\frac{\alpha_{10}}{2}\sum_{n=1}^{N}\delta t\tau_p\left\|\mu_p D^1_{\mathrm{B},1,1}p^n-\mu_p\partial_t p^n\right\|^2+\frac{1}{2\alpha_{10}}\sum_{n=1}^{N}\delta t\tau_p\left\|\mu_p D^1_{\mathrm{B},1,1}e_p^n+\nabla\cdot\boldsymbol{e}_u^n\right\|^2\\
&\quad\leq\frac{\alpha_{10}}{2}\delta t^2\tau_p\|\mu_p\partial_{tt}p^n\|^2_{\ell^2(\Upsilon,L^2(\Omega))}+\frac{1}{2\alpha_{10}}\tau_p\left\|\mu_p D^1_{\mathrm{B},1,1}e_p^n+\nabla\cdot\boldsymbol{e}_u^n\right\|^2_{\ell^2(\Upsilon,L^2(\Omega))}.
\end{aligned}$$

The third part can be bounded as

$$\begin{aligned}
&-\sum_{n=1}^{N}\delta t\left(\mu_p D^1_{\mathrm{B},1,1}p^n+\nabla\cdot\boldsymbol{u}^n,\tau_p\tau_u\mu_u\nabla\cdot D^1_{\mathrm{B},1,1}\boldsymbol{e}_u^n\right)\\
&\quad=\tau_p\tau_u\mu_u\left[\left(\mu_p D^1_{\mathrm{B},1,1}p^N+\nabla\cdot\boldsymbol{u}^N,\nabla\cdot\boldsymbol{e}_u^N\right)-\left(\mu_p D^1_{\mathrm{B},1,1}p^1+\nabla\cdot\boldsymbol{u}^0,\nabla\cdot\boldsymbol{e}_u^0\right)\right]\\
&\qquad-\tau_p\tau_u\mu_u\left[\sum_{n=1}^{N-1}\delta t\left(\mu_p D^2_{\mathrm{C},2,1}p^n+\nabla\cdot D^1_{\mathrm{B},1,1}\boldsymbol{u}^n,\nabla\cdot\boldsymbol{e}_u^n\right)+\delta t\left(\nabla\cdot D^1_{\mathrm{B},1,1}\boldsymbol{u}^1,\nabla\cdot\boldsymbol{e}_u^0\right)\right]\\
&\quad\leq\tau_p\tau_u\mu_u\left[\frac{\alpha_{11}}{2}\left\|\mu_p D^1_{\mathrm{B},1,1}p^N+\nabla\cdot\boldsymbol{u}^N\right\|^2+\frac{1}{2\alpha_{11}}\left\|\nabla\cdot\boldsymbol{e}_u^N\right\|^2\right]\\
&\qquad+\tau_p\tau_u\mu_u\frac{\alpha_{12}}{2}\left[\sum_{n=1}^{N-1}\delta t\left\|\mu_p D^2_{\mathrm{C},2,1}p^n+\nabla\cdot D^1_{\mathrm{B},1,1}\boldsymbol{u}^n\right\|\right]^2+\tau_p\tau_u\mu_u\frac{1}{2\alpha_{12}}\|\nabla\cdot\boldsymbol{e}_u\|^2\\
&\quad\leq\tau_p\tau_u\mu_u\left[\frac{\alpha_{11}}{2}\delta t^2\left\|\mu_p\partial_{tt}p^N\right\|^2+\frac{1}{2\alpha_{11}}\left\|\nabla\cdot\boldsymbol{e}_u^N\right\|^2\right]\\
&\qquad+\tau_p\tau_u\mu_u\left[\frac{\alpha_{12}}{2}\delta t^2\|\mu_p\partial_{ttt}p\|^2_{\ell^1(\Upsilon,L^2(\Omega))}+\frac{1}{2\alpha_{12}}\|\nabla\cdot\boldsymbol{e}_u\|^2_{\ell^\infty(\Upsilon,L^2(\Omega))}\right].
\end{aligned}$$

Combining all bounds the proof is complete.

4.3.5 Accuracy of the fully discrete methods

Let k be the order of p-interpolation and l the order of $\boldsymbol{u}$-interpolation. Analyzing the a priori error estimates (4.32) for the fully discrete methods with the error functions

Table 4.6: Convergence rates for ASGS-BE and OSS-BE according to variational form

Variational Form	I	II	III
$\left\|\xi_p^n\right\|_{\ell^\infty(L^2)}$, $\|\boldsymbol{\xi}_u^n\|_{\ell^\infty(L^2)}$	$h^{k+\frac{1}{2}} + h^{l+\frac{1}{2}} + \delta t + h^{\frac{1}{2}}\delta t$	$h^{k+\frac{1}{2}} + h^l + \delta t$	$h^k + h^{l+\frac{1}{2}} + \delta t$
$\left\|\mu_u D^1_{\mathrm{B},1,1}\boldsymbol{\xi}_u^n + \nabla\xi_p^n\right\|_{\ell^2(L^2)}$	$h^k + h^l + h^{-\frac{1}{2}}\delta t + \delta t$	$h^{k-\frac{1}{2}} + h^{l-1} + h^{-1}\delta t$	$h^k + h^{l+\frac{1}{2}} + \delta t$
$\left\|\mu_p D^1_{\mathrm{B},1,1}\xi_p^n + \nabla\cdot\boldsymbol{\xi}_u^n\right\|_{\ell^2(L^2)}$	$h^k + h^l + h^{-\frac{1}{2}}\delta t + \delta t$	$h^{k+\frac{1}{2}} + h^l + \delta t$	$h^{k-1} + h^{l-\frac{1}{2}} + h^{-1}\delta t$
Best k, l, h-δt	$k = l$, $\delta t \sim h^{k+\frac{1}{2}}$	$k + \frac{1}{2} = l$, $\delta t \sim h^l$ $k = l$, $\delta t \sim h^l$ $k + 1 = l$, $\delta t \sim h^{l-\frac{1}{2}}$	$k = l + \frac{1}{2}$, $\delta t \sim h^k$ $k = l$, $\delta t \sim h^k$ $k = l + 1$, $\delta t \sim h^{k-\frac{1}{2}}$

Table 4.7: Convergence rates for ASGS-CN and OSS-CN according to variational form

Variational Form	I	II	III
$\left\|\xi_p^n\right\|_{\ell^\infty(L^2)}$, $\|\boldsymbol{\xi}_u^n\|_{\ell^\infty(L^2)}$	$h^{k+\frac{1}{2}} + h^{l+\frac{1}{2}} + \delta t^2 + h^{\frac{1}{2}}\delta t^2$	$h^{k+\frac{1}{2}} + h^l + \delta t^2$	$h^k + h^{l+\frac{1}{2}} + \delta t^2$
$\left\|\mu_u D^1_{\mathrm{B},1,1}\boldsymbol{\xi}_u^n + \nabla\xi_p^{n-\frac{1}{2}}\right\|_{\ell^2(L^2)}$	$h^k + h^l + h^{-\frac{1}{2}}\delta t^2 + \delta t^2$	$h^{k-\frac{1}{2}} + h^{l-1} + h^{-1}\delta t^2$	$h^k + h^{l+\frac{1}{2}} + \delta t^2$
$\left\|\mu_p D^1_{\mathrm{B},1,1}\xi_p^n + \nabla\cdot\boldsymbol{\xi}_u^{n-\frac{1}{2}}\right\|_{\ell^2(L^2)}$	$h^k + h^l + h^{-\frac{1}{2}}\delta t^2 + \delta t^2$	$h^{k+\frac{1}{2}} + h^l + \delta t^2$	$h^{k-1} + h^{l-\frac{1}{2}} + h^{-1}\delta t^2$
Best k, l, h-δt	$k = l$, $\delta t^2 \sim h^{k+\frac{1}{2}}$	$k + \frac{1}{2} = l$, $\delta t^2 \sim h^l$ $k = l$, $\delta t^2 \sim h^l$ $k + 1 = l$, $\delta t^2 \sim h^{l-\frac{1}{2}}$	$k = l + \frac{1}{2}$, $\delta t^2 \sim h^k$ $k = l$, $\delta t^2 \sim h^k$ $k = l + 1$, $\delta t^2 \sim h^{k-\frac{1}{2}}$

given in Tables 4.4 and 4.5 and assuming regular enough solutions, we can summarize the convergence rates as shown in Tables 4.6-4.8. We stress the fact that the convergence rates do depend on the choice of the stabilization parameters, and different convergence orders are obtained for the three discrete variational formulations above. Let us note that the time discretization schemes do not spoil the spatial convergence rates obtained in [67, 68] for the time-continuous case.

Table 4.8: Convergence rates for ASGS-BDF2 and OSS-BDF2 according to variational form

Variational Form	I	II	III
$\left\|\xi_p^n\right\|_{\ell^\infty(L^2)}$, $\|\boldsymbol{\xi}_u^n\|_{\ell^\infty(L^2)}$	$h^{k+\frac{1}{2}} + h^{l+\frac{1}{2}} + \delta t^2$	$h^{k+\frac{1}{2}} + h^l + \delta t^2$	$h^k + h^{l+\frac{1}{2}} + \delta t^2$
$\left\|\mu_u D^1_{\mathrm{B},2,1}\boldsymbol{\xi}_u^n + \nabla\xi_p^n\right\|_{\ell^2(L^2)}$	$h^k + h^l + h^{-\frac{1}{2}}\delta t^2$	$h^{k-\frac{1}{2}} + h^{l-1} + h^{-1}\delta t^2$	$h^k + h^{l+\frac{1}{2}} + \delta t^2$
$\left\|\mu_p D^1_{\mathrm{B},2,1}\xi_p^n + \nabla\cdot\boldsymbol{\xi}_u^n\right\|_{\ell^2(L^2)}$	$h^k + h^l + h^{-\frac{1}{2}}\delta t^2$	$h^{k+\frac{1}{2}} + h^l + \delta t^2$	$h^{k-1} + h^{l-\frac{1}{2}} + h^{-1}\delta t^2$
Best k, l, h-δt	$k = l$, $\delta t^2 \sim h^{k+\frac{1}{2}}$	$k + \frac{1}{2} = l$, $\delta t^2 \sim h^l$ $k = l$, $\delta t^2 \sim h^l$ $k + 1 = l$, $\delta t^2 \sim h^{l-\frac{1}{2}}$	$k = l + \frac{1}{2}$, $\delta t^2 \sim h^k$ $k = l$, $\delta t^2 \sim h^k$ $k = l + 1$, $\delta t^2 \sim h^{k-\frac{1}{2}}$

4.4 Fourier analysis

We show now the results of a Fourier analysis (or von Neumann analysis) in 1D using linear (P1) elements, which serves to study dispersion, dissipation, and stability of the numerical schemes. The analysis is done in an unbounded domain with no forcing terms, but with non-zero initial conditions. The mesh is taken uniform, of size h, and the time step is δt. We focus on variational form I because it has the best convergence properties, as shown in the previous analysis.

Let us consider a solution of the form $p = C_p \mathrm{e}^{\mathrm{i}(kx-\omega t)}$ and $u = C_p \mu_p^{1/2} \mu_u^{-1/2} \mathrm{e}^{\mathrm{i}(kx-\omega t)}$, where C_p is an arbitrary constant such that $[p] = [C_p]$, $[\cdot]$ standing for dimensional group, ω is the angular frequency (temporal frequency) and k is the (angular) wavenumber (spatial frequency). It can be checked that this plane wave is solution of the wave equation in mixed form. The angular frequency and wavenumber are related through the wave speed as $\omega = kc$.

For 1D P1 elements of size $\mathrm{diam}K = h$ we will need the following element matrices:

$$\int_K N_i N_j \Big|_{i,j=1,2} = \frac{h}{6}\begin{pmatrix} 2 & 1 \\ 1 & 2 \end{pmatrix}, \quad \int_K N_i \partial_x N_j \Big|_{i,j=1,2} = \frac{1}{2}\begin{pmatrix} -1 & 1 \\ -1 & 1 \end{pmatrix},$$
$$\int_K \partial_x N_i N_j \Big|_{i,j=1,2} = \frac{1}{2}\begin{pmatrix} -1 & -1 \\ 1 & 1 \end{pmatrix}, \quad \int_K \partial_x N_i \partial_x N_j \Big|_{i,j=1,2} = \frac{1}{h}\begin{pmatrix} 1 & -1 \\ -1 & 1 \end{pmatrix},$$

where N_i is the shape function of node i (in element K). When assembled for just two elements sharing a generic node they give, respectively,

$$M_p = M_u = \frac{h}{6}\begin{pmatrix} 2 & 1 & 0 \\ 1 & 4 & 1 \\ 0 & 2 & 1 \end{pmatrix}, \quad K_p = K_u = \frac{1}{2}\begin{pmatrix} -1 & 1 & 0 \\ -1 & 0 & 1 \\ 0 & -1 & 1 \end{pmatrix},$$
$$M_{S,p} = M_{S,u} = \frac{1}{2}\begin{pmatrix} -1 & -1 & 0 \\ 1 & 0 & -1 \\ 0 & 1 & 1 \end{pmatrix}, \quad K_{S,p} = K_{S,u} = \frac{1}{h}\begin{pmatrix} 1 & -1 & 0 \\ -1 & 2 & -1 \\ 0 & -1 & 1 \end{pmatrix}.$$

Additionally, we define the lumped mass matrices

$$\widetilde{M}_p = \widetilde{M}_u = \frac{h}{2}\begin{pmatrix} 1 & 0 & 0 \\ 0 & 2 & 0 \\ 0 & 0 & 1 \end{pmatrix}.$$

First we will analyze the time semi-discretization, then the space semi-discretization and finally the full discretization. The time discretizations to be considered are the θ and BDF2 methods, whereas the space discretizations to be analyzed are stabilized FE methods (ASGS and OSS). We will often take $t_n = n\delta t$ and $x_j = jh$, where n is the time step and j is the mesh point.

4.4.1 Time semi-discretization

Let us start considering the effect of the time discretization only, without discretizing in space. Let us take $\omega_{\delta t} = k_{\delta t} c_{\delta t}$ and $k_{\delta t} = k$, where the subscript δt denotes temporal

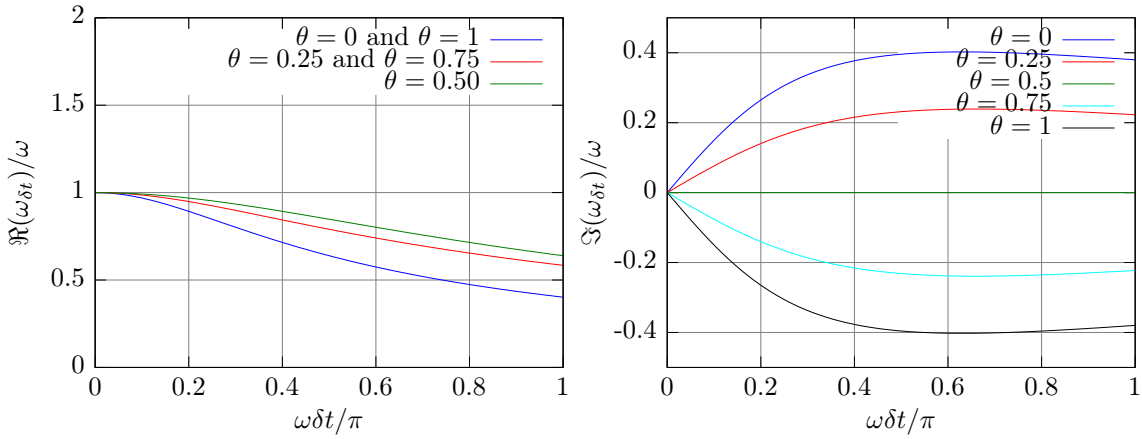

Figure 4.1: θ-method time semi-discretization

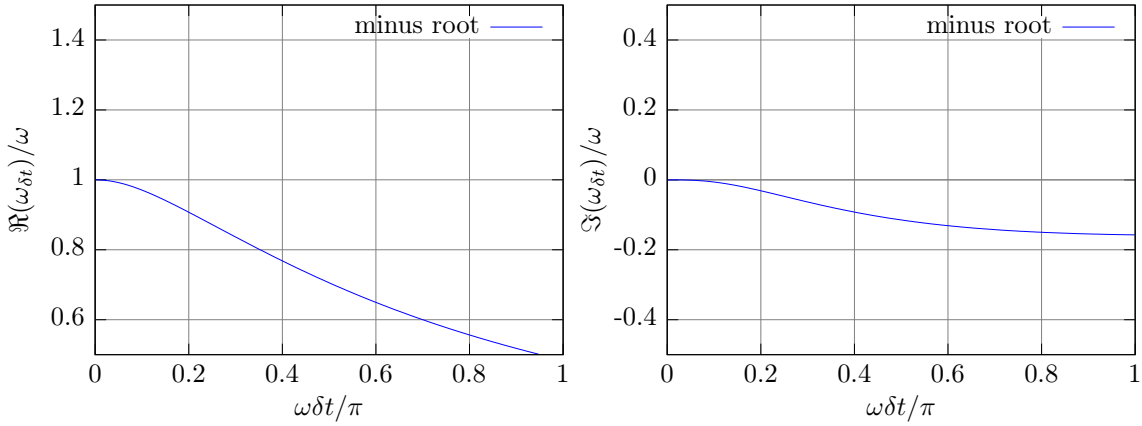

Figure 4.2: BDF2 time semi-discretization

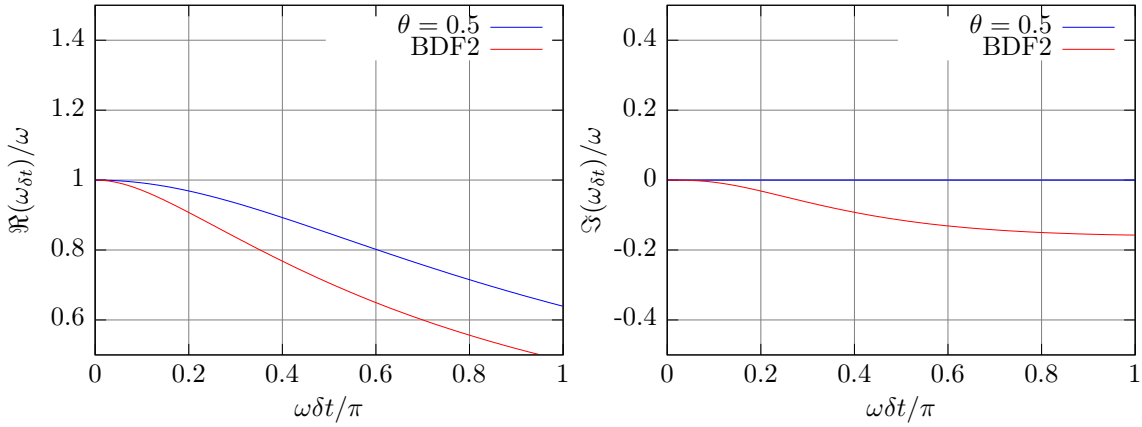

Figure 4.3: Time semi-discretization comparison

semi-discretization. We take a solution (mode) of the form

$$[P^n(x), U^n(x)] = \phi_k \mathrm{e}^{\mathrm{i}(kx-\omega_{\delta t} t_n)} \left[1, \mu_p^{1/2}\mu_u^{-1/2}\right], \tag{4.42}$$

where ϕ_k is a constant that describes the amplitude at $t_n = 0$.

The semi-discrete problem using the θ method is as follows:

$$\begin{aligned}
\frac{\mu_p}{\delta t}(P^{n+1} - P^n) + \theta \frac{\mathrm{d}}{\mathrm{d}x} U^{n+1} + (1-\theta)\frac{\mathrm{d}}{\mathrm{d}x} U^n = 0, \\
\frac{\mu_u}{\delta t}(U^{n+1} - U^n) + \theta \frac{\mathrm{d}}{\mathrm{d}x} P^{n+1} + (1-\theta)\frac{\mathrm{d}}{\mathrm{d}x} P^n = 0,
\end{aligned}$$

where $0 \leq \theta \leq 1$ is a parameter. The backward Euler method corresponds to $\theta = 1$, the forward Euler method to $\theta = 0$ and the trapezoidal rule to $\theta = 0.5$. Replacing $[P^n, U^n]$ from (4.42) we have:

$$\begin{aligned}
\frac{\mu_p}{\delta t}\left(\mathrm{e}^{-\mathrm{i}\omega_{\delta t}\delta t} - 1\right) + \mu_p^{1/2}\mu_u^{-1/2}\left(\mathrm{i}k\theta \mathrm{e}^{-\mathrm{i}\omega_{\delta t}\delta t} + \mathrm{i}k(1-\theta)\right) = 0, \\
\frac{\mu_u}{\delta t}\mu_p^{1/2}\mu_u^{-1/2}\left(\mathrm{e}^{-\mathrm{i}\omega_{\delta t}\delta t} - 1\right) + \mathrm{i}k\theta \mathrm{e}^{-\mathrm{i}\omega_{\delta t}\delta t} + \mathrm{i}k(1-\theta) = 0.
\end{aligned}$$

Both equations are equivalent, so we just analyze one of them. We have that

$$\omega_{\delta t}\delta t = \frac{-1}{\mathrm{i}} \log\left(\frac{1 - (1-\theta)\mathrm{i}\omega\delta t}{1 + \mathrm{i}\omega\delta t\theta}\right).$$

The numerical angular frequency, $\omega_{\delta t}$, is not always real, it is complex for $\theta \neq 0.5$. It can be shown that the angular frequency error is 2nd order in $\omega\delta t$ for $\theta = 0.5$ and only 1st order in $\omega\delta t$ for $\theta \neq 0.5$. Fig. 4.1 shows the angular frequency ratio $\omega_{\delta t}/\omega$ for $0 \leq \omega\delta t/\pi \leq 1$. It can be seen that the θ-method is unconditionally stable for $\theta \geq 0.5$.

On the other hand, the semi-discrete problem using BDF2 is:

$$\begin{aligned}
\frac{\mu_p}{2\delta t}(3P^{n+1} - 4P^n + P^{n-1}) + \frac{\mathrm{d}}{\mathrm{d}x} U^{n+1} = 0, \\
\frac{\mu_u}{2\delta t}(3U^{n+1} - 4U^n + U^{n-1}) + \frac{\mathrm{d}}{\mathrm{d}x} P^{n+1} = 0.
\end{aligned}$$

Following a similar procedure as for the θ method we arrive to

$$\omega_{\delta t}\delta t = \frac{1}{\mathrm{i}} \log(2 \pm \sqrt{1 - 2\mathrm{i}\omega\delta t}).$$

The numerical angular frequency is complex. The root corresponding to $+\sqrt{}$ is spurious, hence we just plot the root corresponding to $-\sqrt{}$. It can be shown that the angular frequency error is 2nd order in $\omega\delta t$. Fig. 4.2 shows the angular frequency ratio $\omega_{\delta t}/\omega$ for $0 \leq \omega\delta t/\pi \leq 1$. It can be seen that the BDF2 method is unconditionally stable.

Now, let us compare the θ-method with $\theta = 1/2$ and BDF2. Fig. 4.3 compares both methods. It can be seen that the θ-method with $\theta = 1/2$ outperforms BDF2 for the wave equation in mixed form both in terms of dispersion and dissipation.

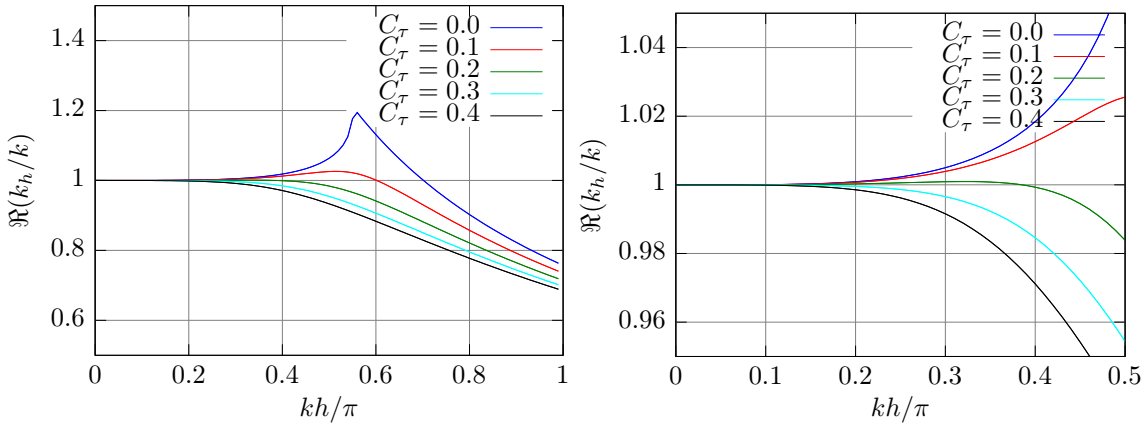

Figure 4.4: ASGS space semi-discretization: real part of the wavenumber ratio (the right picture is a zoom of the left)

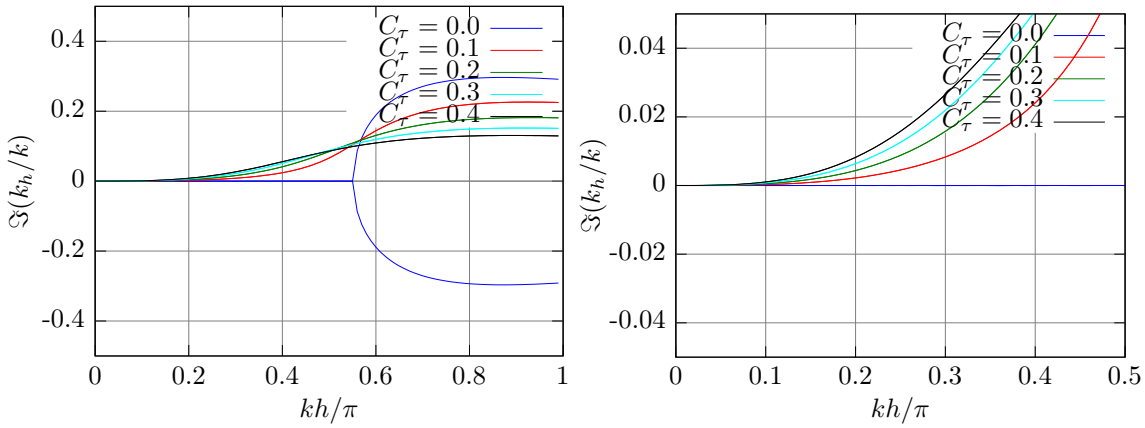

Figure 4.5: ASGS space semi-discretization: imaginary part of the wavenumber ratio (the right picture is a zoom of the left)

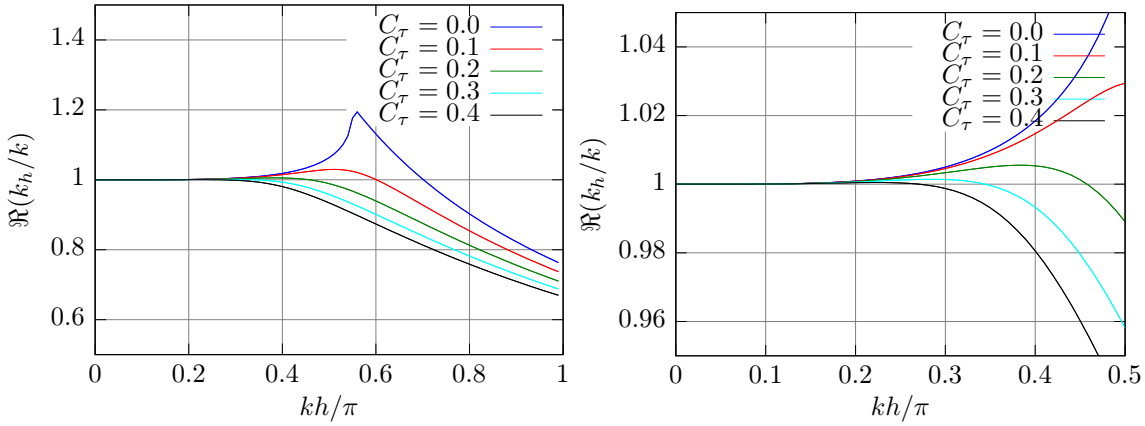

Figure 4.6: OSS space semi-discretization: real part of the wavenumber ratio (the right picture is a zoom of the left)

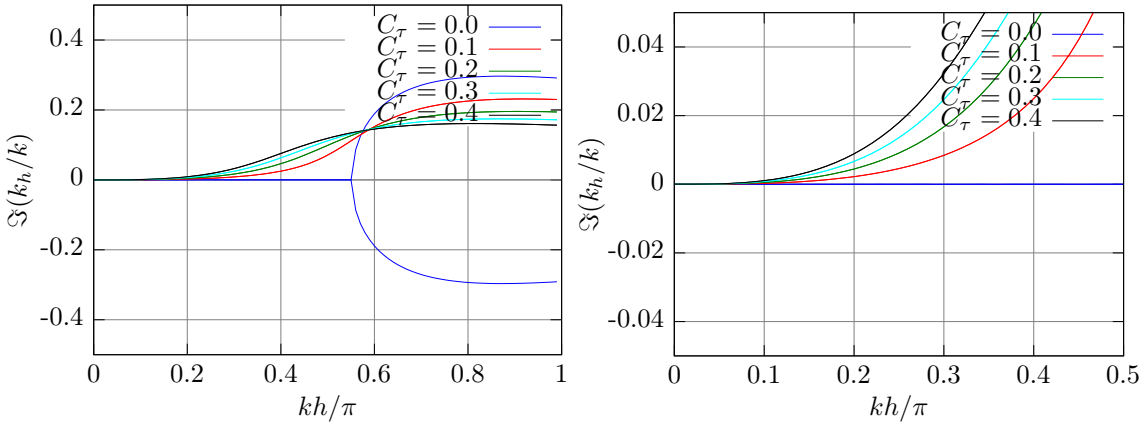

Figure 4.7: OSS space semi-discretization: imaginary part of the wavenumber ratio (the right picture is a zoom of the left)

4.4.2 Space semi-discretization

We analyze now the wave equation in mixed form when the spatial discretization is done using the ASGS and the OSS methods. We take $\omega_h = k_h c_h$ and $\omega_h = \omega$, where the subscript h denotes spatial semi-discretization. We take now

$$[P_j(t), U_j(t)] = \phi_\omega \mathrm{e}^{\mathrm{i}(k_h x_j - \omega t)} \left[1, \mu_p^{1/2}\mu_u^{-1/2}\right], \tag{4.43}$$

where ϕ_ω is a constant that describes the amplitude at $t = 0$.

For the ASGS method, the semi-discrete problem has the matrix structure:

$$\begin{aligned}
\mu_p M_p \frac{\mathrm{d}P}{\mathrm{d}t} + K_u U + \tau_u \mu_u M_{S,u} \frac{\mathrm{d}U}{\mathrm{d}t} + \tau_u K_{S,p} P = 0,\\
\mu_u M_u \frac{\mathrm{d}U}{\mathrm{d}t} + K_p P + \tau_p \mu_p M_{S,p} \frac{\mathrm{d}P}{\mathrm{d}t} + \tau_p K_{S,u} U = 0,
\end{aligned}$$

where a subscript S has been introduced in the matrices with contributions from the stabilization terms. In these equations, P and U do not denote the sequence of solutions in time, but the array of nodal unknowns with time-continuous components. The meaning of P and U in what follows will be determined by the context. We just analyze one of the previous equations because they are equivalent. The j-th row of the first system of equations is

$$\begin{aligned}
\mu_p \frac{h}{6}\left(\frac{\mathrm{d}}{\mathrm{d}t}P_{j-1} + 4\frac{\mathrm{d}}{\mathrm{d}t}P_j + \frac{\mathrm{d}}{\mathrm{d}t}P_{j+1}\right) + \frac{1}{2}(-U_{j-1} + U_{j+1})\\
+ \tau_u \mu_u \frac{1}{2}\left(\frac{\mathrm{d}}{\mathrm{d}t}U_{j-1} - \frac{\mathrm{d}}{\mathrm{d}t}U_{j+1}\right) + \tau_u \frac{1}{h}\left(-P_{j-1} + 2P_j - P_{j+1}\right) = 0.
\end{aligned}$$

Replacing $[P_j, U_j]$ from (4.43) we have:

$$\begin{aligned}
-\mathrm{i}\omega\mu_p \frac{h}{6}\left(\mathrm{e}^{-\mathrm{i}k_h h} + 4 + \mathrm{e}^{\mathrm{i}k_h h}\right) + \frac{1}{2}\mu_p^{1/2}\mu_u^{-1/2}\left(-\mathrm{e}^{-\mathrm{i}k_h h} + \mathrm{e}^{\mathrm{i}k_h h}\right)\\
- \frac{1}{2}\mathrm{i}\omega\tau_u\mu_p^{1/2}\mu_u^{1/2}\left(\mathrm{e}^{-\mathrm{i}k_h h} - \mathrm{e}^{\mathrm{i}k_h h}\right) + \frac{1}{h}\tau_u\left(-\mathrm{e}^{-\mathrm{i}k_h h} + 2 - \mathrm{e}^{\mathrm{i}k_h h}\right) = 0,
\end{aligned}$$

$$\frac{k_h}{k} = -\frac{\mathrm{i}}{kh}\log\left(\frac{-(4kh+12\mathrm{i}C_\tau)\pm\sqrt{36(kh)^2C_\tau^2+72\mathrm{i}khC_\tau+12(kh)^2-36}}{2(kh+3\mathrm{i}-3khC_\tau-6\mathrm{i}C_\tau)}\right).$$

The Maclaurin series for the real and imaginary parts are:

$$\frac{\Re(k_h)}{k} = 1-\frac{15C_\tau^2-1}{180}(kh)^4+\frac{126C_\tau^4-63C_\tau^2+1}{1512}(kh)^6+\dots,$$
$$\frac{\Im(k_h)}{k} = \frac{C_\tau}{12}(kh)^3-\frac{6C_\tau^3-C_\tau}{72}(kh)^5+\dots.$$

It can be shown that k_h is complex and that $\Re(k_h)$ is of order $(kh)^4$ for any C_τ and of order $(kh)^6$ for $C_\tau = 1/\sqrt{15}\approx 0.2582$. Additionally, $\Im(k_h)$ is of order $(kh)^3$ for any $C_\tau > 0$. Fig. 4.4 and Fig. 4.5 show the real and imaginary parts of the wavenumber ratio as a function of kh/π. It can be seen that the Galerkin method ($C_\tau = 0$) is unstable whereas the ASGS method is always stable.

Next, we analyze an OSS method in which a lumped mass matrix (diagonal) is used to project the residual. Additionally, as the projection with a lumped mass matrix is not exactly an L^2 projection, we keep the time derivatives in the residual. Non-lumped (consistent) mass matrices are used for time derivatives. Better than lumped mass matrix approximations to the L^2 projection can be used, but the results obtained are very similar. For instance we could use the family of banded approximate mass matrices from [138].

The matrix form of the semi-discrete problem is:

$$\mu_p M_p\frac{\mathrm{d}P}{\mathrm{d}t}+K_uU+\tau_u\mu_uM_{S,u}\frac{\mathrm{d}U}{\mathrm{d}t}+\tau_uK_{S,p}P-\tau_uM_{S,u}R_u=0,$$
$$M_uR_u=\mu_uM_u\frac{\mathrm{d}}{\mathrm{d}t}U+K_pP,$$
$$\mu_uM_u\frac{\mathrm{d}U}{\mathrm{d}t}+K_pP+\tau_p\mu_pM_{S,p}\frac{\mathrm{d}P}{\mathrm{d}t}+\tau_pK_{S,u}U-\tau_pM_{S,p}R_p=0,$$
$$M_pR_p=\mu_pM_p\frac{\mathrm{d}}{\mathrm{d}t}P+K_uU.$$

As we use a lumped projection, the semi-discrete problem reduces to:

$$\mu_p M_p\frac{\mathrm{d}P}{\mathrm{d}t}+K_uU+\tau_u\mu_uM_{S,u}\frac{\mathrm{d}U}{\mathrm{d}t}+\tau_uK_{S,p}P-\tau_uM_{S,u}\widetilde{M}_u^{-1}\left(\mu_uM_u\frac{\mathrm{d}}{\mathrm{d}t}U+K_pP\right)=0,$$
$$\mu_uM_u\frac{\mathrm{d}U}{\mathrm{d}t}+K_pP+\tau_p\mu_pM_{S,p}\frac{\mathrm{d}P}{\mathrm{d}t}+\tau_pK_{S,u}U-\tau_pM_{S,p}\widetilde{M}_p^{-1}\left(\mu_pM_p\frac{\mathrm{d}}{\mathrm{d}t}P+K_uU\right)=0.$$

Following similar steps as for the ASGS method, we arrive to the expression which relates k_hh with kh:

$$2kh\left(\mathrm{e}^{\mathrm{i}k_hh}+4\mathrm{e}^{2\mathrm{i}k_hh}+\mathrm{e}^{3\mathrm{i}k_hh}\right)+khC_\tau\left(-1+2\mathrm{e}^{\mathrm{i}k_hh}-2\mathrm{e}^{3\mathrm{i}k_hh}+\mathrm{e}^{4\mathrm{i}k_hh}\right)$$
$$+6\mathrm{i}\left(-\mathrm{e}^{\mathrm{i}k_hh}+\mathrm{e}^{3\mathrm{i}k_hh}\right)+3\mathrm{i}C_\tau\left(1-4\mathrm{e}^{\mathrm{i}k_hh}+6\mathrm{e}^{2\mathrm{i}k_hh}-4\mathrm{e}^{3\mathrm{i}k_hh}+\mathrm{e}^{4\mathrm{i}k_hh}\right)=0.$$

Fig. 4.6 and Fig. 4.7 show the real and imaginary parts of the wavenumber ratio as a function of kh/π. As before, the Galerkin method ($C_\tau = 0$) is unstable whereas the OSS method is always stable.

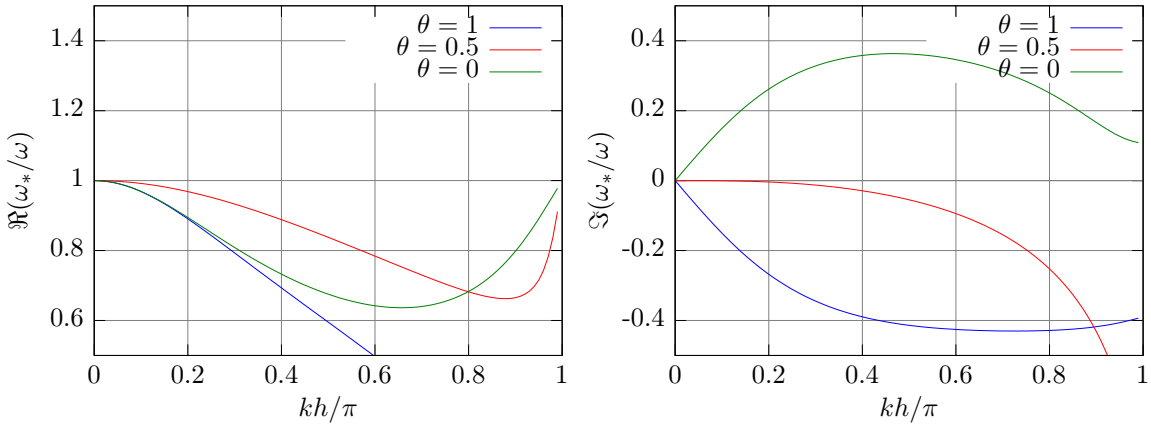

Figure 4.8: ASGS + θ for $r = 1$ and $C_\tau = 0.2$

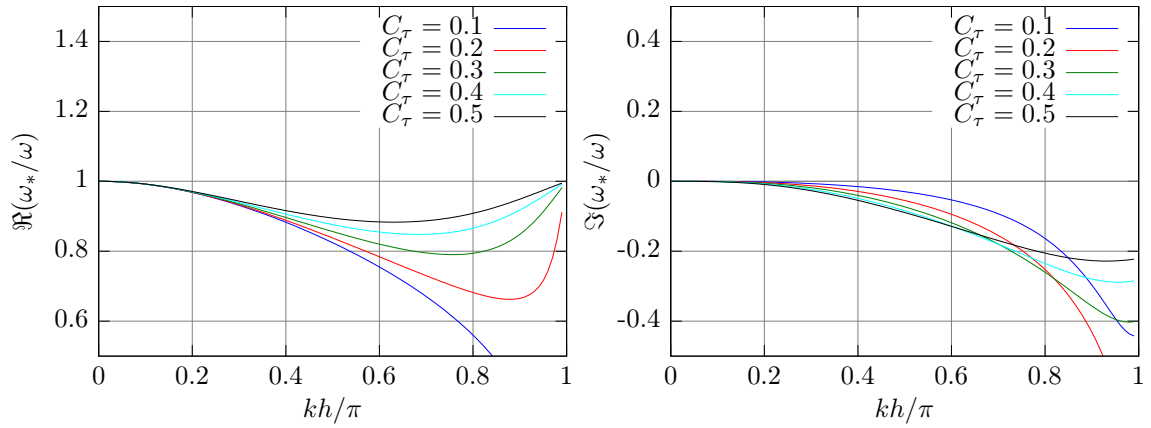

Figure 4.9: ASGS + θ for $r = 1$ and $\theta = 0.5$

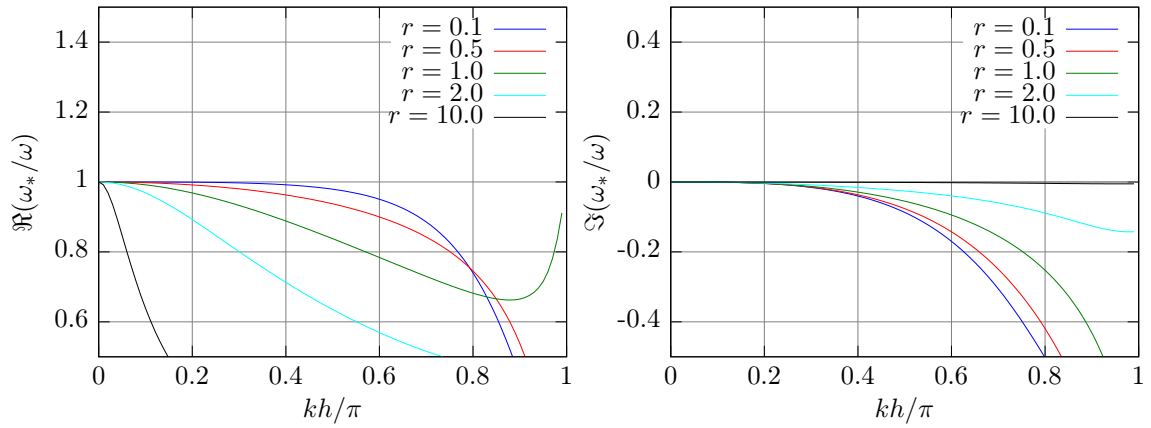

Figure 4.10: ASGS + θ for $C_\tau = 0.2$ and $\theta = 0.5$

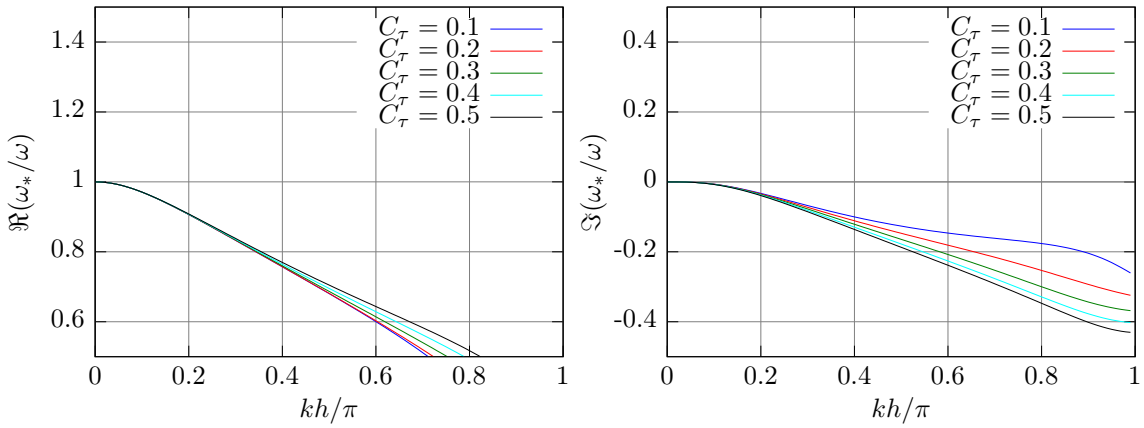

Figure 4.11: ASGS + BDF2 for $r = 1$

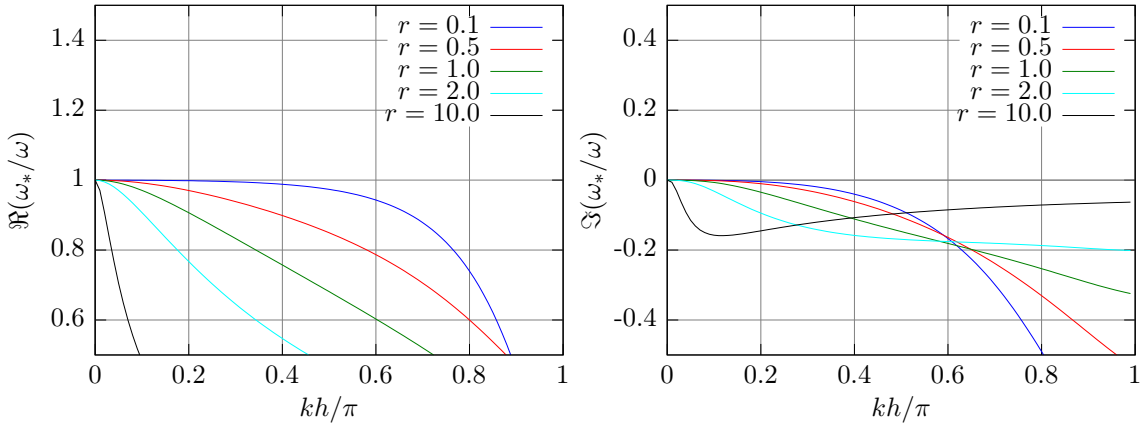

Figure 4.12: ASGS + BDF2 for $C_\tau = 0.2$

4.4.3 Space-time discretization

Finally, we analyze the fully discrete problems arising from the combination of time discretizations (θ and BDF2) and space discretizations (ASGS and OSS). Thus, in total we will analyze four fully discrete problems. We take $\omega_* = k_* c_*$ and $k_* = k$. The subscript $*$ denotes full discretization. We take a mode of the form

$$\left[P_j^n, U_j^n\right] = \phi_k \mathrm{e}^{\mathrm{i}(kx_j - \omega_* t_n)} \left[1, \mu_p^{1/2} \mu_u^{-1/2}\right], \tag{4.44}$$

where ϕ_k describes the amplitude at $t_n = 0$.

Let us define r as the Courant or CFL number as

$$r := c\delta t/h. \tag{4.45}$$

First, we consider the ASGS formulation for the space discretization. With regard to the time integration, we first consider the θ-method. The fully discrete problem is:

$$\frac{\mu_p}{\delta t} M_p \left(P^{n+1} - P^n\right) + \tau_u \frac{\mu_u}{\delta t} M_{S,u} \left(U^{n+1} - U^n\right) + \theta \left(K_u U^{n+1} + \tau_u K_{S,p} P^{n+1}\right) + (1-\theta)\left(K_u U^n + \tau_u K_{S,p} P^n\right) = 0,$$

$$\frac{\mu_u}{\delta t} M_u \left(U^{n+1} - U^n\right) + \tau_p \frac{\mu_p}{\delta t} M_{S,p} \left(P^{n+1} - P^n\right) + \theta \left(K_p P^{n+1} + \tau_p K_{S,u} U^{n+1}\right) + (1-\theta)\left(K_p P^n + \tau_p K_{S,u} U^n\right) = 0.$$

We concentrate in one of the equations because both will be equivalent for the current analysis. The j-th row of the system of equations is

$$\begin{aligned}
&\frac{\mu_p h}{6\delta t}\left(P_{j-1}^{n+1} + 4P_j^{n+1} + P_{j+1}^{n+1} - P_{j-1}^n - 4P_j^n - P_{j+1}^n\right) + \frac{\tau_u \mu_u}{2\delta t}\left(U_{j-1}^{n+1} - U_{j+1}^{n+1} - U_{j-1}^n + U_{j+1}^n\right) \\
&\quad + \theta\left(\frac{1}{2}\left(-U_{j-1}^{n+1} + U_{j+1}^{n+1}\right) + \tau_u \frac{1}{h}\left(-P_{j-1}^{n+1} + 2P_j^{n+1} - P_{j+1}^{n+1}\right)\right) \\
&\quad + (1-\theta)\left(\frac{1}{2}\left(-U_{j-1}^n + U_{j+1}^n\right) + \tau_u \frac{1}{h}\left(-P_{j-1}^n + 2P_j^n - P_{j+1}^n\right)\right) = 0,
\end{aligned}$$

and replacing $\left[P_j^n, U_j^n\right]$ from (4.44) we get

$$\begin{aligned}
&\mu_p \frac{h}{6\delta t}\left(\mathrm{e}^{\mathrm{i}(-kh-\omega_*\delta t)} + 4\mathrm{e}^{\mathrm{i}(-\omega_*\delta t)} + \mathrm{e}^{\mathrm{i}(kh-\omega_*\delta t)} - \mathrm{e}^{\mathrm{i}(-kh)} - 4 - \mathrm{e}^{\mathrm{i}(kh)}\right) \\
&+ \frac{1}{2\delta t}\tau_u \mu_p^{\frac{1}{2}} \mu_u^{\frac{1}{2}}\left(\mathrm{e}^{\mathrm{i}(-kh-\omega_*\delta t)} - \mathrm{e}^{\mathrm{i}(kh-\omega_*\delta t)} - \mathrm{e}^{\mathrm{i}(-kh)} + \mathrm{e}^{\mathrm{i}(kh)}\right) \\
&+ \theta\left(\frac{1}{2}\mu_p^{\frac{1}{2}} \mu_u^{-\frac{1}{2}}\left(-\mathrm{e}^{\mathrm{i}(-kh-\omega_*\delta t)} + \mathrm{e}^{\mathrm{i}(kh-\omega_*\delta t)}\right) + \frac{1}{h}\tau_u\left(-\mathrm{e}^{\mathrm{i}(-kh-\omega_*\delta t)} + 2\mathrm{e}^{\mathrm{i}(-\omega_*\delta t)} - \mathrm{e}^{\mathrm{i}(kh-\omega_*\delta t)}\right)\right) \\
&+ (1-\theta)\left(\frac{1}{2}\mu_p^{\frac{1}{2}} \mu_u^{-\frac{1}{2}}\left(-\mathrm{e}^{\mathrm{i}(-kh)} + \mathrm{e}^{\mathrm{i}(kh)}\right) + \frac{1}{h}\tau_u\left(-\mathrm{e}^{\mathrm{i}(-kh)} + 2 - \mathrm{e}^{\mathrm{i}(kh)}\right)\right) = 0.
\end{aligned}$$

Using the definition of r from (4.45) we arrive to:

$$\frac{\omega_*}{\omega} = \frac{-1}{\mathrm{i}rkh}\log\left(\frac{2 + \cos(kh) - 3\mathrm{i}C_\tau \sin(kh) - (1-\theta)(3\mathrm{i}r\sin(kh) + 6rC_\tau(1-\cos(kh)))}{2 - 3\mathrm{i}C_\tau \sin(kh) + \cos(kh) + 3\mathrm{i}r\theta\sin(kh) + 6r\theta C_\tau(1-\cos(kh))}\right).$$

Fig. 4.8, Fig. 4.9, and Fig. 4.10 show the real and imaginary parts of the angular frequency ratio keeping two parameters fixed. It can be seen that $\theta = 0$ (forward Euler or explicit Euler scheme) is unconditionally unstable. This is similar to what happens with forward in time-centered in space finite differences (FTCS) applied to the pure advection equation in 1D.

Next, we consider the ASGS with the BDF2 time integration. The fully discrete problem is:

$$\begin{aligned}
&\frac{\mu_p}{2\delta t} M_p\left(3P^{n+2} - 4P^{n+1} + P^n\right) + \tau_u \frac{\mu_u}{2\delta t} M_{S,u}\left(3U^{n+2} - 4U^{n+1} + U^n\right) \\
&\qquad + K_u U^{n+2} + \tau_u K_{S,p} P^{n+2} = 0, \\
&\frac{\mu_u}{2\delta t} M_u\left(3U^{n+2} - 4U^{n+1} + U^n\right) + \tau_p \frac{\mu_p}{2\delta t} M_{S,p}\left(3P^{n+2} - 4P^{n+1} + P^n\right) \\
&\qquad + K_p P^{n+2} + \tau_p K_{S,u} U^{n+2} = 0.
\end{aligned}$$

Following a similar procedure as before, we arrive to

$$\left(3\mathrm{e}^{-2\mathrm{i}\omega_*\delta t} - 4\mathrm{e}^{-\mathrm{i}\omega_*\delta t} + 1\right)\left((2 + \cos(kh)) - 3\mathrm{i}C_\tau\left(\sin(kh)\right)\right)$$

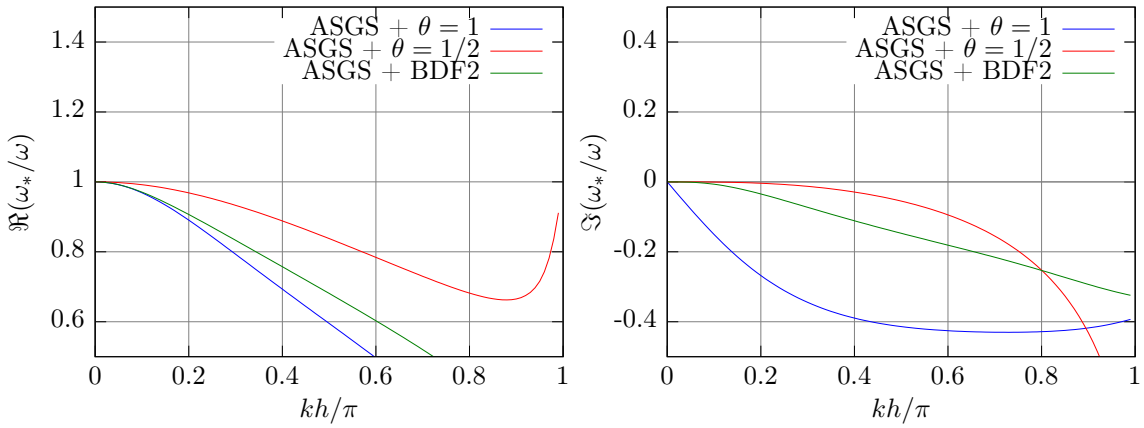

Figure 4.13: Fully discrete ASGS with $C_\tau = 0.2$ and $r = 1$

$$+\mathrm{e}^{-2\mathrm{i}\omega_* \delta t}\left(6\mathrm{i}r\left(\sin(kh)\right) + 12rC_\tau\left(1-\cos(kh)\right)\right) = 0.$$

Fig. 4.11 and Fig. 4.12 show the angular frequency ratio for the fully discrete problem. It can be seen that this combination of spatial and temporal discretization is stable.

Fig. 4.13 compares the fully discrete ASGS method with the two time integration schemes shown previously. It can be seen that the θ method performs better than BDF2 for small enough kh.

Next, we aim to analyze the properties of the OSS stabilized formulation. When using the θ-method for the time integration, the fully discrete problem is:

$$\begin{aligned}
&\frac{\mu_p}{\delta t} M_p\left(P^{n+1}-P^n\right) + \tau_u \frac{\mu_u}{\delta t} M_{S,u}\left(U^{n+1}-U^n\right) - \tau_u M_{S,u}\widetilde{M}_u^{-1}\frac{\mu_u}{\delta t} M_u\left(U^{n+1}-U^n\right)\\
&\quad + \theta\left(K_u U^{n+1} + \tau_u K_{S,p} P^{n+1} - \tau_u M_{S,u}\widetilde{M}_u^{-1} K_p P^{n+1}\right)\\
&\quad + (1-\theta)\left(K_u U^{n} + \tau_u K_{S,p} P^{n} - \tau_u M_{S,u}\widetilde{M}_u^{-1} K_p P^{n}\right) = 0,\\
&\frac{\mu_u}{\delta t} M_u\left(U^{n+1}-U^n\right) + \tau_p \frac{\mu_p}{\delta t} M_{S,p}\left(P^{n+1}-P^n\right) - \tau_p M_{S,p}\widetilde{M}_p^{-1}\frac{\mu_p}{\delta t} M_p\left(P^{n+1}-P^n\right)\\
&\quad + \theta\left(K_p P^{n+1} + \tau_p K_{S,u} U^{n+1} - \tau_p M_{S,p}\widetilde{M}_p^{-1} K_u U^{n+1}\right)\\
&\quad + (1-\theta)\left(K_p P^{n} + \tau_p K_{S,u} U^{n} - \tau_p M_{S,p}\widetilde{M}_p^{-1} K_u U^{n}\right) = 0.
\end{aligned}$$

Following a similar procedure as before we arrive to

$$\begin{aligned}
&\left(\mathrm{e}^{-\mathrm{i}\omega_* \delta t} - 1\right)\left(2\left(2+\cos(kh)\right) + \mathrm{i}C_\tau\left(-2\sin(kh) + \sin(2kh)\right)\right)\\
&+ \left(\theta \mathrm{e}^{-\mathrm{i}\omega_* \delta t} + 1 - \theta\right)\left(6\mathrm{i}r\left(\sin(kh)\right) + 3rC_\tau\left(3 - 4\cos(kh) + \cos(2kh)\right)\right) = 0.
\end{aligned}$$

Fig. 4.14, Fig. 4.15, and Fig. 4.16 show the angular frequency ratio for this fully discretized problem.

Next, we consider the OSS-BDF2 fully discrete problem:

$$\begin{aligned}
&\frac{\mu_p}{2\delta t} M_p\left(3P^{n+2} - 4P^{n+1} + P^n\right) + \tau_u \frac{\mu_u}{2\delta t} M_{S,u}\left(3U^{n+2} - 4U^{n+1} + U^n\right) + K_u U^{n+2}\\
&\quad + \tau_u K_{S,p} P^{n+2} - \tau_u M_{S,u}\widetilde{M}_u^{-1}\left(\frac{\mu_u}{2\delta t} M_u\left(3U^{n+2} - 4U^{n+1} + U^n\right) + K_p P^{n+2}\right) = 0,
\end{aligned}$$

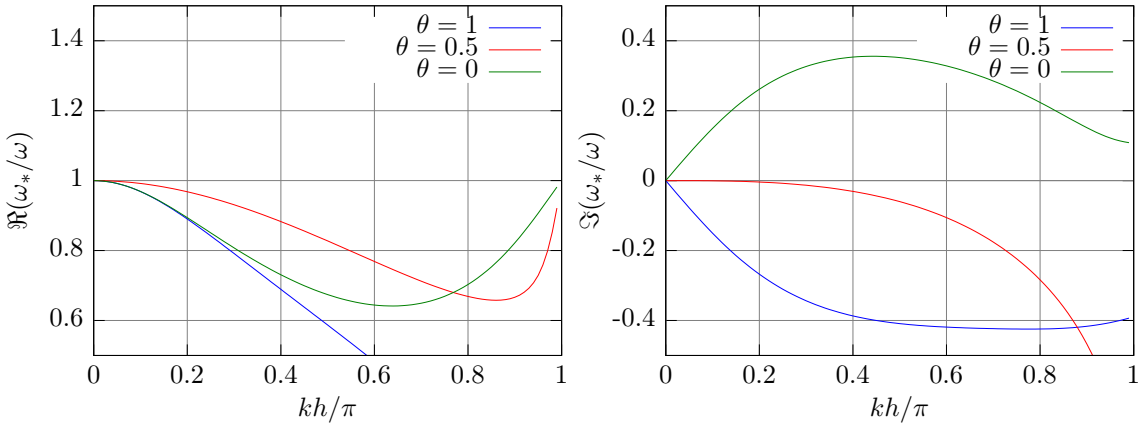

Figure 4.14: OSS + θ for $r = 1$ and $C_\tau = 0.2$

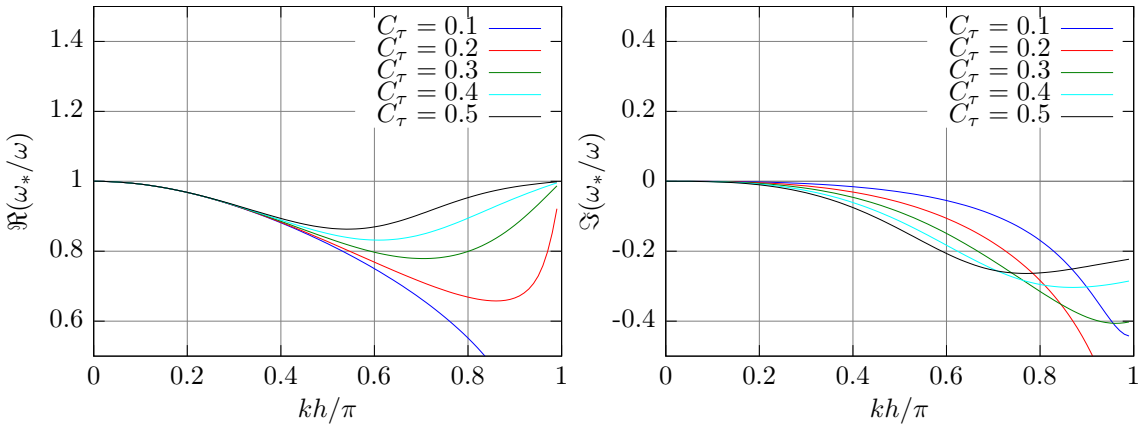

Figure 4.15: OSS + θ for $r = 1$ and $\theta = 0.5$

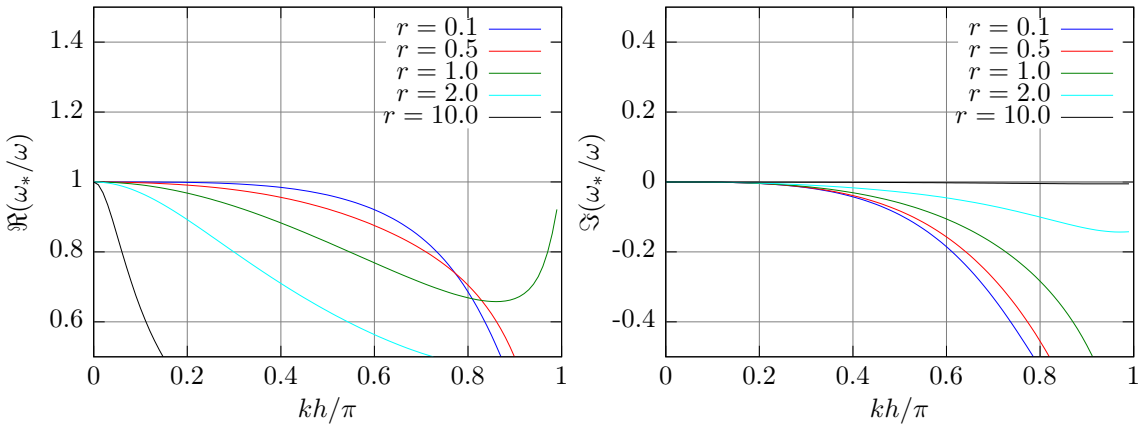

Figure 4.16: OSS + θ for $C_\tau = 0.2$ and $\theta = 0.5$

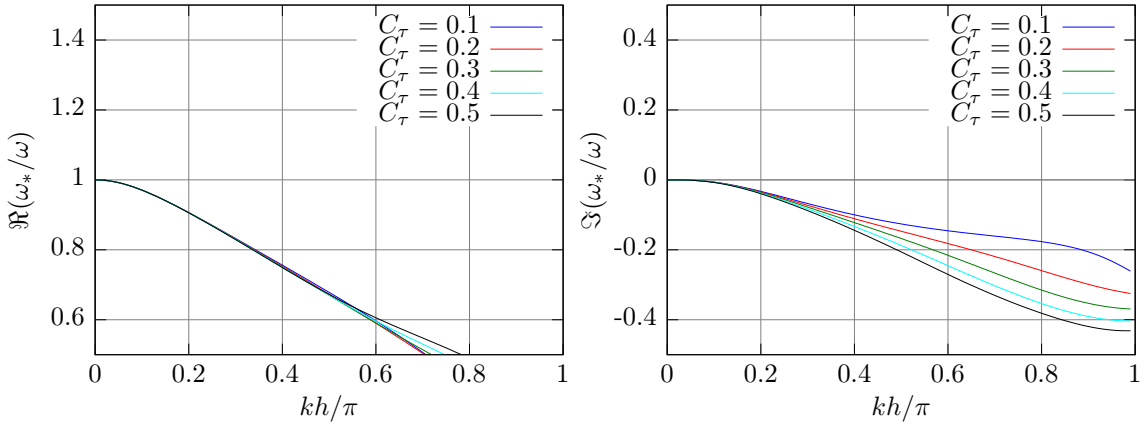

Figure 4.17: OSS + BDF2 for $r = 1$

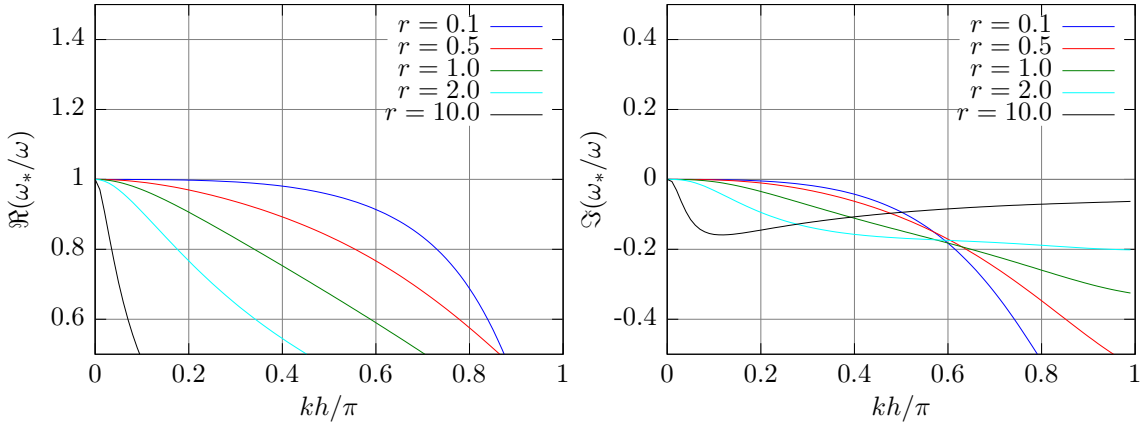

Figure 4.18: OSS + BDF2 for $C_\tau = 0.2$

$$\frac{\mu_u}{2\delta t} M_u \left(3U^{n+2} - 4U^{n+1} + U^n\right) + \tau_p \frac{\mu_p}{2\delta t} M_{S,p} \left(3P^{n+2} - 4P^{n+1} + P^n\right) + K_p P^{n+2}$$
$$+ \tau_p K_{S,u} U^{n+2} - \tau_p M_{S,p} \widetilde{M}_p^{-1} \left(\frac{\mu_p}{2\delta t} M_p \left(3P^{n+2} - 4P^{n+1} + P^n\right) + K_u U^{n+2}\right) = 0.$$

Following a similar procedure as before we get

$$\left(3\mathrm{e}^{-2\mathrm{i}\omega_*\delta t} - 4\mathrm{e}^{-\mathrm{i}\omega_*\delta t} + 1\right)\left(2\left(2 + \cos(kh)\right) + \mathrm{i}C_\tau\left(-2\sin(kh) + \sin(2kh)\right)\right)$$
$$+ \mathrm{e}^{-2\mathrm{i}\omega_*\delta t}\left(12\mathrm{i}r\left(\sin(kh)\right) + 6rC_\tau\left(3 - 4\cos(kh) + \cos(2kh)\right)\right) = 0.$$

Fig. 4.17 and Fig. 4.18 show the real and imaginary parts of the angular frequency ratio.

The plots comparing time marching schemes for the OSS method are very similar to the ones for ASGS and are not shown for succinctness. The fully discrete ASGS and OSS methods perform similarly according to this analysis, so we do not show a side by side comparison of both methods.

4.5 Numerical results

In this section we present two sets of numerical results. First, convergence tests are presented and compared with the predicted convergence rates obtained from convergence

Table 4.9: Experimental δt convergence rates for ASGS-BE method using $Q1/Q1$ spatial interpolation

Variational Form	I		II		III		I	
δt vs. h	$\delta t \sim 0.5h$						$\delta t \sim 4.5h^{1.5}$	
	Num	Min	Num	Min	Num	Min	Num	Min
$\|p^n - p_h^n\|_{\ell^\infty(L^2)}$	1.00	1	1.00	1	1.01	1	1.00	1
$\|\boldsymbol{u}^n - \boldsymbol{u}_h^n\|_{\ell^\infty(L^2)}$	1.02	1	1.02	1	1.02	1	1.01	1
$\|\nabla(p^n - p_h^n)\|_{\ell^2(L^2)}$	1.00	0.5	1.00	0	1.00	1	0.66	2/3
$\|\nabla\cdot(\boldsymbol{u}^n - \boldsymbol{u}_h^n)\|_{\ell^2(L^2)}$	1.00	0.5	1.00	1	1.00	0	0.66	2/3

analysis. Then, numerical solutions of a wave propagation problem are compared in order to see the differences of the fully discrete methods.

4.5.1 Convergence tests

Let us consider a two dimensional transient problem with analytical solution to investigate the convergence properties of the stabilized FE formulations proposed. The spatial domain is the unit square $(0,1)\times(0,1)$ and the temporal domain is $(0,1)$. The forcing terms $[f_p, \boldsymbol{f}_u]$ are chosen such that the exact solution is $p = \sin(\pi x)\sin(\pi y)\cos\left(\frac{\pi}{3}t\right)$ and $\boldsymbol{u} = [p, p]$ with $\mu_p = \mu_u = 1$. On the boundary we prescribe $p = 0$ ($\Gamma = \Gamma_p$). The initial condition is taken as the exact solution at $t = 0$. Various mesh sizes and time step sizes have been used to generate the results. We have used isotropic bilinear ($Q1$) and biquadratic ($Q2$) meshes of sizes $h = 0.05$, 0.025, 0.01, 0.005 and 0.002. The stabilization algorithmic constant C_τ has been taken as 0.05 for $Q1$ elements and 0.4 for $Q2$ elements. The the length scale of the problem has been taken as $\mathrm{L}_0 = \sqrt[d]{\mathrm{meas}(\Omega)} = 1$.

In Tables 4.9-4.20 we show the convergence rates with respect to the time step size δt for various stabilization methods (ASGS and OSS), time integrators (BE/CN/BDF2) and spatial interpolations ($Q1$ and $Q2$). The numerical experiments have been carried out modifying the time step size and the mesh size at the same time. The relationship $(\delta t, h)$ is shown in each table for each variational form with the respective proportionality constant and power, $\delta t \sim C_s h^s$. The power constant s has been chosen as $s = 1$ for all the variational forms and, additionally, it has been chosen such that the best convergence is achieved for equal interpolation of the unknowns ($k = l$). It is observed than in all cases the numerical rate of convergence obtained (Num) is greater than or equal to the minimum one predicted by the convergence analysis (Min).

4.5.2 Numerical comparison

In Section 4.4 we analyzed dispersion and dissipation analytically through Fourier techniques. We present now a simple test to verify experimentally the predictions of the Fourier analysis. Let us consider a 1D problem in $\Omega = (0, L) = (0, 1)$ and $\Upsilon = (0, 0.8)$, and let us solve the mixed wave equation with $\mu_p = 1$, $\mu_u = 1$, zero initial conditions and boundary conditions $p(0, t) = \sin(\omega t)$ and $p(L, t) = 0$. We compare the solutions obtained with the fully discrete methods at $t = 0.6$.

Table 4.10: Experimental δt convergence rates for OSS-BE method using $Q1/Q1$ spatial interpolation

Variational Form	I		II		III		I	
δt vs. h	$\delta t \sim 0.5h$						$\delta t \sim 4.5h^{1.5}$	
	Num	Min	Num	Min	Num	Min	Num	Min
$\|p^n - p_h^n\|_{\ell^\infty(L^2)}$	1.00	1	1.00	1	1.01	1	1.00	1
$\|\boldsymbol{u}^n - \boldsymbol{u}_h^n\|_{\ell^\infty(L^2)}$	1.02	1	1.02	1	1.02	1	1.01	1
$\|\nabla(p^n - p_h^n)\|_{\ell^2(L^2)}$	1.00	0.5	1.00	0	1.00	1	0.66	2/3
$\|\nabla\cdot(\boldsymbol{u}^n - \boldsymbol{u}_h^n)\|_{\ell^2(L^2)}$	1.00	0.5	1.00	1	1.00	0	0.66	2/3

Table 4.11: Experimental δt convergence rates for ASGS-BE method using $Q2/Q2$ spatial interpolation

Variational Form	I		II		III		I		II		III	
δt vs. h	$\delta t \sim 0.5h$						$\delta t \sim 894h^{2.5}$		$\delta t \sim 40h^2$		$\delta t \sim 40h^2$	
	Num	Min	Num	Min	Num	Min	Num	Min	Num	Min	Num	Min
$\|p^n - p_h^n\|_{\ell^\infty(L^2)}$	0.98	1	0.98	1	0.98	1	0.99	1	0.99	1	0.99	1
$\|\boldsymbol{u}^n - \boldsymbol{u}_h^n\|_{\ell^\infty(L^2)}$	0.99	1	0.99	1	0.99	1	1.00	1	1.00	1	1.00	1
$\|\nabla(p^n - p_h^n)\|_{\ell^2(L^2)}$	0.99	0.5	0.99	0	0.99	1	0.98	4/5	0.50	0.5	1.00	1
$\|\nabla\cdot(\boldsymbol{u}^n - \boldsymbol{u}_h^n)\|_{\ell^2(L^2)}$	0.99	0.5	0.99	1	0.99	0	0.99	4/5	1.00	1	0.50	0.5

Table 4.12: Experimental δt convergence rates for OSS-BE method using $Q2/Q2$ spatial interpolation

Variational Form	I		II		III		I		II		III	
δt vs. h	$\delta t \sim 0.5h$						$\delta t \sim 894h^{2.5}$		$\delta t \sim 40h^2$		$\delta t \sim 40h^2$	
	Num	Min	Num	Min	Num	Min	Num	Min	Num	Min	Num	Min
$\|p^n - p_h^n\|_{\ell^\infty(L^2)}$	0.98	1	0.98	1	0.98	1	0.99	1	0.99	1	0.99	1
$\|\boldsymbol{u}^n - \boldsymbol{u}_h^n\|_{\ell^\infty(L^2)}$	0.99	1	0.99	1	0.99	1	1.00	1	1.00	1	1.00	1
$\|\nabla(p^n - p_h^n)\|_{\ell^2(L^2)}$	0.99	0.5	1.02	0	0.99	1	0.98	4/5	0.51	0.5	1.00	1
$\|\nabla\cdot(\boldsymbol{u}^n - \boldsymbol{u}_h^n)\|_{\ell^2(L^2)}$	0.99	0.5	0.99	1	1.03	0	0.99	4/5	0.99	1	0.52	0.5

Table 4.13: Experimental δt convergence rates for ASGS-CN method using $Q1/Q1$ spatial interpolation

Variational Form	I		II		III		I		II		III	
δt vs. h	$\delta t \sim 0.5h$						$\delta t \sim 0.2h^{0.75}$		$\delta t \sim 0.1h^{0.5}$		$\delta t \sim 0.1h^{0.5}$	
	Num	Min	Num	Min	Num	Min	Num	Min	Num	Min	Num	Min
$\|p^n - p_h^n\|_{\ell^\infty(L^2)}$	2.00	1.5	2.00	1	2.00	1	2.60	2	3.38	2	3.39	2
$\|\boldsymbol{u}^n - \boldsymbol{u}_h^n\|_{\ell^\infty(L^2)}$	2.00	1.5	2.00	1	2.00	1	2.64	2	3.72	2	3.72	2
$\|\nabla(p^n - p_h^n)\|_{\ell^2(L^2)}$	1.00	1	1.00	0	1.00	1	1.33	4/3	1.99	0	1.99	2
$\|\nabla\cdot(\boldsymbol{u}^n - \boldsymbol{u}_h^n)\|_{\ell^2(L^2)}$	1.00	1	1.00	1	1.00	0	1.33	4/3	1.99	2	1.99	0

Table 4.14: Experimental δt convergence rates for OSS-CN method using $Q1/Q1$ spatial interpolation

Variational Form	I		II		III		I		II		III	
δt vs. h	$\delta t \sim 0.5h$						$\delta t \sim 0.2h^{0.75}$		$\delta t \sim 0.1h^{0.5}$		$\delta t \sim 0.1h^{0.5}$	
	Num	Min	Num	Min	Num	Min	Num	Min	Num	Min	Num	Min
$\|p^n - p_h^n\|_{\ell^\infty(L^2)}$	2.00	1.5	2.00	1	2.00	1	2.60	2	3.38	2	3.39	2
$\|\boldsymbol{u}^n - \boldsymbol{u}_h^n\|_{\ell^\infty(L^2)}$	2.00	1.5	2.00	1	2.00	1	2.64	2	3.72	2	3.72	2
$\|\nabla(p^n - p_h^n)\|_{\ell^2(L^2)}$	1.00	1	1.00	0	1.00	1	1.33	4/3	1.99	0	1.99	2
$\|\nabla\cdot(\boldsymbol{u}^n - \boldsymbol{u}_h^n)\|_{\ell^2(L^2)}$	1.00	1	1.00	1	1.00	0	1.33	4/3	1.99	2	1.99	0

Table 4.15: Experimental δt convergence rates for ASGS-CN method using $Q2/Q2$ spatial interpolation

Variational Form	I		II		III		I	
δt vs. h	$\delta t \sim 0.5h$						$\delta t \sim 2h^{1.25}$	
	Num	Min	Num	Min	Num	Min	Num	Min
$\|p^n - p_h^n\|_{\ell^\infty(L^2)}$	2.01	2	2.00	2	2.00	2	2.00	2
$\|\boldsymbol{u}^n - \boldsymbol{u}_h^n\|_{\ell^\infty(L^2)}$	2.26	2	2.00	2	2.00	2	2.13	2
$\|\nabla(p^n - p_h^n)\|_{\ell^2(L^2)}$	1.99	1.5	1.00	1	2.00	2	1.60	1.6
$\|\nabla\cdot(\boldsymbol{u}^n - \boldsymbol{u}_h^n)\|_{\ell^2(L^2)}$	1.99	1.5	2.00	2	1.00	1	1.60	1.6

Table 4.16: Experimental δt convergence rates for OSS-CN method using $Q2/Q2$ spatial interpolation

Variational Form	I		II		III		I	
δt vs. h	$\delta t \sim 0.5h$						$\delta t \sim 2h^{1.25}$	
	Num	Min	Num	Min	Num	Min	Num	Min
$\|p^n - p_h^n\|_{\ell^\infty(L^2)}$	2.01	2	1.99	2	2.00	2	2.00	2
$\|\boldsymbol{u}^n - \boldsymbol{u}_h^n\|_{\ell^\infty(L^2)}$	2.04	2	1.99	2	2.03	2	2.00	2
$\|\nabla(p^n - p_h^n)\|_{\ell^2(L^2)}$	2.00	1.5	1.00	1	2.00	2	1.60	1.6
$\|\nabla\cdot(\boldsymbol{u}^n - \boldsymbol{u}_h^n)\|_{\ell^2(L^2)}$	2.02	1.5	1.98	2	1.02	1	1.62	1.6

Table 4.17: Experimental δt convergence rates for ASGS-BDF2 method using $Q1/Q1$ spatial interpolation

Variational Form	I		II		III		I		II		III	
δt vs. h	$\delta t \sim 0.5h$						$\delta t \sim 0.2h^{0.75}$		$\delta t \sim 0.1h^{0.5}$		$\delta t \sim 0.1h^{0.5}$	
	Num	Min	Num	Min	Num	Min	Num	Min	Num	Min	Num	Min
$\|p^n - p_h^n\|_{\ell^\infty(L^2)}$	2.00	1.5	2.00	1	2.00	1	2.66	2	3.93	2	3.93	2
$\|\boldsymbol{u}^n - \boldsymbol{u}_h^n\|_{\ell^\infty(L^2)}$	2.00	1.5	2.00	1	2.00	1	2.67	2	4.04	2	4.04	2
$\|\nabla(p^n - p_h^n)\|_{\ell^2(L^2)}$	1.00	1	1.00	0	1.00	1	1.32	4/3	1.99	0	1.99	2
$\|\nabla\cdot(\boldsymbol{u}^n - \boldsymbol{u}_h^n)\|_{\ell^2(L^2)}$	1.00	1	1.00	1	1.00	0	1.32	4/3	1.99	2	1.99	0

Table 4.18: Experimental δt convergence rates for OSS-BDF2 method using $Q1/Q1$ spatial interpolation

Variational Form	I		II		III		I		II		III	
δt vs. h	$\delta t \sim 0.5h$						$\delta t \sim 0.2h^{0.75}$		$\delta t \sim 0.1h^{0.5}$		$\delta t \sim 0.1h^{0.5}$	
	Num	Min	Num	Min	Num	Min	Num	Min	Num	Min	Num	Min
$\|p^n - p_h^n\|_{\ell^\infty(L^2)}$	2.00	1.5	2.00	1	2.00	1	2.66	2	3.93	2	3.93	2
$\|\boldsymbol{u}^n - \boldsymbol{u}_h^n\|_{\ell^\infty(L^2)}$	2.00	1.5	2.00	1	2.00	1	2.67	2	4.04	2	4.04	2
$\|\nabla(p^n - p_h^n)\|_{\ell^2(L^2)}$	1.00	1	1.00	0	1.00	1	1.32	4/3	1.99	0	1.99	2
$\|\nabla\cdot(\boldsymbol{u}^n - \boldsymbol{u}_h^n)\|_{\ell^2(L^2)}$	1.00	1	1.00	1	1.00	0	1.32	4/3	1.99	2	1.99	0

Table 4.19: Experimental δt convergence rates for ASGS-BDF2 method using $Q2/Q2$ spatial interpolation

Variational Form	I		II		III		I	
δt vs. h	$\delta t \sim 0.5h$						$\delta t \sim 2h^{1.25}$	
	Num	Min	Num	Min	Num	Min	Num	Min
$\|p^n - p_h^n\|_{\ell^\infty(L^2)}$	2.17	2	2.00	2	2.13	2	2.41	2
$\|\boldsymbol{u}^n - \boldsymbol{u}_h^n\|_{\ell^\infty(L^2)}$	2.19	2	2.00	2	2.00	2	2.34	2
$\|\nabla(p^n - p_h^n)\|_{\ell^2(L^2)}$	1.99	1.5	1.00	1	2.00	2	1.59	1.6
$\|\nabla\cdot(\boldsymbol{u}^n - \boldsymbol{u}_h^n)\|_{\ell^2(L^2)}$	1.99	1.5	2.00	2	1.00	1	1.59	1.6

For $\omega = 10\pi$ a quite coarse pair of mesh and time step sizes is $(h, \delta t) = (0.05, 0.05)$. This allows us to see dispersion and dissipation in the numerical solution when compared with the exact solution $\sin(\omega t - kx)(1 - H(x - ct))$, where H is the Heaviside step function. The algorithmic constant is taken as $C_\tau = 0.1$ and the elements used are P1.

Fig. 4.19 shows the numerical solutions obtained with ASGS and three time marching schemes. CN is the least dissipative while BE is the most dissipative and BDF2 is somewhere in the middle. These numerical results are in agreement with the previous Fourier analysis. OSS behaves similarly and we do not show those results. Figs. 4.20-4.22 compare the ASGS method with the OSS method for the same time integration scheme, showing a very similar numerical behavior.

Table 4.20: Experimental δt convergence rates for OSS-BDF2 method using $Q2/Q2$ spatial interpolation

Variational Form	I		II		III		I	
δt vs. h	$\delta t \sim 0.5h$						$\delta t \sim 2h^{1.25}$	
	Num	Min	Num	Min	Num	Min	Num	Min
$\|p^n - p_h^n\|_{\ell^\infty(L^2)}$	2.18	2	2.02	2	2.14	2	2.42	2
$\|\boldsymbol{u}^n - \boldsymbol{u}_h^n\|_{\ell^\infty(L^2)}$	2.03	2	2.00	2	2.03	2	2.24	2
$\|\nabla(p^n - p_h^n)\|_{\ell^2(L^2)}$	2.00	1.5	1.01	1	2.00	2	1.60	1.6
$\|\nabla\cdot(\boldsymbol{u}^n - \boldsymbol{u}_h^n)\|_{\ell^2(L^2)}$	2.02	1.5	2.00	2	1.03	1	1.64	1.6

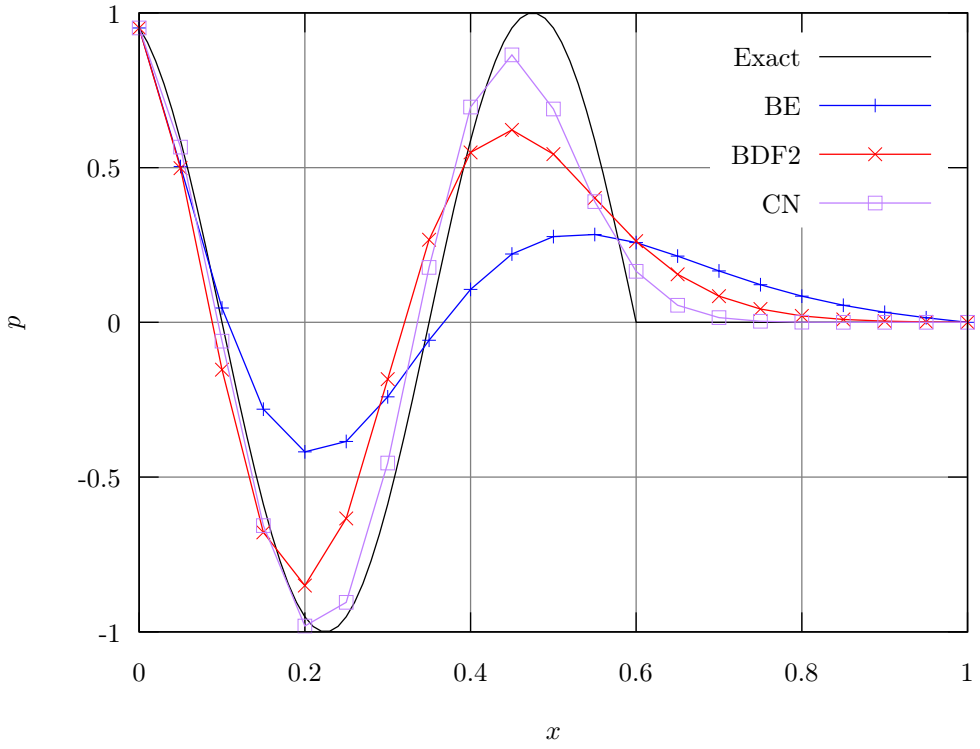

Figure 4.19: Numerical solution using the ASGS formulation and different time marching schemes

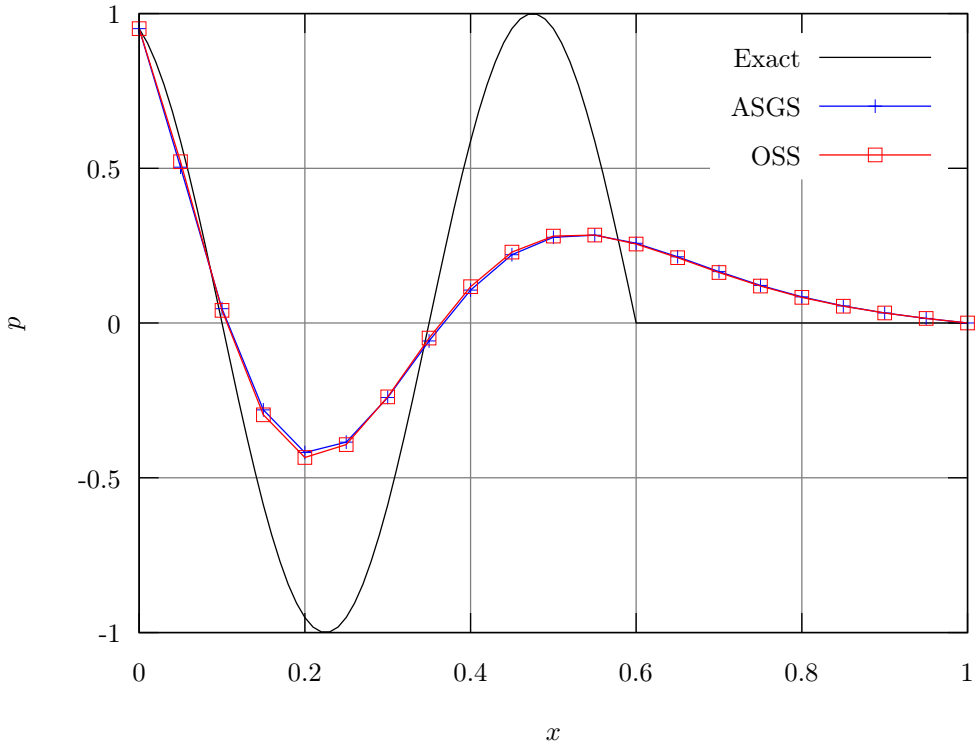

Figure 4.20: Comparison of ASGS and OSS using BE as time integration

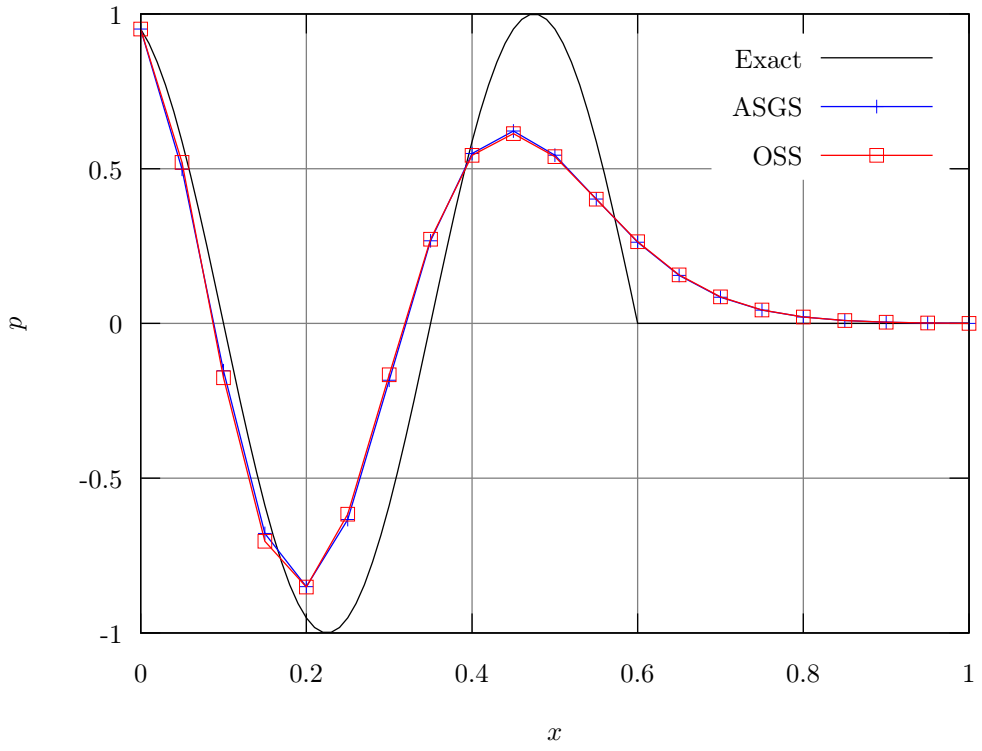

Figure 4.21: Comparison of ASGS and OSS using BDF2 as time integration

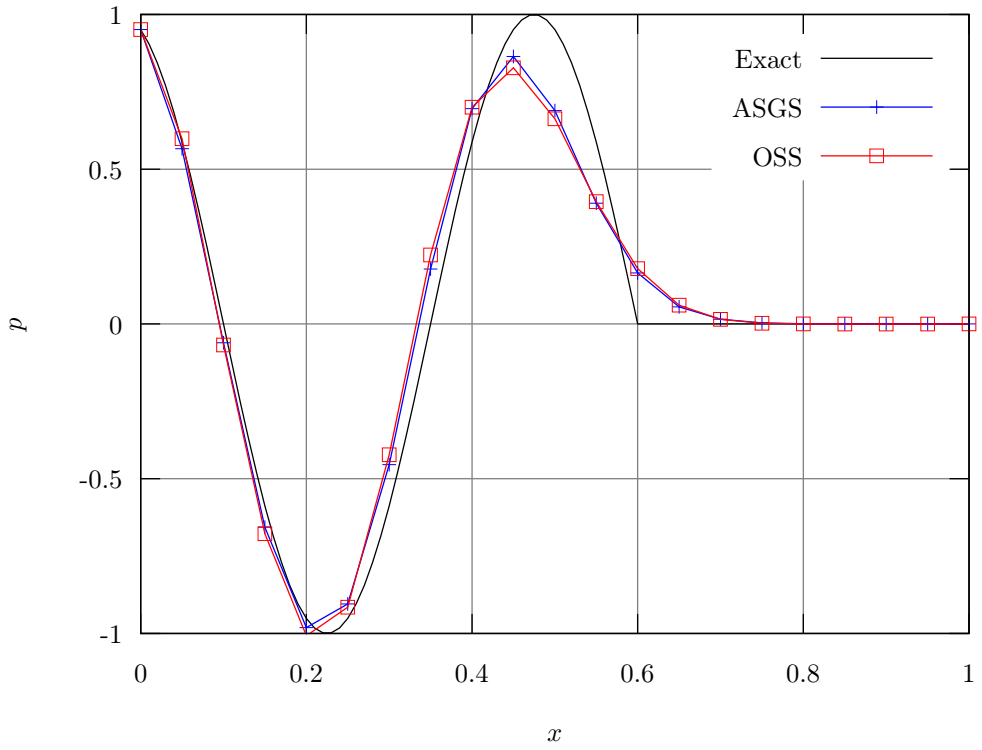

Figure 4.22: Comparison of ASGS and OSS using CN as time integration

4.6 Conclusions

In this work we have presented fully discrete methods arising from the combination of spatial discretization methods, namely stabilized FE methods, and temporal discretization methods (backward Euler, Crank-Nicolson and 2nd order backward differentiation formula) for the mixed wave equation in three different variational forms. The stabilization parameters have been designed such that they mimic the continuous setting.

Stability and convergence has been proved for all combinations of space discretization and time discretization. Stability, dispersion and dissipation of the fully discrete methods in 1D for equal interpolation of $[p, \boldsymbol{u}]$ has been analyzed using Fourier techniques. According to this analysis, CN performs better than BE and BDF2. Additionally, ASGS and OSS perform similarly.

Numerical convergence tests have been performed and the results obtained in the numerical experiments are in agreement with the theoretical predictions. Additionally, the fully discrete methods have been compared qualitatively. This comparison shows the differences in dispersion and dissipation of the methods and is in agreement with the Fourier analysis.

Chapter 5

Applications

This chapter includes material in:
Oriol Guasch, Marc Arnela, Ramon Codina, and Hector Espinoza. "A stabilized finite element method for the mixed wave equation in an ALE framework with application to diphthong production". In: *Journal of Computational Physics* (Oct. 2014). Submitted
as well as additional unpublished numerical application examples.

Here we present various wave propagation examples. The examples include a concentric tube wave propagation problem, an eccentric tube problem, vowel generation and diphthong generation. Some of the results are compared with experiments [139]. All examples involve acoustic wave propagation where the propagation media is air with properties $\mu_p =$ 7.083E-6 m s^2/Kg and $\mu_u = 1.20$ Kg/m^3 which correspond to a sound speed $c = 343$ m/s and a density $\rho_0 = 1.20$ Kg/m^3.

The algorithmic constant for the stabilization parameters was taken as $C_\tau = 0.1$ in all cases. The element size h is based on the volume of the element $h = \sqrt[d]{V_e}$.

5.1 Concentric Tubes

This is a 3D example of wave propagation inside of two concentric tubes of different diameter. In the context of voice simulation, this geometry corresponds to a very rudimentary approximation of the vocal tract in vowel /a/ position. A pressure pulse at the small diameter tube is the input signal and the end of the big diameter tube is the output to free space. Two reference points denoted as 1 and 2 will be used for comparison with experimental results using the concept of transfer function [139].

5.1.1 Space and time domains

The time interval for the simulation is 25 ms. The spatial domain consists of two concentric tubes: one 85 mm long with a diameter of 14 mm and another tube of the same length and a diameter of 29.5 mm as shown in Fig. 5.1. The smaller diameter tube is the sound inlet through a 2 mm diameter hole. Acoustic pressure and velocity are measured at points 1 and 2 for comparison with experimental results.

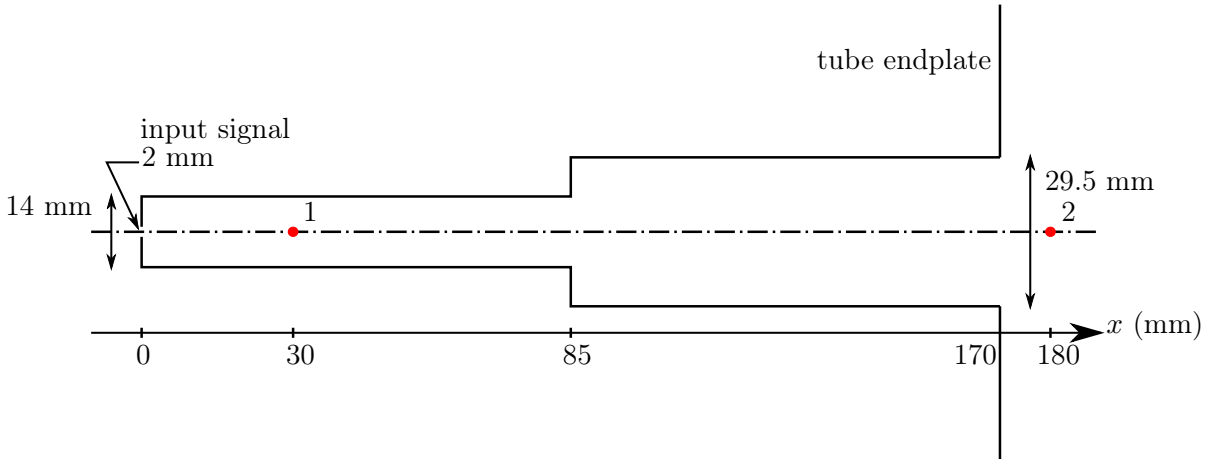

Figure 5.1: Concentric tubes spatial domain

5.1.2 Boundary and Initial conditions

Initial conditions are zero pressure and zero velocity. Boundary conditions consist of three parts. The first part, denoted as Γ_p, corresponds to the 2 mm diameter hole in the small tube. There, a Gaussian pressure pulse is imposed as follows

$$p = \mathrm{e}^{[(t-T_{\mathrm{gp}})0.29T_{\mathrm{gp}}]^2}, \tag{5.1}$$

with $T_{\mathrm{gp}} = 0.646/f_0$ and $f_0 = 10000$ Hz.

The second part of the boundary, denoted as Γ_u, corresponds to the wall of the tubes and the endplate. There, a hard wall boundary condition is applied $\gamma_n \boldsymbol{u} = 0$.

Finally, the third part of the boundary, denoted as Γ_{o}, corresponds to a non-reflecting boundary condition. It is applied on a semi-sphere of radius 150 mm surrounding the tube exit.

The boundary conditions can be seen in Fig. 5.2.

5.1.3 Experimental setup

Fig. 5.3 shows the concentric tubes experimental model and Fig. 5.4 shows the experimental setup.

5.1.4 Spatial and temporal discretization

Space was discretized using tetrahedral elements of size 0.0005 m for the input hole, 0.002 m for the tubes volume and 0.008 m for the surrounding volume. The mesh size for the input hole is based in geometrical considerations (2 mm diameter input hole). The mesh size inside the tubes is based on resolution considerations in order to have around 16 points per wavelength at 10 kHz. The surrounding volume is not important for this simulation, so a big mesh size can be taken. The mesh obtained is around 260K elements and 50K nodes. A cut on the plane $z = 0$ of the mesh used can be seen in Fig. 5.5.

For time discretization a time step $5 \cdot 10^{-6}$ s was used based on a resolution of 16 points per wave period. Several time integration schemes were used to compute the results.

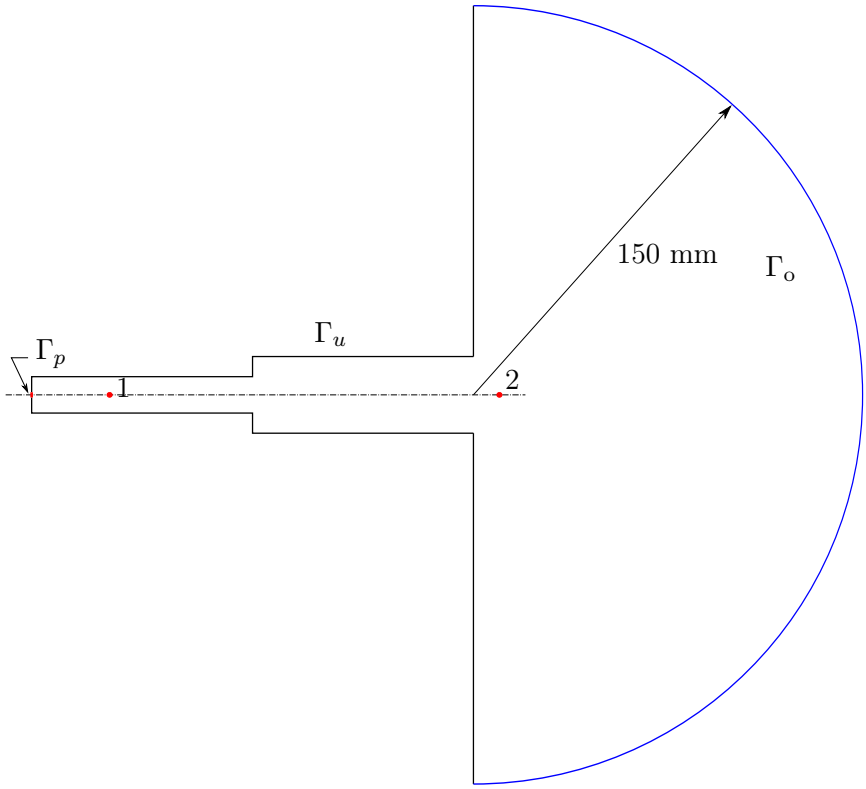

Figure 5.2: Concentric tubes boundary conditions

Figure 5.3: Concentric tubes experiment model

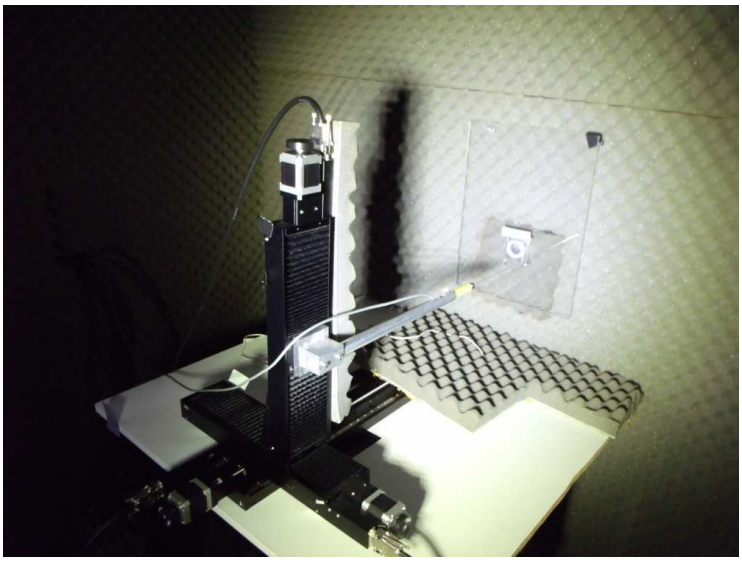

Figure 5.4: Experiment setup

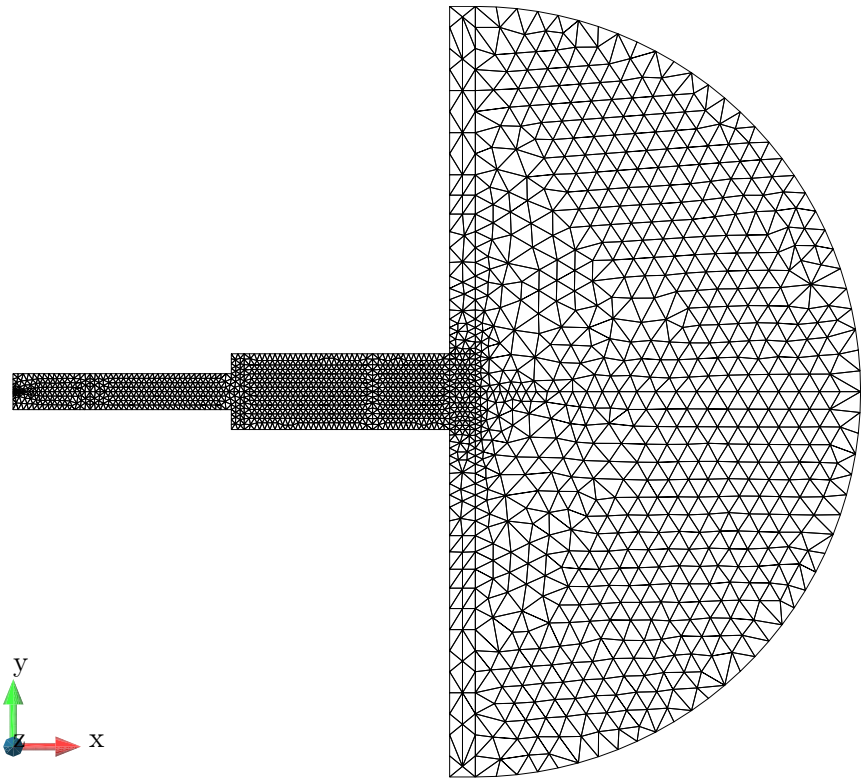

Figure 5.5: Cut on the plane $z = 0$ showing the tetrahedral mesh used

5.1.5 Results

We present the results using ASGS and OSS for spatial discretization and BE, BDF2 and CN for time discretization. Numerical results are compared with experimental results kindly provided by GIPSA-lab through EUNISON project [4]. The comparison is done in the frequency domain using the concept of transfer functions.

Let $H_{12}(f)$ be the pressure-pressure transfer function of point 2 with respect to point 1 at frequency f, let $p_1(t)$ be the pressure at point 1, let $p_2(t)$ be the pressure at point 2 and let $\hat{p}_1(f)$ and $\hat{p}_2(f)$ be the Fourier transforms of $p_1(t)$ and $p_2(t)$ respectively.

Let a signal $p(t)$ be sampled every δt time units with a total of N samples. Its Fourier transform is computed as

$$\hat{p}(f) = \frac{2}{N} \sum_{n=1}^{N} p^n \mathrm{e}^{-2\pi f i n \delta t}, \tag{5.2}$$

and the pressure-pressure transfer function is computed as

$$H_{12}(f) = \frac{\hat{p}_2(f)}{\hat{p}_1(f)}. \tag{5.3}$$

To avoid dealing with complex numbers in the computations, we store the real and imaginary parts of the Fourier transform separately, hence we compute

$$\hat{p}_R = \Re(\hat{p}(f)) = \frac{2}{N} \sum_{n=1}^{N} p^n \cos(-2\pi f n \delta t), \tag{5.4}$$

$$\hat{p}_I = \Im(\hat{p}(f)) = \frac{2}{N} \sum_{n=1}^{N} p^n \sin(-2\pi f n \delta t), \tag{5.5}$$

$$\hat{p}_M = |\hat{p}| = \sqrt{\hat{p}_R^2 + \hat{p}_I^2}, \tag{5.6}$$

$$\hat{p}_\phi = \mathrm{Arg}\,(\hat{p}) = \arctan\left(\frac{\hat{p}_I}{\hat{p}_R}\right). \tag{5.7}$$

Fig. 5.6, 5.7, 5.8 and 5.9 show contour fills of the pressure, velocity magnitude and velocity components on a cut of the domain at $t = 0.003$. These results were obtained using ASGS-CN. The other methods provide similar visual results.

Fig. 5.10, 5.11 and 5.12 show the frequency results obtained with the ASGS-BE, ASGS-BDF2 and ASGS-CN methods respectively compared with experimental results. Fig. 5.13 shows a comparison of BE, BDF2 and CN combined with ASGS spatial discretization. The results obtained with OSS are very similar to the ones obtained with ASGS and are not shown separately. Instead, we show the comparison of ASGS and OSS methods using BDF2 in Fig. 5.14 and using CN in Fig. 5.15.

As can be seen in the results, CN and BDF2 time discretizations provide the best results reproducing the experimental results. Additionally, ASGS and OSS spatial discretizations perform equally.

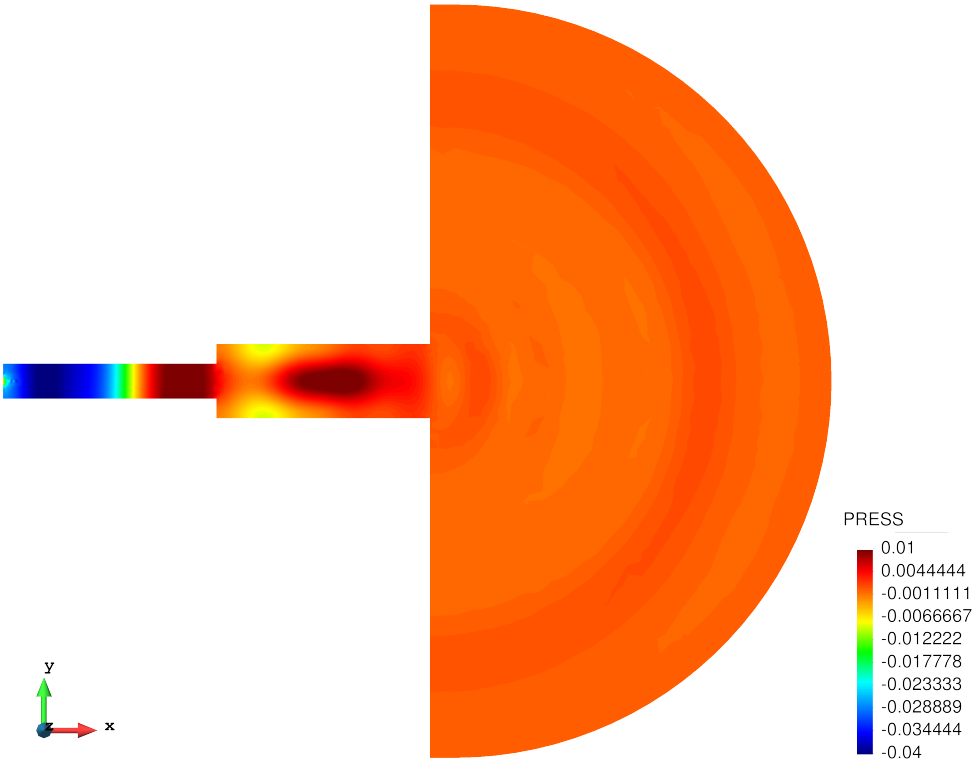

Figure 5.6: Contour fill of the acoustic pressure at $t = 0.003$

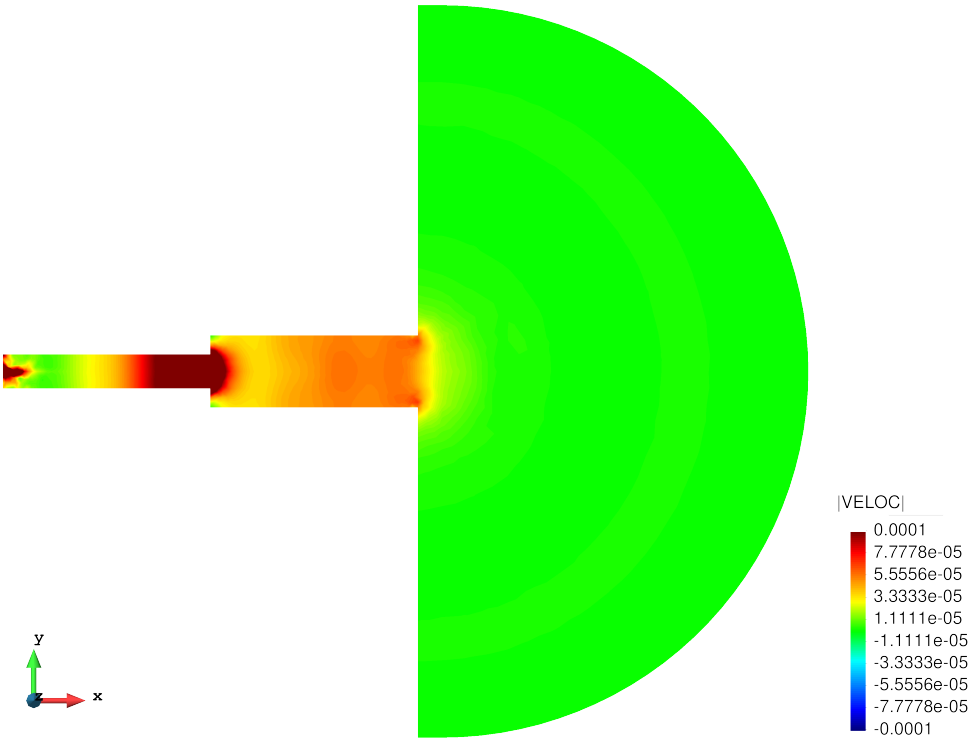

Figure 5.7: Contour fill of the acoustic velocity magnitude at $t = 0.003$

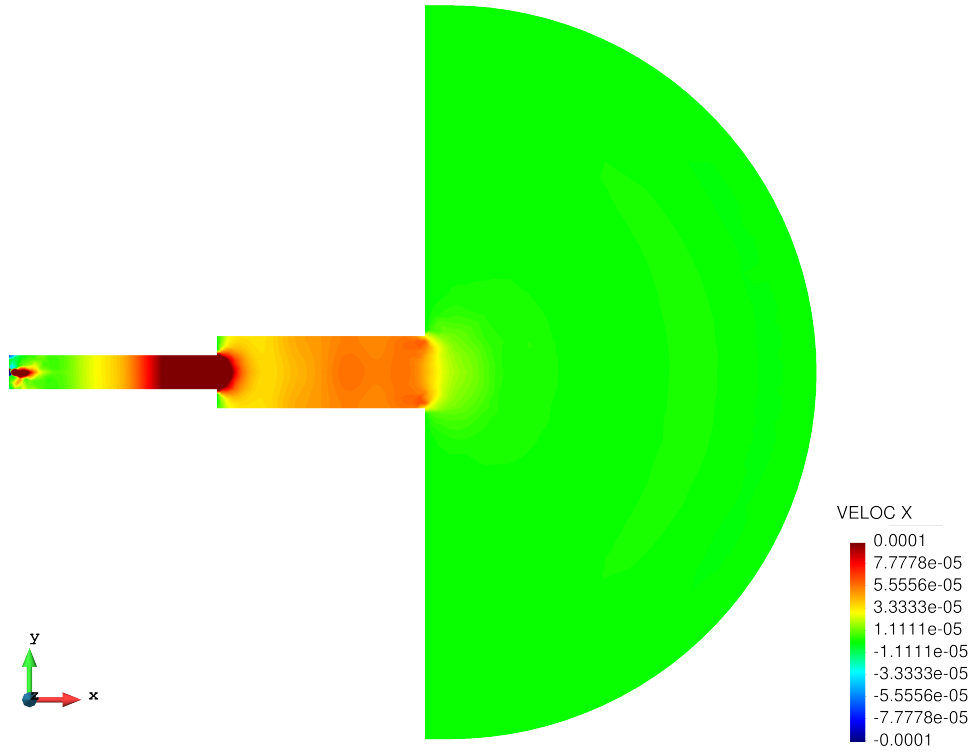

Figure 5.8: Contour fill of the x-component of the acoustic velocity at $t = 0.003$

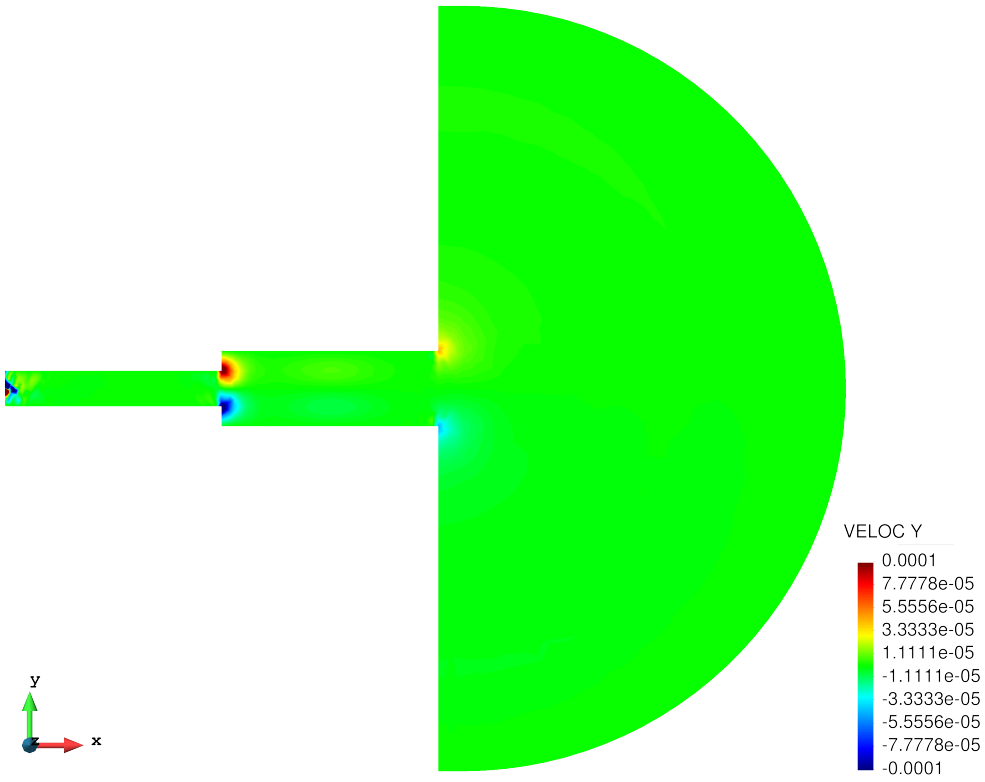

Figure 5.9: Contour fill of the y-component of the acoustic velocity at $t = 0.003$

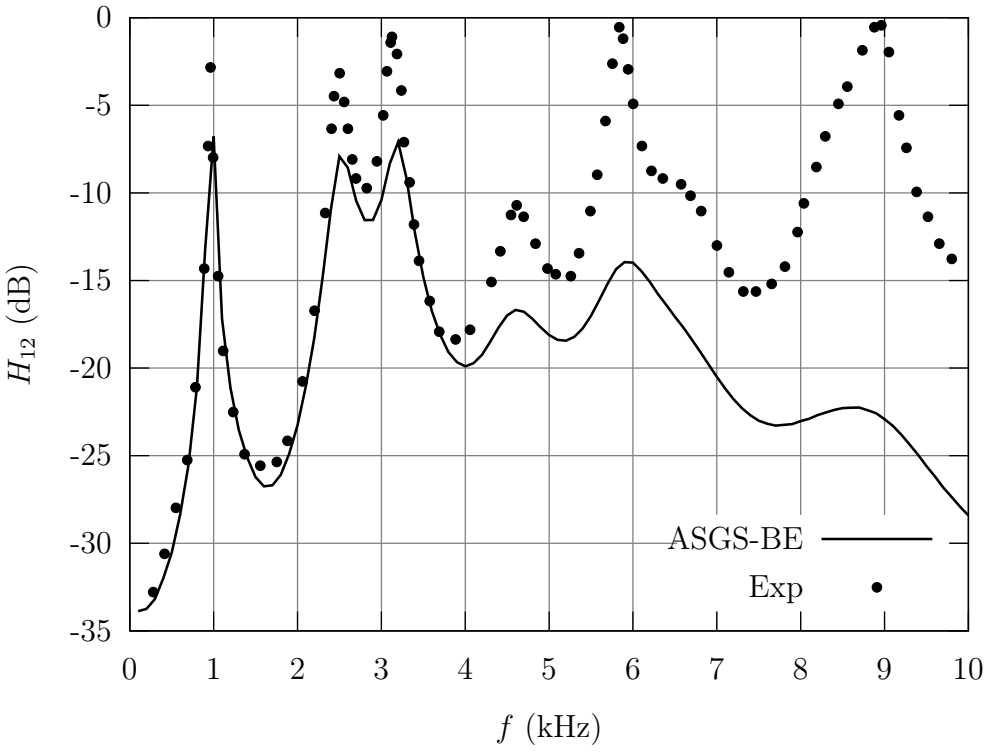

Figure 5.10: Transfer function H_{12} using ASGS-BE

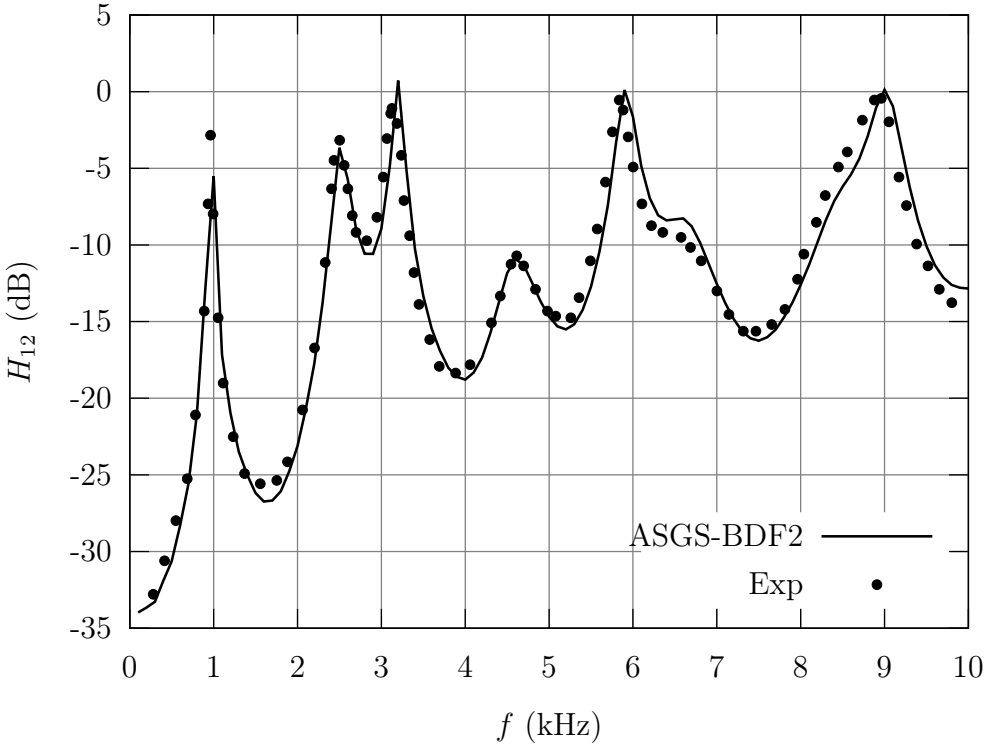

Figure 5.11: Transfer function H_{12} using ASGS-BDF2

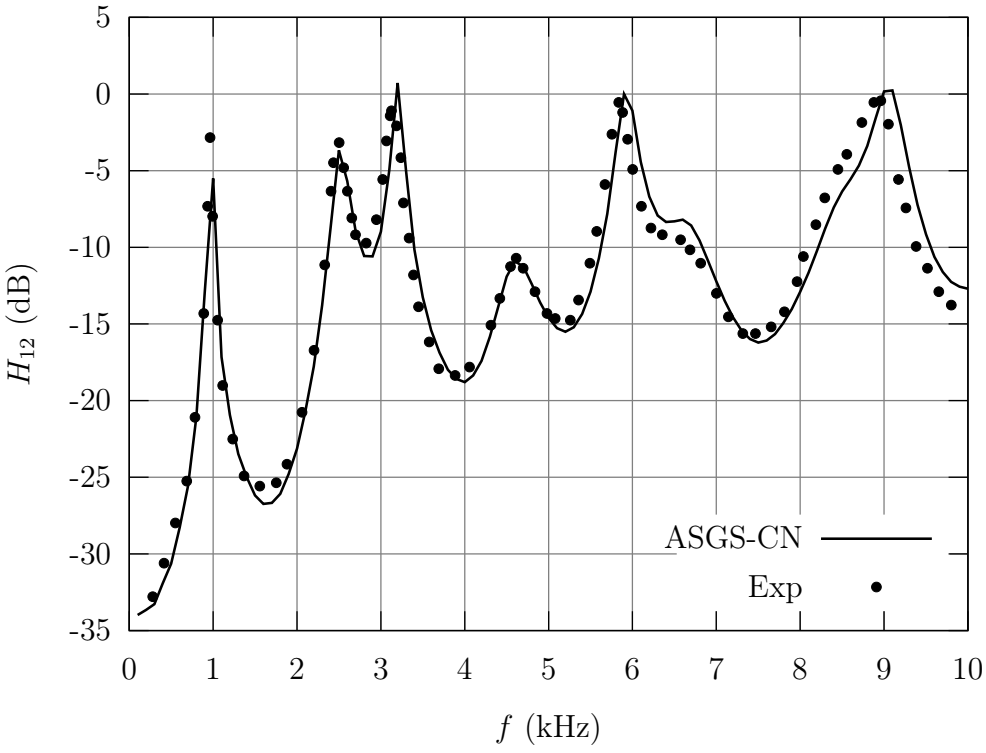

Figure 5.12: Transfer function H_{12} using ASGS-CN

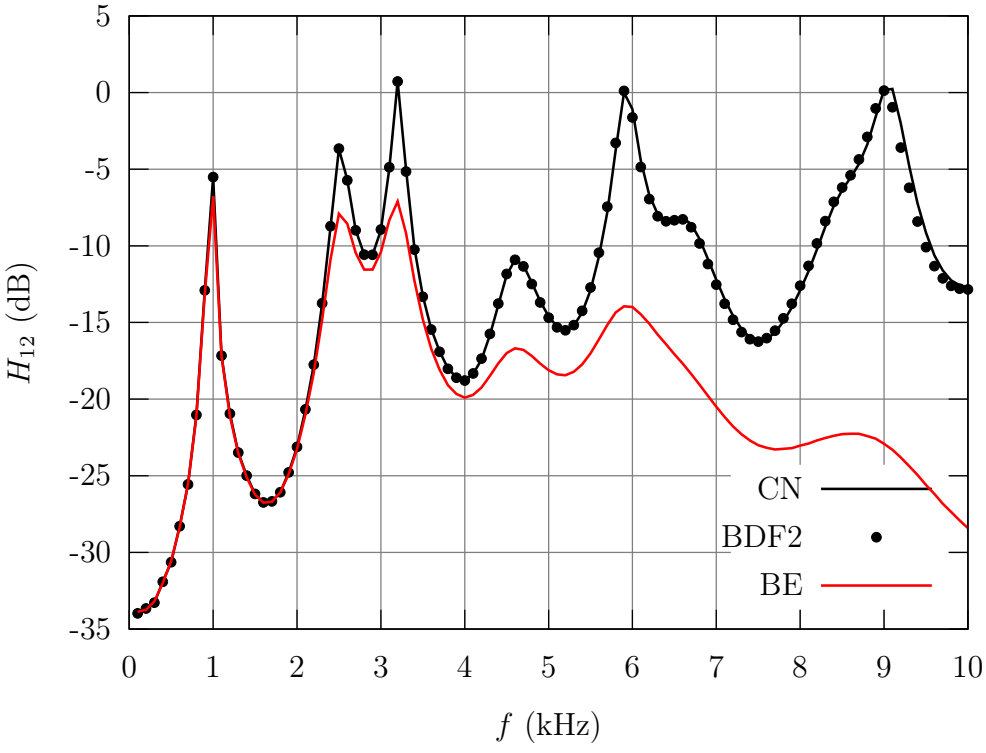

Figure 5.13: Transfer function H_{12} using ASGS

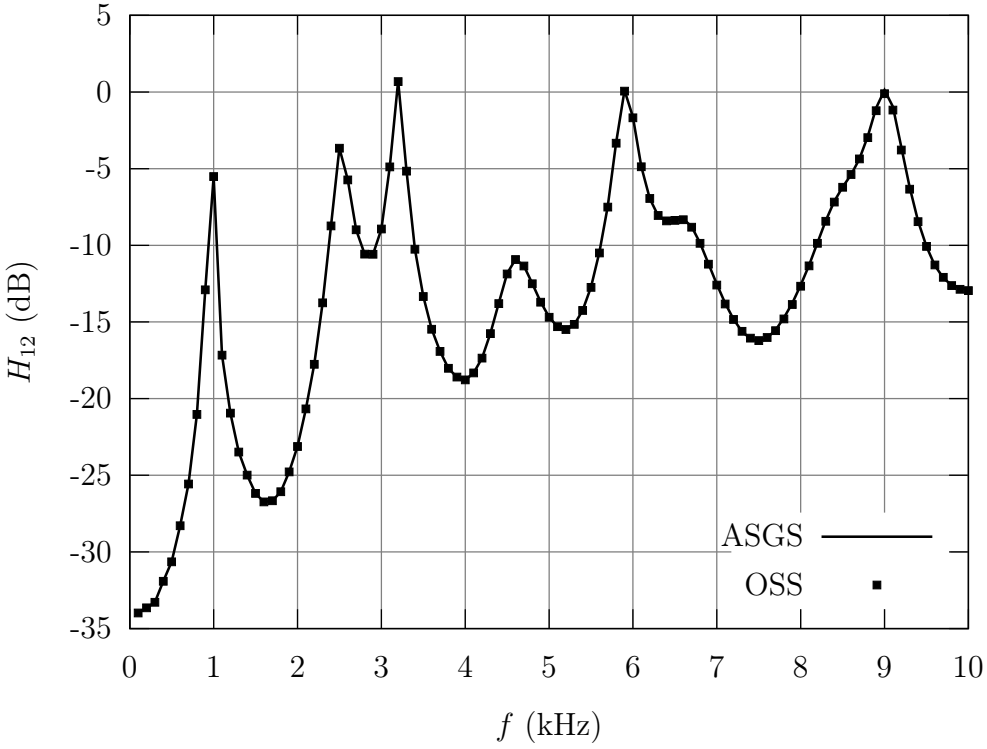

Figure 5.14: Transfer function H_{12} using BDF2

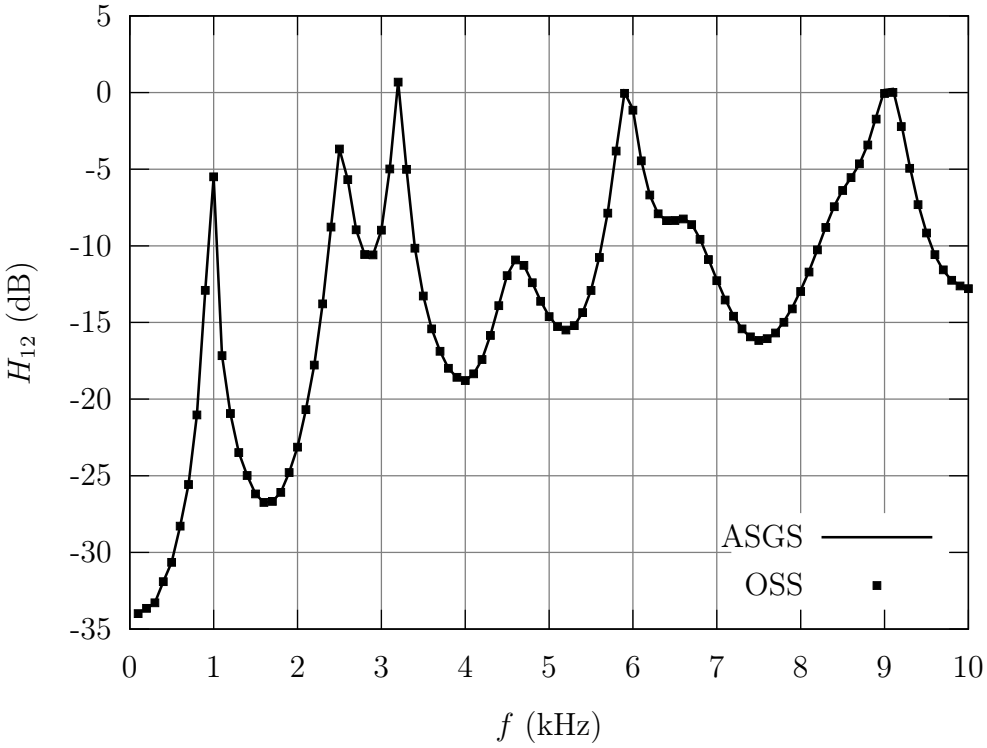

Figure 5.15: Transfer function H_{12} using CN

5.2 Eccentric Tubes

This case is very similar to the concentric tubes case. In the context of voice simulation, this geometry corresponds to a rudimentary approximation of the vocal tract in vowel /a/ position and it is regarded as a better approximation than the concentric tubes because the eccentricity mimics the distribution of cross-sections along the vocal tract. As in the case of the concentric tubes, a pressure pulse at the small diameter tube is the input signal and the end of the big diameter tube is the output to free space.

5.2.1 Space and time domains

The time interval for the simulation is 25 ms. The spatial domain consists of two eccentric tubes: one 85 mm long with a diameter of 14 mm and another tube of the same length and a diameter 29.5 mm as shown in Fig. 5.16. The smaller diameter tube is the sound inlet through a 2 mm diameter hole. Acoustic pressure and velocity are measured at points 1 and 2 for comparison with experimental results [139].

5.2.2 Boundary and Initial conditions

The boundary and initial conditions for this case are the same used in the concentric tubes case. The boundary conditions can be seen in Fig. 5.17.

5.2.3 Experimental setup

Fig. 5.18 shows the eccentric tubes experimental model. The experimental setup is the same as in the concentric tubes case and can be seen in Fig. 5.4.

5.2.4 Spatial and temporal discretization

Space was discretized using tetrahedral elements of size 0.0005 m for the input hole, 0.002 m for the tubes volume and 0.008 m for the surrounding volume. The mesh size for the input hole is based in geometrical considerations (2 mm diameter input hole). The mesh

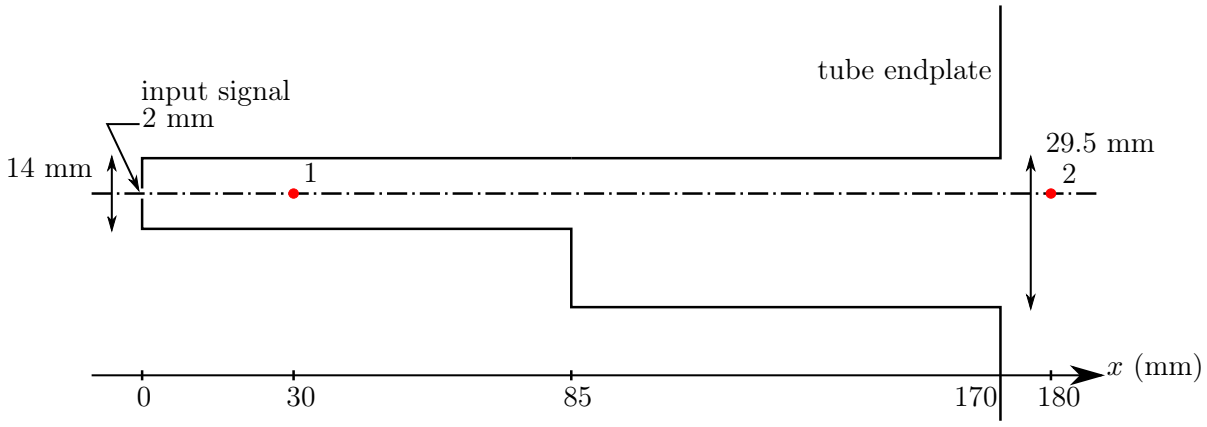

Figure 5.16: Eccentric tubes spatial domain

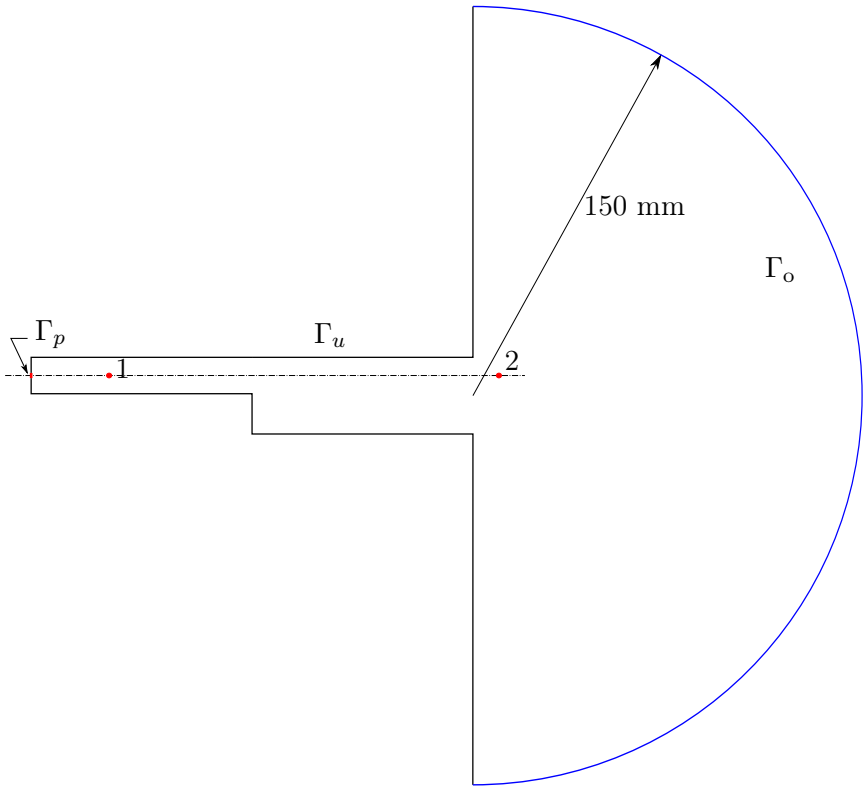

Figure 5.17: Eccentric tubes boundary conditions

Figure 5.18: Eccentric tubes experiment model

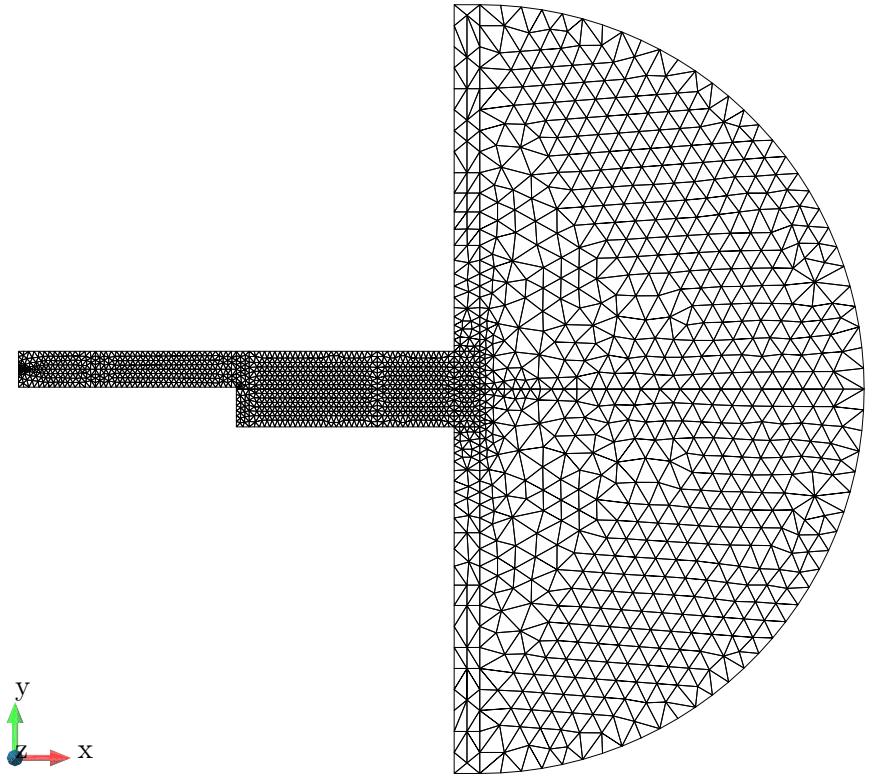

Figure 5.19: Cut on the plane $z = 0$ showing the tetrahedral mesh used

size inside the tubes is based on resolution considerations in order to have around 16 points per wavelength at 10 kHz. The surrounding volume is not important for this simulation, so a big mesh size can be taken. The mesh obtained is around 260K elements and 50K nodes. A cut on the plane $z = 0$ of the mesh used can be seen in Fig. 5.19.

For time discretization a time step $5 \cdot 10^{-6}$ s was used based on a resolution of 16 points per wave period. Several time integration schemes were used to compute the results.

5.2.5 Results

We present the results using ASGS and OSS for spatial discretization and BE, BDF2 and CN for time discretization. Numerical results are compared with experimental results kindly provided by GIPSA-lab through EUNISON project [4]. The comparison is done in the frequency domain using the concept of transfer functions explained before.

Fig. 5.20, 5.21, 5.22 and 5.23 show contour fills of the pressure, velocity magnitude and velocity components on a cut of the domain at $t = 0.003$. These results were obtained using ASGS-CN. The other methods provide similar visual results.

Fig. 5.24, 5.25 and 5.26 show the frequency results obtained with the ASGS-BE, ASGS-BDF2 and ASGS-CN methods respectively compared with experimental results. Fig. 5.27 shows a comparison of BE, BDF2 and CN combined with ASGS spatial discretization. The results obtained with OSS are very similar to the ones obtained with ASGS and are not shown separately. Instead, we show the comparison of ASGS and OSS methods using BDF2 in Fig. 5.28 and using CN in Fig. 5.29.

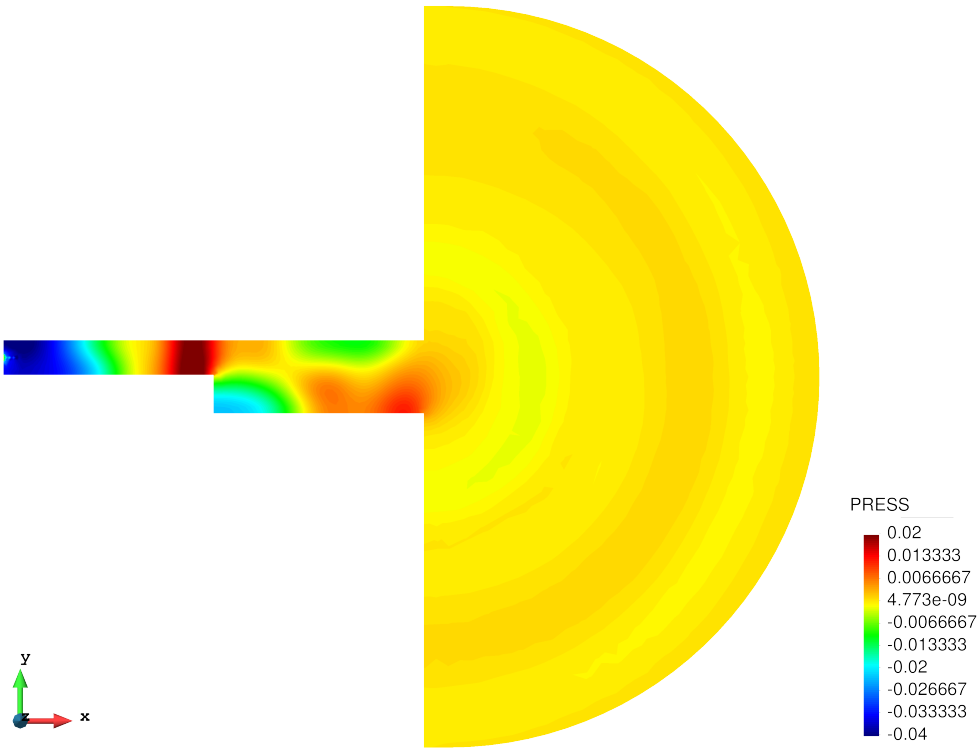

Figure 5.20: Contour fill of the acoustic pressure at $t = 0.003$

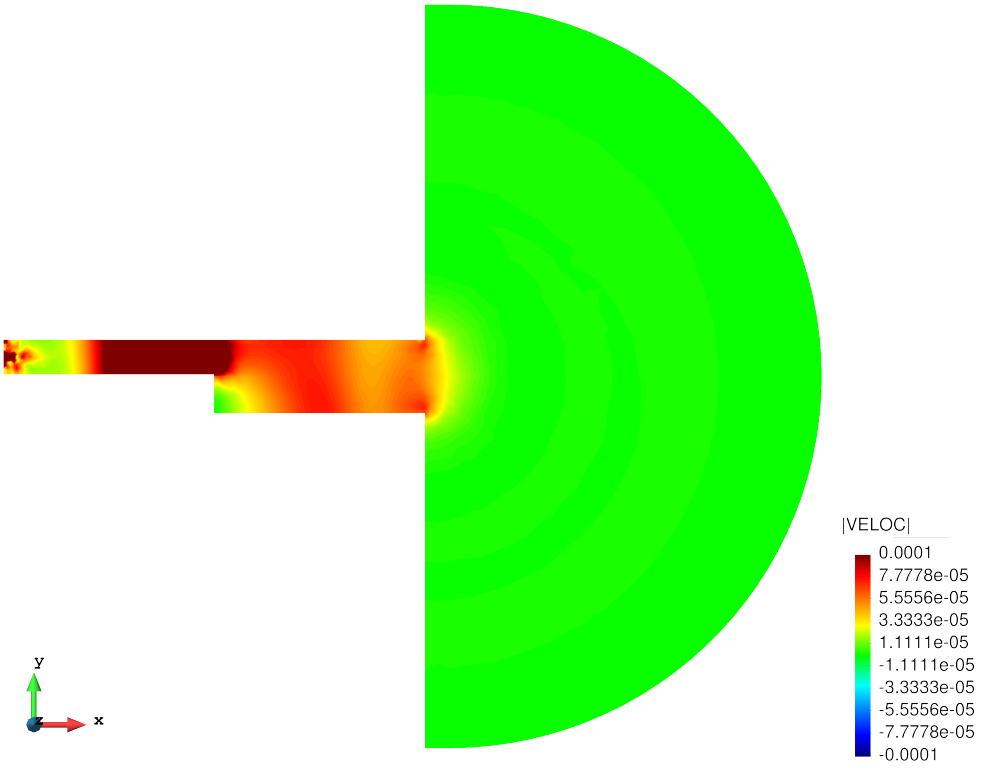

Figure 5.21: Contour fill of the acoustic velocity magnitude at $t = 0.003$

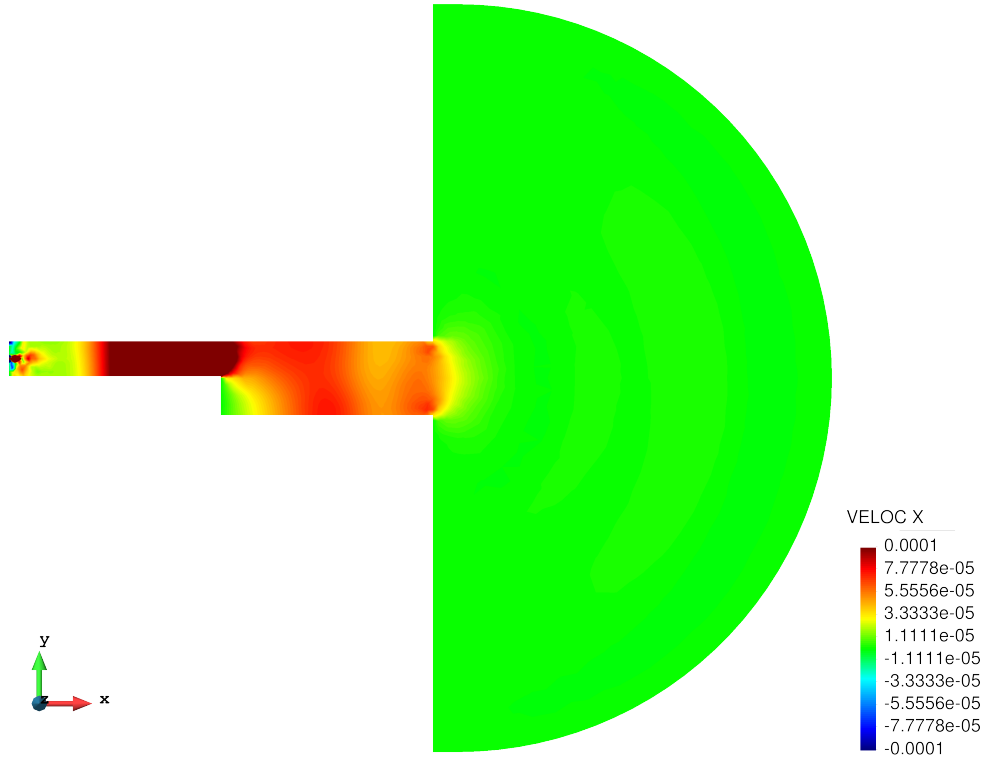

Figure 5.22: Contour fill of the x-component of the acoustic velocity at $t = 0.003$

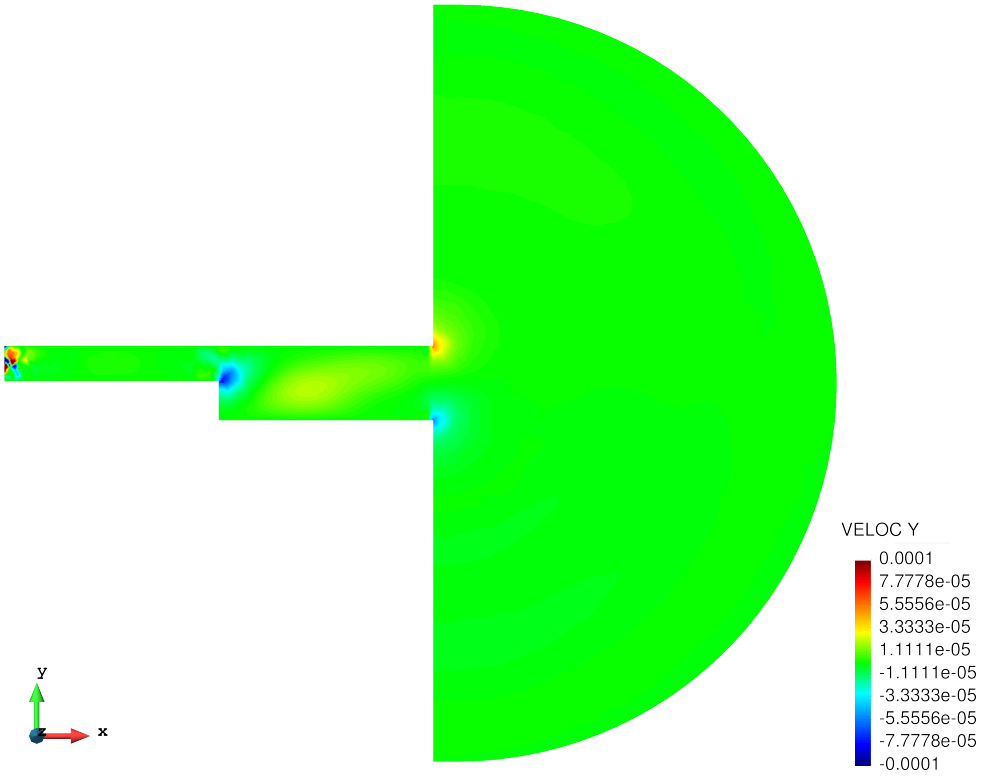

Figure 5.23: Contour fill of the y-component of the acoustic velocity at $t = 0.003$

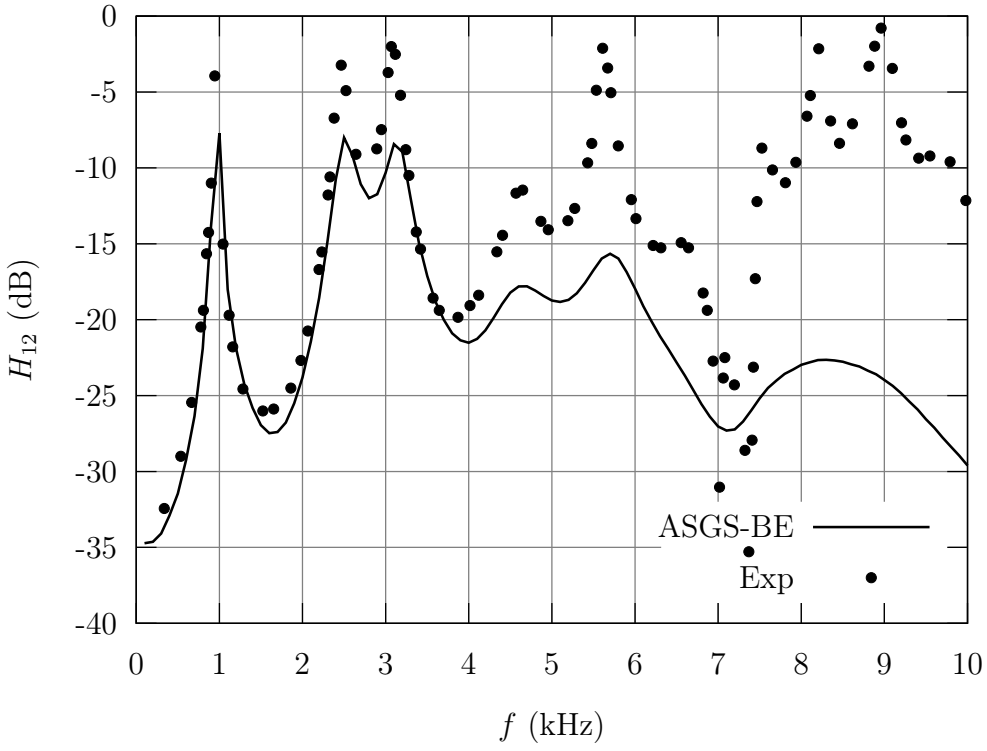

Figure 5.24: Transfer function H_{12} using ASGS-BE

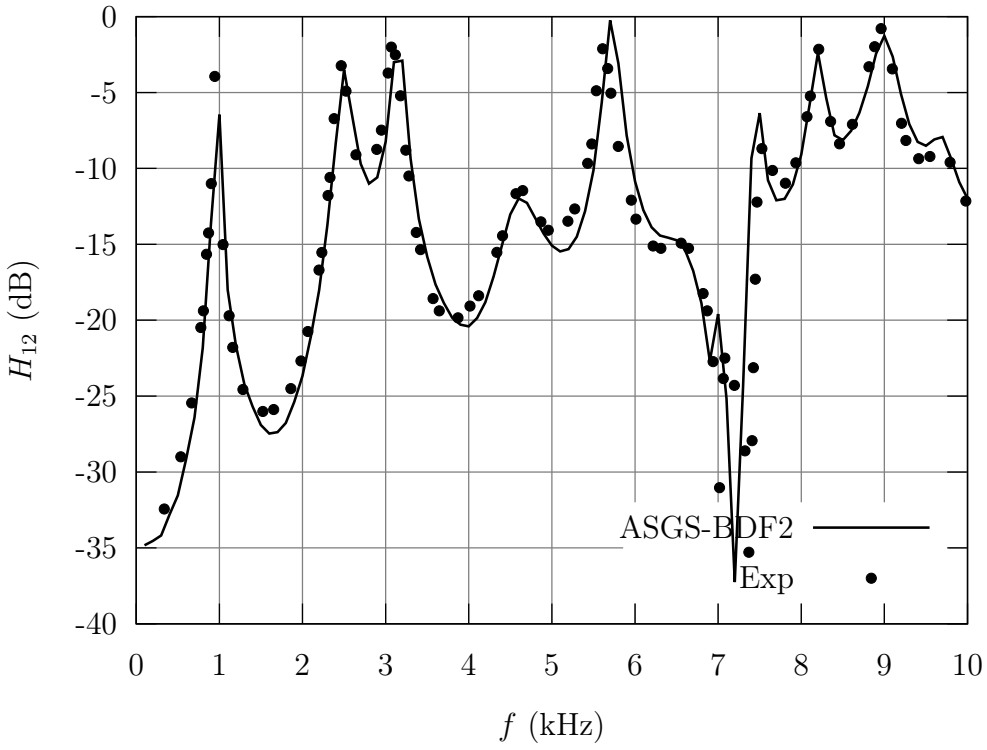

Figure 5.25: Transfer function H_{12} using ASGS-BDF2

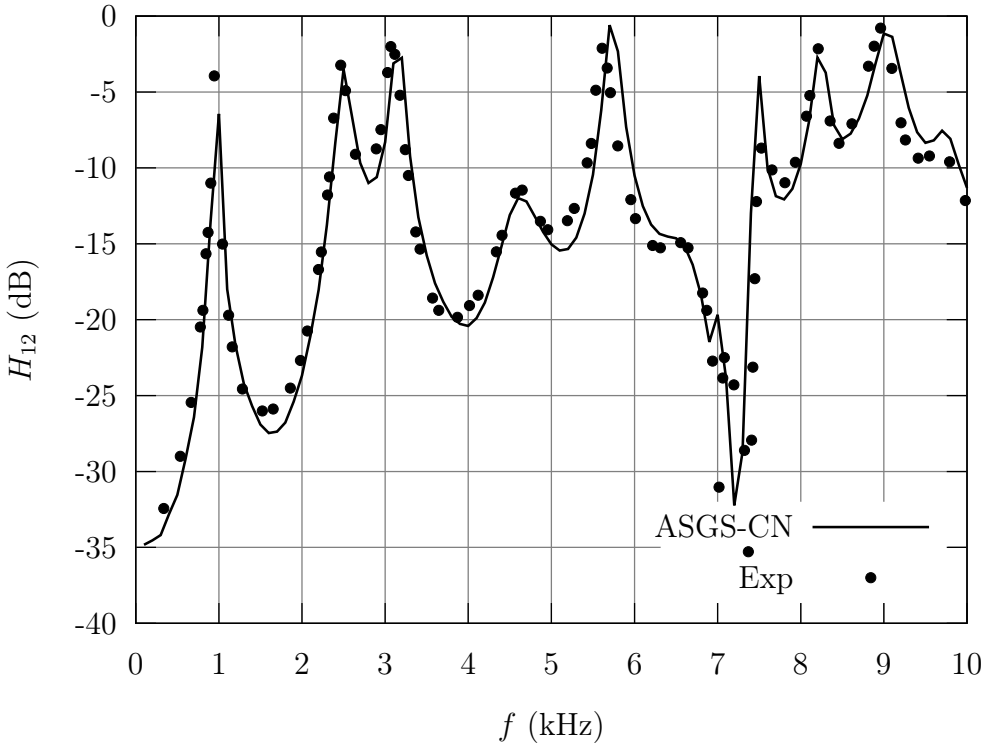

Figure 5.26: Transfer function H_{12} using ASGS-CN

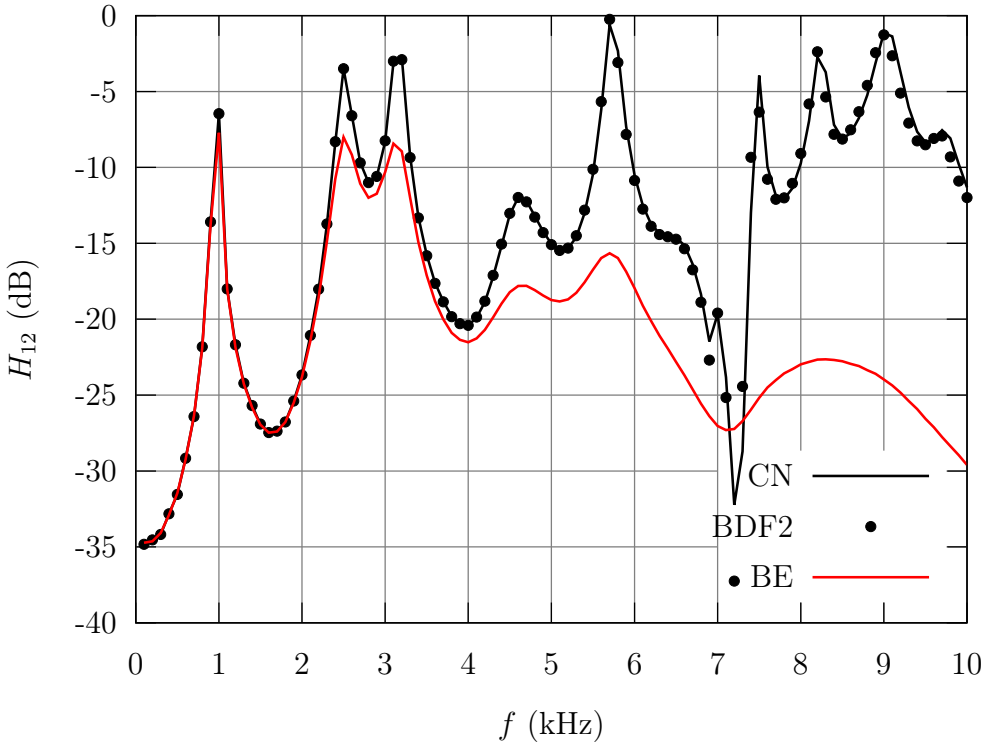

Figure 5.27: Transfer function H_{12} using ASGS

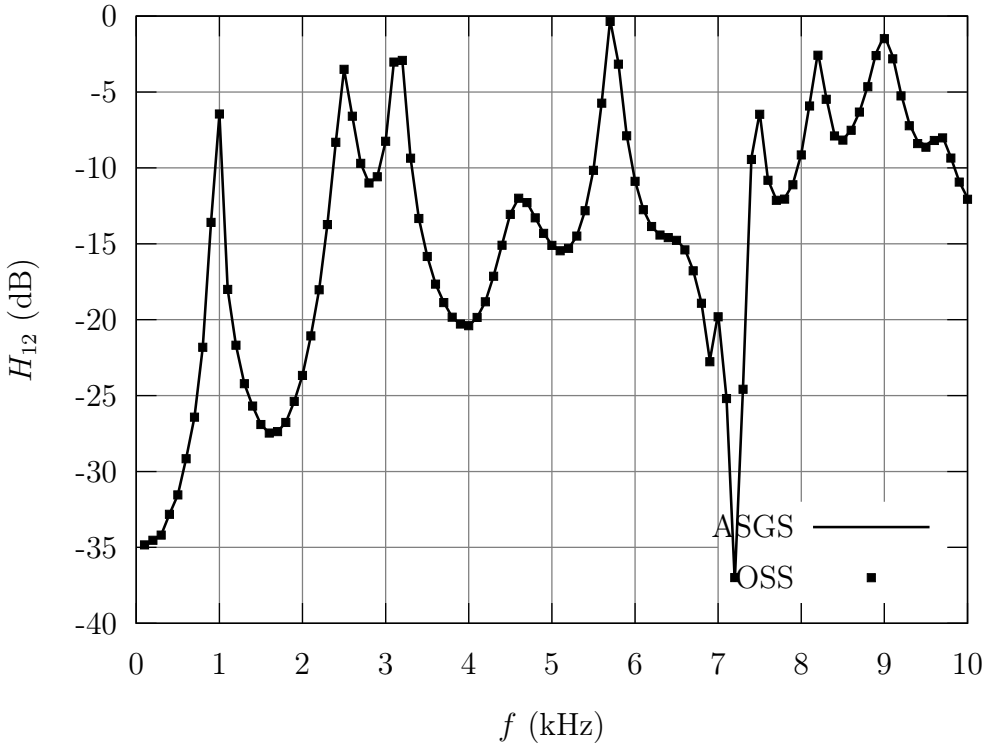

Figure 5.28: Transfer function H_{12} using BDF2

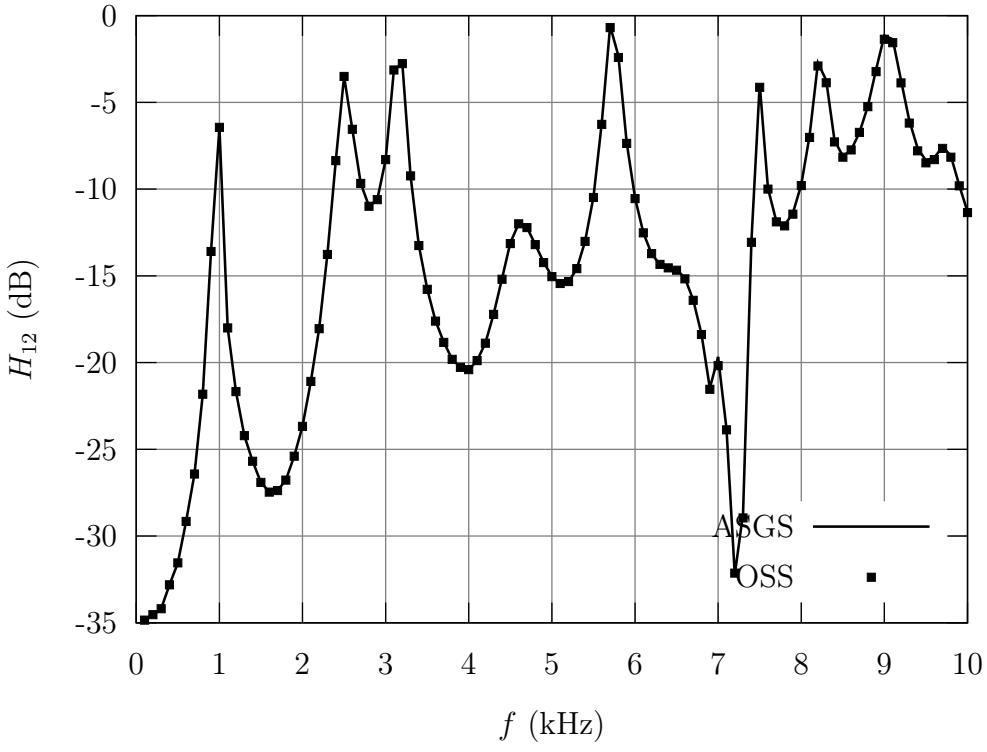

Figure 5.29: Transfer function H_{12} using CN

As can be seen in the results and as happened before in the concentric tubes case, CN and BDF2 provide the best results. Additionally, ASGS and OSS perform equally.

5.3 Vowel generation in 3D

This example consists in the wave propagation inside a realistic vocal tract in /a/ position. The geometry starts at the glottis, extends to the lips and goes onwards to free space. A realistic shape head (without hair) is included in the simulation. The 3D geometry appears in [140] and was kindly provided by the authors.

An input signal is imposed at the glottis (vocal tract inlet). This signal consists in a glottal pulse model of Rosenberg type [5].

Sound is captured in front of the lips and transformed to an audio file that can be heard and compared to the real sounding vowel /a/.

5.3.1 Space and time domains

The time interval for the simulation is 1 s. This time domain was chosen in order to obtain a long enough time series to generate an audio file.

The spatial domain is composed of the vocal tract, the head with all details (lips, nose, eyes, ears) and the open space. Fig. 5.30-5.33 show the various parts of the spatial domain. The open space is modeled by an sphere of radius 0.3 m centered at the mouth.

5.3.2 Boundary and Initial conditions

The initial conditions are zero for both pressure and velocity. The boundary conditions are applied on three different regions of the spatial domain. The first region is the vocal tract inlet where a Rosenberg glottal pulse is imposed in the normal velocity component. The

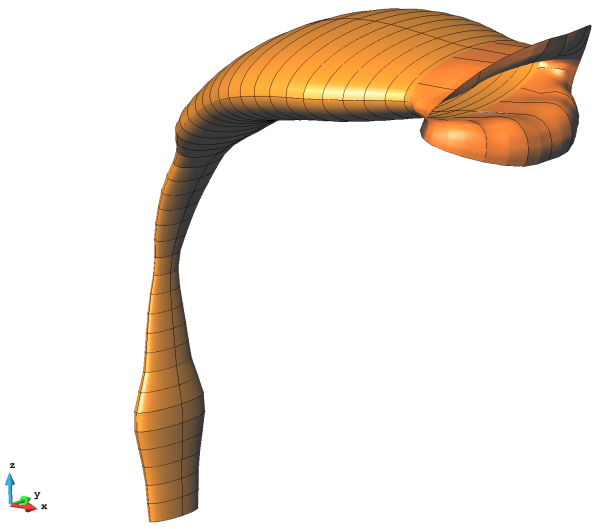

Figure 5.30: Vocal tract in 3D

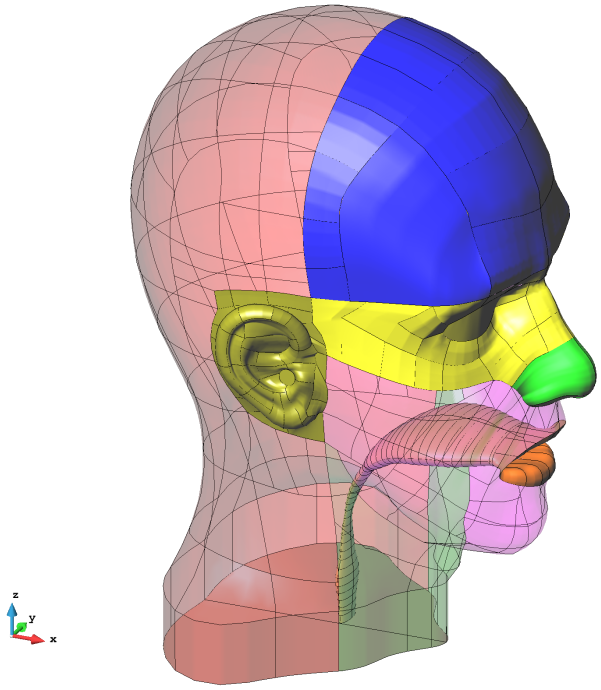

Figure 5.31: Head and vocal tract in 3D

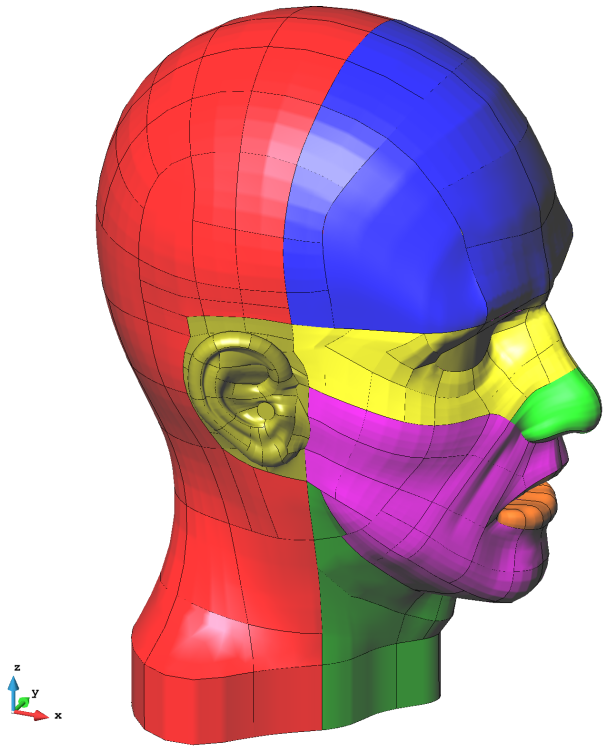

Figure 5.32: Head in 3D

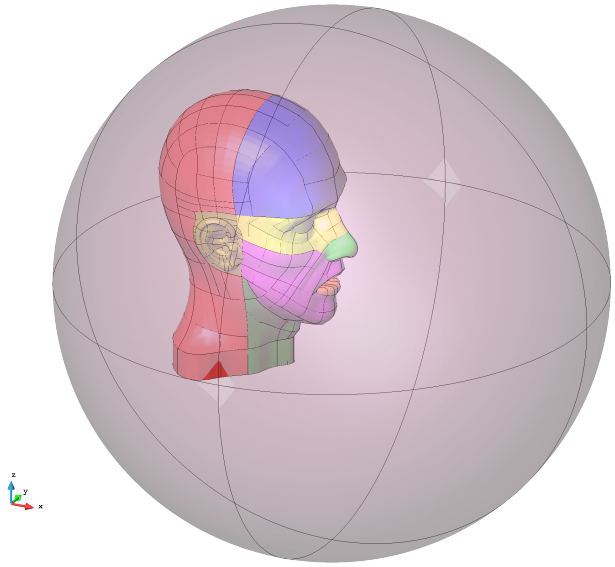

Figure 5.33: Head in 3D embedded into a sphere

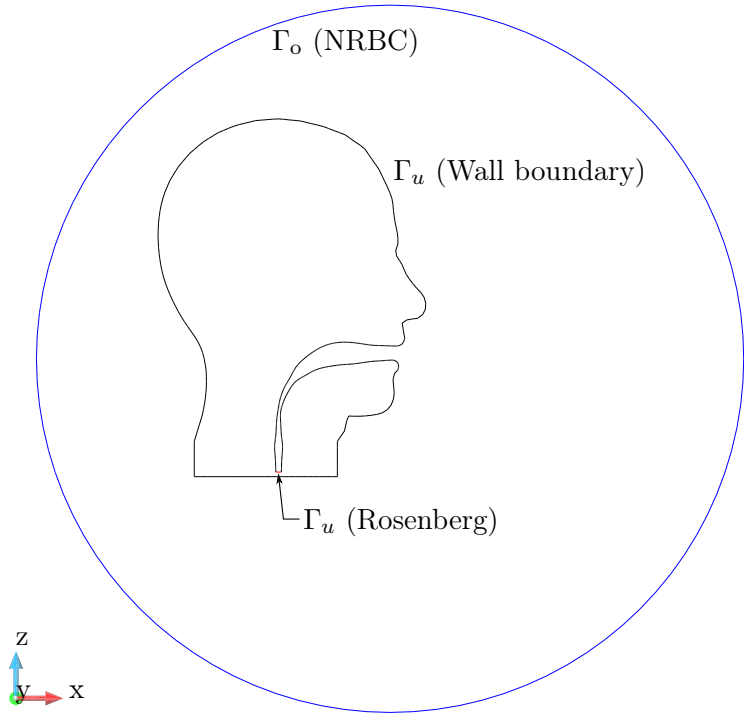

Figure 5.34: Vowel generation in 3D: boundary conditions

second region is the rest of the vocal tract surface and the exterior head surface where a rigid wall boundary condition is imposed. The third and final region is the sphere surface where a non-reflecting boundary condition is imposed. Fig. 5.34 shows a sketch of the boundary conditions.

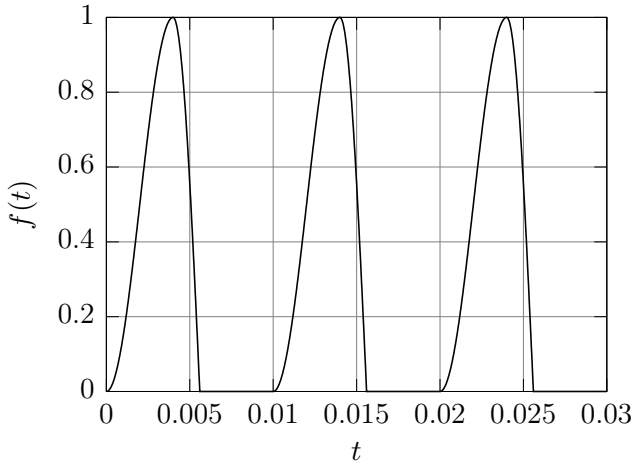

Figure 5.35: Rosenberg glottal pulse model

The Rosenberg glottal pulse model is a train of pulses. Each pulse is defined as follows

$$f(t) = \begin{cases} \frac{A}{2}\left(1 - \cos(\pi \frac{t}{T_p})\right), & 0 \leq t < T_p \\ A\cos\left(\pi \frac{t-T_p}{2T_n}\right), & T_p \leq t < T_n \\ 0, & T_n \leq t < T_0 \end{cases}, \tag{5.8}$$

where A is the amplitude, T_0 is the period of the signal, T_p is the time where the signal stops increasing and T_n is the time where the signal reaches zero again.

We will use $A = 1$, $T_0 = 0.01s$, $T_p = 0.4T_0$ and $T_n = 0.56T_0$. A plot of the Rosenberg glottal pulse can be seen in Fig. 5.35. Jitter and shimmer can be added to the input signal to make it sound more natural.

5.3.3 Spatial and temporal discretization

Space was discretized using tetrahedral elements of size 0.001 m for the vocal tract and lips, 0.005 m for the head surface and 0.02 m for the surrounding volume. The mesh size inside the vocal tract is governed by geometric details of the vocal tract, which measure less than 3 mm. The surrounding volume is not important for this simulation, so a big mesh size can be taken. Of course there is a slow transition from small size to big size. The mesh obtained is around 1M elements and 170K nodes. A cut on the plane $y = 0$ of the mesh used can be seen in Fig. 5.36.

For time discretization a BDF2 scheme with time step $2.5 \cdot 10^{-5}$ s was used.

5.3.4 Results

Figures 5.37, 5.38, 5.39 and 5.40 show contour fills of the pressure, velocity magnitude and velocity components on a cut at $y = 0$ of the domain. The y-velocity component is not shown because it is zero as the plane $y = 0$ is a symmetry plane. These results were obtained using ASGS-BDF2. OSS-BDF2 provides similar visual results.

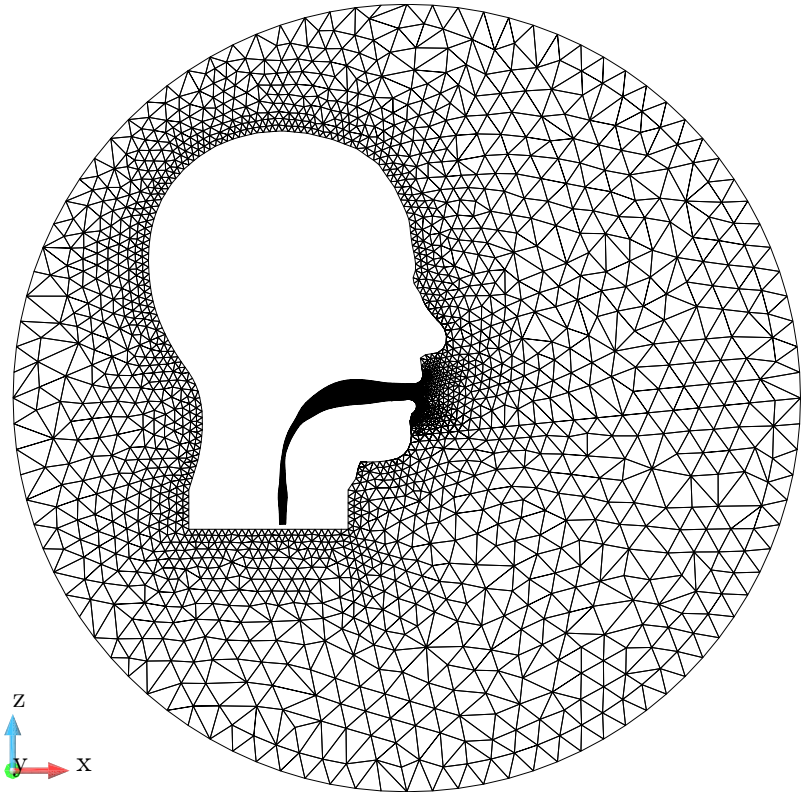

Figure 5.36: Cut on the plane $y = 0$ showing the tetrahedral mesh used

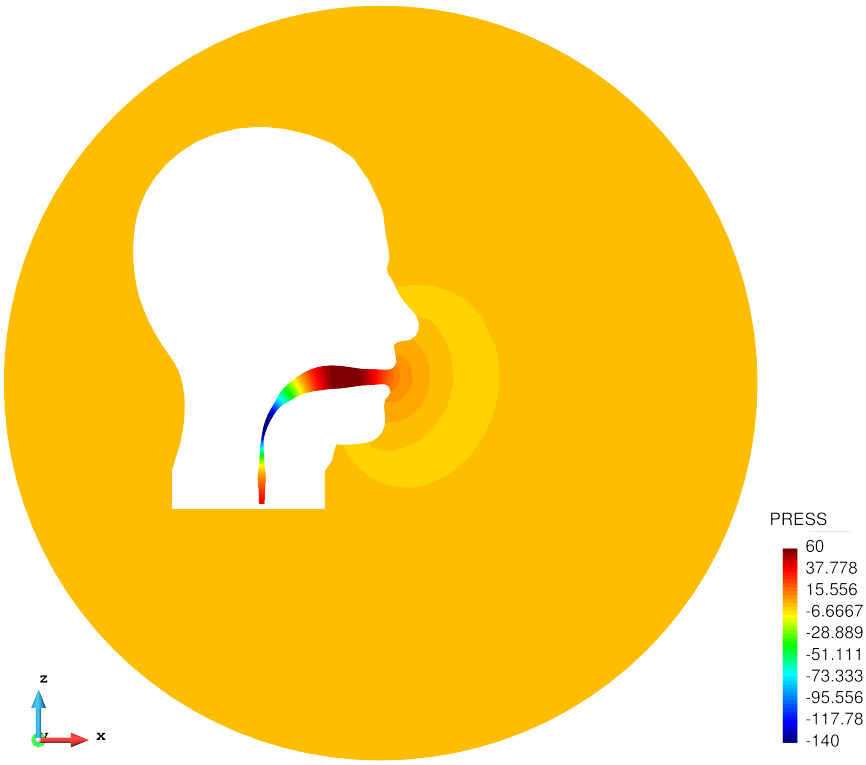

Figure 5.37: Vowel generation in 3D: contour fill of the acoustic pressure

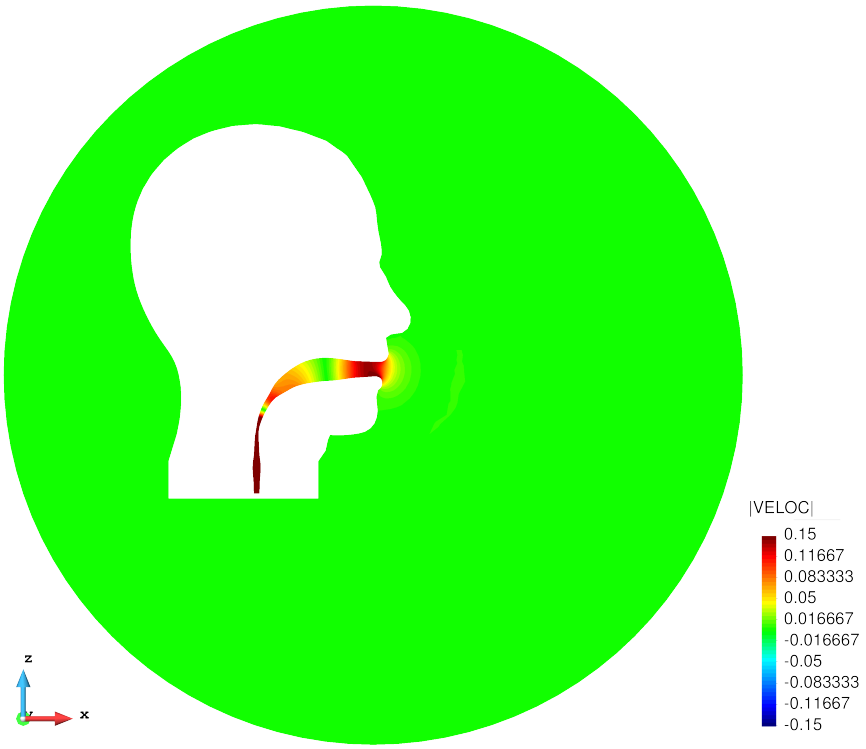

Figure 5.38: Vowel generation in 3D: acoustic velocity magnitude

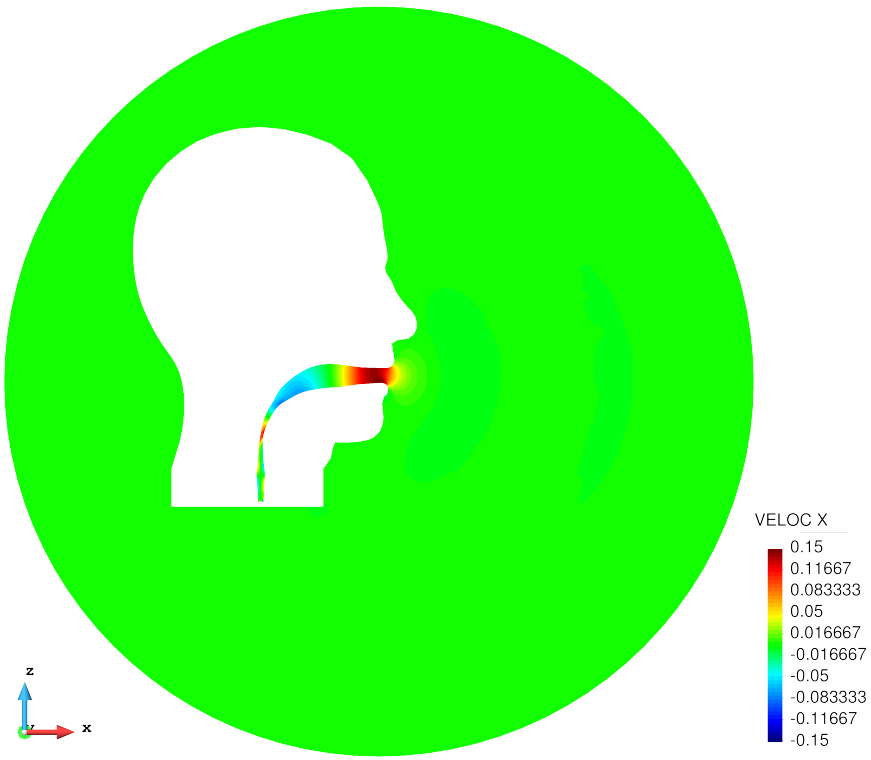

Figure 5.39: Vowel generation in 3D: x-component of the acoustic velocity

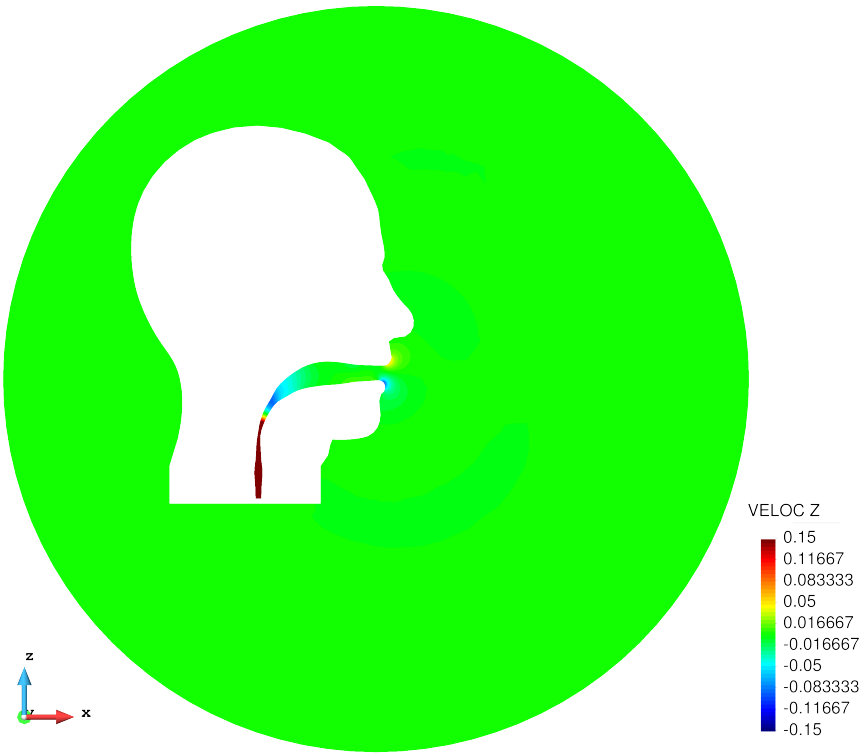

Figure 5.40: Vowel generation in 3D: z-component of the acoustic velocity

From the pressure field obtained, it is possible to extract the sound at each point. One point of interest is in front of the mouth, where an audio file can be generated and the vowel /a/ can be heard.

Additionally, we can compare the spectrum of a human-generated vowel /a/ with the one obtained from our FEM model. Fig. 5.41 shows the comparison. Notice that we have not used any filter for any of the signals. In the next section, specifically in Fig. 5.45 you can see the effects of signal processing techniques.

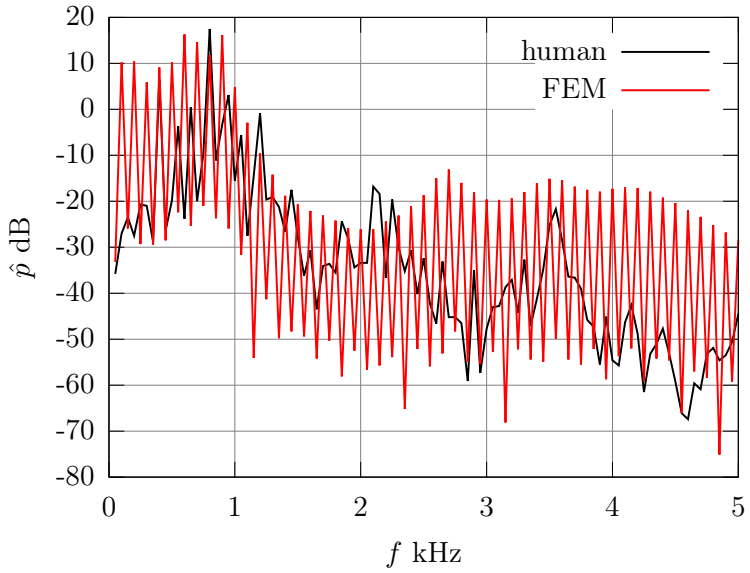

Figure 5.41: Vowel generation in 3D: spectrum comparison

5.4 Diphthong generation in 3D

This example consists in the generation of a diphthong in a 3D domain. The diphthong to be generated is /ai/. The formulation is set in an Arbitrary Lagrangian-Eulerian framework [5]. The mesh is deformed from vowel /a/ position to vowel /i/ position using linear interpolation in time. For an extended version of this example the reader is referred to [5]. There is some signal processing terminology that is not defined anywhere in the thesis but that goes beyond scope.

An input signal is imposed at the glottis (vocal tract inlet). This signal consists in a glottal pulse model of Rosenberg type. Sound is captured near the vocal tract output and compared to the real sounding diphthong /ai/.

5.4.1 Problem statement

The most natural option to deal with wave propagation in moving domains is the mixed wave equation with ALE. The mixed wave equation can be expressed in ALE formulation as:

$$\mu_p \partial_t p - \mu_p \boldsymbol{u}_\mathrm{D} \cdot \nabla p + \nabla \cdot \boldsymbol{u} = f_p, \tag{5.9}$$

$$\mu_u \partial_t \boldsymbol{u} - \mu_u \boldsymbol{u}_\mathrm{D} \cdot \nabla \boldsymbol{u} + \nabla p = \boldsymbol{f}_u, \tag{5.10}$$

where $\boldsymbol{u}_\mathrm{D}$ is the domain velocity. In the discrete setting $\boldsymbol{u}_\mathrm{D}$ will be the mesh velocity. The problem is supplemented with the initial conditions

$$p(\boldsymbol{x}, 0) = 0, \quad \boldsymbol{u}(\boldsymbol{x}, 0) = \boldsymbol{0}, \tag{5.11}$$

and with the boundary conditions

$$p = 0 \text{ on } \Gamma_p, \quad \gamma_n \boldsymbol{u} = 0 \text{ on } \Gamma_u. \tag{5.12}$$

The variational problem can be formulated as finding $p \in C^1(\Upsilon, L^2(\Omega)) \cap C^0(\Upsilon, V_p)$ and $\boldsymbol{u} \in C^1(\Upsilon, L^2(\Omega)) \cap C^0(\Upsilon, V_u)$ such that

$$\mathcal{B}([p, \boldsymbol{u}], [q, \boldsymbol{v}]) = \mathcal{L}([q, \boldsymbol{v}]), \tag{5.13}$$

for all $[q, \boldsymbol{v}] \in [V_p, V_u]$ with $V_p = \{q \in H^1(\Omega) | q = 0 \text{ on } \Gamma_p\}$, $V_u = \{\boldsymbol{v} \in H(\mathrm{div}, \Omega) | \gamma_n \boldsymbol{v} = 0 \text{ on } \Gamma_u\}$, $\boldsymbol{u}_\mathrm{D} \cdot \nabla \boldsymbol{u} \in L^2(\Omega)^d$ and

$$\mathcal{B}([p, \boldsymbol{u}], [q, \boldsymbol{v}]) = (\mu_p \partial_t p - \mu_p \boldsymbol{u}_\mathrm{D} \cdot \nabla p + \nabla \cdot \boldsymbol{u}, q) + (\mu_u \partial_t \boldsymbol{u} - \mu_u \boldsymbol{u}_\mathrm{D} \cdot \nabla \boldsymbol{u} + \nabla p, \boldsymbol{v}), \tag{5.14}$$

$$\mathcal{L}([q, \boldsymbol{v}]) = (f_p, q) + (\boldsymbol{f}_u, \boldsymbol{v}). \tag{5.15}$$

Using stabilized finite elements the space-discrete problem reads: find $[p_h, \boldsymbol{u}_h]$ such that

$$\mathcal{B}_s([p_h, \boldsymbol{u}_h], [q_h, \boldsymbol{v}_h]) = \mathcal{L}_s([q_h, \boldsymbol{v}_h]), \tag{5.16}$$

for all test functions $[q_h, \boldsymbol{v}_h] \in [V_{p,h}, V_{u,h}]$ where

$$\begin{aligned} \mathcal{B}_s([p_h, \boldsymbol{u}_h], [q_h, \boldsymbol{v}_h]) = \mathcal{B}([p_h, \boldsymbol{u}_h], [q_h, \boldsymbol{v}_h]) &+ (P'(\mu_p \partial_t p_h - \mu_p \boldsymbol{u}_\mathrm{D} \cdot \nabla p_h + \nabla \cdot \boldsymbol{u}_h), \tau_u \nabla \cdot \boldsymbol{u}_h) \\ &+ (P'(\mu_u \partial_t \boldsymbol{u}_h - \mu_u \boldsymbol{u}_\mathrm{D} \cdot \nabla \boldsymbol{u}_h + \nabla p_h), \tau_p \nabla p_h), \end{aligned} \tag{5.17}$$

$$\mathcal{L}_s([q_h, \boldsymbol{v}_h]) = \mathcal{L}([q_h, \boldsymbol{v}_h]) + (P'(f_p), \tau_u \nabla \cdot \boldsymbol{v}_h) + (P'(\boldsymbol{f}_u), \tau_p \nabla q_h), \tag{5.18}$$

with the stabilization parameters τ_p and τ_u defined as

$$\tau_p = \frac{h}{C_1(\mu_p \mu_u)^2 |\boldsymbol{u}_\mathrm{D}| + C_2} \sqrt{\frac{\mu_u}{\mu_p}}, \quad \tau_u = \frac{h}{C_1(\mu_p \mu_u)^2 |\boldsymbol{u}_\mathrm{D}| + C_2} \sqrt{\frac{\mu_p}{\mu_u}}. \tag{5.19}$$

The projection operator $P'(\cdot)$ can be chosen as either the identity to obtain the ASGS method or the $L^2(\Omega)$-orthogonal projection to obtain the OSS method.

The time discretization is straightforward and BE, CN and BDF2 methods can be applied.

With regard to the motion of the computational mesh, it will be prescribed by the known displacement at the domain boundaries. The motion of the boundary nodes becomes smoothly transmitted to the inner mesh nodes through diffusion, i.e. using the standard strategy of solving the Laplacian equation for the node displacements $\boldsymbol{w}(\boldsymbol{x}, t)$. Therefore, at each time step n+1 we will solve the additional equation

$$\nabla^2 \boldsymbol{w}^{n+1} = 0 \text{ in } \Omega \tag{5.20}$$

with boundary conditions

$$\boldsymbol{w}^{n+1} = {\boldsymbol{x}_\mathrm{m}}^{n+1} - {\boldsymbol{x}_\mathrm{m}}^{n} \text{ on } \Gamma_\mathrm{m}, \quad \gamma_n \boldsymbol{w}^{n+1} = 0 \text{ on } \Gamma_\mathrm{f}, \tag{5.21}$$

and the mesh node positions being updated according to

$${\boldsymbol{x}_\mathrm{D}}^{n+1} = {\boldsymbol{x}_\mathrm{D}}^{n} + \boldsymbol{w}^{n+1}. \tag{5.22}$$

Γ_m represents the boundary of Ω evolving with prescribed displacement $\boldsymbol{x}_\mathrm{m}(\boldsymbol{x}, t)$, whereas Γ_f denotes a fixed boundary of Ω. From the displacements $\boldsymbol{w}(\boldsymbol{x}, t)$ one can compute the mesh velocity using an appropriate time integration scheme (e.g. BE).

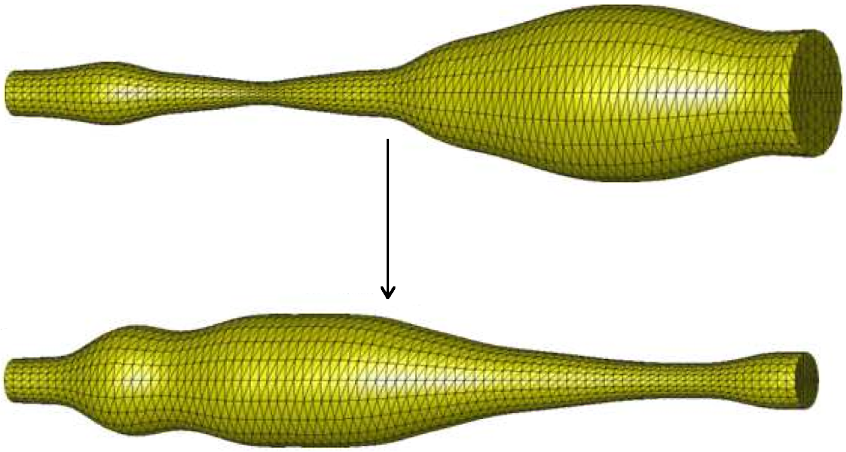

Figure 5.42: Simplified vocal tract in 3D: /a/ position and /i/ position

5.4.2 Space and time domains

The time interval for the simulation is 0.2 s. The spatial domain is is a simplified 3D model of the vocal tract consisting in circular concentric cross-sections as shown in Fig. 5.42.

5.4.3 Boundary and Initial conditions

The initial conditions are zero for both pressure and velocity. The initial mesh condition is an average between the two extreme positions in order to avoid excessive mesh distortion. The boundary conditions are applied on three different regions of the spatial domain. The first region is the vocal tract inlet where a Rosenberg glottal pulse is imposed. The second region is the rest of the vocal tract surface where a rigid wall boundary condition is imposed. The third and final region is the vocal tract output where $p = 0$ is imposed.

To increase the naturalness of the diphthong, the glottal pulses have been enhanced introducing a pitch curve for the fundamental frequency, adding some shimmer to the signal amplitude and applying a fade in/out to the global signal.

5.4.4 Spatial and temporal discretization

Space was discretized using tetrahedral elements of size 0.002 m for the whole vocal tract. The mesh can be seen in Fig. 5.42. The stabilization parameters were taken as $C_1 = 0.01$ and $C_2 = 10$. For time discretization a BDF2 scheme with time step $1.25 \cdot 10^{-5}$ s was used.

5.4.5 Results

Fig. 5.43 shows a contour fill of the pressure at different time steps together with the mesh movement. These results were obtained using ASGS-BDF2.

From the pressure field obtained, it is possible to extract the sound at each point. One point of interest is near the vocal tract outlet, where an audio file can be generated and the diphthong /ai/ can be heard.

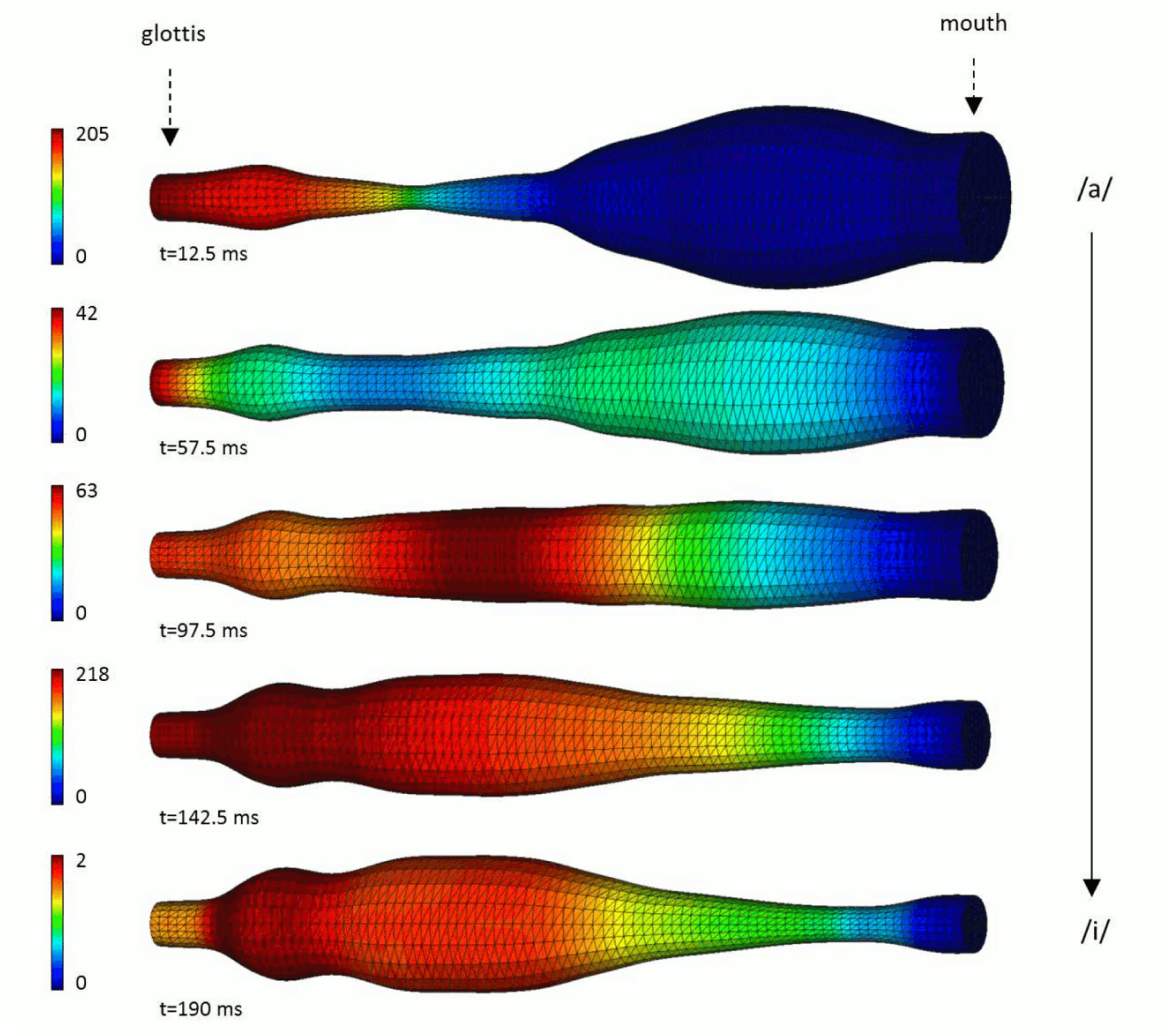

Figure 5.43: Diphthong generation in 3D: contour fill of the acoustic pressure

Fig. 5.44 shows the pressure evolution at the vocal tract outlet.

Fig. 5.45 shows the spectrogram corresponding to the acoustic pressure in Fig. 5.44. This has been computed using a Hamming window with a frame width of 20 ms and an overlap of 1 ms. As usually done in speech processing, a pre-emphasis FIR filter with coefficients [1 -0.97] has been applied to enhance the visualization of the high frequency range. In the first curve of the spectrogram, corresponding to vowel /a/, we can clearly identify the two formants of vowel /a/. Similarly, the last curve of the spectrogram corresponds to vowel /i/ and its two formants an also be clearly recognized. The trajectories of the two formants F1 and F2, which separate apart from /a/ to /i/, have been highlighted to appreciate clearly their evolution.

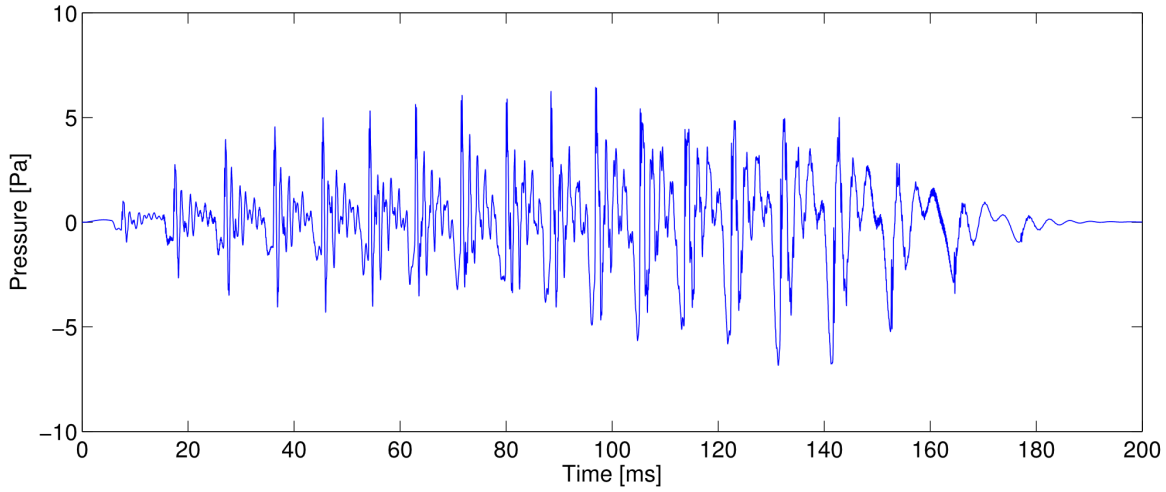

Figure 5.44: Diphthong generation in 3D: pressure evolution at the vocal tract outlet

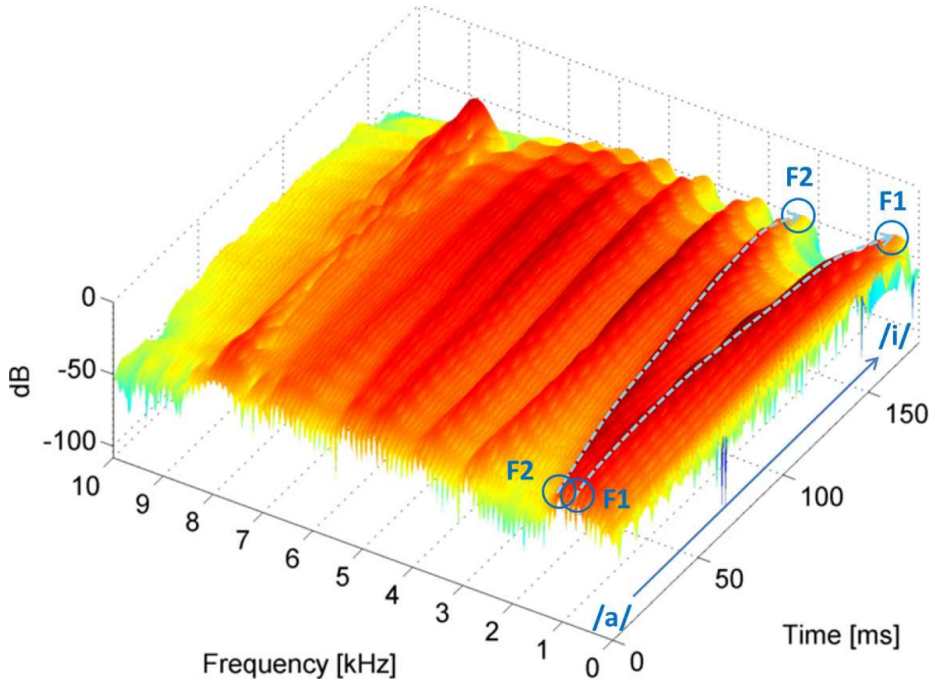

Figure 5.45: Diphthong generation in 3D: pressure spectrogram for diphthong /ai/

Chapter 6

Conclusions

6.1 Achievements

One achievement of this work is the formulation and analysis of two stabilized finite element methods for solving the wave equation in mixed form. The variational problem can be cast in three different variational forms, each one requiring a certain regularity on the unknowns. The formulation includes ASGS and OSS methods taylored to work in three different functional frameworks in which the regularity requirements of the scalar space are transferred to the vector one or vice-versa. The analysis includes stability and convergence for both stabilization methods and for all variational forms. Additionally, numerical tests were performed to compare numerical results with theoretical predictions.

Another achievement is the formulation and analysis of a non-reflecting boundary condition (NRBC) that fits into the stabilization methods and functional settings. The introduction of the NRBC motivated a slight modification of the functional framework and working norms in which we were able to prove stability and convergence of the formulations. Numerical convergence tests were performed to compare with theoretical convergence predictions. Finally, many numerical examples were solved in 2D and 3D to show the capabilities of the NRBC.

Moreover, time marching schemes applied to the mixed wave equation were implemented and analyzed. One part of the analysis includes stability and convergence of the fully discrete schemes. The other part involves stability, dispersion and dissipation analysis with the aid of Fourier techniques. A 1D example was solved to compare numerical results with Fourier predictions which yielded good agreement between both.

Furthermore, various wave propagation problems were solved and some of them compared simulation results with experimental results. These problems are mainly 3D and include realistic geometries. One of the main results is voice simulation inside the vocal tract and open space in order to reproduce a vowel /a/ starting from a glottal signal as input. Another main result is diphthong simulation using an ALE formulation.

6.2 Concluding Remarks

The implementation of the mixed wave equation with the discretization methods described in this thesis is not difficult. The only implementation difficulty for time-dependent-

only problems as this one is that space/time discretization is always coupled. In other words, when implementing a (full) discretization method from zero and it does not work as expected, the implementation error can be anywhere. Finding the error cannot be tackled by first solving a steady-state version of the problem, then making it work and finally solving the time-dependent version.

The implementation of the non-reflecting boundary condition described in this thesis is straightforward. It only involves terms on the boundary. There is no need of an additional layer of absorbing material which introduces extra degrees of freedom. Anyway, I have not worked with absorbing layers to give a more informed comparison of both. In the application examples the NRBC has worked very well when using a smooth NRBC-surface. This is reflected in the close agreement between numerical simulations and experiments. In the benchmark cases, despite using square geometries in 2D or cubes in 3D, the NRBC has given good results in the sense of monotonous energy dissipation.

Let us consider the stability of the spatial discretization methods (ASGS and OSS). Both methods are stable with respect to their respective working norm(s)/external forces norm(s) pairs. I have to mention that the regularity requirements of the external forces for stability differs for ASGS and OSS. Nevertheless, for the same value of the stabilization algorithmic constant, both ASGS and OSS exhibit the same stability in practice. That is, there are no node-to-node oscillations and the results look visually similar.

Let us consider the accuracy of the spatial discretization methods with respect to the error in the unknowns in their respective norm(s). The spatial discretization methods presented, namely ASGS and OSS, can exhibit up to optimal convergence rates depending on the variational form. However, the convergence proofs presented are not sharp enough leaving the theoretical convergence rates as quasi-optimal at best.

6.3 Future Work

The wave equation in mixed form was solved using stabilized finite element methods allowing us to use equal interpolation spaces for both the scalar and vector unknowns and avoiding inf-sup stable elements. Additional stabilization sophistications still need to be formulated, implemented and analyzed such as dynamic sub-scales. Furthermore, a fractional step scheme for the formulation needs to be developed in order to solve bigger problems more efficiently.

More accurate non-reflective boundary conditions applied to the mixed wave equation need to be researched. It is said that the Sommerfeld boundary condition is zero-order accurate ($J = 0$), although we found it is order $J = 0.66$ in 2D.

In this work we analyzed and implemented up to 2nd order time marching schemes (BE, BDF2 and CN). Higher order schemes should be explored such as Runge-Kutta and symplectic Runge-Kutta. Additional energy-preserving or momentum-preserving schemes should be considered and analyzed as well.

The wave equation in mixed form has proven useful for dealing with moving domains in ALE formulation since it is not possible to express the irreducible wave equation in a moving domain. Stability and convergence of the ALE formulation has yet to be analyzed. Additionally, aeroacoustics in moving domains has to be developed through the computation of source terms from the incompressible flow solver.

References

[1] Nigel Peake and Anthony B. Parry. "Modern Challenges Facing Turbomachinery Aeroacoustics". In: *Annual Review of Fluid Mechanics* 44 (2012), pp. 227–228. DOI: 10.1146/annurev-fluid-120710-101231 (cit. on p. 1).

[2] Edward M. Greitzer and H. N. Slater. *N+3 Aircraft Concept Designs and Trade Studies*. Tech. rep. tech report. MIT, Aurora Flight Sciences, and Pratt & Whitney Team, Mar. 2010 (cit. on p. 1).

[3] Rajat Mittal, Byron D. Erath, and Michael W. Plesniak. "Fluid Dynamics of Human Phonation and Speech". In: *Annual Review of Fluid Mechanics* 45.1 (2013), pp. 437–467. DOI: 10.1146/annurev-fluid-011212-140636 (cit. on p. 1).

[4] *Extensive UNIfied-domain SimulatiON of the human voice (EUNISON)*. FP7-ICT-2011-C 308874. 2015. URL: http://fp7eunison.com/ (cit. on pp. 1, 125, 133).

[5] Oriol Guasch, Marc Arnela, Ramon Codina, and Hector Espinoza. "A stabilized finite element method for the mixed wave equation in an ALE framework with application to diphthong production". In: *Journal of Computational Physics* (Oct. 2014). Submitted (cit. on pp. 1, 2, 25, 121, 139, 146).

[6] Manfred Kaltenbacher, Stefan Zörner, and Andreas Hüppe. "On the importance of strong fluid-solid coupling with application to human phonation". In: *Progress in Computational Fluid Dynamics, an International Journal* 14.1 (2014), pp. 2–13 (cit. on p. 1).

[7] Manfred Kaltenbacher. "Computational acoustics in multi-field problems". In: *Journal of Computational Acoustics* 19.01 (2011), pp. 27–62. DOI: 10.1142/S0218396X11004286. eprint: http://www.worldscientific.com/doi/pdf/10.1142/S0218396X11004286. URL: http://www.worldscientific.com/doi/abs/10.1142/S0218396X11004286 (cit. on pp. 1, 18).

[8] Peter Hagedorn and Anirvan DasGupta. *Vibration and Waves in Continuous Mechanical Systems*. John Wiley & Sons, 2007 (cit. on pp. 10, 12).

[9] Nikolaos Kampanis, Vassilios Dougalis, and John Ekaterinaris. *Effective Computational Methods for Wave Propagation*. Chapman & Hall, 2008 (cit. on p. 11).

[10] Thomas Rossing. *Handbook of Acoustics*. Springer, 2007 (cit. on p. 11).

[11] Arnold Sommerfeld. *Partial differential equations in physics*. Elsevier, 1949 (cit. on pp. 12, 54).

[12] Marcus J. Grote and Christoph Kirsch. "Dirichlet-to-Neumann boundary conditions for multiple scattering problems". In: *Journal of Computational Physics* 201.2 (2004), pp. 630–650. ISSN: 0021-9991. DOI: 10.1016/j.jcp.2004.06.012. URL: http://www.sciencedirect.com/science/article/pii/S002199910400258X (cit. on p. 13).

[13] David P. Nicholls and Nilima Nigam. "Exact non-reflecting boundary conditions on general domains". In: *Journal of Computational Physics* 194.1 (2004), pp. 278–303. ISSN: 0021-9991. DOI: 10.1016/j.jcp.2003.09.006. URL: http://www.sciencedirect.com/science/article/pii/S0021999103004832 (cit. on p. 13).

[14] Bjorn Engquist and Andreq Majda. "Absorbing boundary conditions for numerical simulation of waves". In: *Mathematics of Computation* 31.139 (1977), pp. 629–651 (cit. on pp. 13, 54).

[15] Robert L. Higdon. "Absorbing boundary conditions for difference approximations to the multidimensional wave equation". In: *Mathematics of computation* 47.176 (1986), pp. 437–459 (cit. on p. 13).

[16] Dan Givoli and Beny Neta. "High-order non-reflecting boundary scheme for time-dependent waves". In: *Journal of Computational Physics* 186.1 (2003), pp. 24–46. ISSN: 0021-9991. DOI: 10.1016/S0021-9991(03)00005-6. URL: http://www.sciencedirect.com/science/article/pii/S0021999103000056 (cit. on pp. 13, 54).

[17] John R. Dea, Francis X. Giraldo, and Beny Neta. "High-order non-reflecting boundary conditions for the linearized 2-D Euler equations: No mean flow case". In: *Wave Motion* 46.3 (2009), pp. 210–220. ISSN: 0165-2125. DOI: 10.1016/j.wavemoti.2008.11.002. URL: http://www.sciencedirect.com/science/article/pii/S0165212508001029 (cit. on pp. 13, 54, 72, 75, 77).

[18] Edward Dean and Roland Glowinski. "Domain decomposition methods for mixed finite element approximations of wave problems". In: *Computers and Mathematics with Applications* 38.7-8 (1999), pp. 207–214. DOI: 10.1016/S0898-1221(99)00251-5 (cit. on p. 13).

[19] Christophe Bogey and Christophe Bailly. "Three-dimensional non-reflective boundary conditions for acoustic simulations: far field formulation and validation test cases". In: *Acta Acustica* 88.4 (2002), pp. 463–471 (cit. on p. 13).

[20] Roland Glowinski and Serguei Lapin. "Solution of a Wave Equation by a Mixed Finite Element - Fictitious Domain Method". In: *Computational Methods in Applied Mathematics* 4.4 (2004), pp. 431–444. DOI: 10.2478/cmam-2004-0024 (cit. on pp. 13, 54–56, 61, 80, 81).

[21] Zhenpeng Liao, Huang L. Wong, Yan Baipo, and Yifan Yang. "A transmitting boundary for transient wave analyses". In: *Sientia Sinica* 27.10 (1984), pp. 1063–1076 (cit. on p. 13).

[22] Alan Bamberger, Patrick Joly, and Jean E. Roberts. "Second-order absorbing boundary conditions for the wave equation: a solution for the corner problem". In: *SIAM Journal on Numerical Analysis* 27.2 (1990), pp. 323–352. DOI: 10.1137/0727021 (cit. on p. 13).

[23] Marcus Grote and Joseph Keller. "Exact Nonreflecting Boundary Conditions for the Time Dependent Wave Equation". In: *SIAM Journal on Applied Mathemathics* 55.2 (1995), pp. 280–297. DOI: 10.1137/S0036139993269266 (cit. on pp. 13, 54).

[24] Andrzej J. Safjan. "Highly accurate non-reflecting boundary conditions for finite element simulations of transient acoustics problems". In: *Computer Methods in Applied Mechanics and Engineering* 152.1-2 (1998), pp. 175–193. ISSN: 0045-7825. DOI: 10.1016/S0045-7825(97)00188-6. URL: http://www.sciencedirect.com/science/article/pii/S0045782597001886 (cit. on p. 13).

[25] Bradley Alpert, Leslie Greengard, and Thomas Hagstrom. "Nonreflecting Boundary Conditions for the Time-Dependent Wave Equation". In: *Journal of Computational Physics* 180.1 (2002), pp. 270–296. DOI: 10.1006/jcph.2002.7093 (cit. on p. 13).

[26] Steen Krenk. "Unified formulation of radiation conditions for the wave equation". In: *International Journal for Numerical Methods in Engineering* 53.2 (2002), pp. 275–295. ISSN: 1097-0207. DOI: 10.1002/nme.268 (cit. on p. 13).

[27] ZhenHuan Teng. "Exact boundary condition for time-dependent wave equation based on boundary integral". In: *Journal of Computational Physics* 190.2 (2003), pp. 398–418. ISSN: 0021-9991. DOI: 10.1016/S0021-9991(03)00281-X. URL: http://www.sciencedirect.com/science/article/pii/S002199910300281X (cit. on p. 13).

[28] Thomas Hagstrom, Assaf Mar-Or, and Dan Givoli. "High-order local absorbing conditions for the wave equation: Extensions and improvements". In: *Journal of Computational Physics* 227.6 (2008), pp. 3322–3357. ISSN: 0021-9991. DOI: 10.1016/j.jcp.2007.11.040. URL: http://www.sciencedirect.com/science/article/pii/S0021999107005360 (cit. on p. 13).

[29] Isaac Harari, Igor Patlashenko, and Dan Givoli. "Dirichlet-to-Neumann Maps for Unbounded Wave Guides". In: *Journal of Computational Physics* 143.1 (1998), pp. 200–223. DOI: 10.1006/jcph.1998.5960 (cit. on p. 13).

[30] Ata Mugan and Gregory M. Hulbert. "Nonreflecting boundary conditions in acoustics for finite element methods based upon off-surface boundary integral equations". In: *Computer Methods in Applied Mechanics and Engineering* 188.1-3 (2000), pp. 289–306. ISSN: 0045-7825. DOI: 10.1016/S0045-7825(99)00153-X. URL: http://www.sciencedirect.com/science/article/pii/S004578259900153X (cit. on p. 13).

[31] Tasos Papanastasiou, Nikos Malamataris, and Kevin Ellwood. "A New Outflow Boundary Condition". In: *International Journal for Numerical Methods in Fluids* 14 (1992), pp. 587–608. DOI: 10.1002/fld.1650140506 (cit. on p. 13).

[32] Morten Wang and Tony Sheu. "Implementation of a free boundary condition to Navier-Stokes equations". In: *International Journal of Numerical Methods for Heat & Fluid Flow* 7.1 (1997), pp. 95–111. DOI: 10.1108/09615539710156228 (cit. on p. 13).

[33] Maxim Ol'shanskii and Vladimir M. Staroverov. "On simulation of outflow boundary conditions in finite difference calculations for incompressible fluid". In: *International Journal for Numerical Methods in Fluids* 33.4 (2000), pp. 499–534. DOI: 10.1002/1097-0363(20000630)33:4<499::AID-FLD19>3.0.CO;2-7 (cit. on p. 13).

[34] Jean-Pierre Berenger. "A perfectly matched layer for the absorption of electromagnetic waves". In: *Journal of Computational Physics* 114.2 (1994), pp. 185–200. ISSN: 0021-9991. DOI: 10.1006/jcph.1994.1159. URL: http://www.sciencedirect.com/science/article/pii/S0021999184711594 (cit. on pp. 13, 54).

[35] Barbara Kaltenbacher, Manfred Kaltenbacher, and Imbo Sim. "A modified and stable version of a perfectly matched layer technique for the 3-d second order wave equation in time domain with an application to aeroacoustics". In: *Journal of Computational Physics* 235 (2013), pp. 407–422. ISSN: 0021-9991. DOI: 10.1016/j.jcp.2012.10.016. URL: http://www.sciencedirect.com/science/article/pii/S0021999112006055 (cit. on pp. 13, 54).

[36] Julen Diaz and Patrick Joly. "A time domain analysis of PML models in acoustics". In: *Computer Methods in Applied Mechanics and Engineering* 195.29-32 (2006), pp. 3820–3853. DOI: 10.1016/j.cma.2005.02.031 (cit. on pp. 13, 54).

[37] YangQing Zeng, JianQi He, and QingHuo Liu. "The application of the perfectly matched layer in numerical modeling of wave propagation in poroelastic media". In: *Geophysics* 66.4 (2001), pp. 1258–1266. DOI: 10.1190/1.1487073 (cit. on p. 13).

[38] Eliane Bécache, Dhia Bonnet-Ben, and Legendre Guillaume. "Perfectly matched layers for time-harmonic acostics in the presence of a uniform flow". In: *SIAM Journal on Numerical Analysis* 44.3 (2006), pp. 1191–1217. DOI: 10.1137/040617741 (cit. on p. 13).

[39] Alfredo Bermúdez, Luis Hervella-Nieto, Andrés Prieto, and Rodolfo Rodríguez. "An optimal perfectly matched layer with unbounded absorbing function for fime-harmonic acoustic stattering problems". In: *Journal of Computational Physics* 223.2 (2007), pp. 469–488. DOI: j.jcp.2006.09.018 (cit. on p. 13).

[40] Isaac Harari and Michael Slavutin. "Analytical and Numerical Studies of a Finite Element PML for the Helmholtz Equation". In: *Journal of Computational Acoustics* 8.1 (2000), pp. 121–137. DOI: 10.1142/S0218396X0000008X (cit. on p. 13).

[41] Quing-Huo Liu and Jianping Tao. "The perfectly matched layer for acoustic waves in absorptive media". In: *Journal of the Acoustical Society of America* 102.4 (1997), pp. 2072–2082. DOI: 10.1121/1.419657 (cit. on p. 13).

[42] Quan Qi and Thomas L. Geers. "Evaluation of the Perfectly Matched Layer for Computational Acoustics". In: *Journal of Computational Physics* 139 (1998), pp. 166–183. DOI: 10.1006/jcph.1997.5868 (cit. on pp. 13, 14, 54, 72, 81, 82).

[43] Andreas Hüppe and Manfred Kaltenbacher. "Stable matched layer for the acoustic conservation equations in the time domain". In: *Journal of Computational Acoustics* 20.01 (2012), p. 1250004. DOI: 10.1142/S0218396X11004511. eprint: http://www.worldscientific.com/doi/pdf/10.1142/S0218396X11004511. URL: http://www.worldscientific.com/doi/abs/10.1142/S0218396X11004511 (cit. on pp. 13, 54).

[44] Xiaojuen Yuan, David Borup, James W. Wiskin, Michael Berggren, Rick Eidens, and Steven A. Johnson. "Formulation and Validation of Berenger's PML absorbing boundary for the FTDT simulation of acoustic scattering". In: *IEE Transactions on Ultrasonics, Ferroelectrics and Frequency Control* 44.4 (1997), pp. 816–822. URL: http://ieeexplore.ieee.org/stamp/stamp.jsp?tp=&arnumber=655197&isnumber=14267 (cit. on p. 13).

[45] Jean-Pierre Berenger. "Three-Dimensional Perfectly Matched Layer for the Absorption of Electromagnetic Waves". In: *Journal of Computational Physics* 127.2 (1996), pp. 363–379. DOI: jcph.1996.0181 (cit. on p. 13).

[46] Raj Mittra and Umit Pekel. "A new look at the perfectly matched layer (PML) concept for the reflectionless absorption of electromagnetic waves". In: *Microwave and Guided Wave Letters, IEEE* 5.3 (1995), pp. 84–86. DOI: 10.1109/75.366461. URL: http://ieeexplore.ieee.org/stamp/stamp.jsp?tp=&arnumber=366461&isnumber=8397 (cit. on p. 13).

[47] Steven Cummer. "A simple, nearly perfectly matched layer for general electromagnetic media". In: *Microwave and Wireless Components Letters, IEEE* 13.3 (2003), pp. 128–130. DOI: 10.1109/LMWC.2003.810124 (cit. on p. 13).

[48] Fang Q. Hu. "A stable, perfectly matched layer for linearized Euler equations in unsplit physical variables". In: *Journal of Computational Physics* 173.2 (2001), pp. 455–480. DOI: 10.1006/jcph.2001.6887 (cit. on p. 15).

[49] Steffen Marburg and Bodo Nolte. *Computational Acoustics of Noise Propagation in Fluids*. Springer, 2008 (cit. on p. 15).

[50] Ardavan F. Oskooi, Lei Zhang, Avniel Yehuda, and Steven Johnson. "The failure of perfectly matched layers, and towards their redemption by adiabatic absorbers". In: *Optics Express* 16.15 (2008), pp. 11376–11392. DOI: 10.1364/OE.16.011376. URL: http://www.opticsexpress.org/abstract.cfm?URI=oe-16-15-11376 (cit. on p. 15).

[51] Simon K. Richards, Xin Zhang, Xiaoxian Chen, and Philip A. Nelson. "The evaluation of non-reflecting boundary conditions for duct acoustic computation". In: *Journal of Sound and Vibration* 270.3 (2004), pp. 539–557. DOI: 10.1016/j.jsv.2003.09.042 (cit. on pp. 15, 54).

[52] Jay C. Hardin, J. Raymond Ristorcelli, and Christopher K.W. Tam, eds. *ICASE/LaRC Workshop on Benchmark Problems in Computational Aeroacoustics (CAA)*. National Aeronautics and Space Administration, Langley Research Center, 1995 (cit. on pp. 15, 72).

[53] Milo D. Dahl, ed. *Fourth Computational Aeroacoustics (CAA) Workshop on Benchmark Problems*. NASA, Glenn Research Center, 2004 (cit. on pp. 15, 16, 72).

[54] Gianluca Lazzi and Om P. Gandhi. "On the optimal design of the PML absorbing boundary condition for the FDTD code". In: *IEEE Transactions on Antennas and Propagation* 45.5 (1997), pp. 914–917. DOI: 10.1109/8.575651 (cit. on p. 15).

[55] Ching-Lie Li, Chien-Wei Liu, and Shao-Hon Chen. "Optimization of a PML absorber's conductivity profile using FDTD". In: *Microwave and Optical Technology Letters* 37.5 (2003), pp. 380–383. DOI: 10.1002/mop.10924 (cit. on p. 15).

[56] Tim Colonius and Sanjiva Lele. "Computational aeroacoustics: progress on nonlinear problems of sound generation". In: *Progress in Aerospace Sciences* 40.6 (2004), pp. 345–416. DOI: 10.1016/j.paerosci.2004.09.001 (cit. on p. 18).

[57] Meng Wang, Jonathan B. Freund, and Sanjiva K. Lele. "Computational Prediction of Flow-Generated Sound". In: *Annual Reviews of Fluid Mechanics* 38.1 (2006), pp. 483–512. DOI: 10.1146/annurev.fluid.38.050304.092036 (cit. on p. 19).

[58] Andreas Hüppe and Manfred Kaltenbacher. "Spectral finite elements for computational aeroacoustics using acoustic perturbation equations". In: *Journal of Computational Acoustics* 20.02 (2012), p. 1240005. DOI: 10.1142/S0218396X1240005X. eprint: http://www.worldscientific.com/doi/pdf/10.1142/S0218396X1240005X. URL: http://www.worldscientific.com/doi/abs/10.1142/S0218396X1240005X (cit. on p. 19).

[59] Michael J. Lighthill. "On sound generated aerodynamically I. General Theory". In: *Proceedings of the Royal Society of London* 211 (1952), pp. 564–587 (cit. on p. 21).

[60] Michael J. Lighthill. "On Sound Generated Aerodynamically. II. Turbulence as a Source of Sound". In: *Proceedings of the Royal Society of London* (1954), pp. 1–32 (cit. on p. 21).

[61] N. Curle. "The influence of solid boundaries upon aerodynamic sound". In: *Proceedings of the Royal Society of London* 231.1187 (1955), pp. 505–514. DOI: 10.1098/rspa.1955.0191 (cit. on pp. 21, 23).

[62] Owen M. Phillips. "On the generation of sound by supersonic turbulent shear layers". In: *Journal of Fluid Mechanics* 9 (01 Aug. 1960), pp. 1–28. ISSN: 1469-7645. DOI: 10.1017/S0022112060000888. URL: http://journals.cambridge.org/article_S0022112060000888 (cit. on pp. 21, 23).

[63] John E. Ffowcs-Williams and David L. Hawkings. "Sound generation by turbulence and surfaces in arbitrary motion". In: *Philosophical Transactions of the Royal Society of London. Series A, Mathematical and Physical Sciences* 264.1151 (1969), pp. 321–342 (cit. on pp. 21, 23).

[64] Marvin Goldstein. "A generalized acoustic analogy". In: *Journal of Fluid Mechanics* 488 (June 2003), pp. 315–333. ISSN: 1469-7645. DOI: 10.1017/S0022112003004890. URL: http://journals.cambridge.org/article_S0022112003004890 (cit. on pp. 21, 24).

[65] Kenneth S. Brentner and Feri Farassat. "Analytical comparison of the acoustic analogy and Kirchhoff formulation for moving surfaces". In: *AIAA journal* 36.8 (1998), pp. 1379–1386. DOI: 10.2514/2.558 (cit. on p. 23).

[66] Siegfried Wagner, Rainer Bareiß, and Gianfranco Guidati. *Wind Turbine Noise*. Springer-Verlag, 1996 (cit. on p. 23).

[67] Santiago Badia, Ramon Codina, and Hector Espinoza. "Stability, Convergence, and Accuracy of Stabilized Finite Element Methods for the Wave Equation in Mixed Form". In: *SIAM Journal on Numerical Analysis* 52.4 (May 2014), pp. 1729–1752. DOI: 10.1137/130918708 (cit. on pp. 25, 27, 55, 62, 64, 65, 67–69, 83, 86–88, 90, 91, 101).

[68] Hector Espinoza, Ramon Codina, and Santiago Badia. "A Sommerfeld non-reflecting boundary condition for the wave equation in mixed form". In: *Computer Methods in Applied Mechanics and Engineering* 276 (July 2014), pp. 122–148. ISSN: 0045-7825. DOI: 10.1016/j.cma.2014.03.015. URL: http://www.sciencedirect.com/science/article/pii/S0045782514001017 (cit. on pp. 25, 53, 86–88, 91, 101).

[69] Hector Espinoza, Ramon Codina, and Santiago Badia. "On some time marching schemes for the stabilized finite element approximation of the mixed wave equation". In: *Computer Methods in Applied Mechanics and Engineering* (Dec. 2014). Submitted (cit. on pp. 25, 85).

[70] Ramon Codina, Hector Espinoza, and Santiago Badia. "Linear waves in mixed form: functional settings and stabilized finite element approximation". In: *6th Scientific Computing Seminar / VMS 2012*. Christian-Albrechts-Universität zu Kiel. June 2012. URL: http://www.math.uni-kiel.de/numerik/braack/conf/vms2012/ (cit. on p. 25).

[71] Hector Espinoza, Ramon Codina, and Santiago Badia. "Wave Equation in Mixed Form: Stability and Convergence Estimates using Stabilized Finite Element Methods". In: *Congress on Numerical Methods in Engineering CNM 2013*. Sociedad Española de Métodos Numéricos en Ingeniería (SEMNI). June 2013. URL: http://congress.cimne.com/metnum2013/ (cit. on p. 25).

[72] Oriol Guasch, Marc Arnela, Ramon Codina, and Hector Espinoza. "A stabilized arbitrary Lagrangian Eulerian finite element method for the mixed wave equation with application to diphthong production". In: *WCCM XI*. IACM and ECCOMAS. July 2014. URL: http://www.wccm-eccm-ecfd2014.org/ (cit. on p. 25).

[73] Hector Espinoza, Ramon Codina, and Santiago Badia. "Numerical analysis and benchmarking of a Sommerfeld-type non-reflecting boundary condition for the wave equation in mixed form". In: *WCCM XI*. IACM and ECCOMAS. July 2014. URL: http://www.wccm-eccm-ecfd2014.org/ (cit. on p. 25).

[74] Marc Arnela, Oriol Guasch, Ramon Codina, and Hector Espinoza. "Finite element computation of diphthong sounds using tuned two-dimensional vocal tracts". In: *7th Forum Acusticum*. Polish Acoustics Society and European Acoustics Association. Sept. 2014. URL: http://www.fa2014.pl/ (cit. on p. 25).

[75] Oriol Guasch, Marc Arnela, Ramon Codina, and Hector Espinoza. "Stabilized finite element formulation for the mixed convected wave equation in domains with driven flexible boundaries". In: *NOVEM 2015*. INSA. Apr. 2015. URL: http://novem2015.sciencesconf.org/ (cit. on p. 25).

[76] Ramon Codina, Marc Arnela, Oriol Guasch, and Hector Espinoza. "Waves in time dependent domains". In: *10th International Workshop on Variational Multiscale and Stabilized Finite Elements (VMS2015)*. German Association for Computational Mechanics (GACM). Garching, Germany, Feb. 2015. URL: http://www.lnm.mw.tum.de/vms2015/ (cit. on p. 26).

[77] Ramon Codina, Oriol Guasch, Marc Arnela, and Hector Espinoza. "Approximation of waves written in mixed form in time dependent domains". In: *Congresso de Métodos Numéricos em Engenharia*. Instituto Superior Técnico. June 2015. URL: http://www.dem.ist.utl.pt/cmn2015/ (cit. on p. 26).

[78] Franco Brezzi and Michel Fortin. *Mixed and hybrid finite element methods*. New York, NY, USA: Springer-Verlag New York, Inc., 1991. ISBN: 0-387-97582-9 (cit. on pp. 27, 55).

[79] Douglas Arnold, Franco Brezzi, and Michel Fortin. "A stable finite element for the Stokes equations". In: *Calcolo* 21 (4 1984), pp. 337–344. ISSN: 0008-0624. DOI: 10.1007/BF02576171 (cit. on pp. 27, 55).

[80] Franco Brezzi, Jim Douglas Jr, and L. Donatella Marini. "Two families of mixed finite elements for second order elliptic problems". In: *Numerische Mathematik* 47.2 (June 1985), pp. 217–235. ISSN: 0029-599X, 0945-3245. DOI: 10.1007/BF01389710. URL: http://link.springer.com/article/10.1007/BF01389710 (visited on 03/20/2013) (cit. on pp. 27, 55).

[81] Jean-Claude Nédélec. "A new family of mixed finite elements in $\mathbb{R}^3$". In: *Numerische Mathematik* 50.1 (Jan. 1986), pp. 57–81. ISSN: 0029-599X, 0945-3245. DOI: 10.1007/BF01389668. URL: http://link.springer.com/article/10.1007/BF01389668 (visited on 03/20/2013) (cit. on pp. 27, 55).

[82] Todd Arbogast and Dana Brunson. "A computational method for approximating a Darcy-Stokes system governing a vuggy porous medium". In: *Computational Geosciences* 11 (3 2007), pp. 207–218. ISSN: 1420-0597. DOI: 10.1007/s10596-007-9043-0 (cit. on pp. 27, 55).

[83] Kent-Andre Mardal, Xue-Cheng Tai, and Ragnar Winther. "A Robust Finite Element Method for Darcy-Stokes Flow". In: *SIAM Journal on Numerical Analysis* 40.5 (2002), pp. 1605–1631. DOI: 10.1137/S0036142901383910. eprint: http://epubs.siam.org/doi/pdf/10.1137/S0036142901383910. URL: http://epubs.siam.org/doi/abs/10.1137/S0036142901383910 (cit. on pp. 27, 55).

[84] Eliane Bécache, Patrick Joly, and Chrysoula Tsogka. "An Analysis of New Mixed Finite Elements for the Approximation of Wave Propagation Problems". In: *SIAM Journal on Numerical Analysis* 37.4 (2000), pp. 1053–1084. DOI: 10.1137/S0036142998345499 (cit. on pp. 27, 28, 55).

[85] Eliane Bécache, Patrick Joly, and Chrysoula Tsogka. "A New Family of Mixed Finite Elements for the Linear Elastodynamic Problem". In: *SIAM Journal on Numerical Analysis* 39.6 (2002), pp. 2109–2132. DOI: 10.1137/S0036142999359189. eprint: http://epubs.siam.org/doi/pdf/10.1137/S0036142999359189. URL: http://epubs.siam.org/doi/abs/10.1137/S0036142999359189 (cit. on pp. 27, 55).

[86] Charalambos Makridakis. "On mixed finite element methods for linear elastodynamics". In: *Numerische Mathematik* 61 (1 1992), pp. 235–260. ISSN: 0029-599X. DOI: 10.1007/BF01385506 (cit. on pp. 27, 55).

[87] Thomas J.R. Hughes. "Multiscale phenomena: Green's functions, the Dirichlet-to-Neumann formulation, subgrid scale models, bubbles and the origins of stabilized methods". In: *Computer Methods in Applied Mechanics and Engineering* 127.1-4 (1995), pp. 387–401. ISSN: 0045-7825. DOI: 10.1016/0045-7825(95)00844-9. URL: http://www.sciencedirect.com/science/article/pii/0045782595008449 (cit. on pp. 27, 63, 90).

[88] Santiago Badia and Ramon Codina. "Stokes, Maxwell and Darcy: A single finite element approximation for three model problems". In: *Applied Numerical Mathematics* 62.4 (2012), pp. 246–263. ISSN: 0168-9274. DOI: 10.1016/j.apnum.2011.07.001. URL: http://www.sciencedirect.com/science/article/pii/S0168927411001097 (cit. on p. 27).

[89] Thomas J.R. Hughes, Gonzalo R. Feijoo, Luca Mazzei, and Jean-Baptiste Quincy. "The variational multiscale method-A paradigm for computational mechanics". In: *Computer Methods in Applied Mechanics and Engineering* 166.1-2 (1998), pp. 3–24. ISSN: 0045-7825. DOI: 10.1016/S0045-7825(98)00079-6. URL: http://www.sciencedirect.com/science/article/pii/S0045782598000796 (cit. on pp. 28, 31, 63, 90).

[90] Ramon Codina. "Finite element approximation of the hyperbolic wave equation in mixed form". In: *Computer Methods in Applied Mechanics and Engineering* 197.13-16 (2008), pp. 1305–1322. ISSN: 0045-7825. DOI: 10.1016/j.cma.2007.11.006. URL: http://www.sciencedirect.com/science/article/pii/S0045782507004550 (cit. on pp. 28, 31, 33, 34, 55, 64, 86, 90).

[91] Santiago Badia and Ramon Codina. "Unified Stabilized Finite Element Formulations for the Stokes and the Darcy Problems". In: *SIAM Journal on Numerical Analysis* 47.3 (2009), pp. 1971–2000. DOI: 10.1137/08072632X. eprint: http://epubs.siam.org/doi/pdf/10.1137/08072632X. URL: http://epubs.siam.org/doi/abs/10.1137/08072632X (cit. on pp. 28, 34, 50, 64, 90).

[92] Patrick Joly. "Variational Methods for Time-Dependent Wave Propagation Problems". In: *Topics in Computational Wave Propagation*. Ed. by Mark Ainsworth et al. Vol. 31. Lecture Notes in Computational Science and Engineering. Springer Berlin Heidelberg, 2003, pp. 201–264. ISBN: 978-3-642-55483-4. DOI: 10.1007/978-3-642-55483-4_6 (cit. on p. 28).

[93] Tunc Geveci. "On the application of mixed finite element methods to the wave equations". In: *Modélisation mathématique et analyse numérique* 22.2 (1988), pp. 243–250. ISSN: 0764-583X. URL: http://cat.inist.fr/?aModele=afficheN%5C&cpsidt=7795462 (cit. on p. 28).

[94] Eleanor Jenkins, Béatrice Rivière, and Mary Wheeler. "A Priori Error Estimates for Mixed Finite Element Approximations of the Acoustic Wave Equation". In: *SIAM Journal on Numerical Analysis* 40.5 (2002), pp. 1698–1715. DOI: 10.1137/S0036142901388068 (cit. on p. 28).

[95] Donald A. French. "A space-time finite element method for the wave equation". In: *Computer Methods in Applied Mechanics and Engineering* 107.1-2 (1993), pp. 145–157. ISSN: 0045-7825. DOI: 10.1016/0045-7825(93)90172-T. URL: http://www.sciencedirect.com/science/article/pii/004578259390172T (cit. on p. 28).

[96] Ohannes Karakashian and Charalambos Makridakis. "Convergence of a Continuous Galerkin Method with Mesh Modification for Nonlinear Wave Equations". In: *Mathematics of Computation* 74.249 (2005), pp. 85–102. ISSN: 00255718. URL: http://www.jstor.org/stable/4100238 (cit. on p. 28).

[97] Ramon Codina. "Analysis of a stabilized finite element approximation of the Oseen equations using orthogonal subscales". In: *Applied Numerical Mathematics* 58.3 (2008), pp. 264–283. ISSN: 0168-9274. DOI: 10.1016/j.apnum.2006.11.011. URL: http://www.sciencedirect.com/science/article/pii/S0168927406002194 (cit. on pp. 31, 33, 49, 62, 89).

[98] Ramon Codina. "Stabilized finite element approximation of transient incompressible flows using orthogonal subscales". In: *Computer Methods in Applied Mechanics and Engineering* 191.39-40 (2002), pp. 4295–4321. ISSN: 0045-7825. DOI: 10.1016/S0045-7825(02)00337-7. URL: http://www.sciencedirect.com/science/article/pii/S0045782502003377 (cit. on pp. 32, 63, 90).

[99] Ramon Codina. "Stabilization of incompressibility and convection through orthogonal sub-scales in finite element methods". In: *Computer Methods in Applied Mechanics and Engineering* 190.13-14 (2000), pp. 1579–1599. ISSN: 0045-7825. DOI: 10.1016/S0045-7825(00)00254-1. URL: http://www.sciencedirect.com/science/article/pii/S0045782500002541 (cit. on pp. 32, 63, 90).

[100] Ramon Codina, Jordi Blasco, Gustavo Buscaglia, and Antonio Huerta. "Implementation of a stabilized finite element formulation for the incompressible Navier-Stokes equations based on a pressure gradient projection". In: *International Journal for Numerical Methods in Fluids* 37 (2001), pp. 419–444 (cit. on p. 33).

[101] Santiago Badia. "On stabilized finite element methods based on the Scott-Zhang projector. Circumventing the inf-sup condition for the Stokes problem". In: *Computer Methods in Applied Mechanics and Engineering* 247-248 (2012), pp. 65–72. ISSN: 0045-7825. DOI: 10.1016/j.cma.2012.07.020. URL: http://www.sciencedirect.com/science/article/pii/S0045782512002435 (cit. on p. 33).

[102] Santiago Badia and Ramon Codina. "Stabilized continuous and discontinuous Galerkin techniques for Darcy flow". In: *Computer Methods in Applied Mechanics and Engineering* 199.25-28 (2010), pp. 1654–1667. ISSN: 0045-7825. DOI: 10.1016/j.cma.2010.01.015. URL: http://www.sciencedirect.com/science/article/pii/S0045782510000241 (cit. on p. 33).

[103] Santiago Badia and Ramon Codina. "Analysis of a Stabilized Finite Element Approximation of the Transient Convection-Diffusion Equation Using an ALE Framework". In: *SIAM Journal on Numerical Analysis* 44.5 (2006), pp. 2159–2197. DOI: 10.1137/050643532. eprint: http://epubs.siam.org/doi/pdf/10.1137/050643532. URL: http://epubs.siam.org/doi/abs/10.1137/050643532 (cit. on pp. 34, 64, 65, 86, 91, 92).

[104] L. Ridgway Scott and Shangyou Zhang. "Finite element interpolation of nonsmooth functions satisfying boundary conditions". In: *Mathematics of Computation* 54.190 (1990), pp. 483–493. DOI: 10.1090/S0025-5718-1990-1011446-7 (cit. on p. 43).

[105] Dan Givoli. "High-order local non-reflecting boundary conditions: a review". In: *Wave Motion* 39.4 (2004), pp. 319–326. ISSN: 0165-2125. DOI: 10.1016/j.wavemoti.2003.12.004. URL: http://www.sciencedirect.com/science/article/pii/S0165212503001203 (cit. on pp. 53, 54).

[106] Semyon V. Tsynkov. "Numerical solution of problems on unbounded domains. A review". In: *Applied Numerical Mathematics* 27.4 (1998), pp. 465–532. ISSN: 0168-9274. DOI: 10.1016/S0168-9274(98)00025-7. URL: http://www.sciencedirect.com/science/article/pii/S0168927498000257 (cit. on pp. 53, 54).

[107] Daniel Appelö and Gunilla Kreiss. "Application of a perfectly matched layer to the nonlinear wave equation". In: *Wave Motion* 44.7-8 (2007), pp. 531–548. ISSN: 0165-2125. DOI: 10.1016/j.wavemoti.2007.01.004. URL: http://www.sciencedirect.com/science/article/pii/S0165212507000145 (cit. on p. 54).

[108] Ying Zhou and Zhijian Wang. "Absorbing boundary conditions for the Euler and Navier-Stokes equations with the spectral difference method". In: *J. Comput. Phys.* 229.23 (Nov. 2010), pp. 8733–8749. ISSN: 0021-9991. DOI: 10.1016/j.jcp.2010.08.007 (cit. on p. 54).

[109] Fang Q. Hu. "A Perfectly Matched Layer absorbing boundary condition for linearized Euler equations with a non-uniform mean flow". In: *Journal of Computational Physics* 208.2 (2005), pp. 469–492. ISSN: 0021-9991. DOI: 10.1016/j.jcp.2005.02.028. URL: http://www.sciencedirect.com/science/article/pii/S0021999105001117 (cit. on p. 54).

[110] Jan S. Hesthaven. "On the Analysis and Construction of Perfectly Matched Layers for the Linearized Euler Equations". In: *Journal of Computational Physics* 142.1 (1998), pp. 129–147. ISSN: 0021-9991. DOI: 10.1006/jcph.1998.5938. URL: http://www.sciencedirect.com/science/article/pii/S0021999198959381 (cit. on pp. 54, 72).

[111] Dan Givoli. "Computational Absorbing Boundaries". In: *Computational Acoustics of Noise Propagation in Fluids*. Ed. by Steffen Marburg and Bodo Nolte. Vol. 31. Springer Berlin Heidelberg, 2008, pp. 145–166. ISBN: 978-3-540-77447-1. DOI: 10.1007/978-3-540-77448-8_6 (cit. on p. 54).

[112] Mi Zhao, Xiuli Du, Jingbo Liu, and Heng Liu. "Explicit finite element artificial boundary scheme for transient scalar waves in two-dimensional unbounded waveguide". In: *International Journal for Numerical Methods in Engineering* 87.11 (2011), pp. 1074–1104. ISSN: 1097-0207. DOI: 10.1002/nme.3147 (cit. on p. 54).

[113] Eliane Bécache, Dan Givoli, and Thomas Hagstrom. "High-order Absorbing Boundary Conditions for anisotropic and convective wave equations". In: *Journal of Computational Physics* 229.4 (2010), pp. 1099–1129. ISSN: 0021-9991. DOI: 10.1016/j.jcp.2009.10.012. URL: http://www.sciencedirect.com/science/article/pii/S0021999109005579 (cit. on p. 54).

[114] Julen Diaz and Patrick Joly. "An Analysis of Higher Order Boundary Conditions for the Wave Equation". In: *SIAM Journal of Applied Mathematics* 65.5 (2005), pp. 1547–1575. DOI: 10.1137/S0036139903436145 (cit. on p. 54).

[115] Alvin Bayliss and Eli Turkel. "Radiation boundary conditions for wave-like equations". In: *Communications on Pure and Applied Mathematics* 33.6 (1980), pp. 707–725. ISSN: 1097-0312. DOI: 10.1002/cpa.3160330603 (cit. on p. 54).

[116] Robert L. Higdon. "Numerical absorbing boundary conditions for the wave equation". In: *Mathematics of computation* 49.179 (1987), pp. 65–90 (cit. on p. 54).

[117] Joseph B. Keller and Dan Givoli. "Exact non-reflecting boundary conditions". In: *Journal of Computational Physics* 82.1 (1989), pp. 172–192. ISSN: 0021-9991. DOI: 10.1016/0021-9991(89)90041-7 (cit. on p. 54).

[118] Viktor S. Ryaben'Kii and Semyon V. Tsynkov. "Artificial boundary conditions for the numerical solution of external viscous flow problems". In: *SIAM journal on numerical analysis* 32.5 (1995), pp. 1355–1389 (cit. on p. 54).

[119] Francis Collino. "High order absorbing boundary conditions for wave propagation models: straight line boundary and corner cases". In: *Second International Conference on Mathematical and Numerical Aspects of Wave Propagation*. SIAM, 1993, pp. 161–171 (cit. on p. 54).

[120] Clarence W. Rowley and Tim Colonius. "Discretely Nonreflecting Boundary Conditions for Linear Hyperbolic Systems". In: *Journal of Computational Physics* 157.2 (2000), pp. 500–538. ISSN: 0021-9991. DOI: 10.1006/jcph.1999.6383. URL: http://www.sciencedirect.com/science/article/pii/S0021999199963830 (cit. on p. 54).

[121] Murthy N. Guddati and John L. Tassoulas. "Continued-Fraction absorbing boundary conditions for the wave equation". In: *Journal of Computational Acoustics* 08.01 (2000), pp. 139–156. DOI: 10.1142/S0218396X00000091. URL: http://www.worldscientific.com/doi/abs/10.1142/S0218396X00000091 (cit. on p. 54).

[122] Thomas Hagstrom and Timothy Warburton. "A new auxiliary variable formulation of high-order local radiation boundary conditions: corner compatibility conditions and extensions to first-order systems". In: *Wave Motion* 39.4 (2004), pp. 327–338 (cit. on p. 54).

[123] Peter Monk. *Finite element methods for Maxwell's equations*. Oxford University Press, 2003 (cit. on p. 62).

[124] Julien Berland, Christophe Bogey, and Christophe Bailly. "Low-dissipation and low-dispersion fourth-order Runge–Kutta algorithm". In: *Computers & Fluids* 35.10 (2006), pp. 1459–1463. ISSN: 0045-7930. DOI: 10.1016/j.compfluid.2005.04.003. URL: http://www.sciencedirect.com/science/article/pii/S0045793005000575 (cit. on p. 86).

[125] Kostas Tselios and Theodore E. Simos. "Runge-Kutta methods with minimal dispersion and dissipation for problems arising from computational acoustics". In: *Journal of Computational and Applied Mathematics* 175.1 (2005), pp. 173–181. ISSN: 0377-0427. DOI: 10.1016/j.cam.2004.06.012. URL: http://www.sciencedirect.com/science/article/pii/S0377042704002511 (cit. on p. 86).

[126] Hui Xu and Pierre Sagaut. "Optimal low-dispersion low-dissipation LBM schemes for computational aeroacoustics". In: *Journal of Computational Physics* 230.13 (2011), pp. 5353–5382. ISSN: 0021-9991. DOI: 10.1016/j.jcp.2011.03.040. URL: http://www.sciencedirect.com/science/article/pii/S0021999111002014 (cit. on p. 86).

[127] Jiequan Li and Zhicheng Yang. "The von Neumann analysis and modified equation approach for finite difference schemes". In: *Applied Mathematics and Computation* 225 (2013), pp. 610–621. ISSN: 0096-3003. DOI: 10.1016/j.amc.2013.09.046. URL: http://www.sciencedirect.com/science/article/pii/S0096300313010254 (cit. on p. 86).

[128] Jan Nordström. "Conservative Finite Difference Formulations, Variable Coefficients, Energy Estimates and Artificial Dissipation". In: *Journal of Scientific Computing* 29.3 (2006), pp. 375–404. ISSN: 0885-7474. DOI: 10.1007/s10915-005-9013-4 (cit. on p. 86).

[129] Patrick Joly and Jerónimo Rodríguez. "Optimized higher order time discretization of second order hyperbolic problems: Construction and numerical study". In: *Journal of Computational and Applied Mathematics* 234.6 (2010), pp. 1953–1961. ISSN: 0377-0427. DOI: 10.1016/j.cam.2009.08.046. URL: http://www.sciencedirect.com/science/article/pii/S037704270900524X (cit. on p. 86).

[130] Yajuan Sun and PSP Tse. "Symplectic and multisymplectic numerical methods for Maxwell's equations". In: *Journal of Computational Physics* 230.5 (2011), pp. 2076–2094 (cit. on p. 86).

[131] Erik Burman and Miguel A. Fernández. "Galerkin Finite Element Methods with Symmetric Pressure Stabilization for the Transient Stokes Equations: Stability and Convergence Analysis". In: *SIAM Journal on Numerical Analysis* 47.1 (2008), pp. 409–439. DOI: 10.1137/070707403. eprint: http://epubs.siam.org/doi/pdf/10.1137/070707403. URL: http://epubs.siam.org/doi/abs/10.1137/070707403 (cit. on p. 86).

[132] Erik Burman. "Consistent SUPG-method for transient transport problems: Stability and convergence". In: *Computer Methods in Applied Mechanics and Engineering* 199.17-20 (2010), pp. 1114–1123. ISSN: 0045-7825. DOI: 10.1016/j.cma.2009.11.023. URL: http://www.sciencedirect.com/science/article/pii/S0045782509003983 (cit. on p. 86).

[133] Juan C. López-Marcos. "Crank-Nicolson method". In: *Encyclopedia of Mathematics*. Springer, 2012, p. 1 (cit. on p. 86).

[134] Gunwoo Noh, Seounghyun Ham, and Klaus-Jürgen Bathe. "Performance of an implicit time integration scheme in the analysis of wave propagations". In: *Computers & Structures* 123 (2013), pp. 93–105. ISSN: 0045-7949. DOI: 10.1016/j.compstruc.2013.02.006. URL: http://www.sciencedirect.com/science/article/pii/S0045794913000540 (cit. on p. 86).

[135] Alexander V. Idesman, Himadri Samajder, Eugenio Aulisa, and Padmanabhan Seshaiyer. "Benchmark problems for wave propagation in elastic materials". In: *Computational Mechanics* 43.6 (2009), pp. 797–814. ISSN: 0178-7675. DOI: 10.1007/s00466-008-0346-3 (cit. on p. 86).

[136] Ramon Codina, Javier Principe, Oriol Guasch, and Santiago Badia. "Time dependent subscales in the stabilized finite element approximation of incompressible flow problems". In: *Computer Methods in Applied Mechanics and Engineering* 196.21-24 (2007), pp. 2413–2430. ISSN: 0045-7825. DOI: 10.1016/j.cma.2007.01.002. URL: http://www.sciencedirect.com/science/article/pii/S0045782507000035 (cit. on p. 90).

[137] Santiago Badia and Ramon Codina. "On a multiscale approach to the transient Stokes problem: Dynamic subscales and anisotropic space-time discretization". In: *Applied Mathematics and Computation* 207.2 (2009), pp. 415–433. ISSN: 0096-3003. DOI: 10.1016/j.amc.2008.10.059. URL: http://www.sciencedirect.com/science/article/pii/S0096300308008291 (cit. on p. 90).

[138] Jean-Luc Guermond and Richard Pasquetti. "A correction technique for the dispersive effects of mass lumping for transport problems". In: *Computer Methods in Applied Mechanics and Engineering* 253 (2013), pp. 186–198. ISSN: 0045-7825. DOI: 10.1016/j.cma.2012.08.011. URL: http://www.sciencedirect.com/science/article/pii/S0045782512002630?v=s5 (cit. on p. 107).

[139] Rémi Blandin, Marc Arnela, Rafael Laboissière, Xavier Pelorson, Oriol Guasch, Annemie Van Hirtum, and Xavier Laval. "Effects of higher order propagation modes in vocal tract like geometries". In: *The Journal of the Acoustical Society of America* 137.2 (2015), pp. 832–843 (cit. on pp. 121, 131).

[140] Marc Arnela, Oriol Guasch, and Francesc Alías. "Effects of head geometry simplifications on acoustic radiation of vowel sounds based on time-domain finite-element simulations". In: *The Journal of the Acoustical Society of America* 134.4 (2013), pp. 2946–2954. DOI: 10.1121/1.4818756. URL: http://scitation.aip.org/content/asa/journal/jasa/134/4/10.1121/1.4818756 (cit. on p. 139).

[141] *TeX Live*. 2014. URL: https://www.tug.org/texlive/.

[142] *biblatex - Bibliographies in LaTeX using BibTeX for sorting only*. 2014. URL: https://www.ctan.org/pkg/biblatex.

[143] *biber - A BibTeX replacement for users of biblatex*. 2014. URL: https://www.ctan.org/pkg/biber.

[144] *LaTeX*. 2015. URL: http://en.wikibooks.org/wiki/LaTeX.

[145] *TeX*. 2015. URL: http://en.wikibooks.org/wiki/TeX.

[146] *Library of Congress Recommended Format Specifications*. LOC RFS. 2015. URL: http://www.loc.gov/preservation/resources/rfs/.

[147] *Fedora Workstation*. 2015. URL: https://getfedora.org/en/.

[148] *GCC, the GNU Compiler Collection*. 2014. URL: https://gcc.gnu.org/.

[149] *Open MPI: Open Source High Performance Computing*. 2014. URL: http://www.open-mpi.org/.

[150] *PETSc: Portable, Extensible Toolkit for Scientific Computation*. 2014. URL: http://www.mcs.anl.gov/petsc/.